universität wien

# DISSERTATION / DOCTORAL THESIS

Titel der Dissertation /Title of the Doctoral Thesis

„Towards Scalable Photonic Entanglement Generation“


verfasst von / submitted by

Rui Ferreira Vasconcelos, MSc


angestrebter akademischer Grad / in partial fulfilment of the requirements for the degree of

Doktor der Naturwissenschaften (Dr. rer. nat.)

Wien, 2019 / Vienna, 2019

| | |
|---|---|
| Studienkennzahl lt. Studienblatt / degree programme code as it appears on the student record sheet: | A 796 605 411 |
| Dissertationsgebiet lt. Studienblatt / field of study as it appears on the student record sheet: | Physik |
| Betreut von / Supervisor: | Univ.-Prof. Dr. Philip Walther |
| Mitbetreut von / Co-Supervisor: | Dr. Michael Trupke |

# Abstract

The realisation of quantum computers and networks, beyond proof-of-principle quantum information processing and prototyping, awaits the scaling up of the underlying physical platforms. By increasing the number of quantum bits (qubits) under experimental control, these devices will overtake their classical counterparts in solving certain tasks. From this perspective, this thesis focuses on the scalable generation of photonic cluster states for measurement-based quantum computation.

Over the last decade, photonic entanglement generation was most commonly realised by spontaneous parametric down conversion (SPDC) in non-linear crystals, whose probabilistic nature constituted a major hurdle to scaling up. To overcome this issue, alternative, proposed schemes relied on sequential operations on a single-photon emitter (SPE), to deterministically produce strings of entangled photons. The series of experiments that constitute this thesis portrays the transition from SPDC- to SPE-based photonic entanglement-generation schemes.

Firstly, a SPDC source is characterised and modified to produce 4-qubit cluster states. These are then applied to the demonstration of elements of measurement-based error correction, where an arbitrary logical qubit is protected against phase noise, by encoding into the cluster state. Arising errors are detected by syndrome readout and the initially encoded state is recovered. This demonstration shows a building block of measurement-based quantum computing, towards a realistic fault-tolerant scenario.

Secondly, a scalable SPE-based entanglement-generation protocol, which resorts to a single optical transition of an emitter and an unbalanced polarising interferometer, is presented. By employing a single transition to produce photonic time-bin qubits, this scheme relaxes the stringent requirements placed upon the emitter by similar protocols and, therefore, widens the range of platforms suited for photonic entanglement generation. The interferometer, then, converts the photonic qubits from a time-bin basis into a polarisation basis, where quantum gates and tomography can be performed.

The basic unit of the proposed iterative scheme is experimentally demonstrated, using a nitrogen-vacancy (NV) centre as the single-photon emitter, to produce an entangled state between a spin of the NV centre and the polarisation of an emitted photon. Finally, the outlook for this work is examined – a Purcell enhanced NV centre would overcome some of the experimental limitations, which currently restrict the size of the cluster state to two qubits. This would be possible with current technology and could enable the production of linear cluster states with hundreds of photons. Operating several such SPEs in parallel, would open up the possibility to produce 3-dimensional cluster states, constituting a universal resource for fault-tolerant quantum computing and communication.

# Zuzammenfassung

Für die Realisierung von echten Quantencomputern und Quantennetzwerken über die vorhandenen einfachen Laborsystem hinaus, muss die Zahl der Quantenbits (Qubits) und der notwendigen Kontrollsysteme drastisch erhöht werden. Dies wird es Quantencomputern ermöglichen bestimmte wichtige Probleme um ein vielfaches schneller zu lösen als ihre klassischen Pendants. In der vorliegenden Arbeit wird es darum gehen experimentelle Grundlagen zu schaffen für diese Skalierung von einfachen Quantensystemen hin zu photonischen Clusterzuständen.

In der Vergangenheit wurde für die Verschränkung von Photonen die spontane parametrische Fluoreszenz (SPDC) Technik verwendet. Diese arbeitet mit nicht-linearen Kristallen zur Photonenverschränkung, allerdings ist diese Technik aufgrund ihrer„spontanen“ zufälligen Natur nur schwer zu skalieren. Dieses Problem wird in dieser Arbeit dadurch umgangen, dass ein alternativer Ansatz mit sequenziell arbeitenden Einzelphotonenquelle (SPE) benutzt wird. Hierdurch wird eine Kette aus verschränkten Photonen erzeugt. Diese Arbeit beschreibt die Weiterentwicklung vom SPDC Ansatz zur SPE basierten Photonenerzeugung anhand von mehrerer Experimente.

Zuerst wird eine SPDC-Quelle benützt, um einen 4-Qubit Clusterzustand zu erzeugen. Dieser wird dann benutzt um eine messungsbasiert- Quantenfehlerkorrektur durchzuführen. Hierfür wird ein logisches Qbit in einem Clusterszustand gespeichert, dass danach Umgebungseinflüssen ausgesetzt wird. Anschließend wird das logische Qubit aus dem Clusterzustand rekonstruiert. Dies demonstriert die Möglichkeit von messungs-basiertem Quantencomputing in einem realistischen Szenario.

Anschließend wird in dieser Arbeit ein SPE basiertes Verschränkungsprotokoll vorgestellt. Dieses basiert auf nur einem einzigem optischen Übergang und einem asymmetrischen Interferometer mit zwei unterschiedlich langen Armen. Der optische Übergang wird benutzt um ein photonisches Qubit zu erzeugen. Dieser Prozess wird kontinuierlich wiederholt. Das Interferometer dient nun dazu die zeitlichen Unterschiede auszugleichen und zwei hintereinander erzeugte Qubits zu verschränken und in einer polarisieren Basis auszugeben. Quantentomographie wird anschließend durchgeführt, um die Quantennatur des Prozesses aufzuzeigen.

Die Grundbausteine des vorgeschlagenen Protokolls werden in dieser Arbeit vorgestellt und die experimentellen Details diskutiert. Das benützte Quantensystem ist das Stickstoff-Fehlstellen-Zentrum (NV Centre); dieses wird als Einzelphotonenquelle benützt. Leider war es nicht möglich mit dem derzeitigen Experiment Photonenzustände mit mehr als zwei Photonen herzustellen. Der Grund hierfür war die hohe experimentelle Verlustrate der Photonen und die starken Phononen-Seitenbänder des NVs. In Zukunft werden wir versuchen

dieses Problem mithilfe eines NVs zu überwinden, das den Purcell Effekt nutzt. Dies wird uns eine deutlich höherer Sammeleffizienz ermöglichen und Verluste minimieren. Dadurch wird es möglich werden Clusterzustände mit hunderten von Photonen aufzubauen. Ein weiterer Schritt ist die Erweiterung auf mehrere SPEs die parallel operieren, was es ermöglichen würde 3-dimensionale Clusterszustände zu realisieren. Dies sollte zu einer deutlichen Erhöhung der Fehlertoleranz von Quantenzuständen beitragen.

# Contents


1 Introduction 1

1.1 Context and Thesis Overview . . . 1
1.2 Basics of Quantum Information Theory . . . 4
1.2.1 Qubits . . . 4
1.2.2 Qubit Implementations . . . 6
1.2.3 Quantum Control of Qubits . . . 7
1.2.4 Quantum State Fidelity . . . 10
1.2.5 Entanglement . . . 10
1.3 Cluster States and Measurement-Based Quantum Computation . . . 12
1.4 Basics of Quantum Error Correction . . . 17

2 Photonic Entanglement Generation 20

2.0.1 Spontaneous Parametric Down-Conversion . . . 21
2.0.2 Setup for SPDC Generation of Cluster States . . . 23
2.1 Experimental Measurement-Based Quantum Error Correction . . . 26
2.2 Photonic Entanglement Generation by a Single-Photon Emitter . . . 31
2.3 Photonic Entanglement Generation with One Optical Transition . . . 33

3 The Nitrogen-Vacancy Defect Centre 37

3.1 Historical Perspective and General Properties . . . 38
3.2 Diamond Structure and Properties . . . 39
3.3 The NV Centre and its Electronic Structure . . . 40
3.4 The Optical Ground State and the Spin Qubit . . . 44
3.5 The Optical Excited State . . . 46
3.6 The Singlet State Manifold and Intersystem Crossing . . . 49
3.7 Vibronic and Temperature Effects . . . 51
3.8 The Photochromic Effect . . . 52

4 Experimental Methods **54**
4.1 The Diamond Sample . . . 54
4.2 The Optical Interface . . . 55
4.2.1 NV Allocation for SIL Fabrication . . . 55
4.2.2 Fabrication of Solid Immersion Lenses . . . 60
4.2.3 The Optical Setup . . . 61
4.2.4 Readout and Coherent Control of Optical Transitions . . . 67
4.3 The Microwave Interface . . . 77
4.3.1 Mapping Spin Transitions . . . 77
4.3.2 Coherent Control of Spin Transitions . . . 80
4.4 Time-to-Polarisation Conversion . . . 85
4.4.1 Setup Description and Operation . . . 85
4.4.2 The Interferometer Phase $\Delta\varphi$ . . . 90

5 Iterative Initialisation of the NV centre spin **104**
5.1 The Physical Model . . . 105
5.2 Spin Initialisation Routines . . . 111
5.2.1 Electronic and Nuclear Initialisation . . . 111
5.3 Summary and Outlook . . . 114

6 Spin-Photon Entanglement Generation and Verification **116**
6.1 Experimental Sequence . . . 117
6.1.1 Preparation . . . 117
6.1.2 Entanglement Generation . . . 118
6.1.3 Tomography . . . 120
6.2 Partial Tomography and Entanglement Verification . . . 122
6.3 Imperfections of the System and Outlook . . . 129
6.4 Outlook . . . 135

7 Appendix **139**
7.1 The Hamiltonian of the NV Optical Ground State . . . 139
7.2 Demonstrating Elements of Measurement-Based Quantum Error Correction . . . 143
7.2.1 Fidelities of Resource Cluster States . . . 143
7.2.2 Encoded States and Decoding Fidelities . . . 145

References **161**

# Acknowledgments

This thesis work reflects the collective work of an extended group of people, who in many different ways contributed to its realisation and to whom I am truly, deeply grateful.

Cameron Salter and Sarah Reisenbauer were my laboratory partners for several years and shared with me countless hours of team work, among frustrations and triumphs. The constant exchange of ideas, viewpoints and, ultimately, knowledge deeply enriched my learning experience. This thesis is also theirs.

Georg Wachter and Daniel Wirtitsch contributed immensely to our projects, through inventive fixes to all kinds of technical challenges arising in the lab. Thank you!

I am grateful to Michael Trupke, who provided me with invaluable support and tutorship throughout these years, always with prompt, keen interest and ingenious solutions to the most varied scientific problems. Philip Walther and Michael Trupke set the basis for this doctoral work, way before it started and through its duration, with such dedication and discretion that I never had to worry with diversions from outside the laboratory. This extends to the CoQuS program and the University of Vienna, which laid the infrastructure that made everything possible. Thank you for this opportunity!

Amir Moqanaki, Chiara Greganti, Francesco Massa and Jonas Zeuner walked next to me through the hardships and joys of the PhD program and brought lightness into my life through their invaluable friendship.

I must acknowledge also my loving family, which has supported me unconditionally through life.

Rui Vasconcelos

# 1 Introduction

## 1.1 Context and Thesis Overview

Quantum physics stands as one of the most successful theories in the description of Nature. Since its conception in the 1900s its implications span the whole spectrum of human experience: from the technical development of the semiconductor industry to the philosophical discussion of free will, from the minute details of atomic dynamics to the macroscopic workings of cell biology.

The first quantum revolution in the beginning of the 20$^{th}$ century marks the birth of quantum mechanics, breaking with the old paradigm of classical physics. A century of prolific progress in physics ensued, placing us on the brink of a second quantum revolution [1] where the maturing of quantum science allows us to finally turn towards the emerging field of quantum engineering, with the promise of abounding new technologies, in three commonly identified categories: metrology [2], communication [3] and information processing (QIP) [4]. This thesis work falls within the ambitions of QIP.

The realization of these new ideas required however a physical platform whose quantum properties could be harnessed with a high degree of control, to encode quantum bits (qubits) and, ultimately, build a quantum computer. Therefore, at the turn of the century a collective worldwide scientific effort led to the emergence of the most varied physical platforms intended

for quantum information processing. These included cavity QED [5], superconducting qubits [6], trapped ions [7], photons [8, 9], liquid state NMR [10], solid state NMR (e.g. quantum dots and NV centres) [11, 12], among several others.

To beat their classical correspondents and finally prove their practical utility, moving from proofs-of-principle to realistic scenarios, these platforms must be scaled up to larger systems, to allow the encoding and processing of progressively greater amounts of information. The main focus of this thesis is to scale up photonic entangled states, specially cluster states [13], in the context of quantum information processing. Note, however, that the generation and distribution of entanglement is a multi-purpose task which ultimately serves the development of quantum networks, with more encompassing applications [14].

To date, the most common approach to photonic entanglement generation relies on spontaneous down-conversion (SPDC) in non-linear media [8, 15–17] as its building block. However, strategies to scaling up such technology are critically hindered by the probabilistic nature of the down-conversion process, limiting their efficiency. This could be overcome, *in principle*, by adopting alternative approaches based on deterministic on-demand single-photon emitters (SPE), as laid by the Lindner-Rudolph protocol [18, 19] with the promise of deterministic generation of photonic entanglement. Such strategies are further motivated by the extraordinary advances in the realisation of solid-state SPEs [20], which present a low resource overhead and high-fidelity performances.

The chronology of this dissertation portrays the shift from SPDC to SPE-based entanglement-generation protocols. Firstly, a SPDC source, capable of producing 4-qubit photonic entangled states, was characterised and modified to demonstrate a measurement-based quantum error correction code. Secondly, building on the previous protocol by Lindner and Rudolph [18], a new SPE-based scheme for entanglement generation was proposed and its basic unit experimentally realised, by generating and then demonstrating spin-photon entanglement, using a nitrogen-vacancy centre as single photon emitter.

Current entanglement-generation protocols based on SPEs place stringent requirements on the emitters, demanding a costly high degree of control over their properties. The presented alternative relaxes some of these constraints, widening the range of usable emitters and rendering scaling more resource-efficient. This is achieved by using a single optical transition to produce photonic time-bin qubits and an unbalanced polarising interferometer to later convert the generated photons into a polarisation basis, where coherent gates and tomography are more easily performed. Due to the entanglement generation being facilitated by this conversion step, the protocol is identified throughout this text as the time-to-polarisation (TPC) entangling scheme.

The aforementioned demonstration of a quantum error correction code, where a logical

qubit, encoded in a SPDC-produced four-qubit cluster state, is protected against phase noise, similarly relates to the problem of scaling up a quantum system. Despite the increase in size, the internal operation of the quantum systems must remain as isolated from the environment as possible, for leaking of information leads to decoherence and corruption of the encoded states. This becomes particularly relevant when the depth of the algorithms is increased and errors accumulate over the computational steps. In realistic scenarios it is then necessary to detect and correct arising errors, to render the computation fault-tolerant [21].

During the experimental execution of the SPE-based entangling scheme, a new iterative method to polarise the electronic and nuclear spins of the NV centre by population trapping through resonant optical pumping was devised. This approach benefits from a low hardware demand and high resilience to experimental imperfections when compared with alternative existing approaches. It is therefore presented as one of the main results of this work.

The layout of this thesis is the following:

- **Chapter 1** contextualises the need for scaling up quantum systems in the framework of quantum information, presenting the limitations of SPDC sources for scaling photonic entanglement generation and the advantage provided by SPE-based protocols. A brief theoretical introduction to the topics discussed throughout this work is presented.
- **Chapter 2** introduces protocols used in photonic entanglement generation of cluster states. A novel scalable SPE-based scheme is presented, requiring a single optical transition and time-to-polarisation (TPC) conversion of the encoding on the emitted photons. The chapter further describes the realisation and operation of a 4-photon cluster state SPDC-based source, which is then applied in the implementation of a measurement-based quantum error correction scheme, for protection of a logical qubit against phase noise.
- **Chapter 3** provides an overview of the physical aspects of the nitrogen-vacancy (NV) centre, as it is the physical system used in the demonstration of the new SPE-based entangling scheme. It includes a description of its ground, excited and singlet state manifolds, together with its energy spectrum and vibronic band.
- **Chapter 4** explores the experimental techniques used in the preparation, control and readout of the NV centre. Furthermore it describes the operation of the unbalanced interferometer used in the time-to-polarisation conversion, as required by the TPC entangling protocol.
- **Chapter 5** introduces a new method for iterative initialisation of the nuclear and

electronic spins of the NV centre, based on redistribution of the spin populations by optical pumping, combined with selective microwave driving of the undesired populations.

- **Chapter 6** describes the experimental sequence leading to the realisation of the fundamental unit of the photonic entanglement-generation TPC scheme. The resulting entangled state is quantitatively described and the imperfections of the system are analysed. Finally, future directions of work are discussed, towards realising a deterministic source of photonic entangled states.

## 1.2 Basics of Quantum Information Theory

### 1.2.1 Qubits

A quantum bit is the fundamental unit of quantum information, the counterpart of the bit in classical computation. While the bit takes the values 0 or 1, the qubit can be found in a superposition state where both 0 and 1 are possible probabilistic outcomes of a measurement. A superposition is mathematically described as a linear combination of two basis states:

$$\begin{aligned} |\psi\rangle \quad &= \quad \alpha\,|0\rangle + \beta\,|1\rangle \\ \\ &\text{with} \quad \alpha,\ \beta \in \mathbb{C} \\ &\qquad\ \ |\alpha|^2 + |\beta|^2 = 1 \end{aligned} \tag{1.1}$$

As $\alpha$ and $\beta$ are complex valued, the qubit is defined in a 2-dimensional complex vector space. The normalising condition on the coefficients $\alpha$ and $\beta$ allows, without loss of generality, to write the superposition as:

$$\begin{aligned} |\psi\rangle \quad &= \quad \cos(\theta/2)\,|0\rangle + e^{i\varphi}\sin(\theta/2)\,|1\rangle \\ \\ &\text{with} \quad \theta \in [-\tfrac{\pi}{2}, +\tfrac{\pi}{2}] \\ &\qquad\ \ \varphi \in [0, 2\pi] \end{aligned} \tag{1.2}$$

This parametrisation of the coefficients makes a geometric interpretation more clear. The qubit state can be represented as a point on the surface of a sphere of radius 1, in a 3-dimensional real space, where $\theta$ and $\varphi$ denote the altitude and the azimuth of the point, respectively, as illustrated in Fig. 1.1 b. This description applies to pure states, for which the observer has full knowledge of the physical system. When otherwise there is uncertainty in the description of the quantum

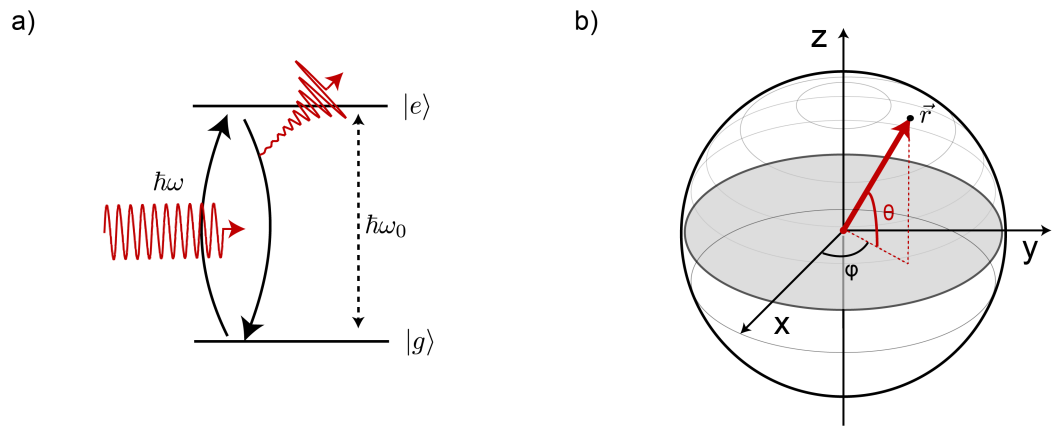


**Figure 1.1: Two level systems**. **a)** Two-level system (qubit) interacting with an external time-dependent field. **b)** The Bloch representation parametrizes the density matrix of the qubit in terms of a Pauli matrix decomposition. The three coefficients of the decomposition make up a real 3-d vector $\vec{r}$ which uniquely determines $\hat{\rho}$ and spans the volume of a sphere of unit radius, the Bloch sphere.

state, as in the case of a statistical mixture, a density matrix $\hat{\rho}$ generalizes the linear combination $|\psi\rangle$ [4]:

$$\begin{aligned} \hat{\rho} \quad &= \quad \tfrac{1}{2}(\hat{Id} + \vec{r}\cdot\vec{\sigma}) \\ \text{with} \quad &\vec{r} = (r_1, r_2, r_3) \\ &\vec{\sigma} = (\hat{\sigma_x}, \hat{\sigma_y}, \hat{\sigma_z}) \end{aligned} \tag{1.3}$$

$\hat{Id}$ is the identity operator and $\hat{\sigma}_i$ are the Pauli matrices. The geometrical interpretation of the quantum state in a 3-d space is still valid, but the state is not limited any more to the surface of the Bloch sphere ($|\vec{r}| = 1$), as for the case of pure states, extending now to points inside the sphere ($|\vec{r}| < 1$). The density matrix is hermitian ($\hat{\rho} = \hat{\rho}^\dagger$), positive ($\rho_{ii} > 0$), with unit trace ($\mathrm{Tr}(\hat{\rho}) = 1$). The components of the vector $\vec{r}$ uniquely determine $\hat{\rho}$ and express the expectation values of the respective Pauli matrices $r_i = \langle\sigma_i\rangle$. While $r_3$ sets the value of the diagonal terms of $\hat{\rho}$, the populations, $r_1$ and $r_2$ determine the off-diagonal entries, the coherences.

The Bloch representation of the qubit constitutes a valuable tool in the visualization of the evolution of quantum states, because any unitary transformation of $\hat{\rho}$ translates into a rotation of the state vector by an angle $\theta$ around an axis $\hat{n}$. The steering of quantum states around the Bloch sphere is the topic of Section 1.2.3.

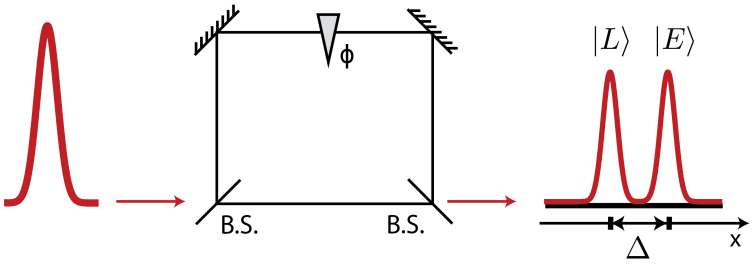


**Figure 1.2: Generation of a time-bin qubit: $|\psi\rangle = \alpha|E\rangle + e^{i\varphi}\beta|L\rangle$ with an unbalanced interferometer**. By tuning the reflectance of the beam splitters (B.S.) and the phase shifter $\varphi$, an arbitrary state can be generated. The action of the interferometer can be reversed such that it is used to perform quantum tomography on a time-bin qubit, by injecting the qubit from the right side and detecting on the two ports on the left side.

### 1.2.2 Qubit Implementations

As any two states of a quantum mechanical system can be used to define a qubit, there are many different experimental realisations of this concept. The qubit platforms found throughout this thesis are briefly presented, together with the corresponding conventions in nomenclature.

In polarisation qubits, single photons carry quantum information in their polarisation degree of freedom by mapping the computational basis $\{|0\rangle, |1\rangle\}$ onto the horizontal $|H\rangle$ and vertical $|V\rangle$ polarisation vectors. The eigenstates of the $\hat{\sigma}_x$ Pauli operator define the diagonal $|D\rangle$ and anti-diagonal $|A\rangle$ states and the eigenstates of the $\hat{\sigma}_y$ operator establish the right $|R\rangle$ and left $|A\rangle$ circular polarisations. Polarisation qubits benefit from negligible decoherence, rendering them suitable for quantum information communication, and high fidelity single qubit gates. The downside is that photons can only interact with one another very weakly, rendering it a difficult task to realise two-qubit gates [9].

Single photons can also carry quantum information on a time-bin basis, in which a single photon is divided in two subpackets, corresponding to two possible arrival times, early $|E\rangle$ and late $|L\rangle$. It is instructive to note that such encoding can be achieved by sending a single photon through an unbalanced Mach-Zender interferometer, as illustrated in Fig. 1.2 [22]. An adapted version of such an apparatus is used in this thesis to convert from a time-bin to a polarisation basis, as described in detail in Section 4.4 . Time-bin qubits are particularly suited for fibre communication exhibiting high resilience to the environment in propagation. The most critical disadvantage, photon loss in optical fibres, can be minimised by operating in the telecom range $\lambda \in [1260, 1625]$ nm [23]. Nonetheless arbitrary single qubit gates remain challenging, due to the necessity for phase-locked interferometers.

Nuclear or electronic spins can also be employed to encode qubits. For the case of a spin-1/2 system the mapping is straightforward, with $|0\rangle$ ($|1\rangle$) corresponding to the $|m_s = +1/2\rangle$

($|-1/2\rangle$) spin projection along $\hat{z}$. For systems with a higher spin number, any choice of a level pair could in principle sustain the qubit. If, on one hand, electronic spins seem more suited to process information due to their fast manipulation and strong coupling to other electronic spins, on the other hand, nuclear spins are good candidates for quantum memories due to their resilience to environment perturbation and consequentially long coherence times [24]. The experimental resource overhead to maintain/control several spin qubits remains high, which constitutes an unsurmounted obstacle for scalability.

### 1.2.3 Quantum Control of Qubits

The most general time-independent Hamiltonian of a two-state system can, similarly to the density matrix $\hat{\rho}$, be expanded in a Pauli basis $\{\hat{\sigma}_i\}$ leading to the following parametrization:

$$\hat{H} = \frac{\hbar}{2}\left(\omega_0 \hat{Id} + \omega_1\hat{\sigma}_x + \omega_2\hat{\sigma}_y + \omega_3\hat{\sigma}_z\right) \tag{1.4}$$

where $\hat{Id}$ is the identity operator and $\omega_i \in \mathbb{R}$. The Pauli gates, identified throughout this manuscript as $(\hat{\sigma}_x, \hat{\sigma}_y, \hat{\sigma}_z)$ or $(X, Y, Z)$, are given by:

$$\hat{\sigma}_x = \begin{bmatrix} 0 & 1 \\ 1 & 0 \end{bmatrix}, \quad \hat{\sigma}_y = \begin{bmatrix} 0 & -i \\ i & 0 \end{bmatrix}, \quad \hat{\sigma}_z = \begin{bmatrix} 1 & 0 \\ 0 & -1 \end{bmatrix} \tag{1.5}$$

The first term of the Hamiltonian represents the zero-point energy of the system, leading to the addition of an overall phase in its evolution and can therefore be neglected:

$$\hat{H} = \frac{\hbar}{2}\left(\omega_1\hat{\sigma}_x + \omega_2\hat{\sigma}_y + \omega_3\hat{\sigma}_z\right) = \frac{\hbar}{2}\left(\vec{\omega}\cdot\vec{\sigma}\right) \tag{1.6}$$

Plugging the Pauli basis expansions of $\hat{H}$ and $\hat{\rho}$ in the Heisenberg equation of motion, $i\hbar\dot{\hat{\rho}} = [\hat{H}, \hat{\rho}]$, a simple equation arises, relating the time evolution of $\vec{r}$ and the Hamiltonian vector $\vec{\omega}$ [25]:

$$\frac{d}{dt}\vec{r} = \vec{\omega} \times \vec{r} \tag{1.7}$$

This expression sets an elucidating parallel between the evolution of a general 2-state quantum system with the classical precession of an angular momentum by action of a torque, as in the precession of a magnetic moment due to a magnetic field, where $\vec{\omega}$ defines the axis of precession.

The interaction of an arbitrary two-state system with a time-varying external field, represented in Fig. 1.1 a, is underpinned by a time-dependent Hamiltonian. For a linearly polarised monochromatic harmonic field, e.g. $\vec{E}(t) \propto \cos(\omega t)\,\hat{x}$, by representing the system in a frame which rotates around the Z-axis at a frequency $\omega$ and performing the rotating wave

approximation [26], the Hamiltonian becomes time-independent and the problem reduces to Eq. 1.7, with $\vec{\omega} = (\omega_0, 0, \delta)$, where $\omega_0$ is the Rabi frequency and $\delta$ is the detuning between the external field and the energy difference between the two levels. Explicitly writing the vector components of Eq. 1.7, it yields:

$$\begin{aligned} \dot{r_1} &= -\delta\, r_2 \\ \dot{r_2} &= \delta\, r_1 + \Omega_0\, r_3 \quad \text{with} \quad \delta = \omega - \omega_0 \\ \dot{r_3} &= -\Omega_0\, r_2 \end{aligned} \tag{1.8}$$

For an electric dipole interaction the Rabi frequency is given by $\Omega_0 = |\vec{d} \cdot \vec{E_0}|/\hbar$, where $\vec{d}$ is the transition dipole moment and $\vec{E_0}$ the electric field amplitude. In the case of a magnetic dipole interaction with a magnetic field $\vec{B}$, the Rabi frequency takes the form $\Omega_0 = |\vec{\mu} \cdot \vec{B_0}|/\hbar$, with $\vec{\mu}$ denoting the magnetic dipole transition moment and $\vec{B_0}$ the field amplitude. These are known as the Bloch equations.

A complete description of the system dynamics must include the interaction with the environment. This is phenomenologically taken into account, by introducing damping terms in the equations of motion, which bring the system to thermal equilibrium. Typically, two types of interactions with the environment are considered: inelastic damping of the populations, characterized by a $T_1$ damping lifetime, also known as longitudinal relaxation time, and elastic relaxation of the coherences, due to events that lead to dephasing without affecting the populations, described by $T_2$, known as transversal relaxation time. These damping effects change the Bloch equations, according to:

$$\begin{aligned} \dot{r_1} &= -\delta\, r_2 - r_1/T_2 \\ \dot{r_2} &= \delta\, r_1 + \Omega_0\, r_3 - r_2/T_2 \\ \dot{r_3} &= -\Omega_0\, r_2 - (r_3 - r_{3,eq})/T_1 \end{aligned} \tag{1.9}$$

where $r_{3,eq}$ defines the populations in thermal equilibrium. These are linear first-order differential equations with constant coefficients and have analytic solutions, known as Torrey´s solutions [27].

In an ideal system, the transition energy between the two levels, $\Delta E$, is constant over time and all experimental runs exhibit the same homogenous decoherence time $T_2$. In reality, changes in the environment of the qubit introduce inhomogeneous fluctuations on $\Delta E$ and the effective transversal relaxation time, identified as $T_2^*$, is shortened according to:

$$\frac{1}{T_2^*} = \frac{1}{T_2} + \frac{1}{T_{\text{inhom}}} \tag{1.10}$$

where $T_{\text{inhom}}$ is the inhomogeneous transversal relaxation time. In experimental terms, $T_2^*$ is extracted with a Ramsey sequence, whereas a spin-echo protocol is necessary to mitigate the inhomogeneous dephasing and probe $T_2$ directly [28]. In the case of the nitrogen-vacancy centre, the inhomogenous decay of coherence is primarily caused by the spin bath of $^{13}$C in the hosting lattice and it can be reverted by dynamical decoupling sequences [29]. In this work, because no decoupling protocol was employed, $T_2^*$ is referred to as the (spin) qubit decoherence time - see Section 4.3.2.

For most of this work, as the time-scale of the spin manipulations is significantly smaller than the longitudinal or transversal relaxation times $T_1$ and $T_2^*$, the integration of the undamped Bloch equations provides a good model of the system. Of particular interest is the case where the population starts in the ground state: setting the initial conditions $r_1 = r_2 = 0$ and $r_3 = 1$ leads to a simple expression for the coherent transfer of population from the ground state to the excited state, by a near-resonant field. The population in the excited state is then given by:

$$P_e(t) = \frac{\Omega_0}{\sqrt{\Omega_0^2 + \delta^2}} \sin^2\left(\sqrt{\Omega_0^2 + \delta^2}\, t/2\right) \tag{1.11}$$

where $t$ is the evolution time and the expression describes the well known Rabi nutations. By tuning the settings of the driving field $(\Omega_0,\ \delta,\ t)$, one can execute arbitrary rotations of a single qubit on the Bloch sphere. Their experimental realisation is described in Section 4.3.

Arbitrary unitary operators in the Hilbert space of $N$ qubits can be decomposed into a product of gates belonging to a set which contains single- and two-qubit operators. Moreover, a set of gates $S$ is said to be *universal for quantum computation* if any $N \times N$ unitary can be approximated to arbitrary precision by a product of gates of $S$. Many sets satisfy this condition [4], such as $S = \{CNOT, H, R_{\pi/8}\}$ or $S = \{\text{Toffoli}, CZ, H\}$, where the definition of the gates follows. The single-qubit gates include the Hadamard gate, $H$, and the $R_{\pi/8}$ gate, given by:

$$H = \frac{1}{\sqrt{2}} \begin{bmatrix} 1 & 1 \\ 1 & -1 \end{bmatrix}, \quad R_{\pi/8} = \begin{bmatrix} \cos(\pi/8) & -\sin(\pi/8) \\ \sin(\pi/8) & \cos(\pi/8) \end{bmatrix} \tag{1.12}$$

Within two-qubit operations, the controlled-not (CNOT) and controlled-phase (CZ) gates are defined according to:

$$CNOT = \frac{1}{\sqrt{2}} \begin{bmatrix} 1 & 0 & 0 & 0 \\ 0 & 1 & 0 & 0 \\ 0 & 0 & 0 & 1 \\ 0 & 0 & 1 & 0 \end{bmatrix}, \quad CZ = \begin{bmatrix} 1 & 0 & 0 & 0 \\ 0 & 1 & 0 & 0 \\ 0 & 0 & 1 & 0 \\ 0 & 0 & 0 & -1 \end{bmatrix} \tag{1.13}$$

The Toffoli gate is a three qubit gate and it is sometimes referred to as the "controlled-controlled-not" gate and is defined as:

$$\text{Toffoli} = \begin{bmatrix} 1 & 0 & 0 & 0 & 0 & 0 & 0 & 0 \\ 0 & 1 & 0 & 0 & 0 & 0 & 0 & 0 \\ 0 & 0 & 1 & 0 & 0 & 0 & 0 & 0 \\ 0 & 0 & 0 & 1 & 0 & 0 & 0 & 0 \\ 0 & 0 & 0 & 0 & 1 & 0 & 0 & 0 \\ 0 & 0 & 0 & 0 & 0 & 1 & 0 & 0 \\ 0 & 0 & 0 & 0 & 0 & 0 & 0 & 1 \\ 0 & 0 & 0 & 0 & 0 & 0 & 1 & 0 \end{bmatrix}. \tag{1.14}$$

### 1.2.4 Quantum State Fidelity

The fidelity can be used to quantify the difference between two quantum states, whether in pure or mixed state form. In the most general case, for two states represented by density operators $\rho_1$ and $\rho_2$, the fidelity is given by:

$$F(\rho_1, \rho_2) = \left[ Tr\sqrt{\sqrt{\rho_1}\rho_2\sqrt{\rho_1}} \right]^2 \tag{1.15}$$

If $\rho_1$ and $\rho_2$ can be expressed as pure states $|\psi_1\rangle$ and $|\psi_2\rangle$, then the fidelity equals the square of the inner-product between the two kets:

$$F(\psi_1, \psi_2) = |\langle\psi_1|\psi_2\rangle|^2 \tag{1.16}$$

Throughout this thesis, the fidelity is used to compare experimentally generated and measured states with the theoretically expected outcomes. Frequently it is also used to quantify the accuracy of operation of coherent gates on single qubits, when the input states are well defined.

### 1.2.5 Entanglement

Entanglement arises as a consequence of quantum superposition in composite systems, constituted by several subsystems. The description of an entangled system is not complete with the separate characterization of its parts; one must account for the joint properties of its constituents, which emerge as statistical correlations among measurements on the different parts of the system. Assume that a system C defined on a Hilbert space $\mathcal{H}_C = \mathcal{H}_A \otimes \mathcal{H}_B$ is composed of a subsystem A in a state $|\psi\rangle_A$ and a subsystem B in a state $|\psi\rangle_B$, defined in the smaller Hilbert space $\mathcal{H}_A$ with an orthonormal basis $|i\rangle_A$ and $\mathcal{H}_B$ with a basis $|j\rangle_B$. An arbitrary

pure state of system C can be generally represented as:

$$|\varphi\rangle_C = \sum_{i,j} a_{ij} |i\rangle_A \otimes |j\rangle_B \tag{1.17}$$

If $|\varphi\rangle_C$ can be factored into a product of states of its individual constituents $|\varphi\rangle_C = |\varphi\rangle_A \otimes |\varphi\rangle_B$, then it is said to be a separable state. Otherwise, if the factorisation is not possible, it is entangled. Examples of two-particle, or bipartite, entangled states are the Bell states:

$$\begin{aligned} |\varphi^{\pm}\rangle &= 1/\sqrt{2}(|0\rangle_A |0\rangle_B \pm |1\rangle_A |1\rangle_B) \\ |\psi^{\pm}\rangle &= 1/\sqrt{2}(|0\rangle_A |1\rangle_B \pm |1\rangle_A |0\rangle_B) \end{aligned} \tag{1.18}$$

which constitute an orthonormal basis for the Hilbert space for two qubits. It is clear that a joint-measurement on the computational basis of the two qubits yields correlated measurements, i.e. with the same output result, for the $|\varphi^{\pm}\rangle$ states and opposite outcomes for the $|\psi^{\pm}\rangle$ Bell-states. Because these (anti-)correlations are perfect, the Bell states are said to be maximally entangled. However, when considering each qubit separately, they are found in a perfectly mixed state $\rho = \hat{Id}/2$, where all measurement outcomes are equally likely. Another entangled state which is frequently found in the literature is the Greenberger-Horne-Zeilinger (GHZ) state:

$$|GHZ\rangle^n = \frac{1}{\sqrt{2}}(|0\rangle^{\otimes n} + |1\rangle^{\otimes n}) \tag{1.19}$$

The definition of entanglement can be generalized to include systems described by statistical mixtures. In such cases, a separable state can be expressed in the form [4]:

$$\hat{\rho} = \sum_i a_i \hat{\rho}_i^{(A)} \otimes \hat{\rho}_i^{(B)} \tag{1.20}$$

where $a_i$ are probabilities and $\hat{\rho}^{(A/B)}$ are the density matrices representing the subsytems A and B. Once again, if the factorisation is not possible then $\hat{\rho}$ is entangled.

Entanglement plays the role of a resource in the implementation of various quantum information protocols, spanning applications in quantum computation, communication and metrology. Examples include quantum teleportation [30], quantum dense coding [31], quantum key distribution [3], teleportation-based quantum computation protocols [32], metrology beyond the standard quantum limit [2] and the conception of a quantum internet [33]. As different applications require distinct degrees of entanglement, methods have been developed to assert whether a state is separable or not and how much entanglement is present in a particular system. Common examples are the Bell-CHSH inequalities, which detect entanglement by showing that a system is non-local; entanglement witnesses, which provide an

observable whose average value determines the system´s separability; or tomography, that retrieves the density matrix of a system to infer then by calculation how much entanglement is present. A systematic review, including other entanglement verification approaches, can be found in Ref. [34].

Entanglement measures are mathematical concepts used to quantify entanglement. Geometric measures focus on the fact that density matrices describing an arbitrary system form a convex set ($\hat{\rho} = \sum_i \hat{\rho}_i$), where the concept of difference between two states arises naturally, similarly to the distance in a vector-space. A commonly found geometric entanglement measure is the quantum relative entropy of entanglement $D_{REE}(\rho)$:

$$D_{REE}(\hat{\rho}) = \min_{\hat{\sigma}} S(\hat{\rho}||\hat{\sigma}) \tag{1.21}$$

which takes the minimum "distance" over the set of separable states $\sigma$; The distance is quantified by the relative entropy between $\hat{\rho}$ and $\hat{\sigma}$, $S(\hat{\rho}||\hat{\sigma}) = \mathrm{Tr}\,\hat{\rho}(\log\hat{\rho} - \log\hat{\sigma})$. Operational entanglement measures, on the other hand, focus on whether a particular state has enough entanglement to perform a certain task. The wide range of possible tasks leads to a great variety of measures. Among the most common, one finds the *distillable entanglement* and *entanglement of formation*. An overview of entanglement measures can be found in Ref. [35]

Within the framework of this thesis, entanglement characterization of the spin-photon state in chapter 6 is achieved through tomography of the generated states and retrieval of the respective fidelities with respect to the expected maximally entangled state:

$$F = \mathrm{Tr}\left(\left|\psi^+\right\rangle\left\langle\psi^+\right|\hat{\rho}\right) = \left\langle\psi^+\right|\hat{\rho}\left|\psi^+\right\rangle \tag{1.22}$$

The same approach is used for the SPDC-generated 4-qubit cluster state in Chapter 2.

## 1.3 Cluster States and Measurement-Based Quantum Computation

The ulterior motive for the proposal and realisation of the spin-photon entanglement generation protocol - Chapter 2 - was the production of an entangled resource state for measurement-based quantum computing (MBQC) [13]. Also the quantum error correction code presented in Chapter 2 is based on the same quantum information processing model, which is therefore briefly introduced in this section.

Quantum information processing is commonly represented in terms of the circuit model in which an initial disentangled state of $n$ qubits $|\psi\rangle^{\otimes n}$ evolves through a set of quantum gates, which undergoes a coherent unitary evolution. The MBQC model is an alternative paradigm which takes an highly entangled state as input, which evolves through a sequence of adaptive

measurements.

The seminal concept was laid by Gottesman-Chuang [36], through a gate which generalizes the concept of teleportation by combining state transfer with an arbitrary unitary on the transferred state. Here, a general state is teleported through a gate, by resorting to Bell state measurements, an entangled resource state and single qubit rotations. This concept is illustrated in the following circuit equivalence where the arbitrary gate $|\psi\rangle \rightarrow U|\psi\rangle$ takes place:

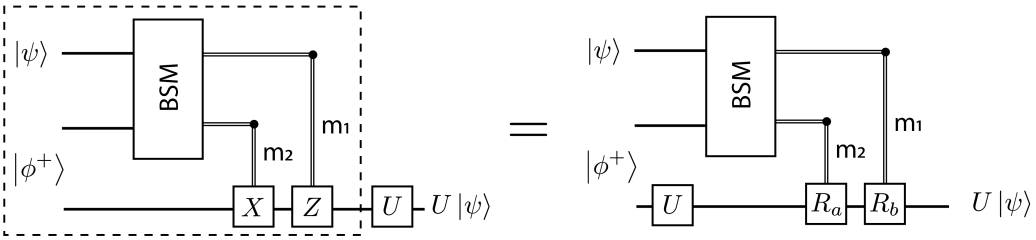


The dashed rectangle indicates the teleportation of an arbitrary state $|\psi\rangle$, BSM stands for Bell state measurement and the two-line wires represent classical qubits which condition the application of the error correcting gates, $X$ and $Z$. On the left side, the state $|\psi\rangle$ is teleported onto the bottom logical qubit and the unitary $U$ then applied to the teleported state. By "sliding" the gate $U$ to the start of the circuit, commuting it with the error correcting gates $X$ and $Z$ to yield $R_a$ and $R_b$, one obtains the same output state $U|\psi\rangle$. Note, nonetheless, that the gate is now embedded in the preparation stage, such that the resource state is $(Id \otimes U)|\varphi^+\rangle$, instead of $|\varphi^+\rangle$. This can be further generalized to implement two-qubit gates as in the following example which realises a CNOT gate:

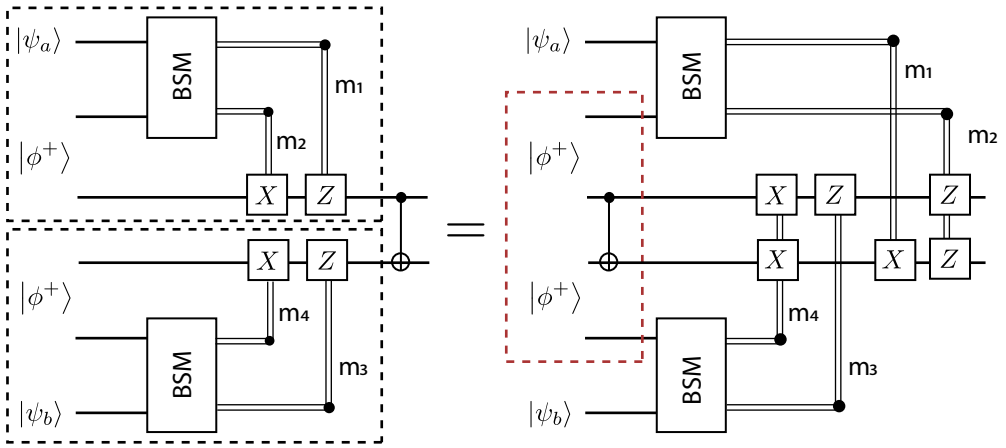


As before, the *CNOT* can be executed after or before the teleportation steps, within the dashed grey rectangles. One obtains an equivalent operation, by commuting the CNOT gate through the circuit towards the state preparation, such that the resource state becomes $CNOT(|\varphi^+\rangle_C |\varphi^+\rangle_T)$. This can be done with any gate in a circuit, being particularly useful for

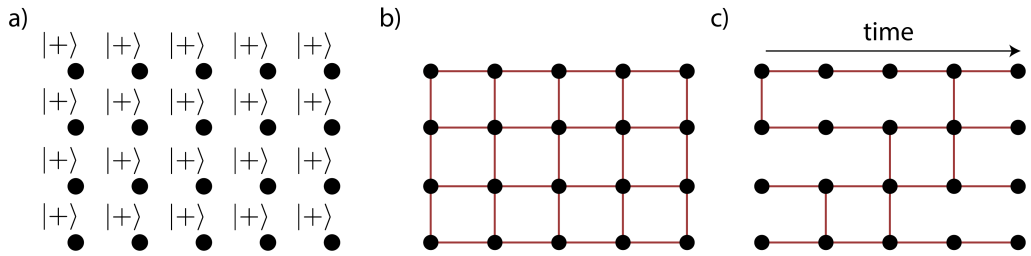


**Figure 1.3: Construction and operation of the cluster states. a)** Each cluster node/qubit is prepared in a $|+\rangle = (|0\rangle + |1\rangle)/\sqrt{2}$ state. **b)** A CZ gate is applied between each pair of neighbouring qubits forming a square lattice graph state. **c)** The cluster state connections are shaped to implement a particular algorithm, through $X$ or $Z$ measurements on single nodes. The one-way computation progresses from left to right through single qubit measurements and feed-forward, as explained in the main text.

probabilistic gates. By moving the non-deterministic steps of a quantum computations to the start, one obtains a deterministic computation at the price of a probabilistic preparation of some entangled resource state.

The promise of this scheme for linear optical quantum computing (LOQC) became clear with the advent of the KLM protocol [37], in which the authors showed how to induce a non-linearity on a two-photon state, by resorting only to waveplates, phase shifters, ancilla photons, and projective measurements, excusing the use of non-linear media. In the KLM protocol a new CNOT implementation is proposed, which resorting to $n$ ancillary photons distributed through $2n$ spatial modes raises the success probability of the gate to $p = (n/(n+1))^2$. By adding ancillary qubits, it is possible to yield near-deterministic 2-photon gates (CNOT, CZ) and consequently near deterministic Bell state measurements and Gottesman-Chuang gates of arbitrary transformations. Crucially, by combining the KLM 2-qubit gates with the Gottesman-Chuang "teleportation trick", the experimental resources to implement an arbitrary unitary in a $n$ qubit space, $U(n)$, scales polynomially.

Despite providing a more resource-efficient LOQC realization, the KLM approach is still very demanding and the practical effort to reach the required number of qubits remains an intimidating if not unrealistic task. Several theoretical attempts followed with the aim to yield a less resource demanding scheme and improve therefore scalability, among which a new model for quantum computation emerged - measurement-based quantum computation (MBQC) [13, 38]. The MBQC model has the remarkable property that all the qubit gates are realised through single-qubit measurements on a highly entangled resource state: a cluster state, which is a subclass of graph states. Furthermore, once the cluster state is available, it allows for deterministic operation through feed-forward gate control [39]. A brief description of the MBQC algorithms ensues.

Graph states are multi-qubit entangled states typically represented in the form of a mathematical graph $G(V, E)$, with vertices $V$ and edges $E$, where each vertex corresponds to a qubit and the edges are representative of entanglement among qubits. A graph state is not a unique quantum state. Instead, it represents a family of states which are equivalent under local unitary single qubit transformations and can be defined in terms of stabilisers: it is the family of states $|G\rangle$ which are simultaneous eigenstates with eigenvalue $+1$, for all the stabiliser operators, defined as:

$$\hat{K}^a = \hat{\sigma}_x^a \prod_{\beta \text{ adjacent to } a} \hat{\sigma}_z^\beta \tag{1.23}$$

for $a \in N_v$, where $N_v$ includes all the vertices of the graph. Each node $a$ leads to the definition of an operator $\hat{K}^a$.

An equivalent definition of graph state specifies, instead, the operations necessary for the generation of such state. Explicitly this can be achieved by preparing each qubit node in a superposition $|+\rangle = (|0\rangle + |1\rangle)/\sqrt{2}$ state and subsequently applying a controlled-Z gate between each node-pair of the intended lattice:

$$|G\rangle = \left( \prod_{\substack{\beta \text{ adjacent to } a, \\ a \in N_v}} CZ^{(a,\beta)} \right) \bigotimes_{a \in N_v} |+\rangle_a \tag{1.24}$$

One-way quantum computing resorts to a particular subclass of graph states, cluster states, which are two-dimensional square lattice graphs, represented in Fig. 1.3, constituting resources for universal quantum computation.

A measurement induced single-qubit rotation on an arbitrary state $|\psi\rangle$ can be implemented by the following circuit:

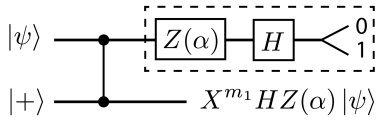


where the map $|\psi\rangle \rightarrow X^{m_1} HZ(a)\,|\psi\rangle$ mapping is realised, as can be checked by inspection. The elements within the dashed rectangle can be reinterpreted as a projective measurement $\hat{M}_1$ between the two orthogonal states:

$$\begin{aligned} |a\rangle &= (|0\rangle + e^{-ia}\,|1\rangle)/\sqrt{2} \\ |a_\perp\rangle &= (|0\rangle - e^{-ia}\,|1\rangle)/\sqrt{2} \end{aligned} \tag{1.25}$$

Note how both projectors lie on the equator of the Bloch sphere. From here onwards, $\hat{M}_i$ identifies a projective measurement on the equator of the Bloch sphere with an arbitrary

azimuthal angle $\alpha$.

This result can be generalized, since an arbitrary rotation in the Bloch sphere can be realised by concatenation of Z-axis rotations and Hadamard gates [4]:

$$R_{\hat{n}}(\theta) = Z(\gamma)X(\beta)Z(\alpha) = H\,HZ(\gamma)\,HZ(\beta)\,HZ(\alpha) \tag{1.26}$$

In the circuit representation, this translates into the following sequence:

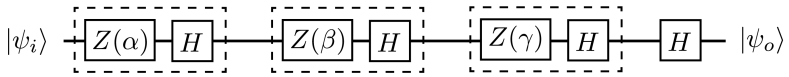


In the MBQC framework, this arbitrary rotation can be expressed as a set of three sequential projective measurements $(\hat{M}_1, \hat{M}_2, \hat{M}_3)$ on three qubits belonging to a linear cluster state:

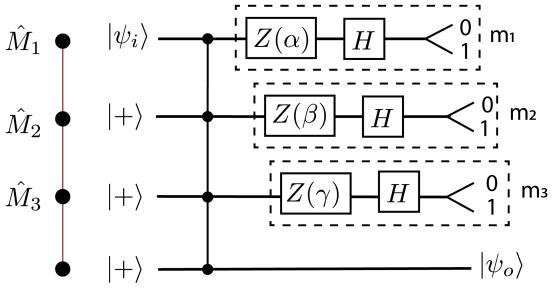


yielding an output state given by:

$$\left|\psi_o\right\rangle = [X^{m_3}HZ(\gamma)]\,[X^{m_2}HZ(\beta)]\,[X^{m_1}HZ(\alpha)]\;\left|\psi_i\right\rangle \tag{1.27}$$

where the superscripts $m_i$ take the values 0 or 1, identifying the output of each measurement. Conveniently, the errors $X^{m_i}$ can be commuted with the Z and H gates such that they are applied last in the output state expression:

$$\left|\psi_o\right\rangle = X^{m_3}Z^{m_2}X^{m_1}[HZ((-1)^{m_2}\gamma)]\,[HZ((-1)^{m_1}\beta)]\,[HZ(\alpha)]\;\left|\psi_i\right\rangle \tag{1.28}$$

where the identity $Z(\alpha)X = XZ(-\alpha)$ was used. Bearing in mind that the desired state is $\left|\psi_o\right\rangle = [HZ(\gamma)]\,[HZ(\beta)]\,[HZ(\alpha)]\;\left|\psi_i\right\rangle$, one can deduce from the previous equation that the error gates $X^{m_3}$, $Z^{m_2}$, $X^{m_1}$ can be cancelled at the end of the computation, by further application of $X$ and $Z$ gates (recall that $XX = ZZ = Id$). Furthermore, as the calculation proceeds, the successive measurement bases have to be adapted, conditional on the result of the previous outcomes: the measurements are adaptive. This feature imposes an arrow of time in the calculation and lends thereby the name "one-way" to this scheme. The circuit that implements the arbitrary single-qubit rotation requires a resource state (cluster-state) built from three $|+\rangle$

states united through three CZ gates. From the cluster state definition in Eq. 1.24 it is straightforward to conclude that it corresponds to a 3 particle linear-cluster state.

The implementation of 2-qubit gates requires a 2d-cluster state, with vertical CZ connections between different rows. Consider two 3-qubit linear clusters, connected by a CZ bond on the intermediate qubits:

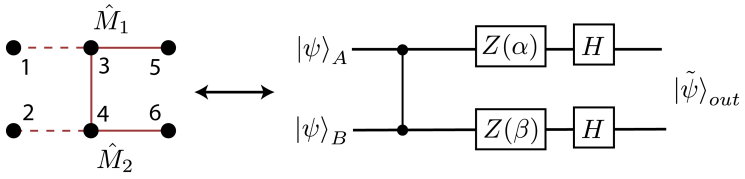


The left representation corresponds to the cluster state picture, whereas the right side shows the equivalent circuit diagram on the logical qubits. As defined before, $\hat{M}_1$ and $\hat{M}_2$ are projectors in the Bloch equator with azimuthal angles $\alpha$ and $\beta$. Assuming that the computation proceeds such that the physical qubits 3 and 4 inherit the states $|\psi\rangle_A$ and $|\psi\rangle_B$, the final state can be written as:

$$\psi_o = [(X_A^{m_1} H_A Z_A(\alpha)) \otimes (X_B^{m_2} H_B Z_B(\beta))] \ \ [CZ_{AB}] \ \ (|\psi\rangle_A \otimes |\psi\rangle_B) \tag{1.29}$$

It is then clear that the CZ gate is in-built in the cluster state, in the form of entanglement between qubits 3 and 4. As arbitrary rotations on a single qubit and the CZ gate are a universal set of operations for quantum computation, so is the measurement-based scheme.

In the pictorial representation of the cluster state of Fig. 1.3 b and c, one can associate each row to a logical qubit and the horizontal links with single-qubit rotations. Vertical links on the other hand allow the realization of 2-qubit gates. The shape of the cluster state therefore determines which algorithm is realised. Starting from a complete lattice, with CZ connections among all nodes, a particular algorithm can be "programmed" by applying $Z$ measurements on single qubits, which has the effect of disconnecting and removing them from the lattice. The algorithm is then executed through single-qubit projective measurements and feed-forward of the corresponding outcomes.

Cluster states have been experimentally realised using photons [8, 40, 41], superconducting qubits [42], trapped ions [43] and squeezed states of light [44, 45]. Other promising platforms for MBQC include neutral cold atoms in optical lattices and hybrid optical-matter schemes, such as quantum dots and NV centers [13].

## 1.4 Basics of Quantum Error Correction

This section contextualises and provides theoretical support to Section 2.1, which reports on the experimental demonstration of elements of measurement based quantum error correction.

Faulty coherent quantum gates and uncontrolled interactions with the environment corrupt information encoded in quantum states. To enable accurate quantum information processing and communication in realistic scenarios, one must be able to track and correct arising errors. This is the task of quantum error correction (QEC) [4, 46], encapsulated in the quantum threshold theorem [21, 47], which states that an arbitrarily deep quantum computation can be performed accurately given that the probability of error per gate is below a critical constant threshold, such that the logical error rate can be suppressed through QEC. The threshold levels are determined by the quantum computing architecture and the subjacent error correction scheme. To provide a rough reference, a CNOT acting on two blocks of encoded qubits by a Steane code has a threshold of $\varepsilon \leq 10^{-4}$. More recent schemes achieved more relaxed thresholds, as high as $\varepsilon \leq 10^{-2}$ [21, 48].

The underlying principle of QEC is to encode information in a redundant manner, such that in the event of data loss or data corruption the original message/state can still be retrieved. Contrarily to classical information, where copying information is physically allowed and used to create redundancy, in the quantum case, the no-cloning theorem forbids such approach.

QEC resorts to entanglement to create redundancy and typically develops in three stages: encoding, syndrome readout and decoding [49]. Encoding entails mapping, through a unitary operation, the basis of a qubit onto a highly entangled physical state, called the quantum code or *codeword*. The type of error the information is protected from depends on the code employed. The state of the codeword is then monitored, by coupling to a set of ancillary qubits, whose readout reveals possible alterations caused by noise. The measurement output of the ancillae is called syndrome readout. Finally, the decoding phase retrieves the original codeword by applying corrective gates conditional on the knowledge obtained through syndrome readout.

At the single qubit level, an error may lead to an arbitrary rotation on the Bloch sphere. However, the syndrome measurement projects the corrupted state onto a discrete set of states, easily corrected by a finite set of gates. This feature is called error discretization and can be more easily understood by expressing a general error in the Pauli basis:

$$\begin{aligned} E_i &= e_0 Id + e_1 X + e_2 Y + e_3 Z \\ &= e_0 Id + e_1 X + e_2 (iXZ) + e_3 Z \end{aligned} \tag{1.30}$$

where the $Y$ operator was rewritten in the second line using the cyclic property of the Pauli matrices and $e_i$ are arbitrary real coefficients. Action of an arbitrary error on the encoded state $|\psi\rangle$ creates a superposition:

$$|\psi\rangle = e_0 |\psi\rangle + e_1 X |\psi\rangle + e_2 XZ |\psi\rangle + e_3 Z |\psi\rangle \tag{1.31}$$

which is collapsed onto one of the terms by the syndrome readout. Each term can be mapped back to $|\psi\rangle$ by a gate that cancels the corresponding Pauli-matrix prefactor. It is easy to see that the bit flip (X), the phase flip (Z) or a combination of both suffices to correct an arbitrary error.

The first quantum error correction code was proposed by Shor[50] and using 9-qubit codewords, CNOT and Hadamard gates corrects for an arbitrary error on a single qubit. Parallel work by Steane [51] led to a protocol able to account for arbitrary independent single qubit errors, resorting to 7-qubit codewords. Further developments led to the CSS codes (Calderbank-Shor-Steane) [52], which brought the resources down to 5-qubit codewords, the minimum requirement for arbitrary single qubit error correction. The development of the stabilizer formalism [53] rendered a compact form of representing quantum codes and thereby proved fruitful in producing new ones.

Proof-of-principle experimental demonstrations of quantum error correction by different platforms followed soon after the theoretical groundwork, spanning different physical platforms, including liquid state NMR qubits [54], linear optics [55] and trapped ions [56, 57].

Recent advances in measurement-based architectures suggest that graph/cluster states are particularly robust against noise and gate imperfections, being especially suited for error correction and entanglement purification routines [58, 59]. Given that QEC only involves Clifford gates and Pauli measurements on single-qubits, the QEC circuit models can be translated to MBQC, in the same way as algorithms [60]- see Section 1.3. In Section 2.1, we report on an experimental demonstration of measurement-based quantum error correction, where a phase-protection code is presented.

# 2

# Photonic Entanglement Generation

## Overview

For the past years the leading technology for generating photonic entanglement has been based on spontaneous down conversion (SPDC) in non-linear crystals. Impressive experimental demonstrations have consistently increased the size of entangled states by concatenating single down-conversion events by means of carefully calibrated interferometers and/or fusion gates [61]. In 2005, Walther et. al [8] generated and characterized the first 4-qubit cluster state. In the following years, several consecutive contributions led by Jianwei Pan and others realised 6-photon [62], 8-photon [15] and 10-photon entanglement [63] relying on similar methods.

Both the probabilistic nature of the SPDC process and the non-unit success rate $P_{succ} \in [0.5, 0.75]$ of fusion gates constitute a significant obstacle to scale up to larger entangled states, without an exponential resource overhead. To surmount this issue, alternative entanglement-generation protocols were devised, which could *in principle* lead to deterministic operation. These employed an on demand atom-like single-photon source with an internal degree of freedom used as an ancillary system to create quantum correlations among emitted photons [18, 19]. Even though deterministic operation is *in principle* achievable, imperfections on the single-photon emitters (SPE) and limited photon collection/detection efficiencies render such schemes probabilistic in practice. Over the last years, remarkable progress in the fabrication and performance of solid-state SPEs[20] offers a positive prospect for the scalable,

resource-efficient operation of such systems, which further motivates entanglement-generation schemes based on atom-like emitters.

In the spirit of this thesis, this chapter portrays the transition of the entanglement-generation protocols from SPDC to scalable atom-like SPE architectures. First, SPDC-based entanglement generation is discussed - Section **??** - along with the presentation of our 4-photon cluster state setup - Section 2.0.2. The performance of the this source was good enough for quantum information applications, as shown by the implementation of a measurement-based quantum error correction protocol, described in Section 2.1. Then Section 2.2 introduces the Lindner-Rudolph (LR) scheme, for production of linear cluster states with an atom-like SPE. Finally, a new scalable entangling scheme is proposed, which by modification of the LR protocol, only requires a single optical transition of the emitter, rendering its realization and operation potentially easier and more resource-effective. The experimental execution of the proposed protocol is presented in Chapter 6.

### 2.0.1 Spontaneous Parametric Down-Conversion

Spontaneous parametric down conversion (SPDC) or its counterpart, second harmonic generation (SHG), occur when an electromagnetic field propagates through a non-linear medium. The non-linearity of a material can be expressed in terms of its electric susceptibility, i.e. how an applied electric field $\vec{E}$ induces an electric polarisation density $\vec{P}$, which can be expressed as a polynomial expansion [64]:

$$P_i = \varepsilon_0 \left( \sum_j \chi^{(1)}_{i,j} E_j + \sum_{j,k} \chi^{(2)}_{i,j,k} E_j E_k + \sum_{j,k,l} \chi^{(3)}_{i,j,k,l} E_j E_k E_l + \dots \right) \tag{2.1}$$

where $P_i$ are the components of $\vec{P}$, $E_i$ the components of the electric field $\vec{E}$, $\varepsilon_0$ is the vacuum permittivity, and $\chi^m$ is the m-order susceptibility tensor. The $\chi^m$ terms of order larger than 1 account for the non-linear behaviour of the medium, covering a wide assortment of phenomena. To name a few, $\chi^2$ is responsible for the Pockels effect, SHG and SPDC; while $\chi^3$ is the basis for the optical Kerr effect and third harmonic generation. Considering Maxwell´s wave equation for a field $\vec{E} = E\hat{z}$:

$$\nabla^2 E - \frac{1}{c^2}\frac{\partial^2 \vec{E}}{\partial t^2} = \mu_0^2 \frac{\partial^2 \vec{P}}{\partial t^2} \tag{2.2}$$

it becomes apparent how the polarisation density $P$ behaves as a source term for the electric field. In the Fourier space the non-linear $\chi^m$ coefficients lead to coupling among different frequency components, justifying the transfer of energy among them. For the particular case of SPDC, the energy in a pump field with frequency $\omega_p$ is transferred onto fields at frequencies $\omega_i$

and $\omega_s$, where the subscripts i and s stand for idler and signal. In the photon picture, the pump photon decays into two photons whose frequencies obey an energy conservation relation $\omega_p = \omega_i + \omega_s$. For a buildup of the down-converted fields to happen, it is necessary that the newly generated photons remain in phase with the pump photons as both propagate through the medium. This is called phase-matching and expresses a momentum conservation condition: $\vec{k_p} = \vec{k_s} + \vec{k_i}$. The efficiency of the SPDC process is sensitive to how closely the phase matching condition is achieved, typically by tuning the angle between the pump beam and the optical axis of the crystal.

For type-I SPDC, the pump beam corresponds to an extraordinary-polarised (e-polarised) beam which generates two ordinary-polarised[1] down-converted photons. For type-II SPDC, as used in this thesis, an e-polarised pump leads to the creation of one e- and another o-polarised photon. In this case, if $\omega_i = \omega_s$, the new photons are emitted along the surface of two cones, one for e- the other for o-polarisation, with intersecting bases[65]. At the intersection points, the "which-cone" information is erased and the resulting photonic state is:

$$|\psi\rangle = \frac{1}{\sqrt{2}}(|H\rangle\,|V\rangle + e^{i\varphi}\,|V\rangle\,|H\rangle) \tag{2.3}$$

which is entangled and can be mapped onto any of the 4 Bell pairs by local unitary transformations. As the extraordinary and ordinary beams experience different refractive indices, a down-conversion event will lead to two photons emerging from the crystal at slightly different times, making them distinguishable in this degree of freedom. To counteract the walk-off effect and erase the time information, a second non-linear medium can be added, aligned in such way that the e-beam now becomes an o-beam and vice-versa, leading to refocusing of the two photons. A practical solution is to add a compensation crystal of the same type as the SPDC medium with half the thickness and rotated by 90° around the optical axis or instead by rotating the polarisation of both beams by 90° with a half-wave-plate. [66].

A full account of SPDC, including its probabilistic nature, requires a quantum mechanical treatment, and so the full formalism is briefly presented. Assuming that the ordinary and extraordinary beams correspond to horizontal and vertical polarisations and that the emission occurs within two spatial modes a and b, corresponding to two intersection points of the emission cones, then the non-collinear type-II SPDC emission can be represented in terms of

[1] The extraordinary and ordinary rays correspond to electric field vectors orthogonal to each other. The ordinary ray is polarised in a direction perpendicular to the optic axis of the medium and the refractive index is independent of direction of propagation. On the contrary, the electric field of the extraordinary ray has components both parallel and perpendicular to the optic axis, resulting in a refractive index which depends on the propagation direction.

the following single-pass Hamiltonian[67]:

$$H = g(a_H^\dagger b_V^\dagger + a_V^\dagger b_H^\dagger) \tag{2.4}$$

where $a$, $b$ and $a^\dagger$, $b^\dagger$ are the usual creation and annihilation operators in modes a and b and the subscripts, H and V, identify the polarisation of emission. Applying the corresponding evolution operator to the vacuum generates the output state:

$$\begin{aligned} |\psi\rangle &= Z \cdot e^{-iH}|0\rangle = Z \cdot \exp\left\{(-i\alpha(a_H^\dagger b_V^\dagger + a_V^\dagger b_H^\dagger))\right\}|0\rangle \\ &= Z \cdot \left(1 - \underbrace{i\alpha(a_H^\dagger b_V^\dagger + a_V^\dagger b_H^\dagger)}_{\text{2-photon emission}} - \underbrace{\alpha^2/2(a_H^\dagger b_V^\dagger + a_V^\dagger b_H^\dagger)^2}_{\text{4-photon emission}} + \ldots\right)|0\rangle \end{aligned} \tag{2.5}$$

where $Z$ is a normalizing constant and $\alpha$ is proportional to the pump intensity. The first order term of the expansion is associated with the probabilistic 2-photon emission, corresponding to the creation of the intended Bell pairs with a probability $p_2 \approx Z^2\alpha^2$. The second order term causes the emission of 4 photons with probability $p_4 \approx Z^2\alpha^4$, leading to a reduction of the purity of the source. With $\alpha$ proportional to the pump intensity, the contribution from higher order terms becomes stronger with increased power. The pumping power is therefore subject to optimization to ensure a good compromise between high emission rate and low higher-order noise.

The generation of indistinguishable Bell pairs from different crystals or different pump passages through the same crystal is crucial for realizing larger entangled states, as in the case of the 4-qubit cluster state reported in this work. Such indistinguishability can only be achieved by using a pulsed pump field with pulses shorter than the coherence time of the down-converted photons[2][68, 69]. However, this leads to the degradation of two-photon interference, since a spectrally broader pump leads to high correlations of the down-converted photons in frequency[70]. By spectral filtering of the entangled photons, with narrow-band interference filters ($\Delta\lambda \approx 1$ nm), the high visibility interference is recovered, at the cost of lower counts.

### 2.0.2 Setup for SPDC Generation of Cluster States

The SPDC-based experimental apparatus used in the generation of 4-qubit cluster states employs a type-II SPDC in a non-collinear configuration, based on a beta-barium-borate (BBO) crystal. The requirement for a high-power pulsed pump field is attained by a mode-locked Ti:sapphire laser, Mira900F, pumped by a 10 W solid state laser, Verdi-V10, at

[2]The typical spectral bandwidth of down-converted photons originating from a 2mm BBO crystal corresponds to a FWHM of $\Delta\lambda \approx 10$ nm. The coherence time can be expressed as $t_c = \lambda^2/(c\Delta\lambda)) = 200$ fs

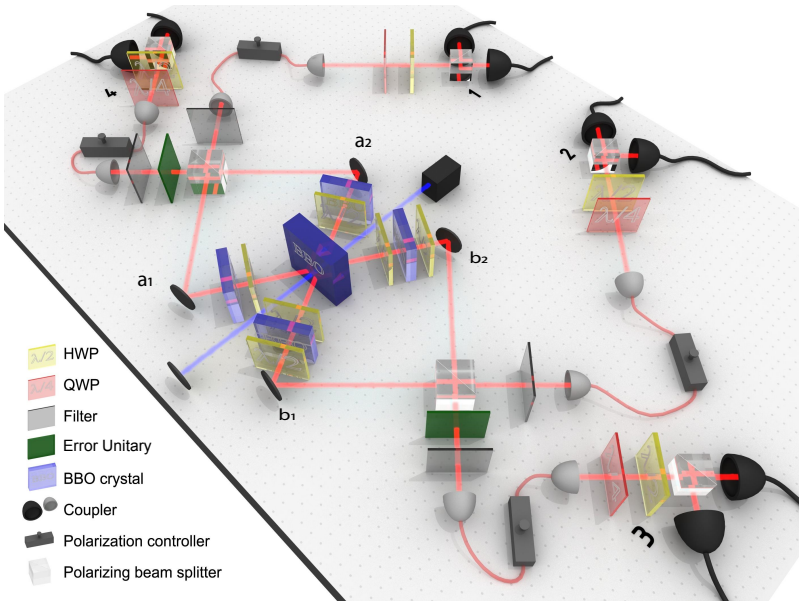


**Figure 2.1: SPDC source used in the generation of the 4-qubit cluster state**. The pulsed UV pump makes a double pass through the 2 mm BBO crystal, yielding entangled photon pairs in the forward and backward modes. The walk-off effects due to birefringence of the BBO are counteracted with compensating 1 mm BBO crystals in each spatial mode. The four emission modes are then overlapped at the polarising-beam-splitters (PBSs) and coupled into single-mode fibers. After polarisation compensation, the photons go through a polarisation tomography stage (QWP+HWP+PBS). Fourfold coincidences signal the creation of the cluster state.

$\lambda = 532$ nm, leading to a pulsed output with a repetition rate of 76 MHz at an average cw-power of 3.0 W at $\lambda = 789$ nm, with a pulse duration of 200 fs. The output is then frequency-doubled through type-I collinear second-harmonic-generation (SHG) to 394.5 nm, by a 2 mm lithium-triborate (LBO) crystal, ensuring a stable source of UV pulses at 0.7 W cw-average, used as a pump field for the SPDC process. The pump beam is filtered with dichroic mirrors to remove residual red light from the SHG process and shaped by cylindrical lenses ensuring a gaussian profile for high down-conversion efficiency.

A double-pass scheme was used in the generation of the 4-qubit cluster state, as depicted in Fig. 2.1 . The UV pulsed pump passes twice through the 2 mm BBO crystal producing an infra-red Bell pair at $\lambda = 789$ nm in the forward direction in the spatial modes $a_1$ and $b_1$ and, after being retro-reflected, another Bell pair in modes $a_2$ and $b_2$. The walk-off of the extraordinary and ordinary down-converted beams is mitigated in each arm by rotating the polarisation by $90^\circ$ and passing the beams through 1mm BBO crystals with the same cut and orientation as the main SPDC crystal. A pair of HWPs in arms $b_1$ and $b_2$, placed after the walk-off crystals, allows one to tune the forward/backward emission into particular Bell pairs, e.g. $\psi^+$ or $\varphi^+$. The $a_1$-$a_2$ and $b_1$-$b_2$

mode pairs are coherently overlapped at two PBSs, by tuning the relative delays with piezo-mounted mirrors. Narrow-band interference filters ($\Delta\lambda = 3$ nm) are used to filter the down-converted photons. The beams are then coupled into single-mode fibers, which after polarisation compensation outcouple onto a polarisation tomography stage, composed of a QWP-HWP-PBS sequence leading to single-photon detectors (PerkinElmer-SPCM AQ4C).

The generation of one $\psi^+$ Bell pair, either in the forward or backward spatial modes, can be conveniently described by the following double-pass[3] Hamiltonian[71]:

$$H = \gamma\left((a_{1H}^\dagger b_{1H}^\dagger + a_{1V}^\dagger b_{1V}^\dagger) + re^{i\Delta\varphi}(a_{2H}^\dagger b_{2H}^\dagger + a_{2V}^\dagger b_{2V}^\dagger)\right) + h.c. \tag{2.6}$$

where the subscripts of the creation operators identify the spatial mode and polarisation of each photon, $r$ is the relative probability of emission into the backward mode and $\Delta\varphi$ is the relative phase between the forward and backward modes, $\gamma$ describes the interaction strength and the hermitian conjugate models a SHG process. The Bell pairs present entanglement visibility of around $V = 94 \pm 1\%$. Reminiscent of the double pass, the description of the four-photon state generation can be extracted from applying $H$ twice to the vacuum state:

$$\begin{aligned} H^2|0\rangle \;=\; & [(a_{1H}^\dagger b_{1H}^\dagger + a_{1V}^\dagger b_{1V}^\dagger)^2 + r^2 e^{i2\Delta\varphi}(a_{2H}^\dagger b_{2H}^\dagger + a_{2V}^\dagger b_{2V}^\dagger)^2 \\ & 2re^{i\Delta\varphi}(a_{1H}^\dagger b_{1H}^\dagger + a_{1V}^\dagger b_{1V}^\dagger)(a_{2H}^\dagger b_{2H}^\dagger + a_{2V}^\dagger b_{2V}^\dagger)]\,|0\rangle \end{aligned} \tag{2.7}$$

The resulting state contains the case where a double-pair is emitted in the forward or the backward modes (upper line), as well as the case where the four photons are spread through the four spatial modes (lower line). Post-selecting the output on four-photon coincidences, where one and only one photon is detected per port, projects the photonic state onto:

$$\begin{aligned} |\psi\rangle \;=\; & 1/2(|V\rangle_1|V\rangle_2|H\rangle_3|H\rangle_4 + r^2 e^{i2\Delta\varphi}|H\rangle_1|H\rangle_2|V\rangle_3|V\rangle_4 \\ & 2re^{i\Delta\varphi}(|H\rangle_1|H\rangle_2|H\rangle_3|H\rangle_4 + |V\rangle_1|V\rangle_2|V\rangle_3|V\rangle_4)) \end{aligned} \tag{2.8}$$

where the photons were relabelled according to the port in which they are detected, following the numeric labels of Fig. 2.1. By adjusting the retro-reflection phase $\Delta\varphi$ and by performing a polarisation rotation on the spatial mode $b_1$ (forward left mode) with a HWP, all coefficients can be balanced (differences in coupling between the backward/forward beams have to be compensated for), to apply local unitary rotations and generate distinct 4-qubit cluster states. A more detailed derivation of the final state can be found in Ref. [66].

The described setup attained a count rate of 0.25 Hz for the generation of 4-qubit linear cluster states, with a fidelity of $F = 65.6 \pm 0.6\%$ .

[3]Note that the polarisation state has been rotated by 90° in arms $b_1$ and $b_2$, with respect to the description found in Eq. 2.4.

## 2.1 Experimental Measurement-Based Quantum Error Correction

To the date of execution of this work, all implementations of measurement-based quantum computation (MBQC) assumed perfect noise-free environments, even though the ability to handle operational or environmental perturbations to the "processing" quantum system is crucial to scaling up quantum computers. The experiment reported in this section demonstrates several building blocks of quantum error correction within a measurement-based architecture, employing a resource cluster state generated by the SPDC source described in the previous section.

This demonstration is based on a platform-independent proposal by Zwerger et. al [60], which performs quantum information processing in encoded states, thereby protecting the logical qubits and quantum gates against external noise and raising the error threshold for fault-tolerant quantum computation to 13% of depolarising noise per particle, at the cost of readily available entangled resource states. Parallel experimental efforts implemented meanwhile the same architecture in an ion trap platform [43].

The theoretical proposal considers resource states that would enable correction of arbitrary single-qubit errors given a resource of sufficient size, by implementation of a measurement-based version of a CSS code. Being limited to 4-qubit states, our experimental realization protects an arbitrary qubit, $|\psi_{in}\rangle = \alpha|0\rangle + \beta|1\rangle$, against phase noise or equivalently against a rotation around the Z-axis of the Bloch sphere.

The basis for this experiment is the 4-qubit cluster state, represented in Fig. 2.2 with qubits numbered from 1 to 4. In the spirit of MBQC, an arbitrary quantum state is redundantly encoded in qubits 2 and 3, by a projective measurement on qubit 1. The codewords are $|0_L\rangle = |+\rangle^{\otimes 2}$ and $|1_L\rangle = |-\rangle^{\otimes 2}$. Further projective measurements on the encoding qubits 2 and 3 reveal whether one of them suffered a phase change and recovers the encoded state in qubit 4. If it is known which of the qubits is affected by noise[4], then it is possible to deterministically recover the initial state - error correction. The steps of the protocol are described in more detail in the coming paragraphs.

### Encoding

The encoding of this protocol relies on a four-qubit box cluster, used as a resource state, depicted in Fig.2.2 a:

$$\begin{aligned} |\psi_{box}\rangle \;=\; & \tfrac{1}{2}[|0\rangle_1|+\rangle_2|+\rangle_3|0\rangle_4 + |0\rangle_1|-\rangle_2|-\rangle_3|1\rangle_4 \\ & + |1\rangle_1|-\rangle_2|-\rangle_3|0\rangle_4 + |1\rangle_1|+\rangle_2|+\rangle_3|1\rangle_4] \end{aligned} \tag{2.9}$$

[4] With a 5-qubit resource state, the syndrome readout would reveal the error location and this assumption would not be necessary.

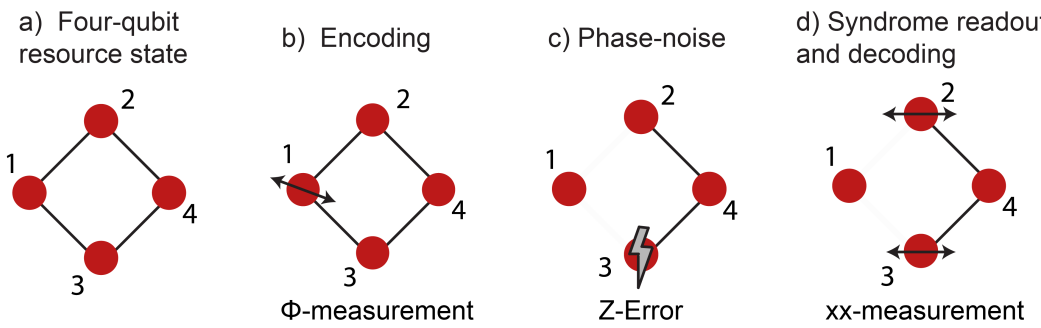


e)

| Error type | No error | $Z_2$ error | $Z_3$ error |
|---|---|---|---|
| Syndrome measurement | $\|++\rangle_{23}$ $\|--\rangle_{23}$ | $\|-+\rangle_{23}$ $\|+-\rangle_{23}$ | $\|+-\rangle_{23}$ $\|-+\rangle_{23}$ |
| Recovery operation | Id X | Id X | Id X |

**Figure 2.2: Protocol for measurement-based quantum error correction**. **a)** A 4-qubit box cluster state is used as the resource state. **b)** A projective measurement in qubit 1 encodes the states in qubits 2 and 3. **c)** The code state is affected by phase noise on qubit 3. **d)** Qubits 2 and 3 are measured in the xx-basis and the readout establishes the recovery operation. **e)** Syndrome readout and recovery operations for a phase flip (Z) on qubit 2 or 3. The recovery gate is either a qubit flip ($X$) or the identity applied to qubit 4.

which is generated by, first, producing the state described in Eq. 2.8:

$$\begin{aligned} |\psi_{lab}\rangle \quad = \quad & 1/2(|0\rangle_1 |0\rangle_2 |0\rangle_3 |0\rangle_4 + |0\rangle_1 |0\rangle_2 |1\rangle_3 |1\rangle_4 \\ & |1\rangle_1 |1\rangle_2 |0\rangle_3 |0\rangle_4 - |1\rangle_1 |1\rangle_2 |1\rangle_3 |1\rangle_4) \end{aligned} \tag{2.10}$$

and then applying local unitary transformations, according to:

$$|\psi_{box}\rangle = (H_1 \otimes H_2 \otimes H_3 \otimes H_4)(SWAP_{24}) \; |\psi_{lab}\rangle \tag{2.11}$$

where the SWAP gate is realised by interchanging the qubits physically. The Hadamard gates, $H$, are absorbed in the measurement basis and dealt with in post-processing.

The resource state was characterized by reconstructing the corresponding density matrix $\rho$, through state tomography. For the instance where no error was introduced, the density matrix is represented in Fig. 2.3 in the $Z \otimes X \otimes X \otimes Z$ eigenbasis, corresponding to a fidelity of $F = 65.6 \pm 0.6\%$, up to local unitary transformations. To mimic Z-errors on qubit 2 and 3, different resource states were produced by applying Z-rotations through QWPs and HWPs in the corresponding output modes, 2 and 4, as signalled in Fig. 2.1 a. Note that due to the

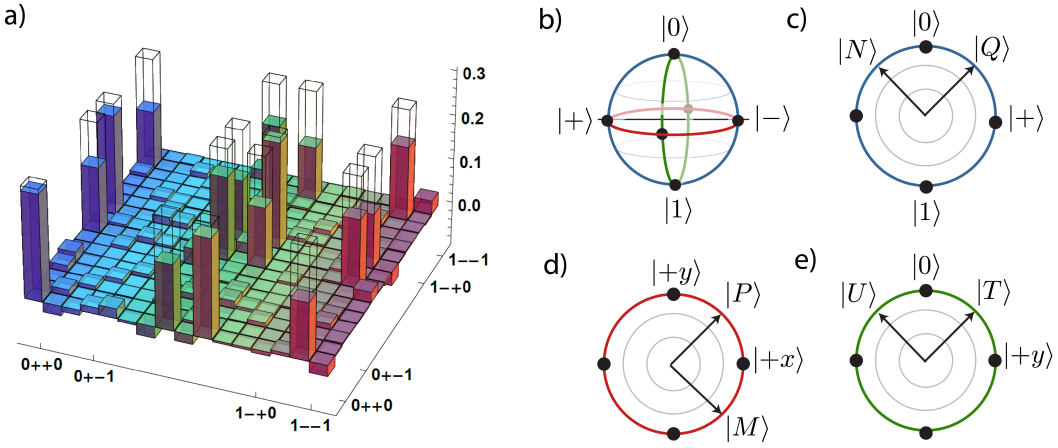


**Figure 2.3: a) Real entries of the density matrix of box cluster state in the eigenbasis of** $Z \otimes X \otimes X \otimes Z$. The wire frames represent the ideal case. The imaginary terms have values below 3.7% and are therefore not represented. **b)** Bloch sphere with xz-plane in blue, xy-plane in red and yz in green. **c)** Encoded states $|N\rangle$ and $|Q\rangle$ within the xz plane. **d)** Encoded states $|P\rangle$ and $|M\rangle$ in the xy plane. **e)** Encoded states $|U\rangle$ and $|T\rangle$ in the yz plane. The analytic definition of the encoded states can be found in Table 7.1 of the appendix.

$SWAP_{24}$ operation, the Z-rotation on mode 4 is mapped onto qubit 3. The resource states used for the cases where a phase error was applied are presented in the appendix section 7.2.

The encoding is realised through a projective measurement on qubit 1, as identified in Fig. 2.2 b, in the basis comprising the outputs $|p_0\rangle = \alpha^* |0\rangle + \beta^* |1\rangle$ and $|p_1\rangle = \beta |0\rangle - \alpha |1\rangle$. If the projection $|p_0\rangle \langle p_0|$ is realised, then the encoding succeeds and the remaining three qubits are found in the following encoded state:

$$\begin{aligned} |\psi_3\rangle \quad = \quad & \tfrac{\alpha}{\sqrt{2}}(|{+}{+}\rangle_{23} |0\rangle_4 + |{-}{-}\rangle_{23} |1\rangle_4) \\ & + \tfrac{\beta}{\sqrt{2}}(|{-}{-}\rangle_{23} |0\rangle_4 + |{+}{+}\rangle_{23} |1\rangle_4) \end{aligned} \tag{2.12}$$

If, otherwise, qubit 1 is projected onto $|p_1\rangle$, then the encoded state is:

$$\begin{aligned} |\psi_3\rangle \quad = \quad & \tfrac{\beta^*}{\sqrt{2}}(|{+}{+}\rangle_{23} |0\rangle_4 + |{-}{-}\rangle_{23} |1\rangle_4) \\ & - \tfrac{\alpha^*}{\sqrt{2}}(|{-}{-}\rangle_{23} |0\rangle_4 + |{+}{+}\rangle_{23} |1\rangle_4) \end{aligned} \tag{2.13}$$

which can be reverted to the successful encoding case, by application of local Pauli operations, e.g. $X_2 Z_2 \otimes Z_3$, if the coefficients $\alpha$ and $\beta$ are real. If $\alpha$ or $\beta$ have an imaginary component, such compensatory operation is not possible and the encoding is probabilistic: the projective measurement has to be repeated until the desired outcome $|p_0\rangle$ is observed.

### Syndrome Readout and Decoding

Consider that a continuous phase error, modelled as a rotation around the Z-axis by an arbitrary angle $\theta$ ($e^{-i\theta/2\,Z}$)[5], can occur in qubit 2 or 3. For simplicity it is assumed that qubit 3 is the one affected; the case for which qubit 2 is perturbed follows along the same lines and hence not explained here. The 3-particle encoded state then becomes:

$$\begin{aligned} \left|\psi_3\right\rangle \;=\; & \cos(\theta/2)\left[\tfrac{\alpha}{\sqrt{2}}(|++0\rangle+|--1\rangle)+\tfrac{\beta}{\sqrt{2}}(|--0\rangle+|++1\rangle)\right] \\ & i\sin(\theta/2)\left[\tfrac{\alpha}{\sqrt{2}}(|+-0\rangle-|-+1\rangle)+\tfrac{\beta}{\sqrt{2}}(-|-+0\rangle+|+-1\rangle)\right] \end{aligned} \tag{2.14}$$

which is divided into terms that have been affected by the Z-rotation and those which have not. The error syndrome is extracted by performing a $XX$-measurement on qubits 2 and 3, leading to four possible readouts: with a probability $p=\cos(\theta/2)^2$ the outcomes $|{+}{+}\rangle$ or $|{-}{-}\rangle$ establish that no Z-rotation occurred, whereas $|{+}{-}\rangle$ or $|{-}{+}\rangle$ indicate a Z-flip on qubit 3 with a probability $p=\sin(\theta/2)^2$. Note that despite the error being a rotation around the Z-axis by an arbitrary angle, the syndrome readout leads to a discretization of the error at the output, easily corrected by a single Pauli operation.

The projective measurements onto $|{+}{+}\rangle_{23}$ or $|{+}{-}\rangle_{23}$ recover the initial state $\left|\psi_{in}\right\rangle$, which is teleported to qubit 4 without requiring any corrective operation; if otherwise qubits 2 and 3 project onto $|{-}{-}\rangle$ or $|{-}{+}\rangle$ then qubit 4 is found in the state $X\left|\psi_{in}\right\rangle$, corrected by applying an $X$ gate. The error syndrome and corresponding corrective gates are summarized in Fig. 2.2 e for the cases where the Z-error acts on qubit 2 or 3. Note also that the syndrome readout and decoding of the state happen within the same step.

The protocol was benchmarked by choosing a set of states $\left|\psi_{in}\right\rangle$, represented in Fig. 2.3, which were encoded onto the resource box cluster state, subject to noise and then recovered in qubit 4, whose state is described by $\rho_4$. The fidelity between the final and initial states, $F=\sqrt{\left\langle\psi_{in}\right|\rho_4\left|\psi_{in}\right\rangle}$, quantifies the success of the protocol. For the cases where no recovery operation was required the fidelities for the different input states fall within the range $[81.0\pm3.6, 99.0\pm0.9]$. For the cases where a $X$ recovery gate was necessary, the fidelities were within the range $[62.9\pm3.9, 98.2\pm0.8]$. A full list of encoded and decoded states, with the respective fidelities, can be found in the Appendix Section 7.2.2.

Due to the non-ideal resource states, the different projections onto qubits 2 and 3 vary slightly, leading to the variance on the fidelities for different input states. An illustration of the experimental procedure is found in Fig. 2.4, where the state $|N\rangle=(|+_i\rangle+e^{-i(\pi/4)}\,|-_i\rangle)/\sqrt{2}$, for $|\pm_i\rangle=(|0\rangle\pm|1\rangle)/\sqrt{2}$, was encoded, subjected to a full phase flip in qubit 3 and finally

[5] A $e^{-i\theta/2\,Z}$ rotation on the $|\pm\rangle$ basis realises the following map: $(|+\rangle\rightarrow\cos(\theta/2)\,|+\rangle+i\sin(\theta/2)\,|-\rangle)$ and $(|-\rangle\rightarrow-i\sin(\theta/2)\,|+\rangle+\cos(\theta/2)\,|-\rangle$

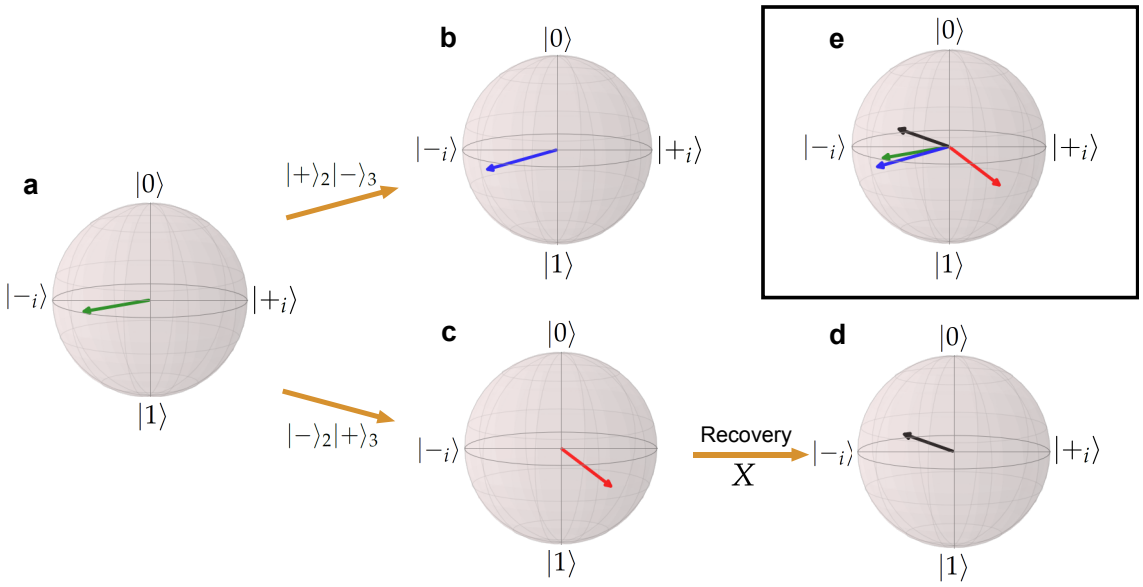


**Figure 2.4: Error correction protocol for the encoded state** $|M\rangle$. **a)** Bloch sphere representation of the state $|M\rangle = (|+x\rangle + e^{i(\pi/4)}|-\rangle)/\sqrt{2}$. **b)** Decoded state when a full phase flip $Z$ acts on qubit 3 and the syndrome readout yields $|+-\rangle_{23}$, requiring no recovery operation. The final state displays a fidelity $F = 0.984 \pm 0.016$. **c)** Representation of qubit 4, in the case where the syndrome reads $|-+\rangle_{23}$, before the recovery operation is applied. **d)** Final state after the recovery operation $X_4$ is applied in post-processing, corresponding to a fidelity $F = 0.941 \pm 0.025$.

decoded/recovered. The fidelities for the full set of encoded states and different error rotations can be found in the appendix, Section 7.2. The leading contribution to the degradation of the fidelities is the phase instability of the 4-arm interferometer that combines the multi-photon emissions from the SPDC process. The error bars in the data result from Poissonian noise in the photon counts. The data acquisition time was 600 s per measurement setting on the box cluster state. For the cases where a Z-error was applied, longer integration times were used: 1800 s for the cases associated with a $\pi$ Z-rotation and 3600 s for a $\pi/2$ Z-rotation.

### Outlook

Having only two intermediate qubits implies that the error location must be known for the correction to retrieve the initial state. Access to larger cluster states surpasses this limitation. The syndrome readout can be generalized by using cluster states as represented in Fig. 2.5 [43, 60], with $n$ intermediate qubits. The codewords are $|0_L\rangle = |+\rangle^{\otimes n}$ and $|1_L\rangle = |-\rangle^{\otimes n}$ and they are able to detect and correct phase flips $Z$ on up to $(n-1)/2$ arbitrary intermediate qubits. Such cluster states are feasible with current SPDC technology.

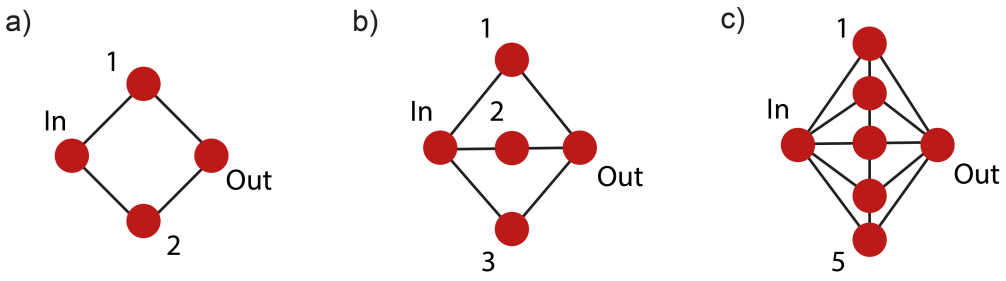


**Figure 2.5: Resource states for phase-flip error correction.** Cluster states with $n = 2$, $n = 3$ and $n = 5$ intermediate qubits which implement a quantum code for phase-flip correction. Simultaneous phase flips on up to $(n-1)/2$ can be detected and corrected.

Similarly, following the prescription of Zwerger et. al [60] scaling to 6-qubit cluster states would enable the protection of a logical qubit from an arbitrary error. By concatenating modules which implement measurement-based coherent gates and error correction, this architecture supports a fault-tolerant one-way quantum computer, given the necessary resource cluster states are readily available. This further confirms the necessity for alternative approaches for deterministic generation of high-fidelity cluster states, which takes us to the next section.

## 2.2 Photonic Entanglement Generation by a Single-Photon Emitter

Consider a two-level system separated by an optical energy gap. Exciting the population from the ground to the excited state is followed by spontaneous decay, to render a single photon. Such system is identified, in this text, as an atom-like single photon emitter (SPE). If the population transfer from ground to excited state is perfect, if there are no alternative decay paths and the emission can be efficiently collected, then a sequence of N-excitation/emission cycles will deterministically produce a train of $N$ photons. If the emitter has one additional controllable degree of freedom $s$ (e.g. another energy level), by intercalating excitation/emission cycles with operations on $s$, one can produce a variety of entangled photonic states. This is the basic idea explored in a proposal by Lindner and Rudolph [18], which employs a SPE to, *in principle*, deterministically generate a linear cluster state. This scheme, also called the cluster state machine gun (CSMG), requires two ground states ($|0\rangle$ and $|1\rangle$), optically coupled to the respective excited states ($|0_e\rangle$ and $|1_e\rangle$) by a pair of degenerate transitions, with selection rules that grant orthogonal polarisations among the two, as illustrated in Fig. 2.6. By creating a superposition between the two ground levels and then running an optical excitation-emission cycle, one generates the following emitter-photon state:

$$\alpha|0\rangle + \beta|1\rangle \rightarrow \alpha|0\rangle|0\rangle_p + \beta|1\rangle|1\rangle_p \tag{2.15}$$

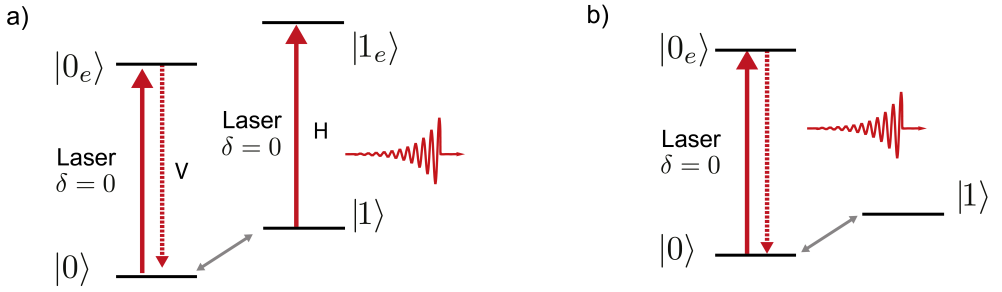


**Figure 2.6: a)** Energy scheme necessary for the Linder-Rudolph protocol. 4 levels are connected by two optical degenerate transitions, associated with photons with orthogonal polarisations. A single optical frequency is tuned to the two transitions, thus exhibiting null detuning, $\delta = 0$. **b)** Energy scheme used in the time-bin / one-transition scheme, involving three energy levels, two of which are coupled by an optical transition. There are no requirements regarding degeneracy or the polarisation of the emitted photons.

where the first ket refers to the emitter and the second to the photon. $|0\rangle_p$ and $|1\rangle_p$ are the two orthogonal emissions, represented in the computational basis. For a maximally entangled state one should set $|\alpha| = |\beta|$ or, equivalently, apply a Hadamard gate when creating the superposition between the ground states. By iteratively performing the Hadamard operation followed by an excitation-emission cycle, a progressively larger cluster state is created, with each cycle adding a new photon to the chain. This can be demonstrated by induction [72]. Assume that the system is described as linear cluster state with $N$ photons. One can generally write it as:

$$|\varphi\rangle_n = |0\rangle |\psi_n\rangle + |1\rangle |\bar{\psi}_n\rangle \tag{2.16}$$

Note that according to the definition of cluster states in Eq. 1.23, the stabilizer centred on the emitter $X_a Z_n$, with $Z_n$ being applied on the photon generated last, must leave the cluster state unchanged. Thereby one can easily establish that $|\bar{\psi}_n\rangle = Z_n |\psi_n\rangle$. By pumping the optical transition and then applying a Hadamard gate, the following map is realised:

$$|0\rangle |\psi_n\rangle + |1\rangle |\bar{\psi}_n\rangle \xrightarrow{\text{Pump}} |0\rangle |\psi_n\rangle |0\rangle_{n+1} + |1\rangle |\bar{\psi}_n\rangle |1\rangle_{n+1} \xrightarrow{\text{H}} |+\rangle |\psi_n\rangle |0\rangle_{n+1} + |-\rangle |\bar{\psi}_n\rangle |1\rangle_{n+1} \tag{2.17}$$

where the last ket indicates the newly emitted photon. The last expression can be rearranged:

$$|\varphi\rangle_{n+1} = |0\rangle \overbrace{(|\psi_n\rangle |0\rangle_{n+1} + |\overline{\psi_n}\rangle |1\rangle_{n+1})}^{|\psi_{n+1}\rangle} + |1\rangle \overbrace{(|\psi_n\rangle |0\rangle_{n+1} - |\overline{\psi_n}\rangle |1\rangle_{n+1})}^{|\overline{\psi_{n+1}}\rangle}, \tag{2.18}$$

which is also stabilised by $X_a Z_n$ and therefore a cluster state with $n+1$ photons. This proves that the pump-Hadamard cycle adds one new photon to the cluster state chain. This operation can

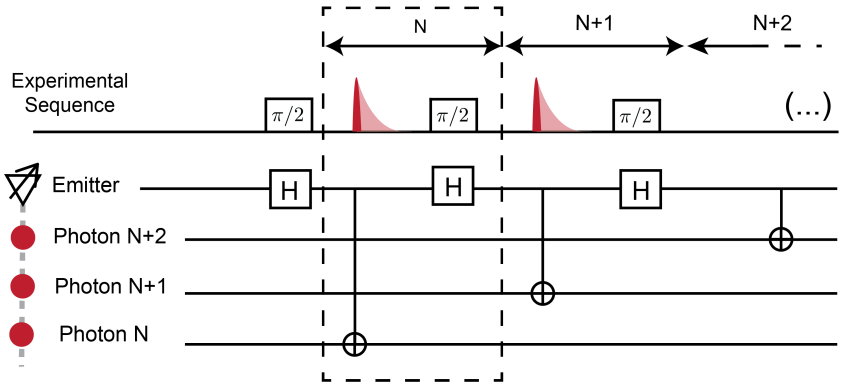


**Figure 2.7: Circuit model representation of the Linder-Rudolph/CSMG protocol.** The optical pump action is equivalent to a CNOT gate with the emitter as control. The Hadamard gate is typically implemented with a $\pi/2$ rotation around the X or Y axis. Each iteration adds a new photon to the linear cluster.

also be represented in terms of the circuit model, as depicted in Fig. 2.7, where the pump operation is equivalent to a CNOT gate between the emitter and the newly generated photon.

The utility of the CSMG has been broadened to include the generation of 2D $(m \times n)$ cluster states with a proposal by Economou [73]. In this scheme, $m$ emitters are required for the extra dimension of the cluster. Each one undergoes iterative pump-Hadamard cycles, intercalated with CZ gates among neighbouring emitters. This sequence repeatedly transfers the entanglement between SPEs onto the linear chains, rendering a square lattice, which is a universal resource for quantum computation. A more sophisticated version of this protocol has been proposed by Russo [72], where the emitter-emitter entangling operation can be applied after the Hadamard-pump cycle. This is advantageous as the CZ gates are typically costly and in this way they can be applied only if the emission is successful. Another extension of the CSMG, advanced by Russo [74], employs a SPE to produce a 2-dimensional cluster state, more specifically, a repeater graph state, with applications in the distribution of photonic entanglement and, thereby, quantum communication.

## 2.3 Photonic Entanglement Generation with One Optical Transition

The CSMG schemes and their derivatives[72, 73] could all in principle lead to a deterministic generation of cluster states. In reality, the requirements of these protocol are not strictly met and the current experimental realizations remain probabilistic. Besides the limited collection efficiency, one of the main obstacles are the non-ideal emitters, which typically have an energy level structure that only approximates the desired 4-level configuration with 2 degenerate transition and orthogonal polarisations. Common issues include limited quantum yield due to

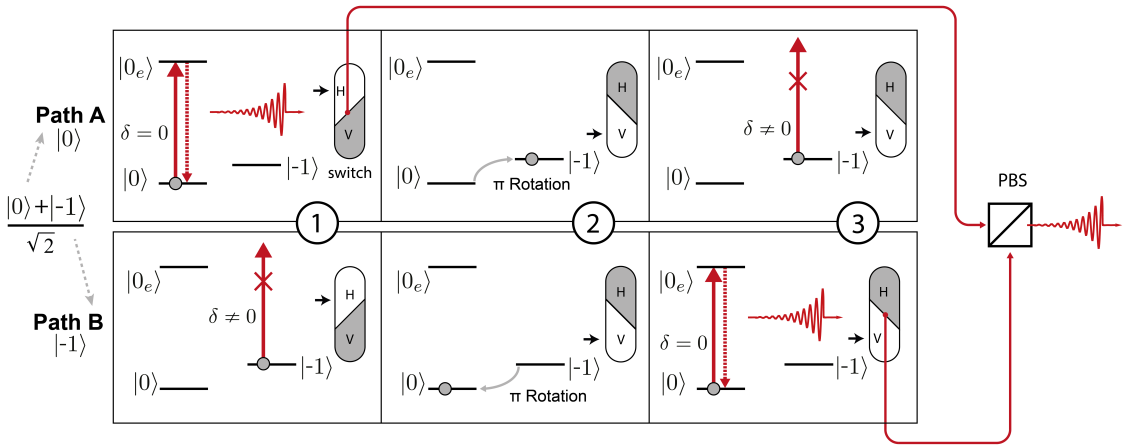


**Figure 2.8: One-transition entanglement generation protocol**. The energy level scheme has a lambda configuration, consisting of an optical transition and an extra internal degree of freedom distinguishing the two ground states. At each iteration, the ground state is found in a superposition between $|0\rangle$ and $|-1\rangle$. The upper pane (A) in the figure illustrates the system evolution for the term initially in $|0\rangle$ and the lower pane (B) in $|-1\rangle$. In panels 1, an optical excitation leads to the generation of a photon of arbitrary but definite polarisation, which is guided by a switch into a delay line where the polarisation is rotated onto $|H\rangle$. The optical excitation does not render a photon in path B, as the corresponding transition is detuned. In panels 2, the the superposition of the ground state is inverted by a $\pi$ rotation. In panels 3, a second optical excitation now leads to the emission of a photon in path B, but not A. This time, the emission is guided by a switch into an optical channel in which the polarisation is rotated onto $|V\rangle$. If the difference in propagation between the two optical channels matches the time difference between the two excitations, then the two wavepackets overlap at the PBS and emerge in one of the outputs in an entangled state $|\psi^+\rangle = |0, V\rangle + |-1, H\rangle$.

alternative decay paths, cross decay channels, non-degenerate optical transitions that need to be engineered to attain degeneracy, unequal luminescence from the two transitions, among others.

The protocol proposed in this thesis, which is experimentally demonstrated in Chapter 6, requires one single optical transition, thus lowering the requirements for the CSMG protocol and widening the range of emitters which adhere to its requirements. This feature removes the necessity to engineer/tune degenerate pairs of transitions and allows one to choose the brightest transition within the emitters´ energy spectrum. This process renders photonic qubits in a time basis and it is assisted by an unbalanced polarising interferometer, which converts from the time-bin to a polarisation basis, where single-qubit gates and tomography can be easily performed.

The required energy-level structure is depicted in Fig. 2.6 b, showing the single optical entangling transition and the ground state with two levels discerned by some internal degree of freedom, e.g. spin. The entangling process, illustrated in Fig. 2.8, starts with a ground state

superposition $|\psi\rangle = (|0\rangle + |1\rangle)/\sqrt{2}$. The diagram is divided in two "stories", depicted in the upper and lower panes, which correspond to the evolution of the system taking either $|0\rangle$ or $|1\rangle$ as a starting state. Upon excitation by an optical $\pi$-pulse, the emitter yields a photon with 50 % probability, which is rotated onto H polarisation and stored in an optical channel $C_1$. Note that the optical excitation has no effect on the $|1\rangle$ term of the ground state superposition. During the storage time, the ground state populations are inverted by a $\pi$-rotation and a second optical excitation ensues, producing an emission with 50 % probability. This wavepacket is rotated onto a V-polarisation state and collected by another optical channel, $C_2$. At this stage the emitter-photon state is entangled in several degrees of freedom: temporal, spatial and polarisation. One could represent it as:

$$|\psi\rangle = (|1\rangle |E\rangle |H\rangle |C_1\rangle \; + \; |0\rangle |L\rangle |V\rangle |C_2\rangle)/\sqrt{2} \tag{2.19}$$

where the first ket refers to state of the emitter, the second represents the early $|E\rangle$ and late $|L\rangle$ emissions, the third the polarisation of the wavepackets, $|H\rangle$ or $|V\rangle$, and the fourth term identifies the spatial route taken by the wavepacket, $|C_1\rangle$ or $|C_2\rangle$.

If the difference in storage time between the two channels differs by the time separation between the two optical excitations, the wavepackets can be overlapped and the time information erased. Using a PBS to recombine the wavepackets in a single path erases the discerning spatial degree of freedom such that the photon state is reduced to a polarisation qubit. The resulting emitter-photon state is then:

$$|\psi\rangle = (|1\rangle |H\rangle \; + \; |0\rangle |V\rangle)/\sqrt{2} \tag{2.20}$$

which constitutes the intended Bell pair. A further Hadamard gate on the emitter leads to a 2-particle cluster state. Comparing this sequence with the original CSMG, it is clear that the single optical excitation on the pair of degenerate optical transitions has been replaced by two optical excitations on a single transition separated by a ground state population inversion.

For future reference, the apparatus responsible for the polarisation rotation, storage of the wavepackets and respective overlap is referred to as a time-to-polarisation (TPC) converter and throughout this thesis the entangling protocol is identified as the *TPC scheme* or *one-transition protocol*. Note that even without the action of the TPC components, after the second optical excitation the system is already entangled on a time-bin basis. The conversion to polarisation is nonetheless necessary to witness entanglement and generate a usable/useful resource state, since single-qubit gates i the time-basis are hard to perform.

To provide a more mathematical description of the protocol, the entangling block of the TPC

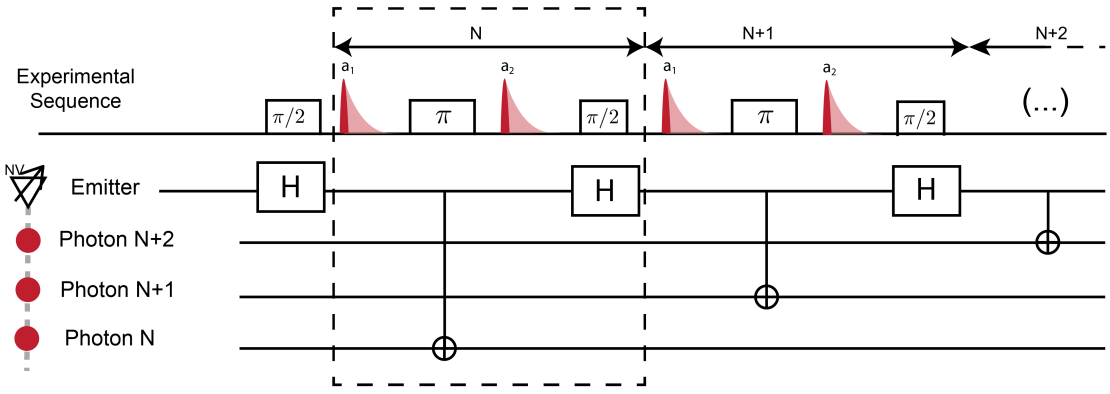


**Figure 2.9: Circuit model of the TPC-based entangling scheme.** The experimental sequence resorts to $\pi$ and $\pi/2$ rotations on the emitter´s ground state populations and optical excitation/emission cycles. The CNOT gates are realised by two optical excitations separated by a $\pi$ rotation. The building block of the scheme is emphasized with a dashed line. Each iteration of this element adds a new photon to the linear cluster.

scheme can be described as:

$$\hat{C} = (H \otimes Id)\, CNOT_{ep}\, (H \otimes Id) \tag{2.21}$$

where the Hadamard gates are applied to the emitter and the $CNOT_{ep}$ takes the emitter as control and the newly generated photon as target. The associated circuit diagram is represented in Fig. 2.9, where, in the spirit of the CSMG scheme, repetition of the entangling block $\left[CNOT_{ep}\, (H \otimes Id)\right]$ leads to the addition of new photons to the linear cluster. Chapter 6 describes the experimental realisation of one entangling block, which constitutes the fundamental unit of the protocol.

The generalisation to the multiphoton case is crucially dependent on the coherence of the emitter qubit, which mediates the phase relation between two consecutive photons of the chain. Therefore it is necessary for the coherence lifetime of the emitter to be longer than the emission of two consecutive photonic qubits. Any loss of coherence translates in a decrease of fidelity of the generated state. Even though this scheme is in principle deterministic, photon loss leads to a non-unity system efficiency $\eta < 1$, which limits the size (photon number) of the generated cluster state. The discussion of the multi-photon outlook is postponed to Section 6.4, where the performance of the scheme is described with respect to realistic experimental conditions.

# 3

# The Nitrogen-Vacancy Defect Centre

## Overview

The negatively charged nitrogen-vacancy centre in diamond, $NV^-$, lies at the centre of this experimental work as a single photon emitter and spin-photon interface. Akin to a molecule enclosed in a diamond lattice shielding it from the environment, the $NV^-$ centre has an electronic spin which hosts a robust matter qubit, whereas photons emitted upon decay from the excited to the ground state encode flying qubits.

This chapter provides an overview of the physical aspects of the centre, starting with the properties of diamond as a host material - Section 3.2 - followed by an account of the electronic structure of the NV centre due to the geometry imposed by the crystal lattice - Section 3.3. The electronic structure naturally unfolds into three categories of energy levels, belonging to the optical ground state manifold, which hosts the matter qubit of the TPC protocol - Section 3.4 -, the optical excited state manifold, which accounts for most of the characteristics of the optical spectrum - Section 3.5 - and the singlet manifold - Section 3.6. The phonon-side-band emission is then discussed as a vibronic effect of the the hosting lattice - Section 3.7 - followed by the ionisation dynamics due to optical pumping - Section 3.8.

## 3.1 Historical Perspective and General Properties

The first observation of the NV centre as a single defect and single photon emitter dates back to 1997 [75] where it prompted a broad enthusiasm of the quantum community, leading to prolific research on various fronts over the past two decades, exemplified ahead.

The NV centre is a bright photostable single photon emitter [76], which occurs naturally or can be produced with a high degree of control over its properties [77–79], including positioning accuracy, spin coherence time and optical linewidth. It possesses, under cryogenic conditions, an electronic spin which can be optically polarised with $\geq 99\%$ fidelity [80] and spin-preserving optical transitions which enable single-shot non-demolition readout of the spin state with $\geq 95\%$ fidelities [81–83]. High precision control over the electronic spin degree of freedom has been achieved using microwave fields in the strong driving regime [84]. Furthermore, due to a weak spin-orbit coupling in the ground state, the NV centre possesses long longitudinal spin relaxation times, $T_1$, reaching 5 ms at room temperature [85] and several hours under cryogenic conditions [86]. Also the electronic spin-dephasing time $T_2^*$ is remarkably long, possibly attaining coherence times in the range of miliseconds to seconds, by means of isotopically purified samples [87] or dynamic decoupling sequences [29], both aimed at reducing the effect of the spin-bath on single NV centres.

The versatility of the NV centre is further broadened by its interface to neighbouring nuclear spins (e.g. $^{13}$C, $^{14}$N,$^{15}$N), which supports the realization of efficient quantum memories and error correction protocols [24, 88, 89]. Nuclear based qubits benefit from highly enduring relaxation times, $T_1$ and $T_2^*$, which can be extended to seconds even at room temperature [90]. Microwave or radio-frequency fields are used for conditional gates between the nuclear and electron spins, supporting high-fidelity nuclear initialization routines ($F \geq 90\%$) and single shot nuclear readout [91].

These capabilities have assisted a steady torrent of remarkable quantum optics experiments surrounding the NV centre, including the demonstration of spin-photon entanglement [92], spin-spin entanglement [83, 93], unconditional teleportation [94], quantum error-correction on matter qubits [95, 96] and distillation of remote entanglement [97]. These establish the building blocks to realize a distributed network of entangled spins, with potential applications in quantum communication [98–100] and quantum information processing [12, 33]. The long repertoire of applications extends further to diverse metrology schemes, where the centre was used as a thermometer [101] and as a magnetic and electric-field sensor [102–104]. The NV centre was moreover employed in fundamental tests of quantum mechanics, spanning quantum process tomography [105], Bell tests [106, 107], among others.

Having mentioned the centre´s main physical features and recent applications, this Chapter

develops on describing its atomic structure and environment, to account for its properties.

## 3.2 Diamond Structure and Properties

Diamond, the host material of the nitrogen-vacancy centre, is formed by a network of carbon atoms arranged in a $Fd\bar{3}m$ cubic lattice [108], where each carbon connects to its four nearest-neighbours through tetrahedral $sp^3$ covalent bonds. Each unit cell has a side length of $a_0 = 0.357$ nm and can be thought of as two interpenetrating face-centred cubic lattices shifted by $a_0/4$ along a diagonal. Such structure allows for a very dense packing of carbon atoms and justifies the hardness of the material.

Via substitution of carbon atoms, naturally or through ion implantation, different defects can occur in the diamond lattice, leading to modification of its absorption spectrum and luminescence, which allows for their identification and cataloguing[109]. While the nitrogen-vacancy (NV) and the silicon-vacancy (SiV) centres are the most commonly researched, other point defects include the nitrogen H3 centre and the nickel NE8 centre, with diminished popularity owing to the poor control over synthesis conditions [110][20]. Boron, oxygen, hydrogen, aluminium, among others, have been reported as substitutional elements in diamond [109], but only as extended defects (as opposed to point defects), and remain uninteresting for quantum applications as potential single photon emitters.

While relatively pure diamond occurs naturally, since the 1950s through a high-temperature high-pressure (HTHP) setting that mimics the natural synthesis conditions, it can be produced in laboratory [111]. Development and application of chemical vapour deposition (CVD) to diamond in the 1980s led to the fabrication of higher quality crystals and this remains as the *de facto* production technique for quantum applications, yielding high purity lattices with very low concentration of impurities, namely nitrogen content below 1ppb. On top of the excellent control over purity and structure, state-of-the-art production yields isotopically purified diamonds, with a depletion of $^{13}C$ reaching 0.3% and a concentration of other paramagnetic impurities below $10^{13}$ $cm^{-3}$ [87], which is particularly relevant in providing a clean magnetic environment within the crystal.

The suitability of diamond as a host of optical emitters relies on its wide bandgap and wide transparency window stretching from the bandgap transition (225 nm) to the phonon band absorption (from 2.5 to 7 µm). In the particular case of the NV and SiV centres, the distance between the defect energy levels and the crystal valence and conduction band is responsible for the stability of the single photon emitter even at room temperatures.

The most common classification system of diamonds is based on optical properties. Type I diamonds have an absorption edge at $\lambda_e = 330$nm, meaning there is significant absorption for

wavelengths smaller than $\lambda_e$, due to high concentration (N>5ppm) of nitrogen. Type I diamond are further composed of two subclasses: (1) type Ia in which nitrogen impurities form aggregates or "platelets" and (2) type Ib where the substitutional nitrogen is found as individual point defects. For the second class of diamonds, type II, the absorption edge coincides with the diamond bandgap (5.47eV, $\lambda = 225$ nm), due to the low concentration of nitrogen (N<5ppm). Type IIa hosts nitrogen as the main impurity and behaves as an electrical insulator, as opposed to type IIb which behaves as a p-type semiconductor, owing to boron as the major defect. A comprehensive review of diamond types and diamond defects can be found in the work by Walker [109]. Most synthetic diamond produced with CVD falls within the type IIa category. In the execution of this work, we have employed ultrahigh purity electronic grade CVD grown diamond, with nitrogen concentrations of N < 1ppb, produced by Diam2tec.

## 3.3 The NV Centre and its Electronic Structure

The nitrogen-vacancy centre is a diamond point defect with a substitutional nitrogen and a neighbouring vacancy, both lying along the $\langle 111 \rangle$ crystallographic direction, as illustrated in Fig. 3.1. In its neutral charge state NV°, five unpaired electrons (three dangling bonds from the nearest carbons and two from the nitrogen atom) form an electronic cloud localized around the vacancy. The capture of an extra electron from the crystal valence band results in the the negatively charged state $NV^-$. Conversion from $NV^-$ to NV° is mediated by a two photon process, in which one of the six electrons is promoted to the continuum of the conduction band [112].

The NV complex can either result naturally from the crystal formation or be introduced artificially, in a controlled fashion, where electron, neutron or proton irradiation techniques are used for the generation of vacancies [77], while Nitrogen implantation is implemented with a focused ion beam [113]. A subsequent annealing step at $\geq$ 600°C gives mobility to the lattice vacancies and fosters the energetically favourable recombination with nitrogens [78], leading to the formation of NV centres.

The nuclei and the lattice electrons that surround the vacancy impose an electrostatic potential with trigonal $C_{3V}$ symmetry on the 6-electron cloud of the $NV^-$, giving rise to discrete energy levels. Density functional theory (DFT) combined with group theory has been used in *ab initio* calculations of the allowed single electron orbitals ($a_1'$, $a_1$, $e_x$ and $e_y$), constructed as

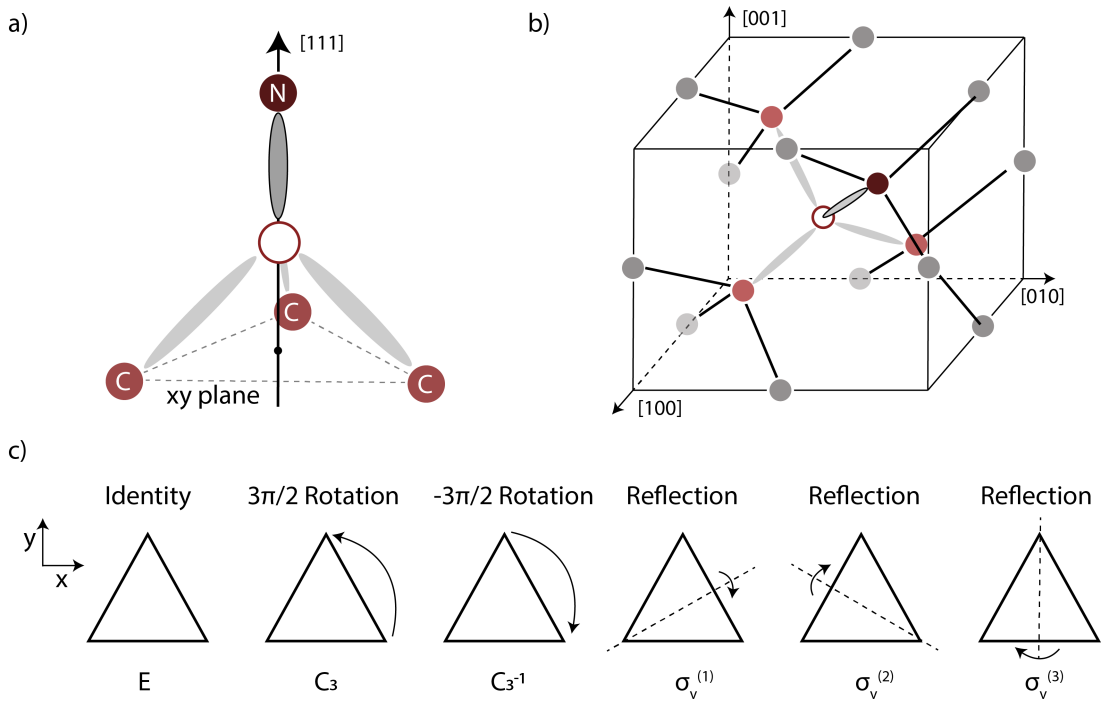


**Figure 3.1: The Nitrogen-Vacancy centre in Diamond. a)** Atomic structure of the NV centre, composed of three carbons, a vacant lattice site and a substitutional nitrogen. The NV-axis links the vacancy with the nitrogen and points along the $\langle 111 \rangle$ crystalographic **b)** The NV centre embedded in a diamond lattice, with its nearest carbon neighbhors, which form a face centred cubid lattice. **c)** $C_{3V}$ symmetry operations of the NV centre used in group theory to symmetrize the allowed wavefunctions, departing from single electron allowed orbitals, and retrieve the eigenstates of the bare Hamiltonian (fine, hyperfine structure and external fields are neglected).

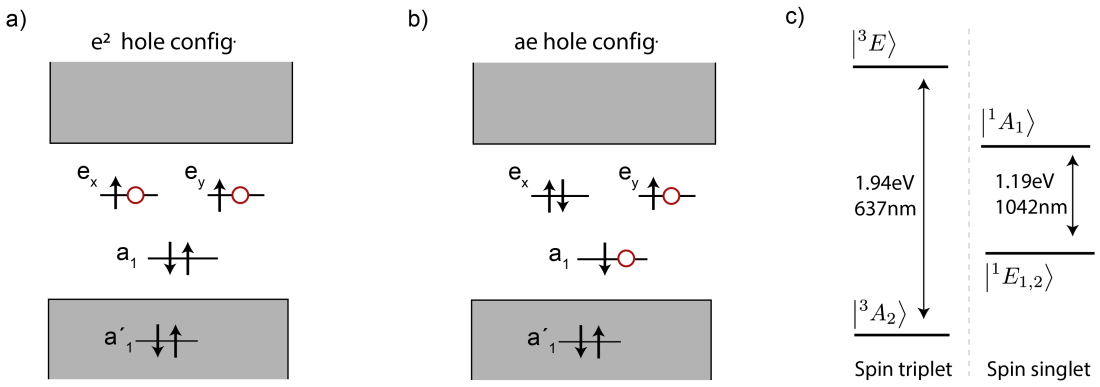


**Figure 3.2: Electronic structure of the NV centre**. **a)** Electron distribution in the optical ground state in a 6-electron $a_1'^2 a_1^2 e^2$ orbital occupation, corresponding to a $e^2$ setting in the 2-hole picture. **b)** In the first excited molecular orbital distribution one electron is promoted from $a_1$ to $e_x$ or $e_y$, resulting in an $a_1'^2 a_1^1 e^3$ electron configuration or a *ae* hole setting. **c)** Symmetrization of the $e^2$ and *ae* hole configurations according to $C_{3V}$ yields wavefunctions which set the gross structure of the NV centre, organized in three manifolds: the optical ground state $|^3A_2\rangle$, the optical excited state $|^3E\rangle$ and the singlet state. Inclusion of the fine and hyperfine terms lifts the degeneracy of each manifold, leading to multiple optical transitions.

linear combination of hybridized $sp^3$ nitrogen $(s_n)$ and $sp^3$ carbon orbitals $(s_1, s_2, s_3)$[114, 115]:

$$\begin{aligned} a_1' &= \alpha(s_1 + s_2 + s_3)/3 + \beta\, s_n \\ a_1 &= \beta(s_1 + s_2 + s_3)/3 + \alpha\, s_n \\ e_x &= (s_1 - s_2 - s_3)/\sqrt{6} \\ e_y &= (s_2 - s_3)/\sqrt{2} \end{aligned} \tag{3.1}$$

which transform according to the $C_{3V}$ point group. While $a_1'$ lies within the valence band of the crystal, $a_1$, $e_x$ and $e_y$ are deep in the band gap -see Fig. 3.2. Hund´s rule and the Pauli exclusion principle can be used to establish the orbital occupation by the six electrons in the ground state: two are lost to the $a_1'$ valence band level and do not play a role in the dynamics of the NV complex, two electrons occupy the $a_1$ orbital and the remaining two are split between the $e_x$ and $e_y$ levels, in a $a_1'^2 a_1^2 e^2$ electron configuration. The promotion of an $a_1$ electron to either $e_x$ or $e_y$ results in the first excited state, in a $a_1'^2 a_1^1 e^3$ configuration, as depicted in Fig. 3.2. Equivalently to distributing the 6 electrons through the respective orbitals, the system can be more simply described in terms of level occupation by 2 holes (in red in Fig. 3.2). In the hole picture, the ground state configuration is labelled as $e^2$ and the first excited state as *ae*.

Departing from the $e^2$ and *ae* hole occupations, group theoretic arguments can be used to build the 2-hole wavefunctions which set the eigenstates of the system. A full account of the

symmetrization of the 2-hole (4 electron) wavefunctions can be found in Ref. [116]. For the electronic ground state $e^2$, an antisymmetric combination $|e_x e_y - e_y e_x\rangle$ minimizes the Coulomb repulsion between the two holes and forms the spin-triplet ground state manifold $|^3A_2\rangle$:

$$|^3A_2\rangle = |e_x e_y - e_y e_x\rangle \otimes \begin{cases} |m_s = +1\rangle \\ |m_s = 0\rangle \\ |m_s = -1\rangle \end{cases} \tag{3.2}$$

where the first ket element denotes the orbital component of the wavefunction and the second element the $z$-spin projection of the spin triplet wavefunction with $|m_s = +1\rangle = |\uparrow\uparrow\rangle$, $|m_s = -1\rangle = |\downarrow\downarrow\rangle$ and $|m_s = 0\rangle = |\uparrow\downarrow + \downarrow\uparrow\rangle$. The associated energy spectrum is analysed in the next section.

For the excited hole configuration $ae$, group theoretical analysis yields the eigenstates of the $|^3E\rangle$ six-state manifold [116]:

$$\begin{aligned} |A_1\rangle &= |ae_- - e_- a\rangle \otimes |+1\rangle - |ae_+ - e_+ a\rangle \otimes |-1\rangle \\ |A_2\rangle &= |ae_- - e_- a\rangle \otimes |+1\rangle + |ae_+ - e_+ a\rangle \otimes |-1\rangle \\ |E_x\rangle &= |ae_x - e_x a\rangle \otimes |0\rangle \\ |E_y\rangle &= |ae_y - e_y a\rangle \otimes |0\rangle \\ |E_1\rangle &= |ae_- - e_- a\rangle \otimes |-1\rangle - |ae_+ - e_+ a\rangle |+1\rangle \\ |E_2\rangle &= |ae_- - e_- a\rangle \otimes |-1\rangle + |ae_+ - e_+ a\rangle |+1\rangle \end{aligned} \tag{3.3}$$

with $|e_\pm\rangle = |e_x\rangle \pm |ie_y\rangle$. The excited state manifold, $|^3E\rangle$, is degenerate under the crystal field potential (Coulomb interaction), which to leading order sets the energy scale of the optical transition $|^3A_2\rangle \leftrightarrow |^3E\rangle$ to $1.94eV$, corresponding to 637 nm. For this reason $|^3A_2\rangle$ and $|^3E\rangle$ are referred to as optical ground and excited states. Inclusion of the spin-orbit, spin-spin and strain terms lift the degeneracy of $|^3E\rangle$ to reproduce the typically observed spectrum upon optical excitation, as discussed in Section 3.5.

Besides the ground $|^3A_2\rangle$ and excited $|^3E\rangle$ manifolds, associated with a spin-1 triplet system, another set of states related to a spin-0 singlet results from the $C_{3V}$ symmetrization of the ground electronic configuration $e^2$:

$$\left.\begin{aligned} |^1E_1\rangle &= |e_x e_x - e_y e_y\rangle \\ |^1E_2\rangle &= |e_x e_y + e_y e_x\rangle \\ |^1A_1\rangle &= |e_x e_x + e_y e_y\rangle \end{aligned}\right\} \otimes |0\rangle$$

where $|o\rangle = |\uparrow\downarrow - \downarrow\uparrow\rangle$ is the spin-singlet wavefunction. $|^1E_{1,2}\rangle$ are degenerate and separated by $1.19eV$ / ($\lambda = 1042$ nm) from the $^1A_1$ singlet level, as in Fig. 3.2 c. The relative energy between the singlet sublevels and the ground/excited states remains debated. Even though these levels do not participate in the observed optical spectrum, they are associated with spin-selective non-radiative transitions which form the basis for the aforementioned optical initialization and readout mechanisms, which will be described in Section 3.6.

Having presented the electronic level structure of the NV centre, the three manifolds (ground, excited and singlet) are looked into more carefully in the next sections.

## 3.4 The Optical Ground State and the Spin Qubit

The energy spectrum of the optical ground state manifold, $|^3A_2\rangle$, is governed by a set of internal and external interactions: (1) spin-spin magnetic coupling between the spins of the two unpaired electrons; (2) spin-spin interaction between the unpaired electrons with the nuclear spin of the nearby $^{14}$N; (3) coupling between the electric quadrupole moment of the nearby $^{14}$N nucleus with the electric potential generated by the molecular orbitals; the electronic (4) and nuclear (5) Zeeman interactions with external magnetic fields and (6) the Stark terms due to external electric $\vec{E}$ and strain $\vec{\delta}$ fields. Due to the antisymmetric superposition of $e_x$ and $e_y$ in the ground state orbital, the $^3A_2$ manifold is not affected to first order by external electric or strain fields [116] and only the magnetic Zeeman interaction is relevant. These contributions are succintly described by the following Hamiltonian [117–119]:

$$H_{gs} = \underbrace{D_{gs}\left[\hat{S}_z^2 - S(S+1)/3\right]}_{\text{(1) Spin-spin}} + \underbrace{A_{gs}^{\parallel}\hat{S}_z\hat{I}_z + A_{gs}^{\perp}\left[\hat{S}_x\hat{I}_x + \hat{S}_y\hat{I}_y\right]}_{\text{(2) Hyperfine}} + \underbrace{P_{gs}\left[\hat{I}_z^2 - I(I+1)/3\right]}_{\text{(3) Electric quadropole}} \tag{3.4}$$

$$+ \underbrace{\mu_B g_{gs}^{\parallel}\hat{S}_z\hat{B}_z + \mu_B g_{gs}^{\perp}\left[\hat{S}_x B_x + \hat{S}_y B_y\right]}_{\text{(4) Electronic Zeeman}} + \underbrace{\mu_N g_N \vec{I}\cdot\vec{B}}_{\text{(5) Nuclear Zeeman}} \tag{3.5}$$

where the first line of the equation refers to the intrinsic properties, while the second line describes the extrinsic interactions, here limited to the Zeeman effect. $D_{gs} = 2.87 \pm 0.01$ GHz is the zero-field-splitting constant, $\hat{S}_a$ and $\hat{I}_a$ are spin-1 operators for the electronic and nuclear spins, $A_{gs}^{\parallel} = -2.16 \pm 0.01$ MHz is the longitudinal hyperfine coupling , $A_{gs}^{\perp} = -2.6 \pm 0.07$ MHz the transversal hyperfine coupling. The $^{14}$N nucleus has a charge quadrupole moment which leads to an electrically mediated correction of $P_{gs} = -4.945 \pm 0.005$ MHz. In the second line, where the Zeeman interaction is considered, $\mu_B$ is the Bohr magneton, $\mu_N$ is the nuclear magneton, $g_{gs}^{\parallel} \approx 2$ and $g_{gs}^{\perp} \approx 2$ the electronic g-factor tensor longitudinal and transversal components, $g_N$ is the nuclear g-factor. Through the

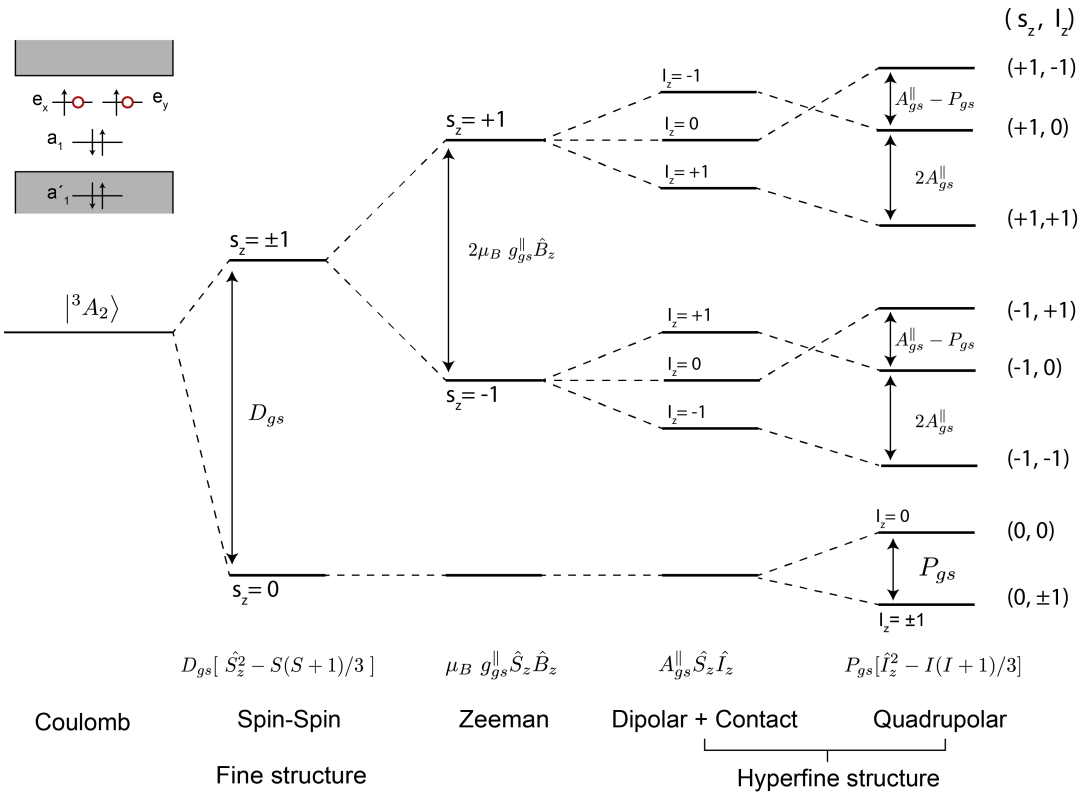


**Figure 3.3: Energy spectrum of the optical ground state of the NV$^-$.** The Coulomb interaction of the electronic cloud with the surrounding nuclei imposes a $C_{3V}$ symmetry on the molecular orbitals. A magnetic dipole interaction between two unpaired spins sets a zero-field-splitting of $D_{gs} = 2.87$ GHz between the electronic spins $s_z \pm 1$ and $s_z = 0$. The Zeeman splitting is associated with a coupling constant of $\mu_B\, g^{\parallel} = 2.803$ MHz G$^{-1}$. The magnetic dipole coupling between the electronic and $^{14}$N nuclear spins includes a pure dipolar contribution and a Fermi contact term amounting to $A^{\parallel}_{gs} = -2.162$ MHz. The $^{14}$N nucleus has a charge quadrupole moment of $P_{gs} = -4.945$ MHz.

Zeeman interaction, an external B-field aligned with the NV axis ($\hat{z}$) lifts the degeneracy between the $s_z = +1$ and $s_z = -1$ electronic spin projections with a coupling constant of $\mu_B\, g^{\parallel} = 2.803$ MHz G$^{-1}$. The value of the constants has been taken from the review work by Doherty et. al [118].

A derivation of the terms of the Hamiltonian together with a description of sensible simplifications can be found in the Appendix. For brevity the simplifications will be simply stated here. Due to the large mistmatch between the zero-field-splitting and the non-axial hyperfine interaction, $A^{\perp}_{gs}$ is typically set to zero in what is known as the secular approximation. The nuclear Zeeman interaction is neglected, as the nuclear magnetic moment is three orders of magnitude smaller than the electronic magnetic moment $\mu_N \approx \mu_B/1000$. As already stated, also Stark tuning terms are ignored due to the symmetry of the electronic spatial wavefunctions.

With this in mind, the total Hamiltonian of Eq. 3.4 can be simplified to:

$$H = D_{gs}\left[\hat{S}_z^2 - S(S+1)/3\right] + A_{gs}^{\parallel}\hat{S}_z\hat{I}_z + P_{gs}\left[\hat{I}_z^2 - I(I+1)/3\right] + \mu_B g_{gs}^{\parallel}\hat{S}_z\hat{B}_z \tag{3.6}$$

which has proven suitable to the description of the physical properties observed within this experimental work. The interactions and resulting energy levels of the simplified Hamiltonian are represented in Fig. 3.3.

As the optical ground state of the NV centre hosts the matter qubit of the entanglement protocol, its description is particularly relevant. Specifically, the logical qubit states $\{|0\rangle, |1\rangle\}$ are realized by the electronic spin states $s_z = 0$ and $s_z = -1$. As each qubit state is formed by a manifold of three hyperfine sublevels, which lead to faster dephasing and decreased fidelity of the coherent gates on the electronic spin, the nuclear spin is also initialized in the execution of the TPC-based spin-photon entangling protocol. Nonetheless, for a perfectly mixed nuclear spin, the spin qubit has a measured phase lifetime of $T_2^* = 1.94 \pm 0.07$ µs, as retrieved with a Ramsey sequence described in Section 4.3.2. Longitudinal relaxation times $T_1$ in the milliseconds range are expected [86].

## 3.5 The Optical Excited State

The energy spectrum of the optical excited state manifold, $|^3E\rangle$, is influenced by (1) spin-orbit coupling, (2) spin-spin interactions, (3) external electric or strain fields and (4) external B-fields. The electric-field and strain perturbations act on the NV centre in a similar manner and will therefore be described ahead indistinguishably. Here the Zeeman coupling is reduced to its axial component since within our experimental settings $\vec{B} = B_0\hat{z}$. Considering these simplifications the excited-state Hamiltonian is given by [116, 120]:

$$H_{ES} = H_{so} + H_{ss} + H_{strain} + H_{Zm} \tag{3.7}$$

with

$$\begin{aligned}
H_{so} &= \lambda_{SO}^{\perp}\left(|A_1\rangle\langle A_1| + |A_2\rangle\langle A_2| - |E_1\rangle\langle E_1| - |E_2\rangle\langle E_2|\right) \\
H_{ss} &= \Delta_{ss}\left(|A_1\rangle\langle A_1| + |A_2\rangle\langle A_2| + |E_1\rangle\langle E_1| + |E_2\rangle\langle E_2|\right) \\
&\quad -2\Delta_{ss}\left(|E_x\rangle\langle E_x| + |E_y\rangle\langle E_y|\right) + \Delta'_{ss}\left(|A_2\rangle\langle A_2| - |A_1\rangle\langle A_1|\right) \\
&\quad +\Delta_{ss}^{mix}\left(|E_1\rangle\langle E_y| + |E_y\rangle\langle E_1| - i|E_2\rangle\langle E_x| + i|E_x\rangle\langle E_2|\right)
\end{aligned} \tag{3.8}$$

$$H_{Zm} = \mu_B\, g_{es}^{\parallel}\, B_z/2 \cdot \left(|A_1\rangle\langle A_2| + |A_2\rangle\langle A_1| - |E_1\rangle\langle E_2| - |E_2\rangle\langle E_1|\right) \tag{3.9}$$

$$H_{strain} = \left(\begin{array}{cc|cc|cc} \multicolumn{2}{c|}{\multirow{2}{*}{O}} & \multicolumn{2}{c|}{\multirow{2}{*}{O}} & \delta_x & -i\delta_y \\ & & & & i\delta_y & -\delta_x \\ \hline \multicolumn{2}{c|}{\multirow{2}{*}{O}} & \delta_x & \delta_y & \multicolumn{2}{c}{\multirow{2}{*}{O}} \\ & & \delta_y & -\delta_x & & \\ \hline \delta_x & -i\delta_y & \multicolumn{2}{c|}{\multirow{2}{*}{O}} & \multicolumn{2}{c}{\multirow{2}{*}{O}} \\ i\delta_y & -\delta_x & & & & \end{array}\right) \tag{3.10}$$

where the strain matrix assumes the ordered basis set $\left\{|A_1\rangle, |A_2\rangle, |E_x\rangle, \left|E_y\right\rangle, |E_1\rangle, |E_2\rangle\right\}$. The axial spin-orbit parameter $\lambda_{SO}^{\perp}$ produces a 5.33 GHz [120] upward shift on the $A_1, A_2$ pair and a downward shift on the $E_1$ and $E_2$ states, as represented in fig 3.4. The excited state axial g-factor is taken as $2.15 \pm 0.04$[120]. The spin-spin coupling $H_{ss}$ contributes to the total Hamiltonian with the diagonal parameters $\Delta_{ss} \approx 0.47$ GHz and $\Delta'_{ss} \approx 1.55$ GHz, leading to the energy corrections represented in Fig. 3.4, and an off-diagonal parameter, $\Delta_{ss}^{mix} \approx 0.125$ GHz, responsible for the slight mixing of the $|E_1\rangle \leftrightarrow \left|E_y\right\rangle$ and $|E_2\rangle \leftrightarrow |E_x\rangle$ basis pairs. Here the spin-orbit and spin-spin parameters are only approximately specified due to some contention in the literature regarding their exact value [116, 121, 122].

Introduction of non-axial components of strain $\delta_x$ and $\delta_y$ leads to mixing of the excited state sublevels and corresponding energies, while axial strain $\delta_z$ displaces all energy levels equally and could be useful for tuning the optical transitions. The effect of non-axial strain on the excited state sublevels is represented in Fig. 3.4, where the eigenvalues of the total Hamiltonian were retrieved for a sweep of $\delta_x$, while holding $\delta_y = 0$. As the strain increases, two spectral branches, $L_x$ and $L_y$, arise and, in the limit of high strain ( $|\delta| \gg \lambda_{SO}^{\perp}$ ), each branch becomes associated with one single spatial wavefunction tensored with distinct spin states. As elaborated later in Section 4.2.4, such high-strain configuration corresponds to the setting found in the working sample of this thesis.

Assuming that the axial g-factor of the excited state is the same as in the optical ground state [123], as is the case at room temperature, then the Zeeman coupling term should also be the equal, with $\mu_B g^{\parallel} \hat{S}_z = 2.803$ MHz G$^{-1}$ [124].

The allowed optical transitions between ground and excited manifolds can be determined by looking at the transition dipole moment between the known wavefunctions of the two sets. Furthermore conservation of angular momentum establishes the polarisation of the corresponding photons. The selection rules for the unperturbed energy levels are succinctly summarised in table 3.1[116]. All transitions ${}^3E \rightarrow {}^3A_2$ exhibit the same dipole moment and share the same radiative decay rate $\Gamma_{{}^3E \rightarrow {}^3A_2} \approx 8$ MHz [125]. However, fits to the fluorescence decay associated with each level are different owing to spin-dependent coupling to the singlet

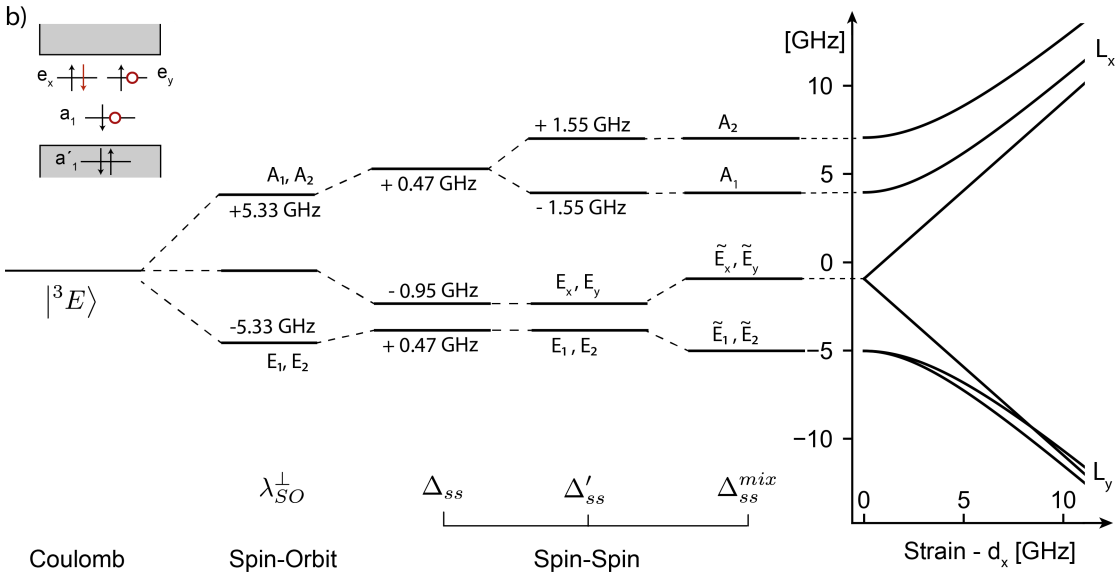


**Figure 3.4: Low temperature energy spectrum of the $|^3E\rangle$ optical excited state sublevels.** The spin-orbit coupling affects only states with non-null spin projection, with a 5.5 GHz shift. The spin-spin interaction is divided in three parts according to the Hamiltonian of Eq. 3.8, where $\Delta_{ss}^{mix}$ is associated with off-diagonal elements and induces some mixing between the base pairs $E_1, E_y$ and $E_2, E_x$. Non-axial strain, $d_x$ or $d_y$, induces splitting of the energy levels in two branches $L_x$ and $L_y$ leading to significant mixing of the basis states, as suggested by the structure of $H_{strain}$ presented in Eq. 3.10. The rightmost graph shows the eigenvalues of the excited state Hamiltonian for a varying $\delta_x$ and $\delta_y = 0$. Subfigure **b)** represents the the electrons/hole ae excited state distribution among the allowed single electron orbitals.

state. Under cryogenic conditions, the dipole-allowed transitions can be individually addressed using resonant laser light or, alternatively, off-resonant light at wavelengths $\lambda \leq 637$ nm which excite the NV to the vibrationally excited states of the $^3E$ manifold, followed by a spin-preserving vibronic relaxation. Off-resonant cycling addresses the transitions collectively and can be employed in the initialization and optical readout of the NV centre.

| | $A_1$ | $A_2$ | $E_1$ | $E_2$ | $E_x$ | $E_y$ |
|---|---|---|---|---|---|---|
| $\|-1\rangle$ | $\hat{\sigma}_+$ | $\hat{\sigma}_+$ | $\hat{\sigma}_-$ | $\hat{\sigma}_-$ | | |
| $\|0\rangle$ | | | | | $\hat{y}$ | $\hat{x}$ |
| $\|+1\rangle$ | $\hat{\sigma}_-$ | $\hat{\sigma}_-$ | $\hat{\sigma}_+$ | $\hat{\sigma}_+$ | | |

**Table 3.1:** Selection rules between the optical excited and ground states, identifying the dipole allowed and forbidden transitions. For the allowed transitions, $\hat{\sigma}_{+(-)}$ identifies the right (left) circular polarisation of the emitted/absorbed photons. $\hat{x}$ and $\hat{y}$ refer to linear polarisation.

For the case of high-strain, each spectral branch, $L_x$ or $L_y$, corresponds to a single spatial wavefunction without angular momentum and therefore $L_x$ and $L_y$ are associated with absorption/emission of photons with linear polarisation $\hat{x}$ and $\hat{y}$. Knowledge of the energies of each level and the respective selection rules, enables one to retrieve the transitions´ spectrum, whose theoretical expectation and respective data is found in Section 4.2.4.

It should be noted that due to a lack of consensus regarding the hyperfine coupling in the excited state at cryogenic temperatures, its presentation has been here ignored in this discussion.

## 3.6 The Singlet State Manifold and Intersystem Crossing

The singlet manifold plays a crucial role in the NV dynamics by offering an alternative decay path from the excited to the optical ground state - see Fig. 3.5. It is composed of two sublevels, with $|^1A_1\rangle$ lying 1.19 eV above $|^1E_{1,2}\rangle$, which couple to the triplet manifolds through spin-dependent non-radiative transitions, called intersystem-crossings (ISC). The alternative decay trajectory starts with an ISC to a vibrationally excited state of $|^1A_1\rangle$, followed by a vibronic decay to $|^1A_1\rangle$ developing in the picosecond timescale [126]. After a lifetime stay of approximately 1 ns, the population drops to $|^1E_{1,2}\rangle$ together with the emission of an infrared 1042 nm photon, where it remains for an average of 370 ns [125]. A second ISC brings the population to the ground state. Owing to the absence of optical photons in this decay path and the long lifetime of $|^1E_{1,2}\rangle$, the singlet manifold is commonly referred to as the dark state.

Regarding the mechanism of the ISC from the excited states (ES) $^3E$ to the singlet manifold, the ES $|A_1\rangle$ has a first-order coupling to the singlet $|^1A_1\rangle$, mediated by a transversal spin-orbit

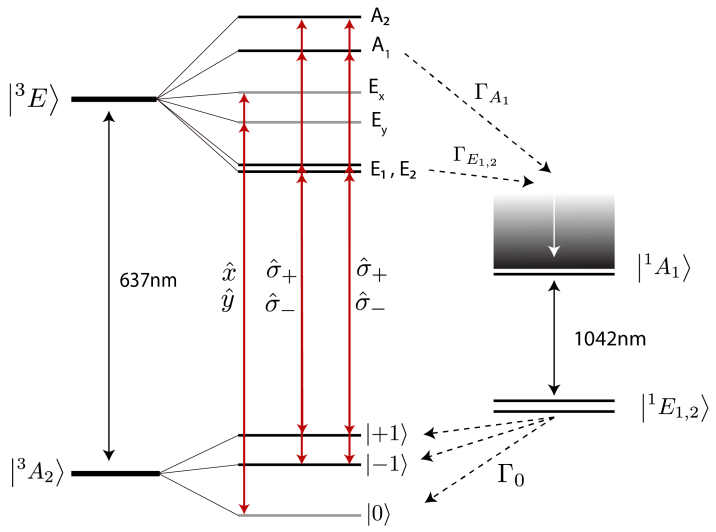


**Figure 3.5: Overview of the NV level structure and transitions.** The red arrows show the dipole allowed transitions between excited and ground state together with associated photon polarisations. The $|A_1\rangle$ and $|E_{1,2}\rangle$ states couple to a vibrationally excited state of the singlet manifold via spin-orbit and electron-phonon interactions with rates $\Gamma_{A_1}$ and $\Gamma_{E_{1,2}}$ respectively. Following a phononic relaxation (white arrow) to $|^1A_1\rangle$ the decay proceeds with the emission of an infra-red photon which brings the population to $|^1E_{1,2}\rangle$. At last, the non-radiative descent from $|^1E_{1,2}\rangle$ to $|^3A_2\rangle$ is believed to be weakly spin-dependent, with no consensus in the literature. As the singlet decay path is favoured by $m_s = \pm 1$ states and does not yield optical photons, it is possible to discern between the electron spin states $m_s = 0$ and $m_s = \pm 1$ based on the average luminescence of the NV centre.

interaction $\lambda_{SO}^{\perp}$; whereas the ES $|E_1\rangle$ and $|E_2\rangle$ do not transit directly to the singlet and must undergo a second-order transition, where a phonon-electron interaction bridges them to $A_1$ before the spin-orbit mediated jump can take place. Intersystem crossings by the remaining excited states ($|E_x\rangle$, $|E_y\rangle$, $|A_2\rangle$) are higher-order processes which occur rarely. The ISC mechanism from the singlet manifold to the ground state $|^3A_2\rangle$ remains an outstanding issue. A thorough analysis of the ISC mechanisms can be found in Ref. [127].

Under cryogenic conditions, $|A_1\rangle$ and $|E_{1,2}\rangle$ show ISC rates of $\Gamma_{A_1}/2\pi = 16 \pm 0.6$ MHz and $\Gamma_{E_{1,2}}/2\pi = 8.3 \pm 0.6$ MHz, respectively. The remaining excited levels decay very weakly through this channel, with estimated rates $\Gamma_{A_2,E_{x,y}} \leq 0.62 \pm 0.021$ MHz. While there is no consensus in the literature regarding the second ISC rate, from $|^1E_{1,2}\rangle$ to $|^3A_2\rangle$, it is agreed that there is a slight preference to fall into $|0\rangle$, with the estimated ratio $\Gamma_{\to 0}/\Gamma_{\to \pm 1} \in \{1.1 - 2\}$ [126].

When performing off-resonant cycling of the optical transitions, the preferential non-radiative depopulation of $|A_1\rangle$ and $|E_{1,2}\rangle$, leads to weaker luminescence of the $m_s = \pm 1$ levels comparatively to $m_s = 0$ states, providing a method for non-resonant optical spin

readout. For the same reason, off-resonant cycling leads to a build up of population on the $|0\rangle$ ground state, thereby initializing the spin qubit. In Chapter 5, an alternative method for the initialization of the electronic and nuclear spins is described.

## 3.7 Vibronic and Temperature Effects

Vibrations of the hosting diamond lattice account for some of the NV centre characteristics, namely (1) its vibronic sidebands in the absorption and emission spectrum, (2) spin mixing in the optical excited state and (3) the aforementioned intersystem crossing between the triplet and singlet manifolds.

For molecules and solid state systems with vibronic degrees of freedom, nuclei positions are modelled according to quantum harmonic oscillators associated with potential wells centered around a equilibrium positions. The motion of the nuclei is described by the vibronic wavefunction of the system $\psi_v$. A change in the electronic wavefunction $\psi_e$ through Coulombic interactions, leads to a readjustment of the equilibrium position of the nuclei; in other words, transitions between a pair of levels typically involve a change in the electronic $\psi_e \rightarrow \tilde{\psi}_e$ and vibronic $\psi_v \rightarrow \tilde{\psi}_v$ wavefunctions [1]. The Franck-Condon principle [128] establishes that the transition probability is proportional to the square of the overlap of the vibrational wavefunctions $\left|\langle \psi_v | \tilde{\psi}_v \rangle\right|^2$, which typically favours jumps between levels with different vibronic modes. Absorption of a photon, represented in Fig. 3.6 a, promotes the system from an electronic level in its vibronic ground state $\psi_e \otimes \psi_{v=0}$, to another electronic level which is most likely vibronically excited, $\tilde{\psi}_e \otimes \psi_{v\geq 1}$. This gives rise to a blue-shifted absorption side band. Relaxation of the vibrational modes brings the system to $\psi_e \otimes \psi_{v=0}$, followed by the emission of a photon that preferentially leaves the system in a vibronically excited electronic ground state $\psi_e \otimes \psi_{v\geq 1}$. While this emission constitutes the phonon-side-band (PSB), see Fig. 3.6 b and c, transitions between the lowest vibrational level ($v = 0$) of two electronic states form the zero-phonon-line. The fraction of the overall emission within the zero-phonon-line (ZPL) is specified by the Debye-Waller factor and amounts to $3\%$ in the case of the NV centre [129]. The blue-shifted absorption enables one to off-resonantly pump the NV centre with a green laser ($\lambda = 520$ nm). The emission PSB is largely incoherent and inadequate for the generation of spin-photon entanglement, which is the reason why it is only employed for the readout of the spin state. ZPL photons, on the other hand, have narrow linewidths (close to lifetime limited) and can be used to prepare spin-photon entangled states.

[1] The Born-Oppenheimer approximation establishes that the wavefunction of the system can be factorised in its electronic and vibrational parts: $\psi = \psi_e \otimes \psi_v$, due to the light mass of electrons comparatively to nuclei. Electronic changes occur extremely fast with respect to the timescale of nuclear motion.

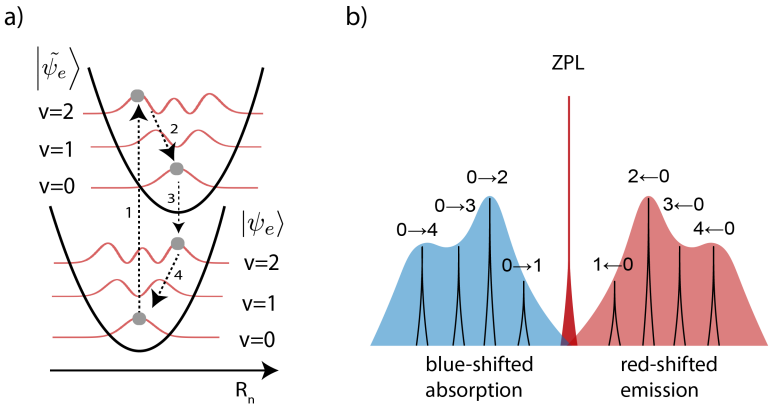


**Figure 3.6: Vibronic effects on the NV centre absorption and emission spectrum. a)** Transition between a pair of electronic states $\psi_e \rightarrow \tilde{\psi}_e$. The population occupies the lowest vibrational mode before being excited to $\tilde{\psi}_e$. Typically the most favourable transitions, as determined by the Franck-Condon principle, require a readjustment of the vibronic mode ($v = 0 \rightarrow v = 2$, in the picture). Conversely decay to the electronic ground state entails a vibronic transition, most likely from $v = 0$ to $v = 2$ modes in this example. Steps (2) and (4) represent the quick vibronic relaxation that occurs within given electronic states. **b)** Vibronic transitions give rise to absorption and emission side bands with respect to the zero-phonon-line where the system never leaves the vibrational ground state.

Non-symmetric vibrational modes, composed of phonons which deform the NV defect such that its $C_{3V}$ symmetry is broken (Jahn-Teller effect), are responsible for a temperature dependent mixing among the excited state $^3E$ levels, as established by works of Fu [130] and Kaiser [131]. The transfer within the excited state orbital doublet (the transfer is bi-directional in a medium strain regime $\delta \approx 10$ GHz) is mediated by a non-radiative two-phonon Raman transition, resulting in the dephasing and homogenous broadening of the ZPL with a $\propto T^5$ temperature dependence, as well as depolarisation of the ZPL emission (at 40K the ZPL emission is completely depolarised). Cryogenic temperatures (4 K) minimize the occupation number of the symmetry breaking vibration modes, reducing spin-relaxation in the excited state and are essential to address optical transitions individually.

The same symmetry breaking phonons account for the intersystem crossing transitions between the triplet and singlet manifolds [127], as briefly described in the previous section.

## 3.8 The Photochromic Effect

Photochromism refers to the reversible change between two chemical states with different spectra, induced by the absorption of radiation [132]. In the case of the NV centre it pertains to the transfer between the neutral charge state $NV^0$ and the state $NV^-$, typically caused by green (520 nm) or red (637 nm) irradiation.

The ionization mechanism ($NV^- \rightarrow NV^0$) is a two-photon process [133], where the first photon excites the $NV^-$ from the ground to the excited state manifold and the second photon promotes the electron to the conduction band. Similarly, the recombination ($NV^0 \rightarrow NV^-$) involves a first excitation of the $NV^0$, followed by the promotion of a valence band electron by the absorption of another photon.

As the $NV^-$ has a ZPL at $\lambda = 637$ nm and the $NV^0$ at 575 nm, excitation with $\lambda \geq 575$ nm will only produce fluorescence in the $NV^-$, providing an easy way to distinguish between the two states. Green excitation, however, causes competing ionization and recombination processes, leading to an equilibrium distribution between the two populations. For reference, Aslam et. al [112] established that at room temperature green excitation ($\lambda = 532$ nm, $P \approx 10$ μW) produces a $75 : 25$ distribution between $NV^-$ and $NV^0$.

# 4

# Experimental Methods

### Overview

This Chapter covers the experimental techniques relevant for the realization of the TPC-based entangling scheme. It includes a description of the diamond sample (Section 4.1), the optical apparatus employed in the preparation and readout of the NV spin (Section 4.2), the microwave setup used for manipulation of the spin degrees of freedom (Section 4.3) and the operation of the interferometer applied in the conversion between time- to polarisation-encoded qubits, as well as in quantum tomography of the photonic qubits (Section 4.4).

## 4.1 The Diamond Sample

The sample used in the execution of this work is a commercially available electronic grade type IIa diamond plate with dimensions $4 \times 1.8 \times 0.4$ [mm] produced by Diam2Tech [111], through plasma enhanced chemical vapour deposition (CVD). It has a nitrogen concentration of $N \leq 1$ ppb and a [111]-oriented surface, which received a "basic-polishing" treatment, according to the company specifications. As discussed ahead, the [111]-cut, ensures maximal collection efficiency by the microscope objective. No nitrogen implantation or annealing were carried out after production.

## 4.2 The Optical Interface

The optical apparatus is responsible for (1) guiding laser light onto the NV centre for optical excitation and (2) collecting/guiding fluorescence from the NV defect to the photon detectors. These are realised by a home-built confocal microscope aided by a solid-immersion-lens (SIL) milled around pre-allocated NVs.

### 4.2.1 NV Allocation for SIL Fabrication

The CVD growth of diamond leads to a homogeneous, but randomly scattered, distribution of defects. Therefore the fabrication of a SIL around a particular impurity, requires the allocation of the defect with respect to a reference: a set of square grids was milled on the diamond surface with a focused ion beam (FIB), to establish a coordinate system (see Fig. 4.1 a. The grids are marked by points forming 10 µm × 10 µm squares, intended to fit in the 20 µm × 20 µm field of view of our microscope. For easier navigation on the diamond surface, each 45 µm × 45 µm grid was assigned a label, indicating its row and column number, with respect to other grids.

The defects and grids are then imaged by a confocal microscope, described in Section 4.2.3, where each allocation steps relies on capturing a fluorescence and a scatter image. The scatter signal is used to localize the grid points and the fluorescence image to establish the position of the defects, as illustrated in Fig. 4.1 a and d. To set the convention for the rest of the discussion, the x-y imaging plane is parallel to the sample surface, while the z-direction goes into the diamond.

To ensure that a certain fluorescent spot corresponds in fact to single emitter, a second order correlation curve $g^{(2)}(\tau)$ is extracted:

$$g^{(2)} = \frac{\langle I(t)I(t+\tau)\rangle}{\langle I(t)\rangle^2} \tag{4.1}$$

where $I(t)$ is the fluorescence intensity at a time $t$. A Hanbury-Brown-Twiss setup is used for this purpose, where the fluorescence is split between two optical paths and the coincidence events between arrival-time windows separated by a specified time-delay $\tau$ are registered; in this manner the $g^{(2)}$ profile is retrieved, up to a normalizing constant, as exemplary illustrated in Fig. 4.1 e. $g^{(2)}(\tau = 0) < 0.5$ confirms the fluorescence originates from a single emitter [76], as two photons cannot be emitted simultaneously.

The xy-allocation relies on recording the distance of a defect to the four closest grid points, as established by the fluorescence and scatter confocal scans. Aberrations of the optical system and inaccuracies on the movement of the piezo stage lead to misestimation of the distance on

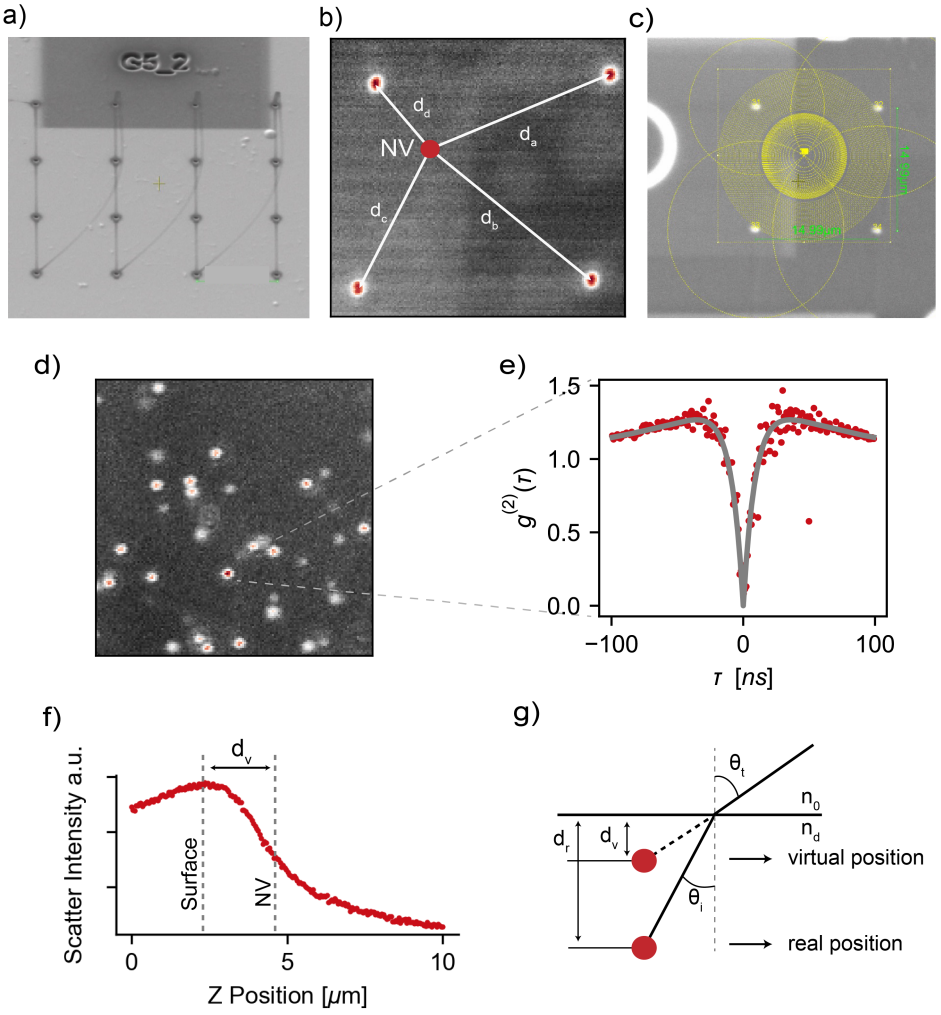


**Figure 4.1: Allocation of NV centres for SIL fabrication. a)** A grid system sets a coordinate reference on the surface of the sample. Each grid has a "G$xy$" label which identifies the relative position with respect to other grids. **b)** Scatter confocal scan of a diamond sample, showing the grid points used for allocation of defects and the respective distance to a color centre detected in a fluorescence scan. **c)** Grid system as imaged by the scanning electron microscope of the FIB. The grid ensures that the position of the allocated NVs is known both in the confocal microscope setup and in the FIB imaging system. The circles in the image show the expected distance between the emitter and the grid points, as measured in the confocal microscope image. **d)** Fluorescence confocal scan of a diamond sample showing several single NV centres. **e)** Second order correlation curve $g^{(2)}(\tau) = 1 + c_2 e^{-t/\tau_2} + c_3 e^{-t/\tau_3}$ [76] from an NV centre. $g^{(2)}(\tau) < 0.5$ ensures that the signal emerges from a single emitter. **f)** Scatter depth scan showing the expected position of the diamond surface and emitter, where the surface is assumed to correspond to the z-position of maximum scatter intensity. **g)** Refraction at the diamond surface leads to the creation of a virtual image of the emitter, displaced from its real position. Therefore a correction factor must be taken into account when estimating the real depth.

imaged structures. The imaging system of the focused ion beam (FIB) also has intrinsic aberrations, which add up to the errors from the confocal microscope. To curb such errors, a deformation $\overleftrightarrow{T}$, including stretch and rotation, is applied in post-processing to the confocal microscope image by a numeric Python script, such that the grid points overlap as closely as possible to the ones imaged by the FIB system. Representing each point of the image as a vector $\vec{r} = (r_x, r_y)$ and applying a transformation $\overleftrightarrow{T}$ yields a new vector $\vec{s} = (s_x, s_y)$, with the transformation given by:

$$\overleftrightarrow{T} : \quad \vec{r} \rightarrow \vec{s}$$

$$\begin{aligned} s_x &= r_x + C_{1x}\, r_x + C_{2x} r_y + C_{xy} r_x r_y \\ s_y &= r_y + C_{1y}\, r_y + C_{2y} r_x + C_{yx} r_y r_x \end{aligned} \tag{4.2}$$

where $C_{1x}$ and $C_{1y}$ induce a linear stretching; $C_{2x}$ and $C_{2y}$ lead to a horizontal or vertical, respectively, skew of the image; $C_{xy}$ and $C_{yx}$ cause a combined stretch+skewing of the coordinates.

The coefficients $C_{1x},\ C_{1y},\ C_{2x},\ C_{2y},\ C_{xy},\ C_{yx}$ are numerically swept within a defined range and the parameter set which ensures the maximum overlap of grid marks between the confocal and the FIB image sets the optimal image deformation. This ensures a good correspondence between the two imaging systems. Its accuracy was tested by milling rings around pre-allocated NVs. After fabrication, the rings were imaged in the confocal setup and the displacement between their and the corresponding defect had a satisfactory standard deviation of $\sigma = 115$ nm, from a sample of 5 ring-NV pairs. The largest error contribution is due to drifting of the sample while milling takes place. This value sets the effective accuracy of our system in the xy- position of milled structures.

The depth of the defects with respect to the diamond surface is estimated by firstly localizing the surface with a confocal scatter scan along the z-axis, as shown in Fig. 4.1 f, and by then measuring the distance between the surface coordinate and the NV position $d_v$, as given by the fluorescence z-scan. Due to refraction at the diamond interface, the NV is imaged at a shallower position than its real location $d_r$. To account for this discrepancy, a correction factor $k = d_r/d_v$ was estimated. Following the diagram of Fig. 4.1 g, for a ray leaving the NV centre at an angle $\theta_i$, through Snell´s law, $d_v$ and $d_r$ are related by:

$$k = \frac{d_r}{d_v} = \frac{n_d \cos(\theta_i)}{n_o \cos(\theta_t)} \tag{4.3}$$

where $n_o$ and $n_d$ are the refractive indices of air and diamond respectively, $\theta_i$ is the angle of incidence at the interface and $\theta_t$ the angle of transmission. It is hence clear that incident rays at

distinct angles $\theta_i$ generate a virtual image at different depths and correspond to distinct correction factors. To account for this, a mean correction factor was estimated by considering a weighted average of $k$, where the power of each ray transmitted through the diamond interface was taken as the weight factor $w(\theta_i)$:

$$\begin{aligned} \langle k \rangle &= \int_0^{\theta_m} k(\theta_i)\, w(\theta_i)\, d\theta_i \Big/ \int_0^{\theta_m} w(\theta_i)\, d\theta_i \\ &\text{with} \\ w(\theta_i) &= A(\theta_i) \times Dip(\theta_i) \times T_F(\theta_i) \end{aligned} \tag{4.4}$$

where $A(\theta_i) = 2\pi \sin(\theta_i)$ is the area of a differential ring containing all rays leaving the dipole source at the same angle, $Dip(\theta_i)$ is the intensity of the dipole radiation and $T_F(\theta_i)$ is the transmission Fresnel coefficient. The limit of the integration domain $\theta_m$ corresponds to the solid angle containing the rays that are captured by the microscope objective and is defined as $\theta_m = \arcsin(\mathrm{NA}/n_d)$, where NA is the numerical aperture of the optical system. Considering a sample with the surface on the [111]-crystallographic plane and an NV with its symmetry axis along the [111]-direction, the fluorescent emission stems from two orthogonal dipoles $D_x$ and $D_y$ oriented parallel to the surface. In a spherical coordinate system with its zenith along the NV symmetry axis, the normalized intensity emission patterns for s-polarised and p-polarised rays are described by [134]:

$$\begin{aligned} D_{x,s} &= \tfrac{3}{8\pi} \sin^2(\theta) \sin^2(\varphi) & D_{y,s} &= \tfrac{3}{8\pi} \sin^2(\theta) \cos^2(\varphi) \\ D_{x,p} &= \tfrac{3}{8\pi} \cos^2(\theta) & D_{y,p} &= \tfrac{3}{8\pi} \cos^2(\theta) \end{aligned} \tag{4.5}$$

with the usual polar $\theta$ and azimuthal $\varphi$ angles. Presuming equal excitation of the two dipoles the average transmitted energy per ray is given by:

$$Dip(\theta_i) = \frac{1}{4} \left[ (D_{x,s} + D_{y,s}) T_s + (D_{x,p} + D_{y,p} T_p) \right] \tag{4.6}$$

where a distinction between the transmission of s and p-rays is necessary, due to the different Fresnel coefficients $T_s$ and $T_p$. Assuming an optical system with NA=0.9, the weighted average of $k$ was numerically estimated to be $\langle k \rangle = 3.26$, allowing us to establish the real depth of the imaged defects: each emitter is $3.26\times$ deeper than shown in its confocal microscope image. For comparison with the lateral positioning accuracy, the vertical accuracy is limited by the longitudinal resolution of the confocal microscope. Taking the Rayleigh criterion for resolution [135], this is given in our case by $r_{axial} = 1.5 n_d \lambda / NA^2 = 2.84$ µm, for the confocal microscope system used in the NV allocation.

The diamond sample used in this work had the surface cut perpendicular to the

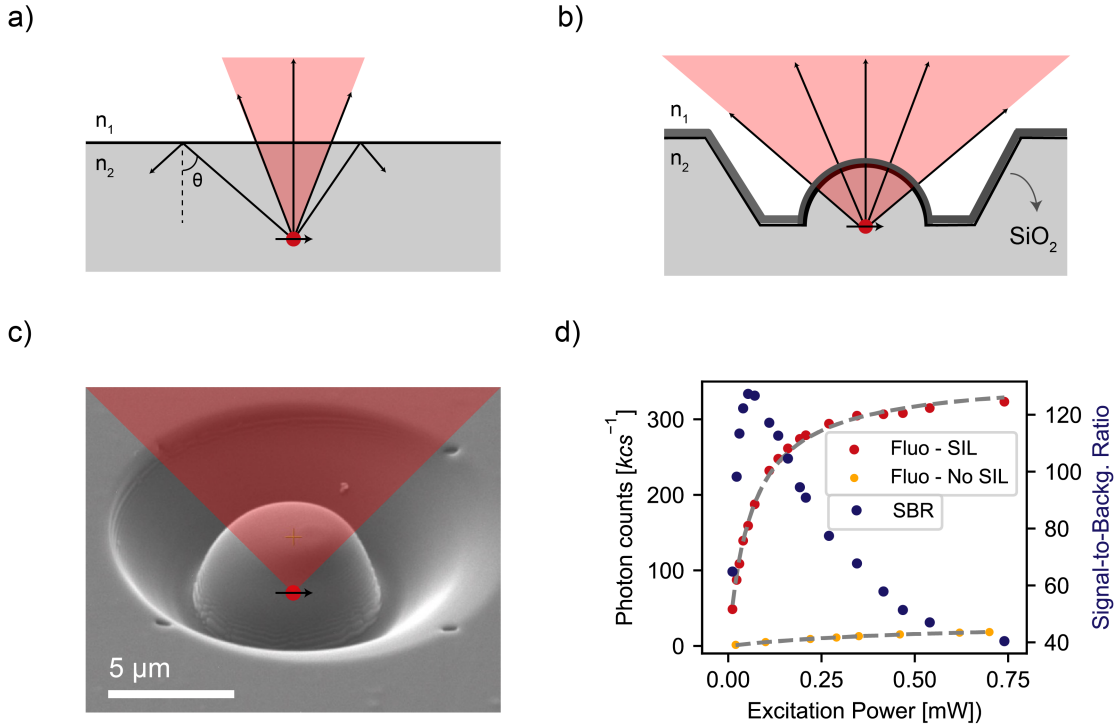


**Figure 4.2: Enhancement of the collection efficiency by solid immersion lenses. a)** Due to the high refractive index mismatch at the diamond-air interface, only a narrow cone of rays leaves the diamond without suffering total internal reflection. **b)** With a SIL milled around the emitter, the fluorescence rays reach the interface at a normal angle, avoiding total internal reflection. A single-layer $SiO_2$ coating further reduces Fresnel reflections. **c)** Image from a scanning electron microscope of a SIL fabricated around an NV centre. **d)** Fluorescence saturation curve of an NV centre before and after the fabrication of a SIL. A 10-fold improvement on the collection was observed and the signal-to-background ratio (blue dots), on the right y-axis, was enhanced by a factor of $18\times$.

[111]-crystallographic direction. Out of the four possible orientations for the nitrogen-vacancy axis, the [111]-direction is the preferred one in experiments as it corresponds to an emission pattern centred around the optical axis of the microscope objective, allowing for a more efficient collection. The luminescence of [111]-defects is not dependent on the polarisation of the off-resonant 520 nm excitation light, which provides a useful fingerprint to single out the NV centres with the desired alignment.

### 4.2.2 Fabrication of Solid Immersion Lenses

When a ray transits between a medium of refractive index $n_2$ to another medium of refractive index $n_1$, total internal reflection (TIR) will occur if the angle of incidence $\theta_i$ is larger than $\theta_{ir}$:

$$\theta_{ir} = \arcsin(n_1/n_2) \tag{4.7}$$

For a diamond-air interface, $n_2 = 2.42$ and $n_1 = 1.0$, the internal reflection angle is $\theta_{ir} = 24.41^\circ$, which significantly limits the collection efficiency from the defect - see Fig. 4.2 a. Quantitatively, the collection efficiency by an objective with numerical aperture NA in a medium with refractive index $n_1$ from a dipole emission within a medium with $n_2$ index is given by [136]:

$$C = \frac{1}{8}(4 - 3\cos(\theta_{max}) - \cos^3(\theta_{max}) + 3[\cos^3(\theta_{max}) - \cos(\theta_{max})]\cos^2(\varphi_{EM})) \tag{4.8}$$

where $\theta_{max} = \arcsin\left(NA \times \frac{n_1}{n_2}\right)$ is the maximum angle of collection and $\varphi_{EM}$ is the angle between the dipole and the optical axis of the objective. Losses due to Fresnel reflections are omitted. Thereby, for $n_2 = 2.42$ and $NA = 0.7$ (NA of cryogenic setup), a collection efficiency $C = 3.1\%$ is expected.

By fabricating a hemispherical lens around the emitter, as illustrated in Fig. 4.2 b, all rays reach the interface at a normal angle and the losses due to total internal reflection are eliminated, therefore expanding the transmitted solid angle to cover a full hemisphere. Note that in such case, the solid angle of collection would be determined by the numerical aperture of the microscope objective.

The lenses were fabricated using a focused ion beam system (FEI Quanta 200 3D), with a 30 kV gallium beam at low current of 1 nA to reduce drift during milling. The lenses were dimensioned such that the NV defect would be at the centre of the semi-hemispherical dome. An iterative parallel-milling sequence [137] was employed for improved shape and performance. While producing a lens, this method, at each step, removes a layer of specific thickness in the shape of a ring with a determined inner and outer diameter. As the iterations progress, the ring´s inner diameter is sequentially increased, yielding a hemispherical dome. A solid immersion lens fabricated with such method is visible in Fig. 4.2 c. For lenses in a diameter range from 2 to 10 µm a fabrication time of 10 to 20 minutes is typical.

Following the fabrication a chemical treatment [115] to remove graphitic carbon, implanted gallium and other surface contaminants was applied. After a 2-minute ultrasonic bath in acetone, followed by another 2-minute bath in isopropanol, the sample was pre-heated to 250°C for 30 minutes in 10 mL of a sulfuric acid $H_2SO_4$ solution. Afterwards 500 mg of potassium nitrate $KNO_3$ were added and the sample was boiled for 2 hours. Finally, the sample was rinsed

in distilled water.

Each SIL was optically characterised by measuring the saturation curve of the color centre underneath, relating the fluorescence intensity to excitation power. The curves were fitted with the function $I(P) = I_0/(1 + P_{sat}/P)$, where $P$ is the excitation power, $P_{sat}$ the saturation power and $I_0$ saturation count rate [138]. By comparing the curves with and without SILs, it was established that the best performance lenses attained a 10-fold enhancement of the saturation intensity $I_0$ (from $I_0 = 33 \pm 1$ to $I_0 = 357 \pm 3$ kcs$^{-1}$), as exemplified in Fig. 4.2 d. Because the lenses enable the formation of a tighter focal spot, a reduced saturation power and background were also expected. This was corroborated by the increase of the signal-to-background ratio (SBR) curve, represented by the blue dots in the same graph, showing a maximum at $SNB = 127$ for this lens, corresponding to an improvement by a factor of 18×.

Due to the large refractive index mismatch, it is expected that 17% of the light leaving the defect is not transmitted at the diamond-air interface owing to Fresnel reflection. The collection efficiency was further improved by deposition of a single-layer silicon dioxide ($SiO_2$) anti-reflection optical coating, with a refractive index n $= 1.45$, represented in Fig. 4.2 b. The film was applied using plasma enhanced chemical vapour deposition with a target thickness of $\lambda/4 = 109$ nm, for maximum transmittance around the zero-phonon-line wavelength $\lambda = 637$ nm.

### 4.2.3 The Optical Setup

A detailed account of the hardware of the optical setup can be found in the legend of Fig. 4.3, while this description focuses on the operation and function of those elements. A confocal microscope setup was built around a closed-cycle cryostat (Montana Cryostation C2) which keeps the diamond sample at 4 K, to suppress phononic broadening of the optical resonances within the zero-phonon-line (ZPL). Cold temperatures are essential to address these transitions individually.

Besides the main cryogenic setup, a second room-temperature confocal microscope setup was built for the NV-centre allocation, whose design overlap partially. For this reason their diagrams were merged in Fig. 4.3, where the gray rectangle highlights the structure common to both setups. Merging the schematics comes at the price of some imprecisions in the room-temperature diagram, noted ahead: the sample is not mounted inside a cryostat but on a flat optical window (Thorlabs WH41050) to reduce back reflections. Another discrepancy between the two microscopes is the choice of objective; while the cryogenic setup required a long working distance objective (Mitutyo 100x Plan APO 0.7 NA), due to the separation between the optical access window and the sample, the room-temperature setup employed a

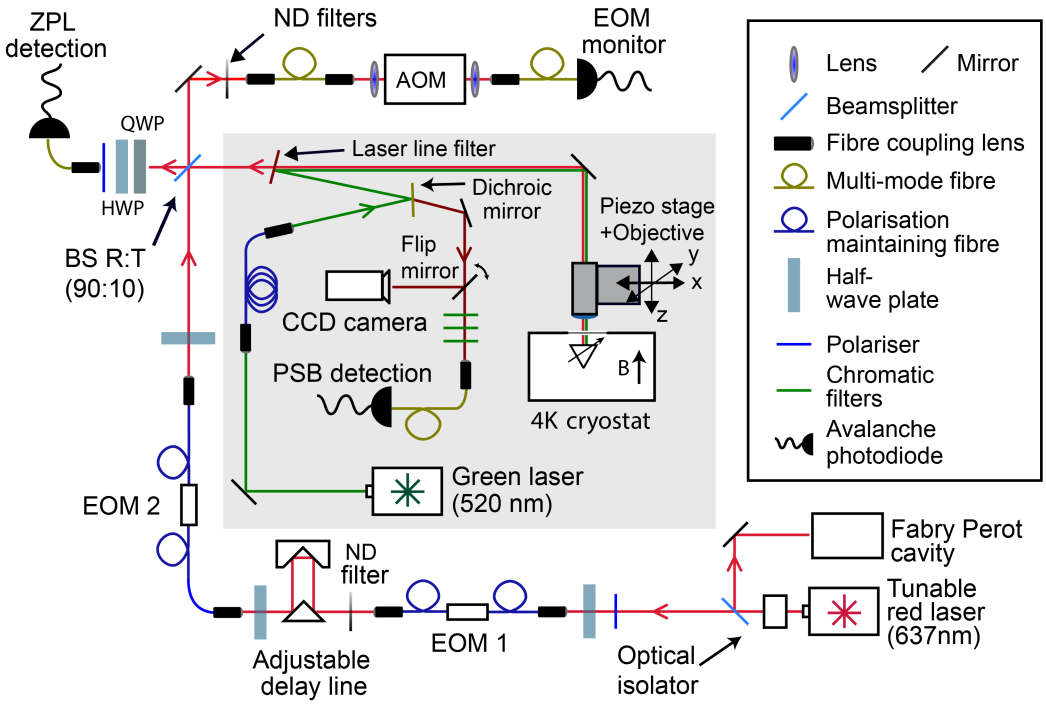


**Figure 4.3: Diagram of the cryogenic confocal microscope (and allocation confocal microscope).** The diamond sample is mounted on the cold finger of a closed-cycle cryostat (Montana Cryostation C2) at 4 K. A raster scan is realised by sweeping the position of a microscope objective (Mitutoyo 100x Plan Apo NA=0.7) with a 3-axis piezo stage (Thorlabs MAX311D/M) with a 20 µm × 20 µm × 20 µm travel range. Off-resonant excitation of the NV defect, used for initialisation of the NV charge state, is performed by a home-built switchable green laser, while resonant excitation is carried by an external cavity narrrow-band tunable diode laser (Toptica DL PRO HP 637). An optical isolator (Thorlabs IO-3-633-LP) was installed at the output of the red laser to ensure good spectral stability. Amplitude modulation of the red field is attained with a cascade of two electro-optic modulators (EOM, Jenoptik AM635) and their transmission is continuously monitored by an APD (EOM monitor) to account for operation drifts, corrected by applying a time-varying voltage bias. The compound operation of the EOMs is optimised through an adjustable delay line. The zero-phonon-line (ZPL) and phonon-side-band (PSB) paths are separated by a 7 nm-width laser line filter at 637 nm (Semrock FF01-637/7). A dichroic mirror (DMLP650) together with chromatic filters (FEL0650, NF533) ensure the removal of scatter green light from the PSB signal. Avalanche photodiodes with low dark counts (Excelitas SPCM) were employed in the detection of the PSB and ZPL signals. A CMOS-camera (Thorlabs DCC1545M) is used for wide field imaging, which is activated by intersecting the PSB path with a flip mirror. **Gray rectangle:** A second optical setup was used in parallel for the pre-allocation of NV defects, sharing many of the features with the optics of the cryogenic setup. Its basic structure is highlighted in gray. Contrarily to the diagram, the samples were not mounted inside a cryostat, remaining at room temperature. A 0.9 NA objective (Olympus UPLFLN 60x) was employed for improved allocation accuracy and the fluorescence resulted from off-resonant excitation.

short working distance objective with higher NA (Olympus UPLFLN 60x 0.9 NA).

The cryostat optical access to the sample space is done through a 0.5 mm thick sapphire window, whose slim profile is intended to reduce wavefront distortion. Despite this, imaging through the window leads to a $\sim 50\%$ reduction of the collection efficiency, suspectedly due to induced wavefront aberrations.

The imaging scan of the confocal microscope is realised by sweeping the position of the microscope objective with respect to the sample, with a closed-loop piezo stage (Thorlabs MAX311D/M). In spite of the feedback operation of the stage, the back and forth movement shows hysteresis, counteracted by performing the scans always along the same direction, i.e. the signal is only acquired when the objective moves from left to right. Typical $20 \times 20\ \mu m^2$ scans, corresponding to $100 \times 100\ px^2$ in the pixel space, with an integration time of $\tau = 50$ ms per pixel, take around 10 minutes. A fluorescence confocal scan is exemplary illustrated in Fig. 4.4 a and b, where the images pertain to a 50 nm nanodiamond from a spin coated solution on a glass slide, for optical characterisation purposes. The image was acquired with the room temperature setup and shows a point spread function (PSF) with a full width at half maximum (FWHM) of FWHM$= 1.02 \pm 0.03$ µm. With a similar procedure, the PSF of the cryogenic optical setup was established with a FWHM$= 1.39 \pm 0.03$ µm. In both cases the measured PSF is broader than would be expected for an ideal confocal microscope, FWHM $\approx 0.4\lambda/\mathrm{NA}$ [135], as the pinhole was deliberately over-dimensioned to allow for an improved collection efficiency, but leading to collection of undesired scattered light in the vicinity of the emitter. For both setups, the pinhole was implemented with a multimode fibre with an 8 µm core (Thorlabs SMF28e).

Leaving the objective, the fluorescence is separated in its zero-phonon-line (ZPL) and phonon-side-band (PSB) components by a narrow linewidth laser line filter (Semrock FF01-637/7), which transmits light at 637 nm. The reflected beam is further filtered using a dichroic mirror (Thorlabs DMLP650) followed by a notch and a long pass filter (Thorlabs NF533 and FELH650) to remove residual scattered green laser light, applied for off-resonant excitation of the NV defect. Finally the beam is coupled into a SMF28e multimode fibre using an aspheric lens (Thorlabs C220TME-B) on a z-axis translation stage to match the position of the focused gaussian beam with the core of the fibre, which guides the PSB photon towards a low dark-count ($200\ cs^{-1}$) avalanche photodiode (APD Excelitas SPCM-AQRH-FC). For the ZPL photon detection we use the same coupling scheme, employing APDs with lower dark counts: $50\ cs^{-1}$.

The PSB signal is not just used for spin readout, but also as input of a feedback loop which controls the piezo stage position to account for drifts, ensuring maximal coupling efficiency. As such drifts are slow, the feedback loop uses long integration times ($\tau = 10\ s$) and the stage position is stepped 0.1 µm at each feedback iteration.

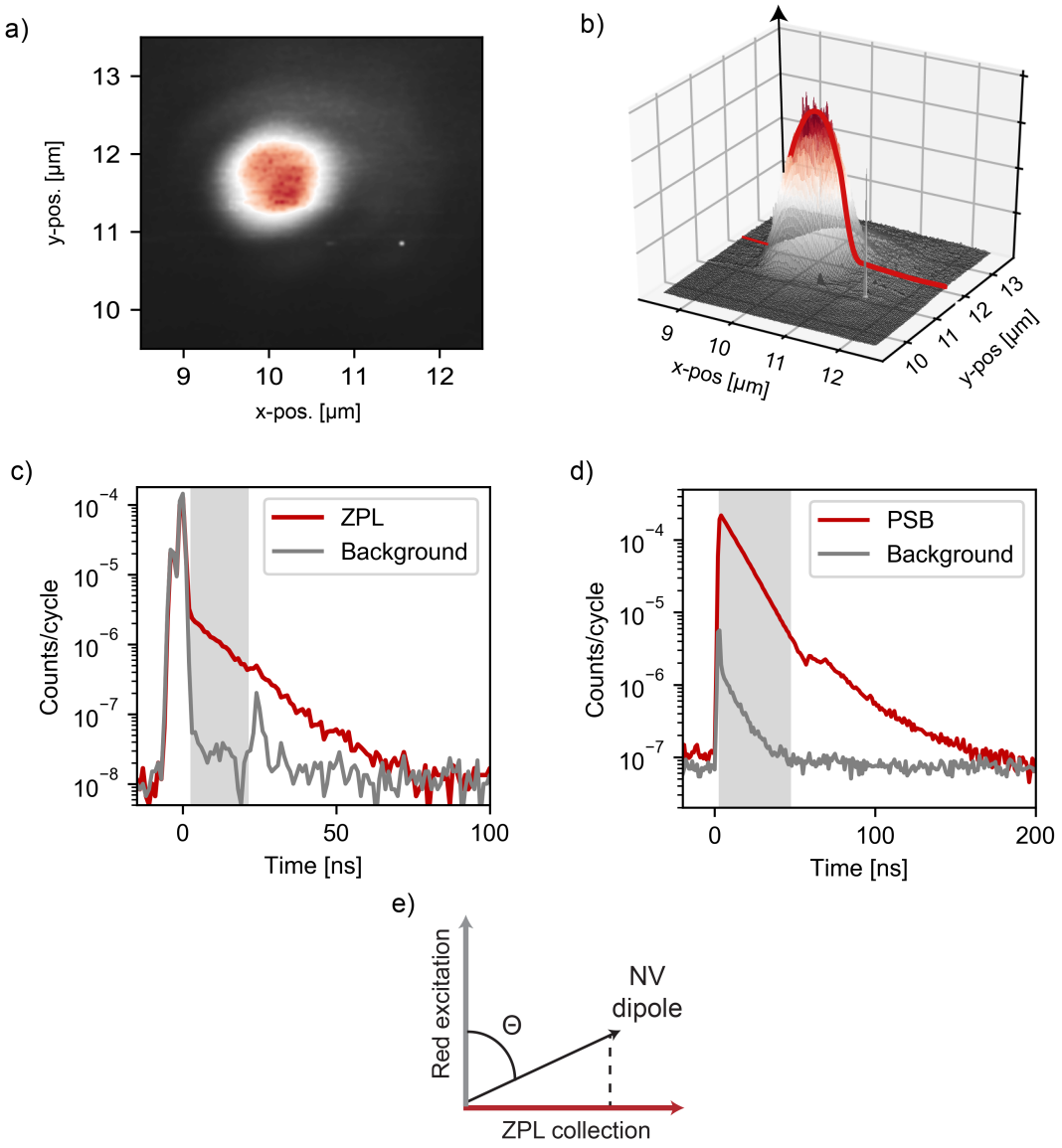


**Figure 4.4: a)** PSB fluorescence scan of a nanodiamond with a 50 nm diameter for characterisation of the point spread function (PSF) of the confocal microscope used for NV-allocation. **b)** Gaussian fit to the PSF of the room temperature setup with a lateral resolution given by FWHM $= 1.02 \pm 0.03$ µm. The PSF of the cryogenic setup has a FWHM $= 1.39 \pm 0.03$ µm. **c)** Fluorescence time trace in the ZPL upon excitation by a resonant pulse on the $m_s = 0$ optical transition. The shaded region indicates the optimal detection window (17 nanos), corresponding to a signal-to-background SBR$= 39 \pm 2$ and a probability of $1.2 \times 10^{-4}$ of detecting a ZPL photon per optical excitation. The background signal was retrieved by detuning the laser by 2 GHz with respect to the working transition. The spike at $t = 24$ ns is due to after pulsing of the detector. **d)** Fluorescence time trace on the PSB, upon resonant optical excitation, corresponding to a SBR$= 130 \pm 1$ within the shaded area and a probability of $1.9 \times 10^{-2}$ of detecting a PSB photon per optical excitation. **e)** Cross polarisation rejection scheme for separation of ZPL fluorescence and scattered laser light.

Due to the long duration of the confocal scans, navigation on the surface of the sample is realised using a wide field imaging system. It relies on a monochromatic CMOS-camera and a $f = 100$ mm lens, which take the PSB beam deviated by a flip-mirror from its confocal trajectory as the input. Therefore, the confocal scanning setup and the wide-field imaging system cannot operate simultaneously.

The optical excitation of the NV defect is performed in two modes: off-resonant excitation by a home-built diode laser at 520 nm, and resonant excitation at 637 nm, by a tunable diode laser (Toptica DL Pro HP 637). The green laser is digitally amplitude modulated by controlling the current fed to the diode, providing rising times in the order of 30 ns. Off-resonant excitation is used for charge state and electronic spin initialisation. During the allocation procedure, off-resonant excitation is also employed to simply generate fluorescence. The modulation of the red laser is more evolved and employs two electro-optic modulators (EOM, Jenoptik AM635) mounted in series and separated by an adjustable delay line, which provides fine tuning of the EOMs transmission windows, to optimize the power throughput and minimize the pulse rising time. Each EOM takes two input voltages: (1) a voltage bias that defines its standby operation and ensures destructive interference at the output and (2) a voltage step which adds to the standby bias and shifts the EOM to the adjacent destructive interference minimum while passing over a point of maximum transmission, to generate a sharp pulse. A different voltage step pulse can be added to the default standby bias to for the generation of small amplitude optical pulses, used for readout of the NV spin state. The voltage bias is constantly drifting and requires continuous updates to ensure minimal leaking in standby mode. For that purpose, the EOM monitor (Fig. 4.3) combined with an acousto-optic-modulator in front of it, used to discriminate particular detection time windows, detect leaking photons and regulate a feedback loop which adjusts the voltage bias each 250 ms. The optimisation addresses one EOM at a time and takes turns between EOM1 and EOM2.

The voltage step for pulse generation is defined by an arbitrary waveform generator (Agilent 33622A) and, contrarily to the voltage bias, it is stable over time and rarely adjusted. Its optimisation relies on a 2D sweep of the two step voltages, one per EOM; the most favourable configuration provides maximal transmission within the pulse and minimal photon leaking thereafter. The flanks of the voltage steps have also been carefully calibrated to minimise transient artifacts and ensure clean optical pulses. Typical pulses have a full width at half maximum in the range $1.6 - 1.9$ ns and an after-pulse suppression of $36 - 39$ dB.

Contrarily to the PSB signal, when performing resonant excitation, the ZPL and scattered light have the same wavelength and chromatic filtering cannot be employed to separate them. Therefore we resort to a combination of two filtering techniques, which are redundant but reinforce each other: time-filtering and cross polarisation excitation.

The filtering due to cross-polarisation excitation is based on collecting the ZPL signal in a linear polarisation state orthogonal to the excitation polarisation, as pictorially explained in Fig. 4.4 e, where $\Theta$ represents the angle between the linear excitation polarisation and the optical transition dipole. The projection of the excitation power along one of the NV dipoles [1] is proportional to $\cos^2(\Theta)$, while the collected ZPL signal is proportional to $\sin^2(\Theta)$. Note that with this technique part of the ZPL signal ($\propto \cos^2(\Theta)$) is thrown out. The value of $\Theta$ is chosen by sweeping the excitation polarisation, with the half-wave plate at the output of EOM2 (Fig. 4.3) and setting $\Theta$ such that the power within one optical red pulse is enough to cause a full population inversion from the addressed ground state. The orthogonality of the collected ZPL signal, with respect to the excitation polarisation, is granted by the polariser and wave plates in front of the ZPL detector. To ensure good supression of scattered light a Glan-Taylor polariser (Thorlabs GT10-A) with a specified extinction ratio of $1:10^5$ was employed.

Time-filtering requires a sharp pulse to excite the NV centre within a time interval much shorter than the lifetime of the excited state and good after-pulse suppression to avoid leaked photons polluting the ZPL fluorescence and ensuring a good signal-to-background ratio. Fig. 4.4 c illustrates a typical ZPL detection time-trace, where the exponential tail of the decay extends far beyond the excitation pulse; the background signal was captured by setting a detuning $\delta = 2$ GHz of the excitation frequency with respect to the $m_s = 0$ working optical transition. At $t = 24$ ns, an APD after-pulsing peak limits the optimal detection window, signaled in gray, to a width of $\tau = 17$ ns. Within such a window there is a probability of $p = 1.2 \times 10^{-4}$ to detect a ZPL photon per optical excitation [2] and the 39 dB EOM supression ensures low background floor associated with a signal-to-background ratio $SBR = 39 \pm 2$. The time trace of the excitation has a kink before the actual pulse, due to a reflection on the EOM monitor, which does not affect the NV centre and the respective fluorescence time trace. Fig. 4.4 d shows the PSB signal resulting from the same excitation pulse, with a probability of photon detection after excitation of $1.9 \times 10^{-2}$ and a SBR$= 130 \pm 1$ within the optimal detection window in gray. These values vary slightly among different experimental runs, due to changes in optical coupling.

The mode profile of the tunable red laser is monitored using a confocal scanning Fabry-Perot cavity (Toptica FPI 100), to ensure single mode operation. For improved spectral stability an optical isolator (Thorlabs IO-3-633-LP) was installed at the output of the red laser. A wavemeter (Toptica WS7) is occasionally used to monitor the laser when searching for optical resonances, mainly after a warm-up cool-down cryogenic cycle.

[1] As explained in the section ahead, the optical transitions from the $m_s = 0$ ground state to the $|E_x\rangle$ or $|E_y\rangle$ levels correspond to two orthogonal emission dipoles. In this work, we solely operate with the $|0\rangle \rightarrow |E_y\rangle$ transition and respective dipole.

[2] The probability of detecting a ZPL photon per optical excitation is identified throughout this manuscript as the ZPL system efficiency. A lower value than $p = 1.2 \times 10^{-4}$ is reported in Chapter 6, where it refers to the system efficiency, measured after propagation through the interferometer.

A LabView/Python interface was developed for experimental control over the various elements of the optical and microwave interface. The time base of the experiment was set by a homebuilt pulse-synthesiser based on a RedPitaya FPGA with a timing resolution of 1 ns. Photon-detection events were registered by a 8-channel time-tagger (TTM8000 Roithner Lasertechnik) with 82.3 ps time resolution. The processing of high data rates generated by the time-tagger, mostly due to the interferometer phase readout, was achieved by distributing the data output through 3 computers, achieving real time processing.

### 4.2.4 Readout and Coherent Control of Optical Transitions

This section focuses on the techniques associated with resonant excitation of optical transitions, which is essential for the readout of the spin populations and for the generation of coherent photons.

#### Mapping Optical Transitions

The optical transitions of the NV centre were identified using photo-luminescent (PLE) spectroscopy. The narrow-linewidth red laser (637 nm) is swept across a frequency range of typically a few (5 to 30) GHz and whenever it comes in resonance with a transition we observe increased fluorescence, measured in the PSB. Low red power, in the range of 0.5 to 2 μW, reduces power broadening. In parallel, a low power (30 μW) green laser pulse is applied to counteract the de-ionizing effect $NV^- \rightarrow NV^0$ of the red beam. A continuous wave (CW) microwave signal tuned to the $m_s = 0 \leftrightarrow m_s = -1$ ground state transition ensures that the spin populations remain distributed, as the resonant red pulse depletes the ground state population it comes in resonance with. The scheme is illustrated in Fig. 4.5 a. Sweeps are run repeatedly to provide good statistics. Each sweep lasts $500 - 1000$ ms, depending on the width of the scanned frequency window. Fig. 4.5 b shows the result of repeated scans, where spectral diffusion in the scale of 10 MHz, supposedly due to laser induced charge fluctuations in the NV environment [93], is visible. In alternative PLE schemes, spectral diffusion is mitigated by using the green pump only as a short pulse at the start of each sweep or by employing a yellow laser (575 nm) instead, which benefits from increased absorption cross-section, thereby requiring less power for charge initialisation. A quick overview of PLE schemes applicable to NV centres can be found in Ref. [115].

To calculate the NV centre optical spectrum, the eigenvectors of the ground and excited manifolds were calculated through diagonalization of the corresponding Hamiltonians $H_{GS}$ and $H_{ES}$, found in Eq. 3.4 and 3.7. Consider the matrices $\hat{M}_{GS}$ and $\hat{M}_{ES}$ whose columns describe the eigenvectors as linear combinations in the ordered unperturbed spin basis $|-1\rangle$ $|0\rangle$, $|+1\rangle$ for the

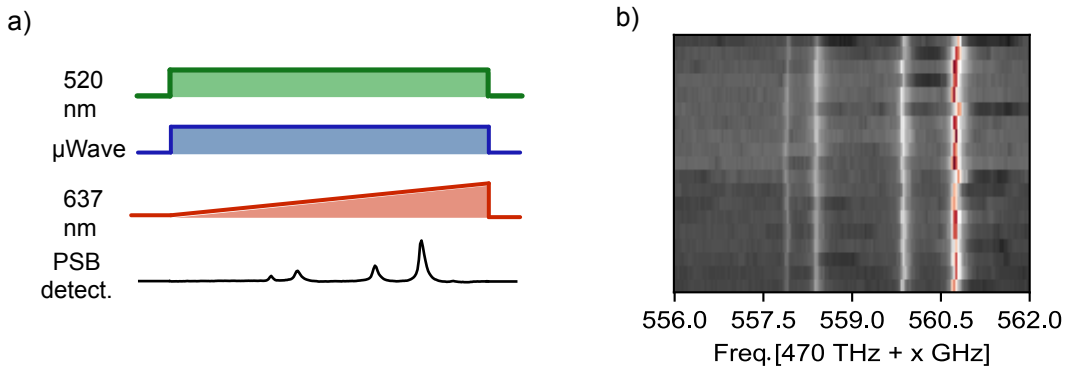


**Figure 4.5: Mapping of the optical transitions of the NV centre. a)** Experimental sequence for photoluminescent excitation (PLE) spectroscopy. The red laser frequency is swept around the zero-phonon-line (637nm), while pumping with CW green light to prevent de-ionization of the NV centre. A CW microwave field to ensure that all electronic spin sub-levels are populated. **b)** PLE spectrum of the NV for individual sweeps, displaying spectral diffusion between different iterations. Four well pronounced optical transitions are visible.

ground state and $|A_1\rangle$, $|A_2\rangle$, $|E_x\rangle$, $|E_y\rangle$, $|E_1\rangle$, $|E_2\rangle$ for the excited state. In terms of linear algebra, the $\hat{M}$ matrices describe the vector transformation from the diagonalised basis $|\tilde{V}\rangle$ to the unperturbed basis $|V\rangle$. The allowed transitions between unperturbed states follow the selection rules already described in Table 3.1 and the transition probability matrix can be written as:

$$T = \begin{pmatrix} \frac{1}{2} & \frac{1}{2} & 0 & 0 & \frac{1}{2} & \frac{1}{2} \\ 0 & 0 & 1 & 1 & 0 & 0 \\ \frac{1}{2} & \frac{1}{2} & 0 & 0 & \frac{1}{2} & \frac{1}{2} \end{pmatrix} \tag{4.9}$$

where the $(i, j)$ entry gives the transition probability between the excited state $|V_j\rangle$ and the ground state $|V_i\rangle$. A more general probability transition matrix $\tilde{T}$, between the "perturbed" states $\tilde{V}$, is given by:

$$\tilde{T} = [\hat{M}^2_{GS}]^T \, [T] \, [\hat{M}^2_{ES}] \tag{4.10}$$

where the second power of the transformation $\hat{M}$ matrices applies to the individual entries, as opposed to a matrix multiplication. $\tilde{T}$ establishes the possible optical transitions, whose frequencies can be extracted from the difference between the eigenenergies of $H_{GS}$ and $H_{ES}$. An illustrative plot of the relative frequency of the optical transitions as a function of strain along the x-axis $\delta_x$ is shown in Fig. 4.6 a. As already noted in Chapter 3, high strains in the xy-plane lead to the separation of two optical branches.

In the PLE measurements only the lower branch could be observed, despite a search covering a 300 GHz spectral window, which is suggestive of a very high strain regime ($|\vec{\delta}| \geq 80$ GHz). It is hypothesised that under such conditions, symmetry breaking phonons enable the

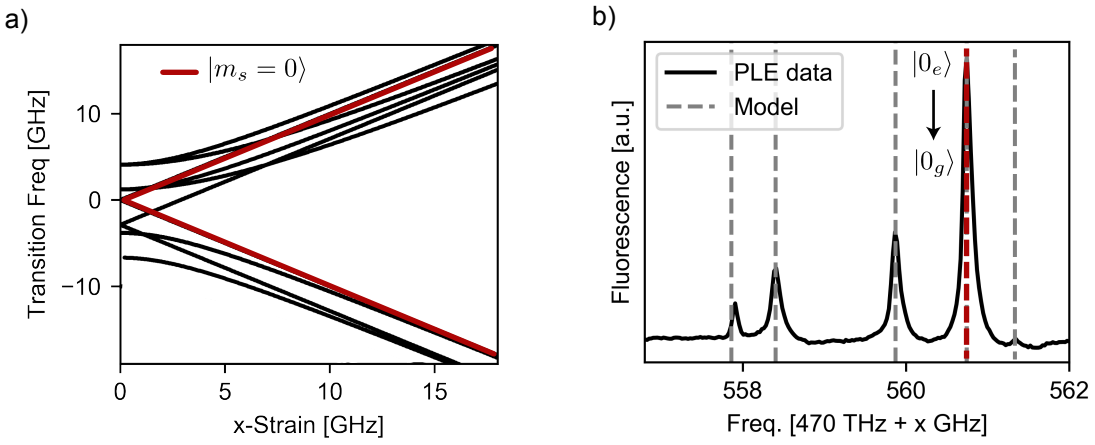


**Figure 4.6: Theoretical and experimental PLE spectrum. a)** Theoretical prediction of relative frequencies of the dipole allowed optical transitions as a function of strain along the x-axis, given a null strain in other directions, $\delta_y = 0$ and $\delta_z = 0$. The red lines identify transitions between the $|0\rangle$ ground state and an eigenstate of the excited manifold with a dominant component with z-spin projection $m_s = 0$. **b)** Measured optical transitions and theoretical position of resonances (dashed lines), from a possible fit corresponding to the lower branch for a strain configuration $\delta_x = 152$ GHz , $\delta_y = 13$ GHz and $\delta_z = 0$ GHz. The main transition corresponds to the $m_s = 0$ electron spin state.

non-radiative relaxation from the upper to the lower branch [130], leading to a reduction of luminescence from the upper branch, alongside a static Jahn-Teller effect that deteriorates the optical absorption selection rules [139]. The comparatively short spin-flip time upon resonant optical excitation (see next Section) is also indicative of a high-strain configuration, due to mixing in the excited state manifold caused by the off-diagonal elements of $H_{ES}$.

The performed measurements were not conducive to a quantitative evaluation of the strain vector $\vec{\delta} = (\delta_x, \delta_y, \delta_z)$. Despite the large uncertainty on $\vec{\delta}$, a reasonably good agreement between the theoretical and experimental lower branch spectra could be achieved, as illustrated in Fig. 4.6 b. In future work, a quantitative treatment could be realised by applying a strain-cancelling electric field, monitored by PLE measurements, to determine the components of $\vec{\delta}$.

By removing the CW microwave field from the PLE sequence, only the tallest transition remained. Logically this transition has to be associated to the $|0\rangle$ electronic spin ground state, since $|-1\rangle$ and $|+1\rangle$ are poorly repopulated. By virtue of its higher luminescence and weaker decay through the singlet manifold (see Section 3.6), it was used as the main working transition throughout this work, for readout and initialisation of the electronic spin state and to generate ZPL photons. In the averaged spectrum of Fig. 4.6 b, the main transition presents a linewidth of $154 \pm 8$ MHz and stands $0.88 \pm 0.01$ GHz away from the adjacent transition with $|\pm 1\rangle$ character, which is a limiting factor for the optical spin readout fidelity, as discussed in the next section.

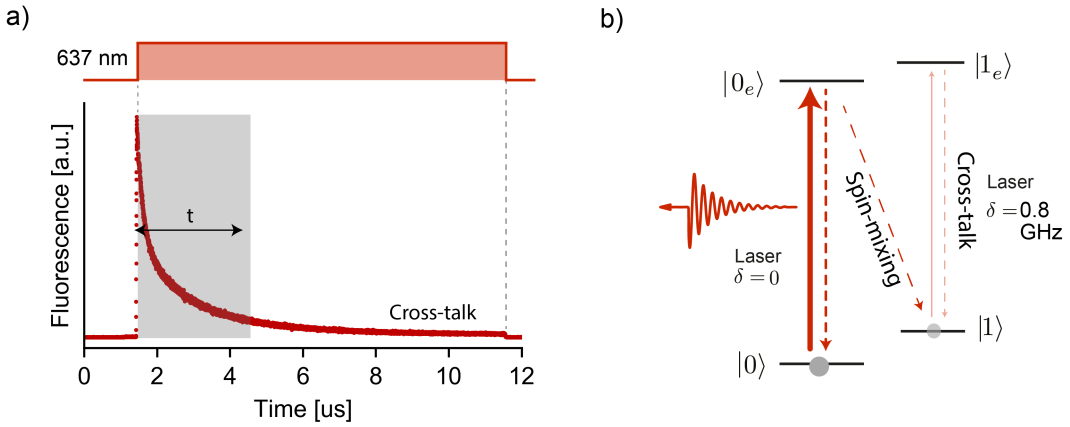


**Figure 4.7: Optical resonant readout of the spin state. a)** Fluorescence profile upon resonant excitation by square resonant pulse on the $|0\rangle \rightarrow |0_e\rangle$ transition. The fluorescence decay is caused by spin-mixing in the excited state, which causes a depletion of the $|0\rangle$ population. Cross talk with the neighbouring optical transitions is responsible for the non-vanishing tail of the decay. The shaded area indicates the optimal integration time or, equivalently, pulse duration for an optimal readout contrast. **b)** Illustration of spin-mixing and cross-talk, the two mechanism which affect the spin readout fidelity. $\delta$ indicates the detuning of the excitation laser light with respect to the optical transitions.

### Optical Resonant Spin Readout

The spin state of the electron is read out using a laser pulse tuned to an optical transition between a queried (ground) state and the corresponding excited state level. For most of this work, we resorted to the $|0\rangle \rightarrow |0_e\rangle$ transition. If the NV centre is found in the $|0\rangle$ state, the excitation-decay cycles yield a fluorescent signal $F_0$, expressed ahead in detected photons per readout. Conversely, being found in a ground state with $m_s = \pm 1$ character, a much weaker cross-talk luminescence $F_1$ is observed, due to the corresponding transition being far-detuned.

The cross-talk mechanism together with non spin-preserving transitions in the excited state manifold (see Section 3.7) impact negatively the fidelity of the resonant readout. While the cross-talk with detuned transitions is responsible for the non-vanishing tail of the decay of the readout signal shown in Fig. 4.7, spin-mixing in the excited state leads to a depletion of the $|0\rangle$ population which causes the decay of the readout signal.

The power and duration of the readout pulses were carefully calibrated. Excessive power leads to a fast depletion of the queried population and increased cross talk, too little power yields a weak readout signal. Also the duration of the pulse also has an optimal point, as a short pulse results in few accumulated photons and a long pulse compromises the signal-to-background ratio (SBR), due to the fluorescence decay. The power of the readout pulses was swept by changing the step factor $s \in [0, 1]$, which regulates the amplitude of the

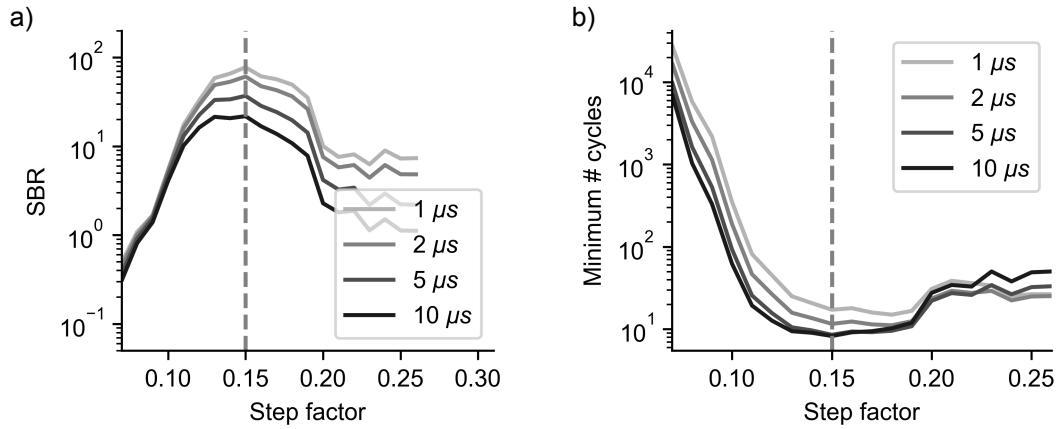


**Figure 4.8: Optimisation of the optical spin readout.a)** Optimisation of the resonant pulse duration and amplitude (step factor) based on signal-to-background ratio. **b)** Optimisation of the resonant pulse duration and amplitude based on number of cycles necessary to distinguish between two spin states $\#_{res}$. A step factor $s = 0.15$ and a pulse duration $t = 5$ µs results in the best readout performance, associated with $\#_{res} = 9$.

voltage pulse applied to the EOM allowing the transmission of light, according to the equation $P = P_0 \sin(s\,\pi/2)$, where $P$ stands for power and $s = 1$ corresponds to maximum transmission. The power and pulse duration optimisation involved maximising the SBR:

$$\mathrm{SBR} = \frac{F_0 - F_1}{F_1} \tag{4.11}$$

where $F_0(F_1)$ represents the average detected phonon-side-band photons per readout, when the population is found in the $|0\rangle$ ($|\pm 1\rangle$) ground state. The parameter sweep and resulting SBR curves are represented in Fig. 4.8 a, which establish the optimal step factor at $s = 0.15$, corresponding to 0.08 µW of CW red laser power. Short pulses (e.g. $t = 1\mu s$) lead to the best SBR, due to the exponential decay of fluorescence, but are not necessarily the most practical as they require more readout cycles. Therefore a second figure of merit, $\#_{res}$, was employed in the optimisation. $\#_{res}$ stands for the minimum number of readout cycles necessary to distinguish between a $|0\rangle$ and a $|\pm 1\rangle$ population. Assuming Poissonian statistics approximated by a Gaussian distribution, the minimum number of readout cycles is given by:

$$\#_{res} = \left( \frac{\sqrt{F_0} + \sqrt{F_1}}{F_0 - F_1} \right)^2 \tag{4.12}$$

The optimisation with respect to $\#_{res}$ is represented in Fig. 4.8 b, which sets the optimal pulse duration at 5 µs with $\#_{res} = 9$ cycles. Fixing the step factor $s = 0.15$ and the pulse duration $t = 5$ µs, leads to $F_0 = (16.7 \pm 0.1)\%$ and $F_1 = (0.2 \pm 0.1)\%$ photons per readout,

corresponding to a contrast $C_F$[3]:

$$C_F = \frac{F_0 - F_1}{F_0 + F_1} = 98.8 \pm 0.2\% \tag{4.13}$$

which compares favourably with similar experimental works, for example $C_F = 0.978$ in Robledo et. al [80]. The expected photon distribution for a readout with 50 cycles is illustrated in Fig. 4.9 a. The low number of photons per readout cycle $n_0 = 0.167$ is partially responsible for the high value of $\#_{res}$, considerably above the single-shot-readout requirement of $\#_{res} = 1$, attained in the same work by Robledo with $n_0 = 6.4$. In our case, the high-strain diamond sample has strong spin-mixing in the excited state manifold, leading to poor cycling transitions, fast decay of the fluorescence during readout and low $n_0$. This can be improved in future work by employing a low-strain sample.

To determine the errors involved in the estimate of the electronic spin population, a simple model has been taken into account. The accumulated photons per readout are given by:

$$R(x) = F_0 x + F_1(1 - x) + B \tag{4.14}$$

where $x$ represents the $|0\rangle$ population; $1 - x$ is the remaining population, found in $|\pm 1\rangle$ . As introduced already, $F_0$ is the average fluorescence per readout associated with $|0\rangle$, whereas $F_1$ is the signal resulting from cross talk and $B$ the background signal resulting from unfiltered scattered light from the diamond surface and dark counts of the photon detectors. In order to be resilient to drifts of the setup (e.g. coupling, power changes), a spin population readout typically involves two projective measurements: (1) $|0\rangle\langle 0|$, implemented by a $m_s = 0$ readout pulse, yielding $R_0$ fluorescent photons and (2) $|\pm 1\rangle\langle \pm 1|$, realised by a $\pi$-microwave that inverts the spin population pulse followed by a $m_s = 0$ pulse to generate $R_1$ photons. The readout is then normalized:

$$R_{norm} \quad = \quad R_0/(R_0 + R_1) \tag{4.15}$$

Plugging of Eq. 4.14 in the normalized readout $R_{norm}$ yields:

$$R_{norm}(x) = \frac{F_0 - F_1}{F_0 + F_1 + 2B}\, x + \frac{B + F_1}{F_0 + F_1 + 2B} \tag{4.16}$$

Calibration measurements using a far-detuned laser pulse established $B = (1.14 \pm 0.02) \times 10^{-3}$ photons per readout, corresponding to a ratio $B/F_0 = 6.8 \times 10^{-3}$. Therefore $B$ can be safely neglected.

[3]The determination of the contrast was carried out in a different data set than the one used for the optimisation of the pulses. For that reason, the presented contrast is marginally better than would have been expected from $SBR = 39$ as shown in the optimisation routine, fig 4.8 a.

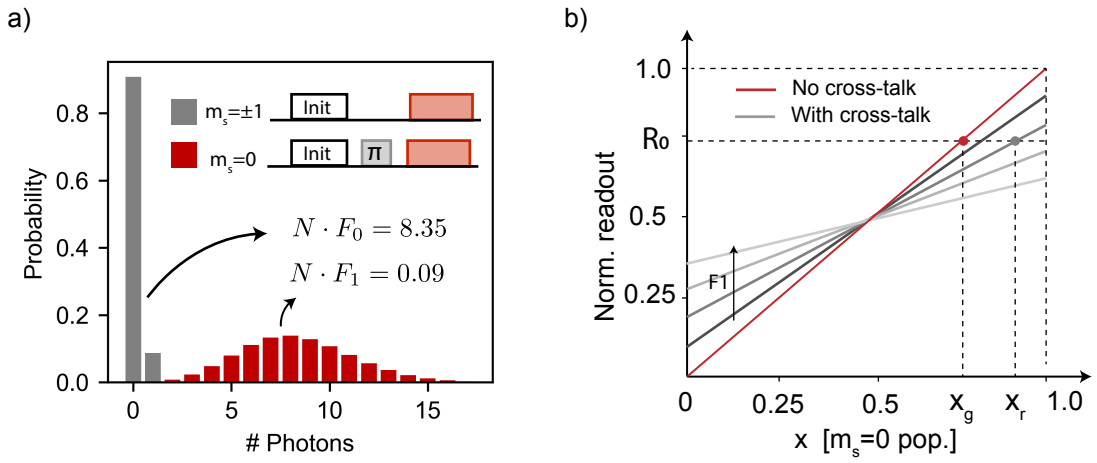


**Figure 4.9: Electron spin readout: contrast and errors. a)** Poissonian distribution of photon events for an integration over $N = 50$ readout cycles, corresponding to a readout contrast of $C = 98.8 \pm 0.2$ %. The two experimental sequences associated with the determination of the spin readout contrast are shown at the top. **b)** Model of the normalized spin readout as a function of the $|0\rangle$ spin population and cross-talk with neighbouring transitions $F_1$. The gray curves show how the normalised readout is affected by increasing $F_1$. The red line illustrates the response of a system with no cross-talk $F_1 = 0$. An upper bound $F_1 \leq 1\%$ was estimated from the range of measured $R_{norm}(x)$ values.

Even though a direct determination of the cross-talk $F_1$ was not possible, based on the range of measured $R_{norm}$ values it is possible to ascertain an upper bound. The effect of $F_1$ in the readout function $R_{norm}(x)$ is shown in Fig. 4.9 b, where the different gray lines intersect the y-axis at $y = F_1/(F_0 + F_1)$ and correspond to increasing values $F_1$. Typical initialisation routines into the $m_s = -1$ level, lead to readout values of $R_{norm} \leq 1\%$. As the maximum cross-talk value compatible with such measurement sets $F_1/(F_1 + F_0) = 1\%$, we know that $F_1 \leq 1\% F_0$. Given that $B << F_0$ and $F_1 << F_0$, the normalized readout can be approximated to $\tilde{R}_{norm} \approx x$. For a generic readout $R_{norm,0}$ the difference between the exact population estimate $x_r$, given by Eq. 4.16, and the approximated population $x_g$, given by $\tilde{R}_{norm} \approx x$, is determined by inverting the $R_{norm}(x)$ and $\tilde{R}_{norm}(x)$ functions to yield $\varepsilon = x_g - x_r$:

$$\varepsilon = -2\frac{F_1 + B}{F_0 + F_1 + 2B}x_r + \frac{B + F_1}{F_0 + F_1 + 2B} \tag{4.17}$$

Thereby we note that for $x_r < 0.5$ ($x_r > 0.5$), the approximation will overestimate (underestimate) the spin population. The maximum error occurs for $x_r = \{0, 1\}$ and always remains below 1%. For this reason, when performing spin tomography we resort to the first-order approximation: $\tilde{R}_{norm} = x$.

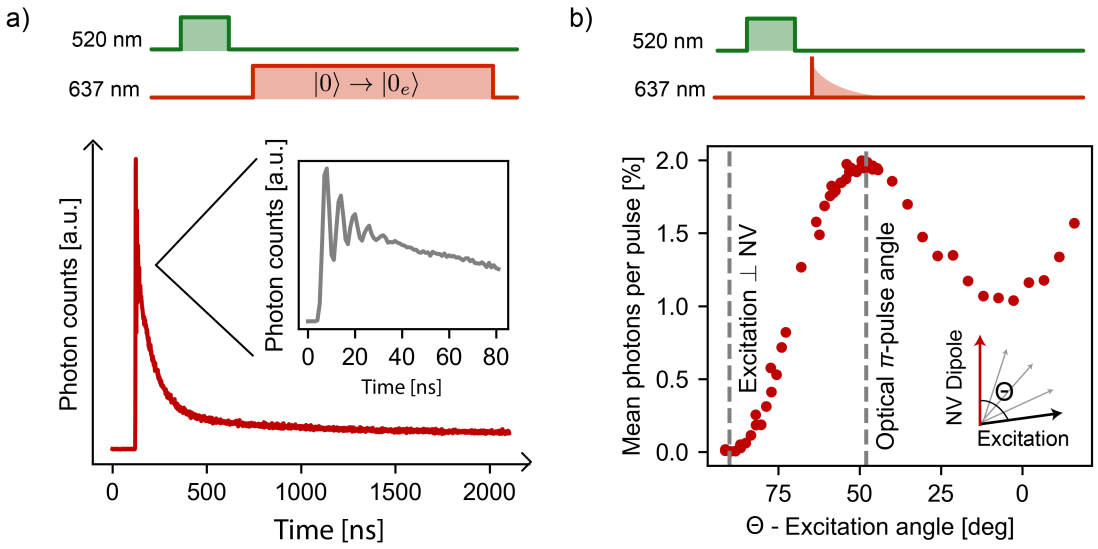


**Figure 4.10: Coherent driving of the $|0\rangle \rightarrow |0_e\rangle$ optical transition with a resonant laser pulse. a)** Fluorescence time trace resulting from pumping the $m_s = 0$ optical transition with a long (2 µs) pulse. The decay of the signal is primarily due to spin mixing in the excited state, leading to the depletion of the $m_s = 0$ ground state population. Coherent Rabi driving is visible in the first section of the pulse (inset), before decoherence evens out the oscillations. **b)** Average accumulated photons within the decay, after pumping of the optical transition with a single sharp FWHM = 1.5 ns pulse, as a function of the projection angle between the excitation polarisation and the NV centre dipole.

### Coherent Control of Optical Transitions

The entanglement generation protocol relies on optical $\pi$-pulses, which transfer the $|0\rangle$ ground state spin population to the corresponding excited state $|0_e\rangle$, followed by the emission and detection of fluorescence. This promotion needs to occur coherently, through short high-power pulses, where the power was carefully tuned to ensure a near exact population inversion and the pulse profile was optimised for an optimal time-filtering of scattered light in the ZPL path. The calibration of the optical $\pi$-pulses is described ahead.

Before any optimisation was performed, the coherent population transfer could be verified by applying a long laser pulse and simultaneous monitoring of the PSB luminescence. For a sufficiently strong laser field, corresponding to a Rabi driving frequency larger than the transition damping rate ($\Omega_0 > \gamma$), Rabi fringes emerge, as in the measurement shown in Fig. 4.10 a. Here the oscillations decohere rapidly (30 ns ) due to the short lifetime of the excited state ($\tau = 13$ ns), the phonon-mediated spin mixing in the excited state and pure dephasing $T_2$ [126]. The remaining decay, observed crearly for $t \geq 40$ ns, is due to the $|0\rangle$ population depletion, as discussed in the previous Section. De-ionisation of the $NV^-$ into $NV^0$ has been excluded for these timescales, by tracking the total population within the three electronic spin

manifolds and observing no decrease.

In the $\pi$-pulse calibration, we attempt a near complete population inversion through fine tuning of the polarisation angle of the excitation light with respect to the NV centre dipole orientation. The laser power and pulse duration (FWHM$\approx$ 1.5 ns) of the optical $\pi$-pulse are typically fixed. As depicted in Fig. 4.10 b, an excitation polarisation normal to the dipole yields minimal fluorescence. Further rotation increases the power projected along the NV centre dipole, resulting in a stronger signal. The optical $\pi$-pulse is realised at the point of maximum photon-yield per excitation pulse, corresponding in the figure with $\Theta = 49.0 \pm 0.5$ deg and a probability of yielding a PSB photon per excitation of $\sim 2\%$.

Similarly to the low-power pulses employed in the spin readout, the optical $\pi$-pulses are negatively affected by cross-talk and spin-mixing in the excited state. Spin-mixing affects the entanglement generation protocol, as a spin-flip following an optical $\pi$-pulse leads to a classically correlated state. For that reason, an attempt was made to quantify the probability of a flip occuring per $\pi$-pulse. In this measurement, the NV centre was prepared in the $|0\rangle$ state, followed by a sequence of optical $\pi$-pulses, separated by $\sim$ 4.5 excited state lifetimes from each other. The process is illustrated in Fig. 4.11 a. The gradual decrease in fluorescence indicates transfer of the spin population out of the resonant ground state $|0\rangle$. Note that the measurements were carried out in a power regime where no contribution from ionization from $NV^-$ to $NV^0$ is present, as attested by auxiliary measurements. For each optical $\pi$-pulse, the population is proportional to the photon counts integrated from the excited state decay. Applying an exponential fit to the integrated photon counts gives a probability of spin-flip per excitation of $13.5 \pm 1.5\%$ [4]. This is a relevant figure because it is expected to affect the fidelity of the spin-photon entanglement generation, as discussed quantitatively in Section 6.3. It should be noted that the use of a low strain NV centre could reduce the spin-flip probability and allow single-shot readout.

Besides spin-mixing within the excited manifold, also cross-excitation leads to the failure of the entanglement generation protocol. Cross-excitation means that the optical $\pi$-pulses have a finite probability of exciting neighbouring resonances. A simple empirical model was devised to quantify the probability of generating a photon due to cross-excitation.

Spin-dependent spectroscopy of the NV-centre revealed that our working transition couples to the $|0\rangle$ ground state, whereas the nearest neighbouring transition, located $\sim$ 0.88 GHz away, is associated with the $|\pm 1\rangle$ states, as described in Section 4.2.4. The model only takes this two resonances into consideration as the other transitions are far-detuned and should not contribute significantly. For a spin population described by $\psi = a_0 |0\rangle + a_{\pm 1} |\pm 1\rangle$, upon excitation by an

[4] The fit is given by $p = \exp(-n_i/k)$, where $n_i$ is the excitation pulse number. The probability per spin-flip is $psf = 1 - \exp(1/k)$.

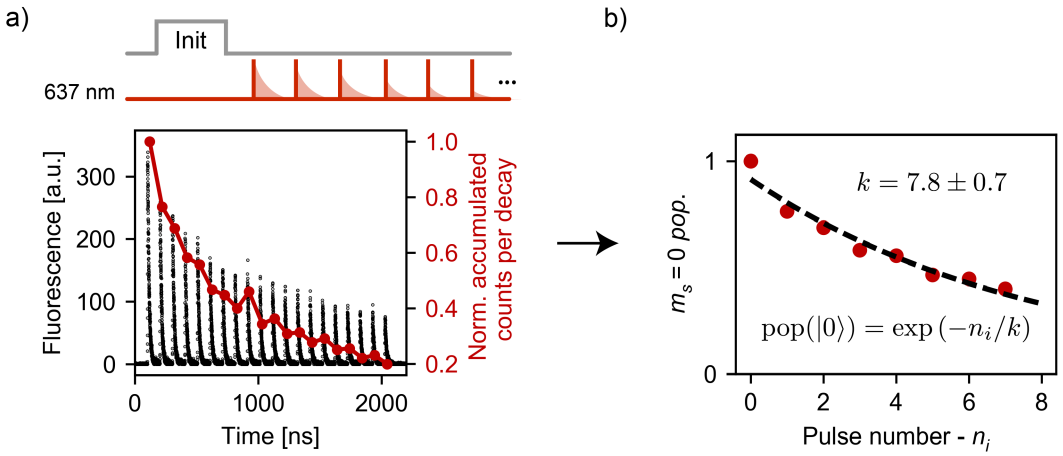


**Figure 4.11: Spin-mixing caused by optical $\pi$-pulses.** a) Sequential depletion of the $|0\rangle$ population due to a train of $\pi$-pulses. b) Fit to the population depletion as a function of number of optical $\pi$-pulses, $n_i$. Each $\pi$-pulse is associated with a decay lifetime of $k = 7.8 \pm 0.7$, corresponding to a probability $13.6 \pm 1.5\%$ of spin transfer into $|\pm 1\rangle$. The error bars due to shot noise are smaller than the symbols.

optical $\pi$-pulse, the probability of photon detection in the PSB is given by:

$$P_\gamma = \eta(|a_0|^2 P_0 + |a_{\pm 1}|^2 P_{\pm 1}) + P_{bkg} \tag{4.18}$$

$P_0$ ($P_{\pm 1}$) describes the probability of photon emission associated with the ground state $|0\rangle$ ($|\pm 1\rangle$) population; $\eta$ is the collection efficiency of our apparatus and $P_{bkg}$ the background counts due to unfiltered laser light scattered off the diamond surface and detector dark counts. According to calibration measurements, $P_{bkg} = (3.4 \pm 0.2) \times 10^{-5}$ for an integration window of 40 ns, around the fluorescence decay.

Furthermore, for an optical $\pi$-pulse it is assumed that $P_0 \approx 1$, as the $m_s = 0$ excited state does not suffer intersystem-crossing leading to non-radiative decay [126]. To determine the remaining unknowns $P_{\pm 1}$ and $\eta$, two measurements M1 and M2 were performed. In M1 the system was initialized in $m_s = -1$, according to the prescription of Section 5.2.1, followed by an optical $\pi$-pulse with a readout $P_{M1} = (6.2 \pm 0.2) \times 10^{-4}$ photons per excitation. In M2 the same initialisation was carried out, followed by a microwave-driven spin population inversion into $m_s = 0$ and then by an optical $\pi$-pulse, yielding $P_{M2} = (15.25 \pm 0.01) \times 10^{-2}$ detected photons per excitation. For both measurements the fluorescent signal was accumulated over $2 \times 10^6$ cycles. The $a_0$, $a_{-1}$, $a_{+1}$ coefficients were determined, using the characterisation described in Section 5.2.1, with $|a_0|^2 = 0.021$, $|a_{-1}|^2 = 0.839$ and $|a_{+1}|^2 = 0.142$. The microwave spin rotation has near-unit fidelity - see next section. By plugging $P_{M1}$ and $P_{M2}$ into Eq. 4.18 and solving the resulting system of equations it has been established that the collection efficiency is $\eta = (1.80 \pm 0.02)\%$ and the chance of yielding a cross-excitation photon is

$P_{\pm 1} = (1.3 \pm 0.2)\%$. Akin to the spin-flip chance due to optical $\pi$-pulses, also the cross-excitation degrades the fidelity of the entanglement generation, whose quantitative discussion is found in Section 6.3.

## 4.3 The Microwave Interface

The control of the NV centre ground state spin transitions is achieved by applying resonant microwave fields of suitable power, modulation and frequency. For that purpose, three microwave sources (wideband synthesizers Analog Devices ADF4351) are interfaced with Arduino microcontrollers, each providing a frequency to drive a particular electronic spin transition - see Fig.4.12. The three sources are multiplexed into a common coaxial path by a 4-port switch (Peregrine EK42442), controlled by a Red Pitaya-based homebuilt pulse-synthesizer (Red Pitaya). As the experimental sequence requires different power levels within a single cycle (e.g. low power slow driving to implement a CNOT gate on the electronic spin, conditional on the nuclear spin; fast driving to realize a high fidelity NOT gate on the electronic spin), the microwave signal is split in two paths by a 50:50 splitter: one path is attenuated by an IQ mixer (Analog Devices ADL5375), the other one proceeds unattenuated. Later a 2-port switch (Mini Ciruits ZASWA-2-50-DR) chooses between the two power modes (high and low), before the second 2-port switch modulates the input CW signal into pulses of varying duration, as determined by the Red Pitaya output. The last element of the microwave chain is a high power broadband amplifier with 45dB of gain (Mini Circuits ZHL-16W-43+).

The cryostat has hermetically sealed SMA to SMP connectors which interface the microwave chain at room temperature with the vacuum environment of the sample chamber. The SMP connectors finally attach to a coplanar waveguide, installed on the cold finger of the cryostat, which supports a 30 µm aluminium wire that spans the sample, carefully placed at $\sim$ 15 µm from the NV centre to be addressed.

The Arduino controllers and the Red Pitaya are connected to a central computer, responsible for regulating the experimental parameters and collecting data. The different elements of the microwave chain are connected via coaxial cables and SMA connectors.

### 4.3.1 Mapping Spin Transitions

Steering the spin populations within the ground state energy levels - Section 3.4 - is a fundamental tool in our experiments. To control these transitions, they had, firstly, to be identified and assigned a frequency, as explained in the following paragraphs.

Electron spin resonance (ESR) [140] can be performed on a single NV centre by applying a

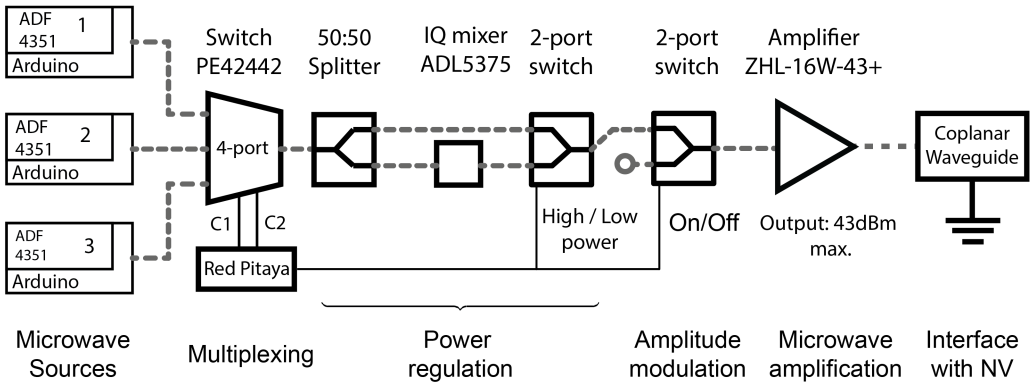


**Figure 4.12: Diagram of the microwave setup**

microwave field of varying frequency ($\nu_v$), while optically pumping the diamond defect. Whenever the field comes in resonance with a spin transition, part of the $m_s = 0$ population is redistributed to one of the $m_s = -1$ or $m_s = +1$ levels resulting in decreased photoluminescence. This spectroscopy method, which relies on optical excitation and detection, is called optically detected magnetic resonance (ODMR). In the laboratory the optical transition is cycled with an off-resonant 520 nm excitation and the photoluminescence is monitored with the PSB detector. The microwave sweeps are carried out repeatedly until the photon readout statistics allow to discern the spectral features.

The measured spectrum of the NV used in this experimental work is presented in Fig. 4.13, showing six transition dips distributed in two manifolds: $m_s = 0 \leftrightarrow m_s = -1$ and $m_s = 0 \leftrightarrow m_s = +1$ transitions. Due to the nuclear spin-1 of the adjacent $^{14}N$ each electronic spin displays hyperfine splitting (for $m_I = 0, \pm 1$) resulting in three resonance lines, as expected from the discussion of Section 3.4. The photoluminescent signal as a function of microwave frequency in Fig. 4.13 is fitted by the following equation[141]:

$$I(\nu_m) = I_0 \sum_i \left(1 - C\mathcal{F}\left(\nu_m - \nu_i, \gamma\right)\right) \tag{4.19}$$

where the sum runs over the various spin transitions, each centred around $\nu_i$. $C$ is the measurement contrast, $I_0$ the intensity base level and $\mathcal{F}(\nu_m, \gamma)$ is the ESR Lorentzian lineshape with a HWHM of $\gamma$:

$$\mathcal{F}(\nu_m, \gamma) = \frac{\gamma^2}{(\nu_m - \nu_i)^2 + \gamma^2} \tag{4.20}$$

$\gamma$ is fundamentally limited by the effective transverse relaxation lifetime $T_2^*$ of the system, but susceptible to power broadening, both by the microwave and the optical field. The presented spectrum has a contrast $C = 9.3 \pm 0.2\%$ and the transition HWHM is $\gamma = 0.37 \pm 0.01$ MHz.

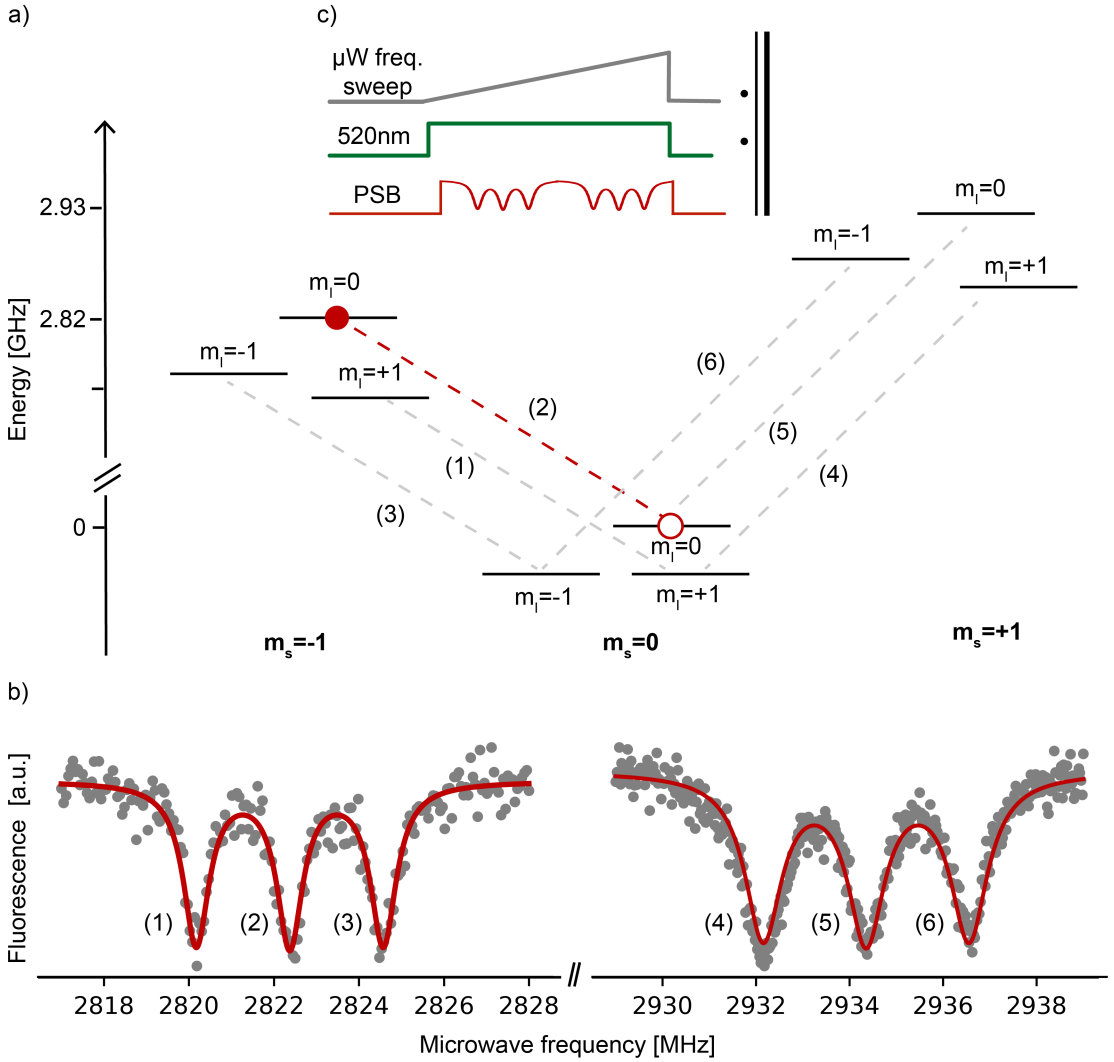


**Figure 4.13: Spectrum of the electronic and nuclear spin transitions. a)** Energy diagram of the optical ground state of the NV centre, spanning three electronic spin states $m_s = 0, \pm 1$, each containing three nuclear sublevels $m_I = 0, \pm 1$. The allowed transitions are illustrated with dashed lines. The red line indicates a possible spin rotation involving the two populations identified with red dots. **b)** ODMR spectrum of the NV centre with respective fit. The numbers in the spectral dips identify the corresponding transitions in the energy map. **c)** Experimental sequence performed to retrieve the ODMR spectrum.

To resolve the hyperfine splitting of the ESR spectrum, the optical pumping was kept at low power (50 μW), along with a weak microwave driving field, as represented in Fig. 4.13 c. From the fit to the data, a hyperfine splitting of $A_{gs}^{\parallel} = (1.19 \pm 0.02)$ MHz was retrieved. The correspondence between the measured resonance spectrum and the ground state spin transitions, presented in Section 3.4, is represented in Fig. 4.13.

Following the discussion of the ground state levels in Chapter 3, the Zeeman splitting shifts the $m_s = \pm 1$ manifolds away from each other. Particular care was devoted to aligning an external magnetic field $\vec{B}_{ext}$ with the NV centre axis, with help of an external coil, to minimise mixing of the unperturbed ground state eigenvectors and causing the observed symmetric separation between the transition groups $(1, 2, 3)$ and $(4, 5, 6)$. Given the two central hyperfine dips in the ODMR spectrum of Fig. 4.13 are located at $\nu_2 = (2822.5 \pm 0.2)$ MHz and $\nu_5 = (2934.4 \pm 0.2)$ MHz and the Zeeman coupling constant is $\mu_B g^{\parallel} = 2.803$ MHz G$^{-1}$, we have estimated an axial B-field of $B_z = 19.96$ G for the presented dataset.

### 4.3.2 Coherent Control of Spin Transitions

The electronic-nuclear spin states $(m_s = -1, m_I = 0)$ and $(m_s = 0, m_I = 0)$, constitute the basis of the matter qubit of this experimental work and the central resonance dip $(m_I = 0)$ of the $m_s = 0 \leftrightarrow m_s = -1$ transition is used for coherent driving of the qubit. The Bloch sphere trajectory of the driven electronic spin state can be described as a rotation around an axis $\vec{\Omega} = (0, \Omega_0, \delta)$ by an angle [5] $\theta = \left|\vec{\Omega}\right| t$ (see Section 1.2.3), defined by the Rabi frequency $\Omega_0$ and the detuning $\delta$ (illustrated in Fig. 4.14 a). The altitude of the rotation axis is given by $\varphi = \arctan(\delta/\Omega_0)$ rad. It becomes then clear that a large detuning lifts the rotation axis away from the Bloch sphere equator, which is undesirable when trying to carry a state evolution from $m_s = 0$ to $m_s = -1$, as a full population inversion becomes impossible. This aspect is illustrated in Fig. 4.14 b, where the maximal possible population inversion, corresponding to $\sqrt{\Omega_0^2 + \delta_i^2}t = \pi$, is plotted for different detuning values.

Generally, the NV centre is found in an incoherent superposition of nuclear spin populations, which due to the hyperfine splitting $A_{gs}^{\parallel} = (1.19 \pm 0.02)$ MHz have different detunings $\delta_i$ and therefore distinct trajectories upon driving by the same microwave field. As an example, setting

[5] Note that the angle of rotation in the Bloch sphere is half of the corresponding algebraic angle, i.e. in the Bloch sphere two orthogonal vectors ($\langle \nu_1 | \nu_2 \rangle = 0$) are collinear but point in opposite directions.

$\delta = 0$ for the $m_I = 0$ population, results in the following rotation axis and respective angles:

$$\begin{array}{lll} \text{Nuclear pop.} & \text{Rotation axis} & \text{Rotation angle} \\ m_I = -1 & \vec{\Omega}_1 = (0, \Omega_0, +A_{HF}) & \theta_1 = \sqrt{\Omega_0^2 + \delta^2}\, t \\ m_I = 0 & \vec{\Omega}_2 = (0, \Omega_0, 0) & \theta_2 = \Omega_0\, t \\ m_I = +1 & \vec{\Omega}_3 = (0, \Omega_0, -A_{HF}) & \theta_3 = \sqrt{\Omega_0^2 + \delta^2}\, t \end{array} \tag{4.21}$$

as schematically illustrated in Fig.4.14 c. The transfer of the electronic spin from the $m_s = 0$ to $m_s = -1$, in a nuclear spin mixture, can be suitably described by adapting Eq. 1.11:

$$P_e(t) = \sum_{i=1,2,3} w_i \frac{\Omega_0^2}{\Omega_0^2 + \delta_i^2} \sin^2\left(\sqrt{\Omega_0^2 + \delta_i^2}\, t/2\right) \tag{4.22}$$

$P_e(t)$ is the population in the excited state (e.g. $m_s = -1$) and $w_i$ are the nuclear spin populations.

To quantify the accuracy of the electronic spin control, the probability to induce a full spin-flip, $F_\pi$, through a $\pi$-rotation, or equivalently the fidelity of a NOT gate, is taken as a figure of merit. Fig. 4.14 d shows the fidelity of a $\pi$-rotation as a function of the Rabi frequency and the $m_I = 0$ nuclear spin population (assuming pop.$(m_I = \pm 1) = (1 - \text{pop.}(m_I = 0))/2$), according to Eq. 4.22. For the instance where no initialisation routine is realised, the nuclear populations are fully thermally mixed ($\Delta E >> k_B T \implies w_1 = w_2 = w_3 = 1/3$) , both at room temperature and under 4 K cryogenic conditions. It becomes apparent from the graph how the initialisation of the nuclear spin into $m_I = 0$ benefits the fidelity of the spin control, where a dashed line identifies the nuclear initialisation fidelity reached in this work ($83.7 \pm 2.3\%$) - see Chapter 5.

Coherent driving between $m_s = 0$ and $m_s = -1$ is illustrated in Fig. 4.14 e, for a thermally mixed nuclear spin population. This measurement comprised an initialisation step into $m_s = 0$ with green light, followed by a microwave pulse of arbitrary duration $\tau$ and a final resonant readout. The PSB readout fluorescence is plotted against the spin driving time $\tau$, showing Rabi nutations over two periods with negligible damping. The non-unity contrast (the photoluminescence has a fixed offset) is mainly due to the imperfect initialisation with off-resonant pumping. A Rabi frequency of $2\pi \cdot 8.93 \pm 0.02$MHz (spin-flip time of 56ns) was attained, corresponding to a NOT gate fidelity $F_\pi = 96.3 \pm 0.1\%$. The same driving field yields $F_\pi = 99.1 \pm 0.1\%$, when the nuclear spin is initialized with a fidelity of $83.7 \pm 2.3\%$, following the experimental prescription described in Section 5.2.1.

The dependence of the Bloch trajectories on the nuclear state hints at the possibility of

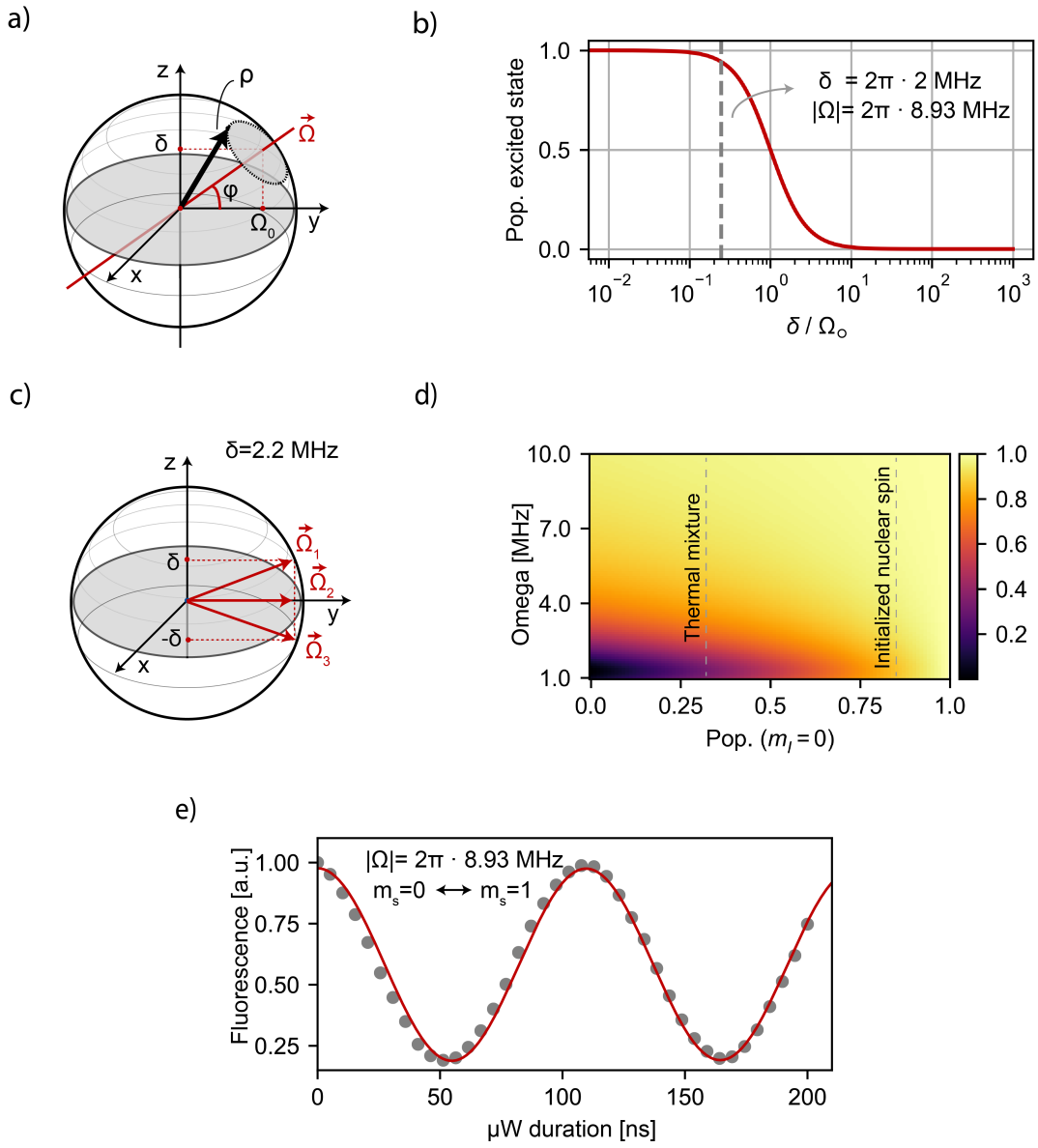


**Figure 4.14: Electronic spin dynamics. a)** Spin state trajectory in the Bloch sphere upon driving by a microwave field of duration $t$. The state vector $\rho$ rotates by an angle $\theta = \sqrt{\Omega_0^2 + \delta^2}t$, around the axis $\vec{\Omega} = (0, \Omega_0, \delta)$, for a Rabi frequency $\Omega_0$ and detuning $\delta$. **b)** Probability of inducing a full spin-flip in a single transition with a $\pi$-rotation, starting in the ground state $m_s = 0$, as a function of the detuning normalized to the Rabi frequency. **c)** Representation of the rotation axis for each of the three nuclear spin populations $m_I = 0, \pm 1$. **d)** Probability of inverting the electronic spin population with a $\pi$-rotation, for an arbitrary nuclear spin population pop$(m_I = 0)$ and pop.$(m_I = +1)$ = pop.$(m_I = -1)$ **e)** Coherent driving of the electronic spin with a spin-flip time of 56 ns, showing no signs of decoherence within the measurement time. The error bars due to shot noise are smaller than the symbols.

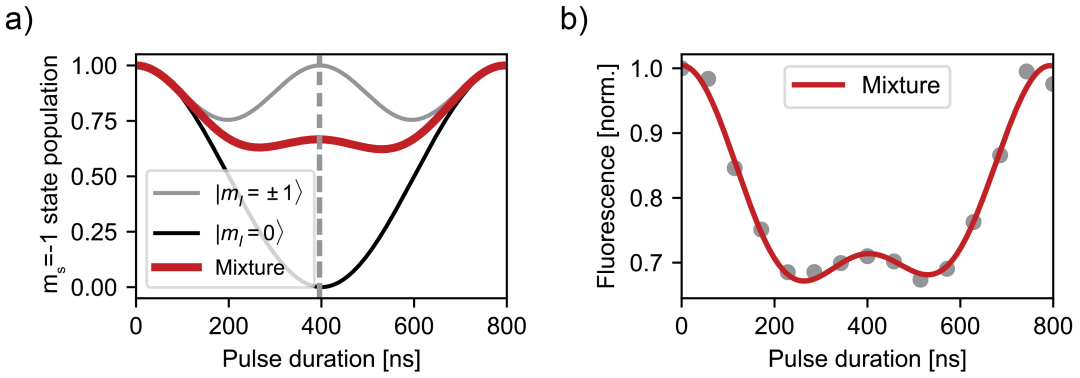


**Figure 4.15: Implementation of a CNOT gate**. The electron spin is the target qubit and the nuclear spin is the control, such that an electronic spin flip is realised if the nuclear spin state is $m_I = 0$. **a)** Evolution of the electronic spin between $m_s = -1$ and $m_s = 0$, for the $m_I = 0$ and $m_I = \pm 1$ nuclear populations, due to driving by a microwave pulse with $\Omega_0 = \sqrt{1/3}\, A_{gs}^{\parallel}$. The red line shows the evolution of a (thermal) balanced mixture between the three nuclear states. For a pulse duration $\tau = 397$ ns, the described CNOT gate is realised. **b)** Measured fluorescence corresponding to the Rabi driving of the electronic spin transition $|0\rangle \rightarrow |-1\rangle$, for a thermal mixture of nuclear states, setting the microwave power to $\Omega_0 = \sqrt{1/3}\, A_{gs}^{\parallel}$.

realizing conditional quantum operations. Particularly, it is possible to implement a CNOT gate targeting the electronic spin, conditional on the nuclear state. If $\delta$ and $\Omega_0$ are chosen such that the rotation angle $\theta_2 = \pi$, which means the $m_I = 0$ population undergoes a full flip, and $\theta_1 = \theta_3 = 2\pi$ , implying the $m_I = \pm 1$ populations are left unchanged, then the intended CNOT is realised. Plugging these constraints into the rotation angles defined in Eq. 4.21, implies the following relation between $\delta$ and $\Omega_0$:

$$\begin{aligned} \theta_2 = \Omega_0 t = \pi \quad \wedge \quad \theta_1 = \theta_3 = \sqrt{\Omega_0^2 + \delta^2}\, t = 2\pi \\ \Longrightarrow \qquad \Omega_0 = \sqrt{\tfrac{1}{3}}\, \delta \end{aligned} \tag{4.23}$$

For $\delta = A_{gs}^{\parallel} = (1.19 \pm 0.02)$ MHz, as estimated from the ODMR spectrum, choosing $\Omega_0 = 1.26$ MHz or a spin-flip time of 395ns, realizes the CNOT operation. The simulation of the $m_s = -1$ population evolution for such pulse is illustrated in Fig. 4.15 a and the corresponding experimental data is presented in Fig. 4.15 b, with $\Omega_0 = 1.269$ MHz and a CNOT gate fidelity $F \geq 0.99$.

To estimate the $T_2^*$ spin dephasing time of the NV centre, a Ramsey sequence $R_y(\pi/2) - \tau - R_y(\pi/2)$, where $R_y(\pi/2)$ is a rotation of the spin qubit by $\pi/2$ in the Bloch sphere and $\tau$ indicates a waiting time for the system to precess freely, was performed with a

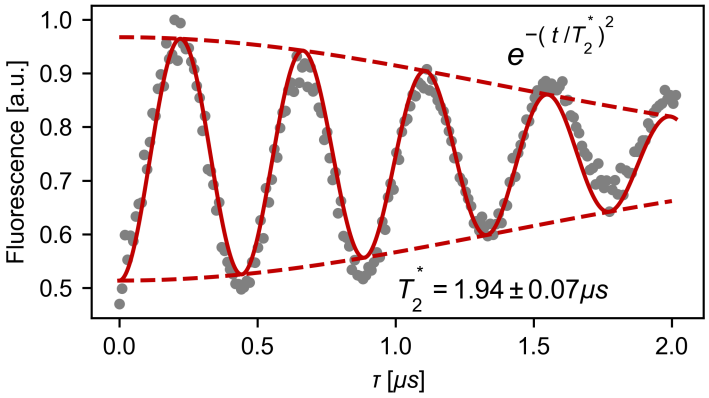


**Figure 4.16: Retrieval of $T_2^*$ by Ramsey sequence on electron spin.**

perfectly mixed nuclear spin population. The Gaussian fit to the decay of the Ramsey fringes, depicted in Fig. 4.16, yields $T_2^* = 1.94 \pm 0.07$ µs. As made clear ahead this is long enough to perform several entanglement-generation iterations. Nonetheless the dephasing due to the spin bath can be largely suppressed by using isotopically purified samples [87] and application of dynamical decoupling techniques [29], reaching a coherence time of several milliseconds, considerably above the time duration of the entanglement generation block of the experimental sequence (350 ns), supporting the possibility to scale the system to multi-photon entanglement.

## 4.4 Time-to-Polarisation Conversion

In this Section the time-to-polarisation conversion (TPC) apparatus is described along with its operation. The algorithm used to retrieve the interferometer phase and associated errors are presented. Finally, the role of the TPC in the tomography of the polarisation qubits is explained.

### 4.4.1 Setup Description and Operation

The entanglement generation scheme proposed and verified in this work relies on the conversion of a photonic qubit between a time-bin $\{E, L\}$ and a polarisation basis $\{H, V\}$, as introduced in Section 1.2.2:

$$\psi = |E\rangle + e^{i\varphi} |L\rangle \quad \rightarrow \quad \tilde{\psi} = |H\rangle + e^{i\varphi} |V\rangle \tag{4.24}$$

The setup which realizes the conversion and photon detection is represented in Fig. 4.17. The ZPL luminescence is filtered by a Glan-Taylor polariser (Thorlabs GT-10A), together with a zero-order polymer quarter-wave plate (QWP Thorlabs WPQ10ME-633) and half-wave-plate (HWP Thorlabs WPH10ME-633), which remove the laser light scattered off the diamond surface and transmit the ZPL photons. The clean ZPL signal then serves as input to a Mach-Zehnder type interferometer with unbalanced polarised arms, where the long path carries H-polarised light and the short path is V-polarised. At the first free-space polarising beam splitter (PBS) the ZPL signal splits equally between the two arms and is then coupled into polarisation-maintaining-fibres (Nufern PM630HP) with lengths of 55 m and 2 m, attached rigidly to an integrated polarising-beam-splitter (PBS, OZ Optics), on which the H- and V-paths are recombined. Due to poorer performance of the PBSs in reflection, with extinction ratios below 20 dB and above 30dB in transmission, the paths are arranged symmetrically such that each beam is reflected once and transmitted once. A length of PM fibre (2 m), also attached to the integrated PBS, leads the recombined wavepackets towards the detection stage, which performs polarisation measurements in two basis (e.g. D/A and R/L)[6] simultaneously. Because the basis pairs are in quadrature with respect to each other, the detection section of the setup is referred to throughout this thesis as quadrature readout stage (or tomography box). The 55 m clew of PM fibre was wound up around a 3 kg aluminium spool, intended as a thermal anchor. Additionally a double layer plexiglas enclosure was placed around the spool to further damp acoustic and thermal perturbations.

The quadrature readout stage is composed of four single-photon-detectors(Excelitas SPCM-AQRH) specified with low dark counts ($< 50$ cs$^{-1}$), each one associated with a

[6] $D(A) = \frac{1}{\sqrt{2}}(H + (-)V), \quad R(L) = \frac{1}{\sqrt{2}}(H + (-)e^{i\pi/2}V)$

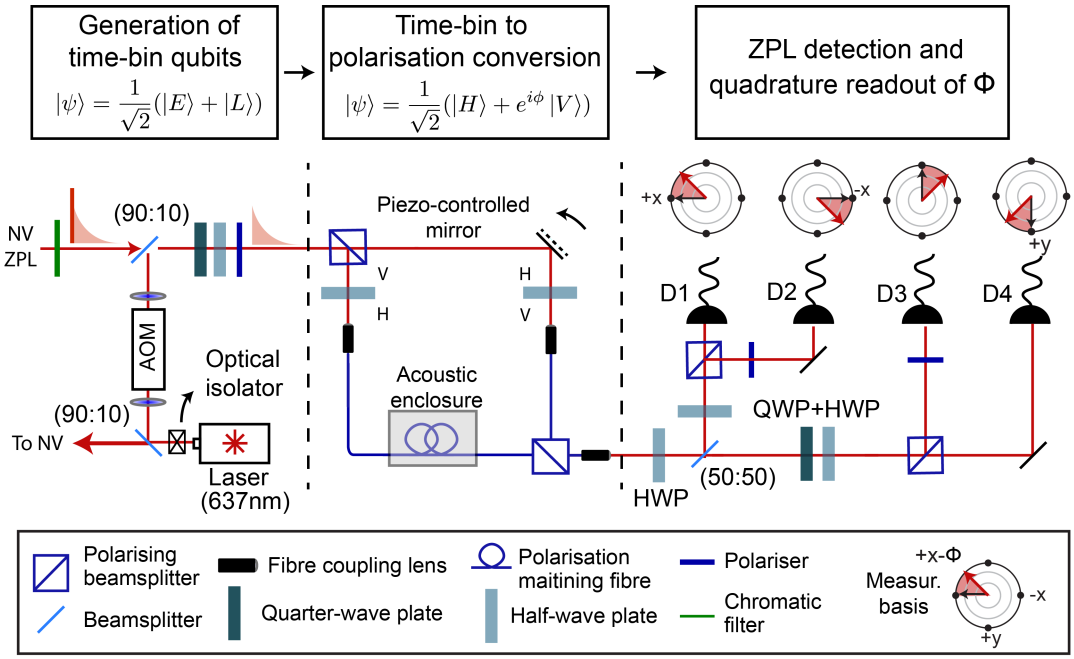


**Figure 4.17: Time-to-polarisation converter (TPC) and detection stage.** An unbalanced Mach-Zehnder interferometer with polarised arms performs the conversion between a time-bin and a polarisation basis. The polarisation qubits are then characterised in the tomography box, composed of 4 detectors performing projective measurements onto the D,A,R,L polarisation states. A piezo-controlled mirror is used to randomise the interferometer phase, as discussed in detail in Section 4.4.2.

polarisation projective measurement, set by a QWP+HWP combination. Zero-order-polymer waveplates (Thorlabs) were employed and as indicated in Fig. 4.17. The reflected arm of each PBS (Thorl. PBS202) is further filtered by a polariser, to compensate for the poor extinction ratio in reflection ($<$ 20 dB). The interferometer phase $\varphi$ was monitored by sending a probing beam, sampled out of the red laser used also for initialisation and resonant readout of the NV, modulated by an AOM (Gooch and Housego AOM 3350) which was transmitive only between entangling runs, such that ZPL photons do not merge with the probing field. An average of 0.5 $\mathrm{Mcs}^{-1}$ probing photons per detector was used. The resulting interference fringes, when measured in two quadratures, reveal unambiguously the value of $\varphi$. The algorithm for phase retrieval is discussed in Section 4.4.2.

As mentioned in Section 2.3, the qubit conversion involves two tasks: (1) rotation of the early (late) bin into H(V)-polarised light and (2) erasure of the time separation between the two wavepackets. In the coming paragraphs it is shown how the evolution of the time-bin wavepacket through the interferometer realizes these two tasks.

Consider a general time-bin qubit, as input of the converter, resulting from the first stage of

the entanglement protocol, with the two wavepackets (E,L) emitted by the NV centre at $t = t_1$ and $t = t_2$ respectively, in a diagonal polarisation state:

$$\left|\psi_{in}\right\rangle = (\alpha \left|t_1\right\rangle + e^{i\varphi}\beta \left|t_2\right\rangle) \otimes \frac{1}{\sqrt{2}}(\left|H\right\rangle + \left|V\right\rangle) \tag{4.25}$$

The H-terms of the superposition travel through the long path for a duration $t = t_L$ accumulating a phase $\varphi_L$ and the V-components through the short arm for $t = t_S$ associated with a phase $\varphi_S$. The photonic state at the output of the converter is:

$$\begin{aligned} \left|\psi_{out}\right\rangle \quad = \quad & \tfrac{1}{\sqrt{2}}(\alpha e^{i\varphi_S} \left|t_1 + t_S\right\rangle \left|V\right\rangle + \alpha e^{i\varphi_L} \left|t_1 + t_L\right\rangle \left|H\right\rangle \\ & + \beta e^{i\varphi_S + \varphi} \left|t_2 + t_S\right\rangle \left|V\right\rangle + \beta e^{i\varphi_L + \varphi} \left|t_2 + t_L\right\rangle \left|H\right\rangle) \end{aligned} \tag{4.26}$$

where the ket associated with time contains an indication of both the time of emission $(t_1,\ t_2)$ and time of propagation through the converter $(t_S,\ t_L)$. By imposing the condition that the time difference in propagation through the converter arms is the same as the time difference in emission of the wavepackets $t_L - t_S = t_2 - t_1$ and, for convenience, redefining the time coordinates $\Delta t = t_2 - t_1 = t_L - t_S$ and $t_0 = t_1 + t_L = t_2 + t_S$, the output state can be expressed as:

$$\begin{aligned} \left|\psi_{out}\right\rangle \quad = \quad & \tfrac{1}{\sqrt{2}}(\alpha \ \left|t_0\right\rangle \left|H\right\rangle + \ e^{i(\varphi - \Delta\varphi)}\beta \left|t_0\right\rangle \left|V\right\rangle + \\ & e^{-i\Delta\varphi}\alpha \left|t_0 - \Delta t\right\rangle \left|V\right\rangle + e^{i\varphi}\beta \left|t_0 + \Delta t\right\rangle \left|H\right\rangle) \end{aligned} \tag{4.27}$$

where a global phase term $e^{i\varphi_L}$ has been factored out and$\Delta\varphi = \varphi_L - \varphi_S$ is the phase difference between the two paths of the TPC converter. It becomes clear that the converted photonic state unfolds in three time-separated wavepackets $\left|t_0 - \Delta t\right\rangle, \left|t_0\right\rangle, \left|t_0 + \Delta t\right\rangle$ corresponding to three arrival times at the detectors. The upper line of Eq. 4.27 contains the terms arriving within the central time bin, whereas the terms of the bottom line are associated with an early arrival time $(t_0 - \Delta t)$ and a late one $(t_0 + \Delta t)$. Photon-clicks in the central arrival time correspond to path-erasing events, as the information whether the photon originated from the early or the late NV centre emission is erased. By post-selecting these photon-clicks, the state $\left|\psi_{out}\right\rangle$ can be simplified to:

$$\left|\tilde{\psi}_{out}\right\rangle = (\ \alpha \left|H\right\rangle + e^{i(\varphi - \Delta\varphi)}\beta \left|V\right\rangle\ ) \otimes \left|t_0\right\rangle \tag{4.28}$$

which encodes the desired polarisation qubit. In other words, within this subspace, the interferometer has realised the intended time-to-polarisation conversion, $\left|E\right\rangle \rightarrow \left|H\right\rangle$ and $\left|L\right\rangle \rightarrow \left|V\right\rangle$. It should be noted that only half of the events fall within the central bin $\left|t_0\right\rangle$. The other half, associated with $\left|t_0 - \Delta t\right\rangle$ and $\left|t_0 + \Delta t\right\rangle$, are path-revealing events, for which it is

known which emission, early or late, originated each photon and the interferometer does not work as a time-to-polarisation converter on the qubit space. These remain nonetheless useful as they contain information about the amplitudes $\alpha$ and $\beta$, allowing to perform tomographic measurements on the $\hat{\sigma}_z$-basis. If a higher conversion yield is desired, a Pockels cell could be used dynamically to rotate the early bin into $H$ polarisation and the late into $V$, before entering the interferometer. In this way, the time-to-polarisation conversion would be successful for all detection events. This is a possible outlook for future work.

The phase associated with the interferometer $\Delta\varphi$ is time-dependent. A rough estimate of the sensitivity of the phase to environmental parameters is provided in the next section. Even though all experimental cycles produce the same time-bin qubit (in a spin-time entangled state), the time-varying $\Delta\varphi(t)$ implies that the produced spin-polarisation entangled state will vary among different cycles. The validation of entanglement by measurement of the photon polarisation therefore requires the value of $\Delta\varphi(t)$ to be known at all times. As mentioned, keeping track of this value is the role of the tomography box. Similarly to using a Pockels cell to boost the entangling rate, locking the interferometer´s phase (e.g. to a Fabry-Perot cavity), would result in all detection events being associated with the same spin-polarisation state, constituting thus a possible future improvement to the current setup.

An alternative design for the interferometer was considered during its assembly, which is worth of note. The phase monitoring or, alternatively, phase locking could have been avoided altogether, if the interferometer was operated in a double-pass scheme. Thereby, a single excitation pulse would pass through the unbalanced interferometer to produce two consecutive excitations. The two resulting fluorescence time-bins would go through the interferometer in the opposite direction, cancelling accumulated phase differences. This elegant approach was not pursued, due to residual backscattering of the excitation pulses into the detectors, produced during propagation in the optical fibre. For a free-space interferometer or in case better optical fibres become available, this design could be of interest.

### Setting up the Tomography Box

The tomography box is composed of four single-photon detectors, forming two pairs $D_1/D_2$ and $D_3/D_4$ which, ideally, implement the quadrature basis pair $D/A$ and $R/L$. This part of the setup is confined in a box to prevent pollution of the ZPL signal by stray light. The ZPL beam is divided with a 50:50 beam splitter, such that one beam is directed towards the $D/A$ stage and the other to $R/L$. Preparing the detection stage to measure in quadrature is routinely done before each experimental run. The steps to ensure its correct functioning are described here, making reference to Fig. 4.18:

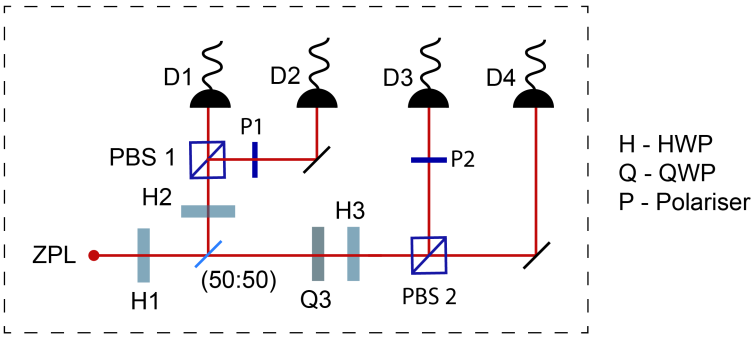


**Figure 4.18:** 4-detector stage, used to readout the interferometer phase $\varphi$ and perform quantum tomography on the photonic qubits. The ZPL beam is split in half to enable simultaneous characterisation in two basis pairs, D/A and R/L. The quarter-wave and half-wave plate (QWP+HWP) combinations allow to set an arbitrary measurement basis in each pair of detectors.

1. Block the long arm of the interferometer, such that only V-polarised light emerges from the interferometer output. Manually adjust the angle of half-wave plates H1 and H2 to produce maximum counts in detector D1. This ensures that the H(V) axis of the converter PM fibre correspond to P(S) polarisation with respect to the beam splitter (BS) surface. Misalignment of the optical axis of the fibre and the BS results in undesired ellipticity on each of the short- and long-arm beams, corresponding to V and H polarised outputs.

2. With maximum intensity in D1, rotate polariser P1 till the counts in D2 are minimized. This polariser setting compensates for leakage of the PBS in reflection. Sweeping the angle of H2 leads to anti-correlated sinusoidal signals in D1 and D2. Typical visibilities [7] are in the range $V = 99.0 - 99.5\,\%$, when both H1 and P1 are optimally set.

3. Set the angle of H2, such that D1 and D2 register the same intensity. At this point, D1/D2 measure in the $D/A$ basis.

4. Remove quarter-wave plate Q3 and follow the same steps for detectors D3 and D4, such that they measure in the D/A basis.

5. Still using the H-polarised output of the converter, insert Q3 and rotate it, till the H-beam is equally split between D3 and D4. This sets D3/D4 to measure in the R/L basis. It can be analytically checked that any other Q3 angle leads to an unequal distribution between D3/D4 corresponding to measuring in a basis other than R/L.

[7] Visibility: $V = (I_{max} - I_{min})/(I_{max} + I_{min})$.

6. Unblock the V-polarised arm of the converter and, for consistency, check whether the D/R and A/L signals have a $\pi/2$ phase difference, i.e. maximum photon counts (max.) in D and minimum (min.) in A correspond to a balanced distribution of counts in R and L at an approximate rate of $0.5 \times (\text{max} + \text{min})$.

Deviations from the perfect basis (D/A, R/L) setting are accounted for in data analysis. The procedure is discussed in Section 4.4.2.

### 4.4.2 The Interferometer Phase $\Delta\varphi$

The high susceptibility of the interferometer to the environment requires its phase to be continuously tracked. In this Section, an illustrative estimate of this susceptibility is provided along with a description of the protocol used to read out the phase $\Delta\varphi(t)$.

#### Susceptibility of the Interferometer Phase and Passive Stabilization

The 53 m arm length difference of the interferometer makes it particularly susceptible to mechanical (e.g. acoustic and thermal) and spectral (e.g. fluctuations in the laser frequency) changes. A simple model is considered here to provide an insight into how the output polarisation is sensitive to the environment. When injecting diagonal polarised light, $|\psi_{in}\rangle = |H\rangle + |V\rangle$ , in the interfermeter it splits equally between the two arms and emerges in a new polarisation state, $|\psi_{out}\rangle = |H\rangle + \exp(i\Delta\varphi)\,|V\rangle$, where $\Delta\varphi = \Delta\varphi(t)$ is the phase difference accumulated in the propagation through the two paths. Assuming that within the time of propagation (262 ns) the optical fiber properties remain constant, $\Delta\varphi(t)$ can be expressed as:

$$\Delta\varphi(t) = \frac{2\pi}{\lambda_0} n(\lambda, T) L(T) \tag{4.29}$$

$\lambda_0$ is the wavelength of the optical field; $n(\lambda, T)$ is the average refractive index of the fibre, dependent on wavelength and temperature; and $L$ is the arm length difference, also a function of temperature through its thermal expansion coefficient. The thermally induced phase variation can be estimated by considering a first-order polynomial expansion of $\Delta\varphi(t)$:

$$\delta(\Delta\varphi) = \frac{\partial\Delta\varphi}{\partial T}\delta T = \frac{2\pi}{\lambda_0} L \left( \frac{\partial n}{\partial T} + n\frac{1}{L}\frac{\partial L}{\partial T} \right) \delta T \tag{4.30}$$

where the thermo-optic coefficient is $\partial n/\partial T = 9.2 \times 10^{-6}\ \text{K}^{-1}$, as extrapolated to our system from to Ref. [142] where it refers to a Corning SMF-28 fibre. The thermal expansion coefficient is $1/L \cdot \partial L/\partial T = 0.4 \times 10^{-6}\ \text{K}^{-1}$ [143] and the refractive index of the fibre (fused silica) was set to $n = 1.4$. Taking these into account, for $\lambda_0 = 637$ nm, the phase change due to temperature

can be approximate by $\delta(\Delta\varphi) = 5006.0\ \mathrm{K}^{-1}\,\delta T$, for which a meager 1.255 mK variation leads to a $2\pi$ shift. Even though a quantitative estimate of the effect of acoustic noise in the interferometer was not carried out, it is worth noting that the output signal was clearly influenced by noise in the room. The apparent susceptibility to acoustic and thermal noise is the reason why attempts were made to passively stabilize the interferometer by employing an enclosure around the fibre spool.

Similarly, the phase change due to a shift of the light frequency $\delta f$ can be estimated from its first-order Taylor polynomial:

$$\delta(\Delta\varphi) = \frac{\partial\Delta\varphi}{\partial f}\,\delta f = \frac{2\pi L}{c}\left(n - \lambda_0\frac{\partial n}{\partial\lambda}\right)\delta f \tag{4.31}$$

where $\partial n/\partial\lambda = -2.9\times10^{-4}\ \mathrm{m}^{-1}$ is the value for chromatic dispersion of fused silica [144]. Estimating Eq. 4.31 for $\lambda_0 = 637$ nm and $n = 1.4$ yields $\delta(\Delta\varphi) = 1.52\times10^{-6}\,\delta f$; for which a frequency displacement of 4.12 MHz produces a $2\pi$ shift. In other words the interferometer has a free-spectral-range of 4.12 MHz. Fluctuations in the frequency or linewidth of the laser in the order of MHz occurring on a timescale smaller than the phase-readout integration time (1ms), are therefore expected to cause a reduction of the visibility [8] of the interferometer output. This effect is displayed in Fig. 4.19 which shows a test measurement where the visibility in one of the detectors is plotted over time. When the path of the red laser beam to the NV centre is blocked avoiding back-reflections, the interferogram visibility displays improved stability. For that reason, despite the 30 dB native isolator, a second optical isolator (Thorl. IO-3-633-LP) had to be used in the red laser output, as indicated in Fig. 4.17.

### Readout of the Interferometer Phase $\Delta\varphi(t)$

The retrieval of the interferometer phase $\Delta\varphi(t)$ from the single-photon-detectors $D_1$, $D_2$, $D_3$ and $D_4$ relies on tracking the respective interferogram signals $D_1(t)$, $D_2(t)$, $D_3(t)$ and $D_4(t)$, where each detector performs a projective measurement in the polarisation space, as determined by the QWP+HWP configuration in front of it. Note that the retrieval of a single-valued phase $\Delta\varphi$ requires at least two non-colinear projective measurements on the interferometer output, which is why we use several detectors, as will be made clear with the discussion ahead. Each signal $D_i(t)$ is then normalised into $\tilde{D}_i(t)$, with a co-domain in the range $[0, 1]$. Then the pairs $[\tilde{D}_1(t), \tilde{D}_2(t)]$, $[\tilde{D}_3(t), \tilde{D}_4(t)]$ are combined to generate the signals $S_{1,2}$ and $S_{3,4}$, respectively, that hold a simple dependence on the interferometer phase $\Delta\varphi(t)$, which is at last inverted to yield $\Delta\varphi(t)$.

[8] Visibility: $V = (I_{max} - I_{min})/(I_{max} + I_{min})$.

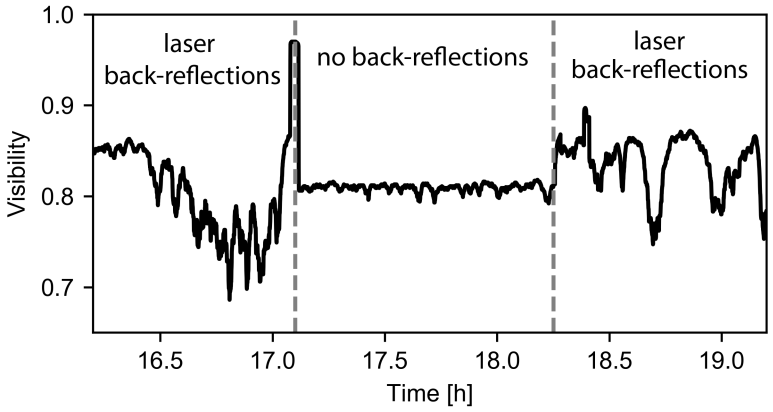


**Figure 4.19: Visibility of the interferogram over time in detector $D_1$.** When the laser path to the NV centre is blocked and the respective back-reflections avoided (middle section of the graph), the interferogram´s visibility exhibits improved stability. The left and right regions on the other hand show the deteriorated performance due to back-reflections.

The data analysis for retrieval of the interferometer phase $\Delta\varphi(t)$ can be summarised by the following sequence:

$$D_i(t) \;\rightarrow\; \tilde{D}_i(t) \;\rightarrow\; S_{ij}(t) \;\rightarrow \Delta\varphi(t) \tag{4.32}$$

This section walks through the quantitative details of the steps involved in this data processing chain.

Assuming that the detectors ($D_1, D_2, D_3$ and $D_4$) are set to measure in the basis pair $D/A$ and $R/L$ and the polarisation state of the interferometer output is $|\psi\rangle = |H\rangle + \exp(i\Delta\varphi(t))\,|V\rangle$, the expected photon counts as a function of the interferometer phase $\Delta\varphi$ are given by:

$$\begin{aligned} D_1 &= A_1/2(1+\cos(\Delta\varphi)) + B_1 \\ D_2 &= A_2/2(1-\cos(\Delta\varphi)) + B_2 \\ D_3 &= A_3/2(1+\cos(\Delta\varphi-\pi/2)) + B_3 \\ D_4 &= A_4/2(1-\cos(\Delta\varphi-\pi/2)) + B_4 \end{aligned} \tag{4.33}$$

where $A_i$ and $B_i$ are the amplitude and offset of each signal. During data analysis, each time-trace is normalized by subtraction of the offset and division by the respective amplitude (e.g $\tilde{D}_i = (D - B_i)/A_i$), to yield $\tilde{D}_1, \tilde{D}_2, \tilde{D}_3, \tilde{D}_4$. Determinaton of the $A_i, B_i$ coefficients for each channel is non-trivial, due to the presence of shot noise, which smudges the minimum and maximum allowed values, as shown in the data of Fig. 4.21. Therefore a careful analysis of the photon-count probability density function with $A_i$ and $B_i$ as variables, $PDF(s, A_i, B_i)$, where $s$ represents photon counts, was required for their determination.

By recording a signal $D_i(t)$ for several minutes, a probability density function (PDF) or

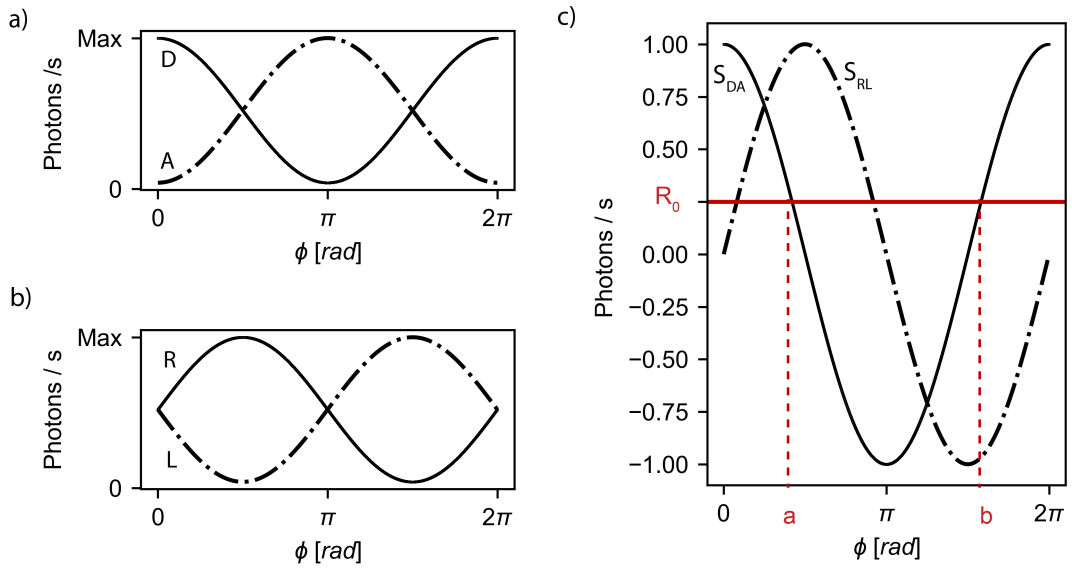


**Figure 4.20: Concept for retrieval of the interferometer phase** $\Delta\varphi$. The polarisation of the output $|\psi\rangle = |H\rangle + \exp(i\Delta\varphi(t))\,|V\rangle$, is measured in two simultaneous basis $\pi/4$ out of phase with respect to each other. **a)** Expected signal for detectors $D_1$ and $D_2$ as a function of $\Delta\varphi$, set to implement projective measurements onto states D (diagonal) and A (anti-diagonal). Both signals are normalised to produce $\tilde{D}_1$ and $\tilde{D}_2$ with a co-domain in the range $[0, 1]$, according to the procedure described in the main text. **b)** Expected signal for detectors $D_3$ and $D_4$, measuring in the R/L basis (right circular, left circular), respectively. These interferograms normalised into $\tilde{D}_3$ and $\tilde{D}_4$. **c)** Combined signals $S_{12}$ and $S_{34}$ as a function of $\Delta\varphi$, where $S_{12} = (\tilde{D}_1 - \tilde{D}_2)/(\tilde{D}_1 + \tilde{D}_2)$ and $S_{34} = (\tilde{D}_3 - \tilde{D}_4)/(\tilde{D}_3 + \tilde{D}_4)$. Note how an arbitrary readout signal $R_0$ is compatible with two possible phase values $a$ and $b$, when only one basis is considered. The readout in the second basis lifts the ambiguity and singles out one phase value. In this case if $S_{34} \geq 0$ ($\leq 0$), then $a$ ($b$) is the solution.

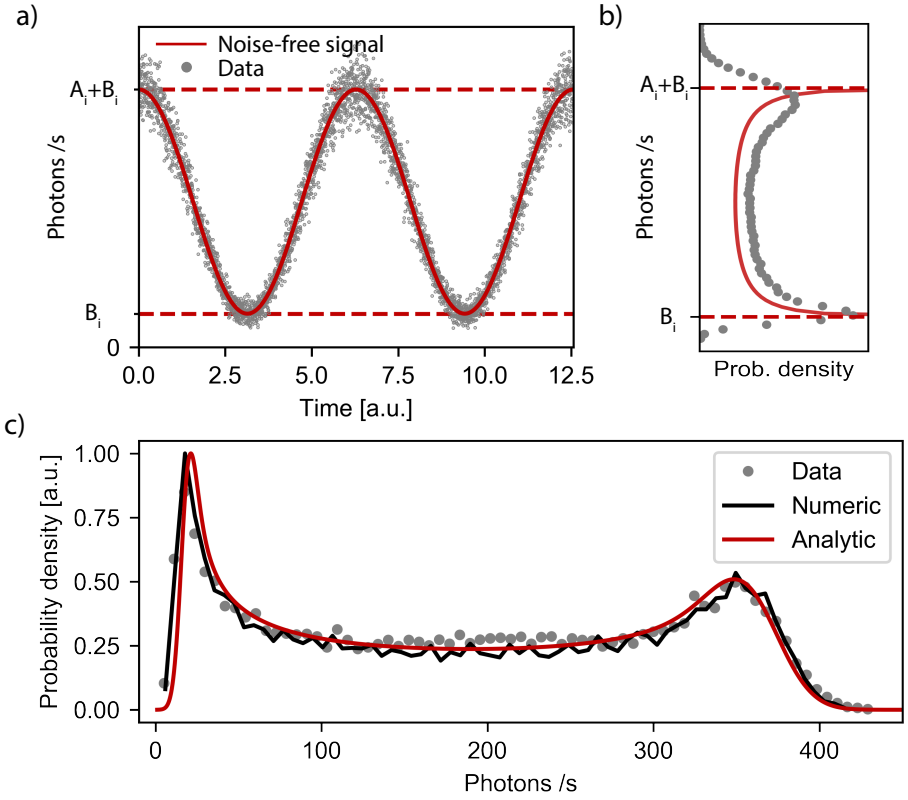


**Figure 4.21: Determination of the normalizing coefficients $A_i$ and $B_i$, corresponding to the amplitude and offset of the interferograms respectively, through the probability density function of the photon counts. a)** Time trace of an arbitrary single-photon-detector from the quadrature readout stage with the corresponding theoretical shot-noise-free curve. **b)** Histogram/probability density function (PDF) of the photon counts and corresponding PDF associated with the noiseless signal in red. The shot noise smears the edges of the distribution below $B_i$ and above $A_i + B_i$. **c)** Fit of the probability density function derived from a histogram of the photon counts. As the theoretical PDF is just a function of $A_i$ and $B_i$, the fit suffices to find the most likely $A_i$ and $B_i$ values to be used in the normalization: $\tilde{D}_1 = (D_1 - B_1)/A_1$. The experimental PDF corresponds to $A = 365 \pm 6$ and $B = 17 \pm 3$

histogram of the phase distribution is retrieved, as in Fig. 4.21 b. To ensure that $\Delta\varphi(t)$ covers the full phase space $[0, 2\pi]$, a piezo-controlled mirror in one arm of the interferometer was swept at 1Hz by approximately one $\lambda_0$. The corresponding theoretical PDF curve is determined by convolving the PDF of the noiseless sinusoidal signal $PDF_{\sin}$ with the shot noise Poissonian distribution, here approximated by a Gaussian $G(\mu, \sigma = \sqrt{\mu})$, with mean value $\mu$ and standard deviation $\sigma$:

$$\begin{aligned} PDF(s, A_i, B_i) &= (PDF_{\sin} \circledast G)(s) \\ &= \int_0^{+\infty} PDF_{\sin}(y, A_i, B_i)\, G(s-y, \sqrt{y})\, dy \end{aligned}$$

where (4.34)

$$\begin{aligned} G(\mu, \sigma) &= \tfrac{1}{\sigma\sqrt{2\pi}} \exp\left\{-\tfrac{1}{2}\left(\tfrac{x-\mu}{\sigma}\right)^2\right\} \\ PDF_{\sin}(s, A_i, B_i) &= \int_0^{+\infty} \tfrac{1}{\pi\sqrt{(-s+B_i)(s-B_i-A_i)}} \end{aligned}$$

The convolved function $PDF(s, A_i, B_i)$ was used to fit the histograms of each channel, exemplary shown in Fig. 4.21 c, corresponding to $A_i = 365 \pm 5$ and $B_i = 17 \pm 3$ in this particular example. The $A_i$ and $B_i$ values were then used to normalize the signals. Data sets corresponding to poor fits ($r^2 \leq 0.6$, where $r$ is the coefficient of determination [145]) were discarded. Typical values of the normalizing coefficients were in the range $A_i \in [350, 400]$ and $B_i \in [10, 20]$, depending on coupling of the probing field into the interferometer and the power of the probing field. To account for possible slow drifts of $A_i$ and $B_i$, data was bunched in intervals of 210 s and an evaluation of the normalizing coefficients was carried out for each.

At last, the normalized variables $\tilde{D}_i$ were used to define the combined signals $S_{12}$ and $S_{34}$, which hold a simple relation to the interferometer phase $\Delta\varphi(t)$:

| $S_{12}$ | $S_{34}$ |
|---|---|
| $S_{12} = (\tilde{D}_1 - \tilde{D}_2)/(\tilde{D}_1 + \tilde{D}_2)$ | $S_{34} = (\tilde{D}_3 - \tilde{D}_4)/(\tilde{D}_3 + \tilde{D}_4)$ |
| $S_{12} = \cos(\Delta\varphi)$ | $S_{34} = \sin(\Delta\varphi)$ |
| $\downarrow$ | $\downarrow$ |
| $\Delta\varphi_1 = \arccos(S_{12})$ | $\Delta\tilde{\varphi}_1 = \arccos(S_{34}) + \pi/2$ |
| $\Delta\varphi_2 = \Delta\varphi_1 + 2(\pi - \Delta\varphi_1)$ | $\Delta\tilde{\varphi}_2 = \Delta\tilde{\varphi}_1 + 2(3\pi/2 - \Delta\tilde{\varphi}_1)$ |

(4.35)

Inversion of the sinusoidal functions, establishes that the $S_{12}$ and $S_{34}$ readouts are compatible with two phase values each, as depicted in Fig. 4.20 c. The intersection between the pairs of allowed phase values $(\Delta\varphi_1, \Delta\varphi_2) \leftrightarrow (\Delta\tilde{\varphi}_1, \Delta\tilde{\varphi}_2)$ establishes the actual interferometer phase

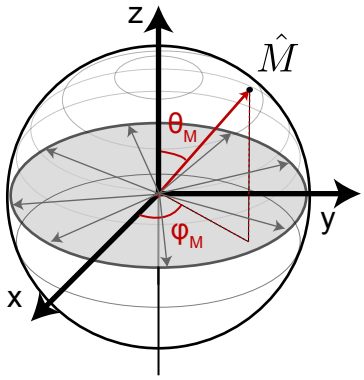


**Figure 4.22:** Depiction of an arbitrary projector $\hat{M}$ on the Bloch sphere, identifying the polar angle $\theta_M$ and the azimuthal angle $\varphi_M$.

$\Delta\varphi(t)$. Note that for optimal phase resolution the basis pairs, $[\tilde{D}_1(t), \tilde{D}_2(t)]$, $[\tilde{D}_3(t), \tilde{D}_4(t)]$, should lie in the equator of the Bloch-sphere in quadrature, i.e. at an angle $\pi/2$ with respect to each other; an exemplar arrangement would be the basis-pair D/A (diagonal/anti-diagonal) and R/L (right/left circular polarisation).

### Readout of the Interferometer Phase $\Delta\varphi(t)$ in an Arbitrary Basis Pair

For improved clarity in the coming mathematical expressions, the notation for the interferometer phase suffers a change from this point onwards: $\Delta\varphi(t)$ is referred to as $\varphi(t)$.

The phase retrieval protocol described so far assumes that the detectors can be set perfectly to measure in the desired basis D/A and R/L. Due to inaccuracies in the setting of the half and quarter-waveplates, this is not strictly true. The data analysis should therefore accommodate for deviations from the ideal D/A - R/L configuration by generalising to other choice of basis.

Consider the output of the interferometer, with phase $\varphi$, in a density matrix formulation, $\hat{\rho}$, and assume an arbitrary projective measurement $\hat{M}_i$ in detector $D_i$ along a unit-vector $\vec{n}_i$ in the Bloch sphere, specified by the polar angle $\theta_M$ and the azimuthal angle $\varphi_M$, as represented in Fig. 4.22:

$$\begin{aligned} \hat{\rho} &= \tfrac{1}{2}(Id + \cos(\varphi)\hat{\sigma}_x + \sin(\varphi)\hat{\sigma}_y) \\ \hat{M}_i &= \tfrac{1}{2}(Id + \vec{n}_i \cdot \vec{\sigma}) \end{aligned} \tag{4.36}$$

where $Id$ is the identity matrix, $\hat{\sigma}_i$ are the usual Pauli-matrices and $\vec{\sigma}_i = (\hat{\sigma}_x, \hat{\sigma}_y, \hat{\sigma}_z)$. The state of the interferometer output is presumed to lie in the equator of the Bloch sphere. The probability of projecting $\hat{\rho}$ onto $\hat{M}_i$ leads to the following photon-count in detector $i$:

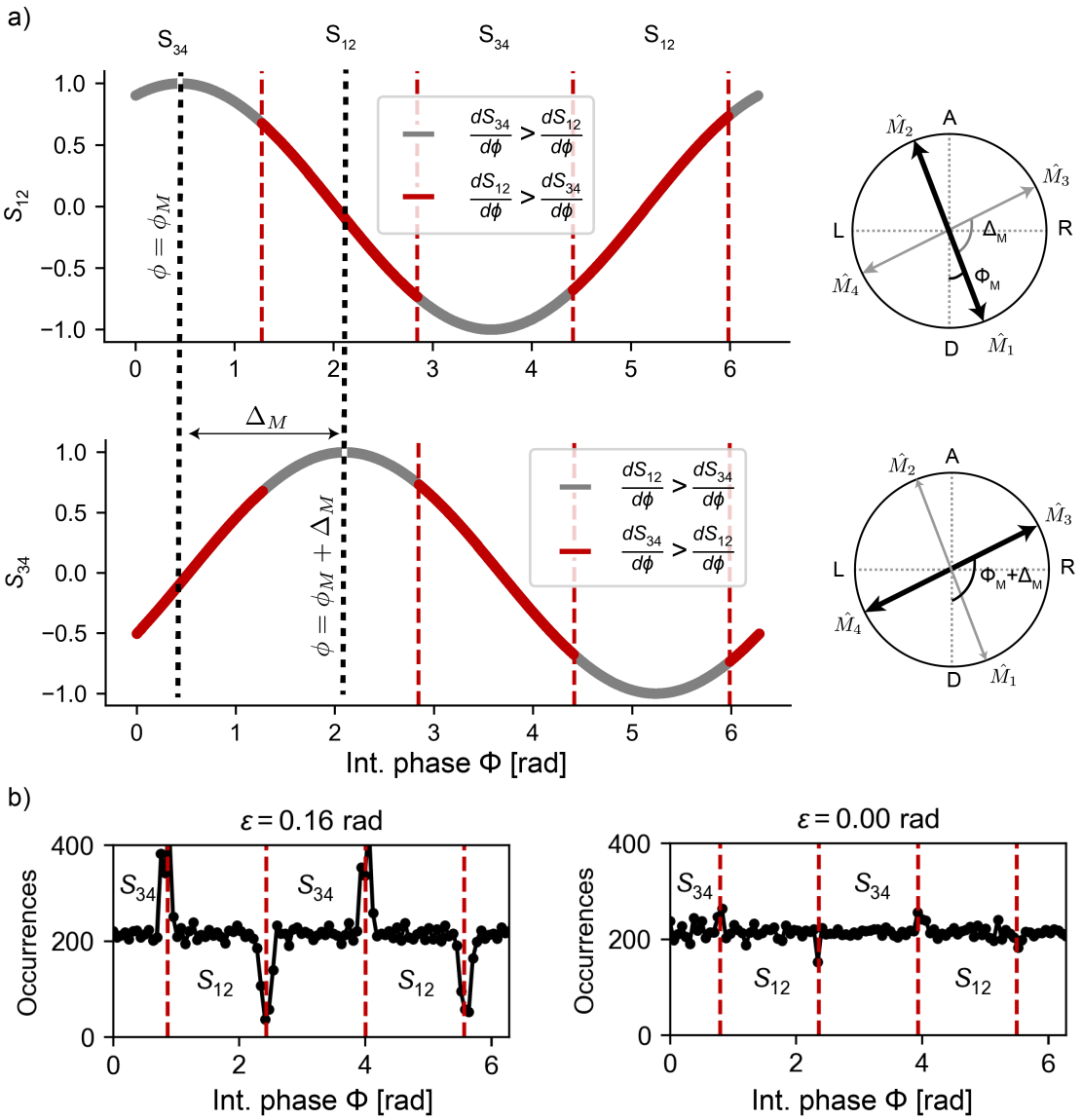


**Figure 4.23: Phase retrieval from an arbitrary selection of basis-pairs:** $\hat{M}_1 - \hat{M}_2$ and $\hat{M}_3 - \hat{M}_4$. **a)** Expected signals $S_{12}$ and $S_{34}$ for an arbitrary choice of basis pairs $(\hat{M}_1 \leftrightarrow \hat{M}_2)$ and $(\hat{M}_3 \leftrightarrow \hat{M}_4)$, showing in red the regions associated with lower phase error due to an higher derivative of the signal (as a function of $\varphi_M$). This condition sets which signal is used as the primary one, as labelled at the top of the figure and described in the main text. The diagrams on the right show a top-view of the Bloch sphere, with the corresponding projective states. **b)** Effect of a misestimate, $\varepsilon$, of $\Delta_{M,exp}$, with $\varepsilon = \Delta_{M,exp} - \Delta_M$ on the phase readout probability distribution, with dashed lines indicating the interface between areas where $S_{12}$ or $S_{34}$ are the primary signals. **Left)** $\varepsilon(\Delta_M) = 0.16$ rad leads to abnormal peaks/dips around the $S_{12}$ and $S_{34}$ boundary regions and the corresponding $\Delta_{M,exp}$ is discarded. **Right)** For $\varepsilon = 0$ rad the phase readout probability distribution becomes uniform.

$$\begin{aligned} D_i &\propto Tr(\hat{\rho}\hat{M}_i) \\ &= \tfrac{1}{2}(1 + \sin(\theta_M)\cos\big(\varphi - \varphi_M\big)) \end{aligned} \tag{4.37}$$

where $\vec{n}_i$ was expanded in its spherical coordinates [9]. If the projective vector $\hat{M}$ raises above or lowers below the equator, the interferogram is compressed by a factor $\sin(\theta_M)$. However the normalization of the photon counts $\tilde{D}_i = (D_i - B_i)/A_i$ removes the compression effect. Additionally, a variation of the azimuthal angle $\varphi_M$ produces a horizontal shift of the interferogram by $-\varphi_M$. As before, by redefining $S_{ij}$, a simple relation between signal and interferometer phase $\varphi$ ensues:

$$\begin{aligned} S_{12} &= (\tilde{D}_1 - \tilde{D}_2)/(\tilde{D}_1 + \tilde{D}_2) &&= \cos\big(\varphi - \varphi_M\big) \\ S_{34} &= (\tilde{D}_3 - \tilde{D}_4)/(\tilde{D}_3 + \tilde{D}_4) &&= \cos\big(\varphi - (\varphi_M + \Delta_M)\big) \end{aligned} \tag{4.38}$$

where $\Delta_M$ is the difference in azimuthal angle between the two basis-pairs. Fig. 4.23 a shows the expected signals for an arbitrary choice of basis and elucidates the definition of the angles. For clarity, the azimuthal angles of the projectors associated with $D_1$ and $D_2$ are $\varphi_M$ and $\varphi_M + \pi$; likewise, $D_3$ and $D_4$ concern $\varphi_M + \Delta_M$ and $\varphi_M + \Delta_M + \pi$. Inversion of the $S_{12}$, $S_{34}$ functions results in explicit expressions for $\varphi$:

$$\begin{array}{cc} S_{12} & S_{34} \\ \varphi_1 = \arccos(S_{12}) + \varphi_M & \tilde{\varphi}_1 = \arccos(S_{34}) + (\varphi_M + \Delta_M) \\ \varphi_2 = \varphi_1 + 2(\pi + \varphi_M - \varphi_1) & \tilde{\varphi}_2 = \tilde{\varphi}_1 + 2(\pi + \varphi_M + \Delta_M - \tilde{\varphi}_1) \end{array} \tag{4.39}$$

Once again the intersection between the pairs $(\varphi_1, \varphi_2) \leftrightarrow (\tilde{\varphi}_1, \tilde{\varphi}_2)$ is used to establish the actual value of interferometer phase $\varphi$.

Shot noise in the detectors time-trace contributes to uncertainty on the phase estimate. Small perturbations can be approximated by a first-order Taylor expansion, $\Delta\varphi = 1/(dS/d\varphi)\Delta S$. Thereby, regions with a small derivative $(dS/d\varphi)$ correspond to a large error, whereas a high derivative value translates into a small error. Therefore if $|dS_{12}/d\varphi| \geq |dS_{34}/d\varphi|$ then signal $S_{12}$ is primary, meaning it is used for the retrieval of the two possible phase values $\varphi_1$ and $\varphi_2$, whereas $S_{34}$ is secondary and employed to decide for one of them (and vice-versa). The regions where each signal is used as primary and the respective boundaries are given by $\varphi = \varphi_M + \Delta_M/2 + n \cdot \pi/2$ and represented in Fig. 4.23 with red dahsed lines. A more detailed discussion of these boundary regions and errors on the phase estimation is postponed to the next Section.

[9] In spherical coordinates, $(x, y, z) = \big(\sin(\theta_M)\cos(\varphi_M),\ \sin(\theta_M)\sin(\varphi_M),\ \cos(\theta_M)\big)$.

A perfect setting of the tomography waveplates would correspond to a difference of azimuthal angle between the basis pairs $D/A$ and $R/L$ of $\Delta_M = \pi/2$. A deviation from this configuration has to be accounted for during data analysis, through the inversion of $S_{1,2}$ and $S_{3,4}$ from equation 4.38, which requires choosing a value for $\Delta_M$. The procedure to establish the experimental $\Delta_{M,exp}$ is best understood by visualizing the effect of its misestimate $\varepsilon(\Delta_{M,exp})$ on the probability density distribution of the retrieved phase values $\varphi$, where $\varepsilon$ is defined as:

$$\varepsilon(\Delta_{M,exp}) = \Delta_{M,exp} - \Delta_M \tag{4.40}$$

$\Delta_M$ is the actual value (to be determined) of the difference in azimuthal angle between the basis pairs and $\Delta_{M,exp}$ is a trial value assumed for $\Delta_M$ in data analysis. In an ideal system all phase values $\varphi$ are equally probable. As soon as there is a mismatch, $\varepsilon \neq 0$, the PDF of retrieved phase values deviates from a uniform distribution presenting dips/peaks around the boundary regions where $S_{12}$ or $S_{34}$ are used as primary. This is depicted in Fig. 4.23 b, where the PDF of the readout phase values is shown for different values of $\varepsilon$. During data analysis, the assumed value $\Delta_{M,exp}$ is swept and the one yielding a uniform phase distribution is taken as the correct one, for which $\Delta_{M,exp} \approx \Delta_M$. This setting is stable and only checked before major experimental runs. As an example, for the measurement where we verified spin-photon entanglement - see Chapter 6 - $\Delta_{M,exp} = 1.59 \pm 0.02$ rad, very close to the ideal D/A, R/L configuration, for which $\Delta_M = \pi/2$.

### Accuracy of the Interferometer Phase $\varphi$ Readout

This section presents: (1) the procedure followed in the optimisation of the integration time $\tau$ of the detectors $D_i$ and (2) the resulting accuracy of the protocol for phase readout $\varphi$.

The interferometer phase $\varphi(t)$ is derived from the signals of the different detectors $D_i$, for $i = 1, 2, 3, 4$. The photon counts of each detector are accumulated over an integration time $\tau$, which was carefully optimised to minimise the uncertainty on the phase readout, $\varepsilon_\varphi$. Note that a very short integration time leads to poor photon statistics per readout and, therefore, a large uncertainty due to shot noise; whereas for a long integration time, the phase evolves and the readout averages over a time-varying phase. The phase readout uncertainty $\varepsilon_\varphi$ can be divided according to these two contributions: (1) shot noise of photon detection and (2) the averaging effect on the evolution of the phase, both dependent on the integration time $\tau$:

$$\varepsilon_\varphi(\tau) = \sqrt{\varepsilon^2_{shot}(\tau) + \varepsilon^2_{av}(\tau)} \tag{4.41}$$

To isolate the contribution of the averaging effect from the shot noise, the output of the interferometer was deviated towards a high-bandwidth photodiode (Thorl. DET36A2) set to

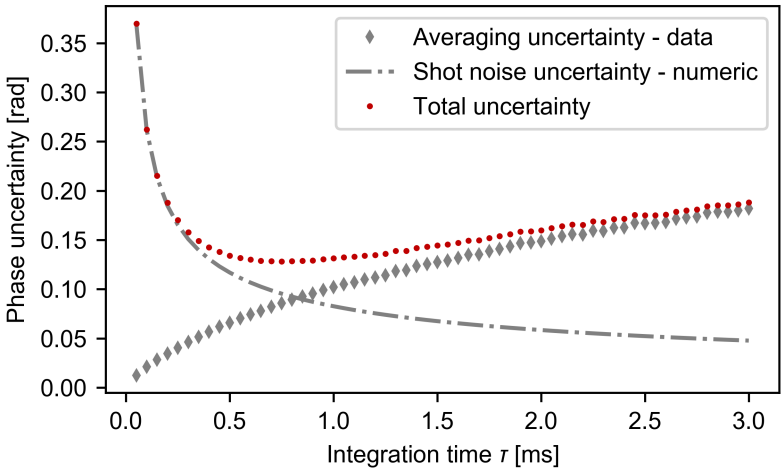


**Figure 4.24: Optimisation of the integration time $\tau$ for readout of the interferometer phase $\varphi$.** The maximum phase uncertainty associated with a single detector $D_i$ is analysed. The shot noise contribution to the uncertainty on the phase estimation is reduced by increasing the integration time $\tau$. Contrarily, a larger $\tau$ leaves more time for the system phase to evolve within the readout, increasing the averaging error. Minimization of the total error occurs around $\tau = 0.75$ ms.

perform a projective measurement in the diagonal polarisation basis. The probing field power was adjusted to around 1 mW in order to fit the photodiode power detection range and the voltage output of the detector was recorded with an oscilloscope at a 200 kHz sampling rate. After normalizing the signal, each voltage point $V_i$ was mapped onto a phase value in a $[0, \pi]$ domain by the relation $\varphi_i = \arccos(V_i)$. Since we were just interested in the average rate of change within short intervals of time, the ambiguity on the phase value from a single basis was irrelevant. The data points were then bunched in time intervals of variable size $\tau$ and the standard deviation within each bunch calculated. The extracted averaging error $\varepsilon_{av}$ is plotted in Fig. 4.24, which expectedly shows a monotonically increasing $\varepsilon_{av}$ with integration time.

The determination of the shot noise contribution $\varepsilon_{shot}(\tau)$ was performed analytically, where a D/A, R/L detector configuration was assumed, in close resemblance to the experimental case. Recall that, for our main experimental run, the difference between the azimuthal angles of the two basis pairs was $\Delta_{M,exp} = 1.59 \pm 0.02$, in comparison to $\Delta_M = \pi/2$ for the ideal case. Furthermore, a maximum photon count rate of $I = 0.5\ \mathrm{Mcs}^{-1}$ in an arbitrary detector $D_i$ was considered. It follows that for an integration time $\tau$ the expected shot noise as a function of the interferometer phase is given by:

$$\sigma_{shot}(\tau, \varphi) = \sqrt{\frac{I \cdot \tau\,(1 + \cos(\varphi))}{2}} \tag{4.42}$$

where it was assumed that $D_i$ measures in the diagonal basis (Eq. 4.33) and background was

neglected. The contribution of the shot noise to the phase uncertainty, considering a single detector, can be deduced by a first-order Taylor expansion of the normalised photon count $\tilde{D}(\varphi)$, leading to:

$$\varepsilon_{shot}(\tau, \varphi) = |d\tilde{D}/d\varphi|^{-1}\, \sigma_{shot} = \sqrt{\frac{2}{I \cdot \tau\,(1 - \cos(\varphi))}} \tag{4.43}$$

where the maximum error occurs at the interfaces between the $S_{12}$ and $S_{34}$ primary regions, depicted for the general case in Fig. 4.23. For a D/A, R/L configuration in the tomography box, an interface region occurs at $\varphi = \pi/4$.

The maximum error curve as a function of integration time, $\varepsilon_{shot}(\tau, \varphi = \pi/4)$, is shown in Fig. 4.24, along with the total phase uncertainty $\varepsilon_{\varphi}$ (in red) resulting from the shot noise and averaging contribution. It suggests an optimal integration time in the range $\tau \in [0.5, 1.0]$ ms.

The phase error $\varepsilon_{phi}$ derived so far is, in fact, an upper-bound on the error, for it considered a single detector and ignored the accuracy gained by combining the different photon counting signals $D_i(t)$. The next paragraphs take into account the full phase retrieval protocol.

A first-order polynomial expansion of the combined signals $S_{ij}$, leads to an expression for the total phase uncertainty: $\Delta\varphi = |dS_{ij}/d\varphi|^{-1}\Delta S$, where $\Delta S$ is the shot noise contribution to the $S_{ij}$ time traces. Solving for the two signals, by taking the derivative of Eqs. 4.38, we obtain:

$$\begin{matrix} S_{12} & & S_{34} \\ \Delta\varphi_{12} = |\sin(\varphi - \varphi_M)|^{-1}\Delta S_{12} & \qquad & \Delta\varphi_{34} = |\sin(\varphi - \varphi_M - \Delta_M)|^{-1}\Delta S_{34} \end{matrix} \tag{4.44}$$

The contribution of the $|dS\ /\ d\varphi|^{-1}$ terms in both signals is plotted in Fig. 4.25 c, showing in dashed lines the regions where both signals yield to the same phase uncertainty. The standard deviation of $S_{ij}$ , $\Delta S$, was estimated numerically, accounting for the propagation of the shot noise associated with the normalized signals of detectors $i$ and $j$, $\tilde{D}_i$ and $\tilde{D}_j$:

$$\Delta S_{ij} = \sqrt{(\frac{\partial S_{ij}}{\partial \tilde{D}_i}\Delta\tilde{D}_i)^2 + (\frac{\partial S_{ij}}{\partial \tilde{D}_j}\Delta\tilde{D}_j)^2} \tag{4.45}$$

for $(i, j) = (1, 2)$ or $(3, 4)$. This is plotted in 4.25 b. It is worth noting how the domains where the shot noise is minimal correspond to maximal uncertainty due to the $\|dS\ /\ d\varphi\|^{-1}$ terms - compare subfigures b and c - indicating how these two elements counteract each other. Finally, the total uncertainty associated with the phase retrieval is plotted in 4.25 d.

For an optimal phase retrieval, it is desirable to choose the readout ($S_{12}$ or $S_{34}$) which provides minimum uncertainty $\Delta\varphi$.

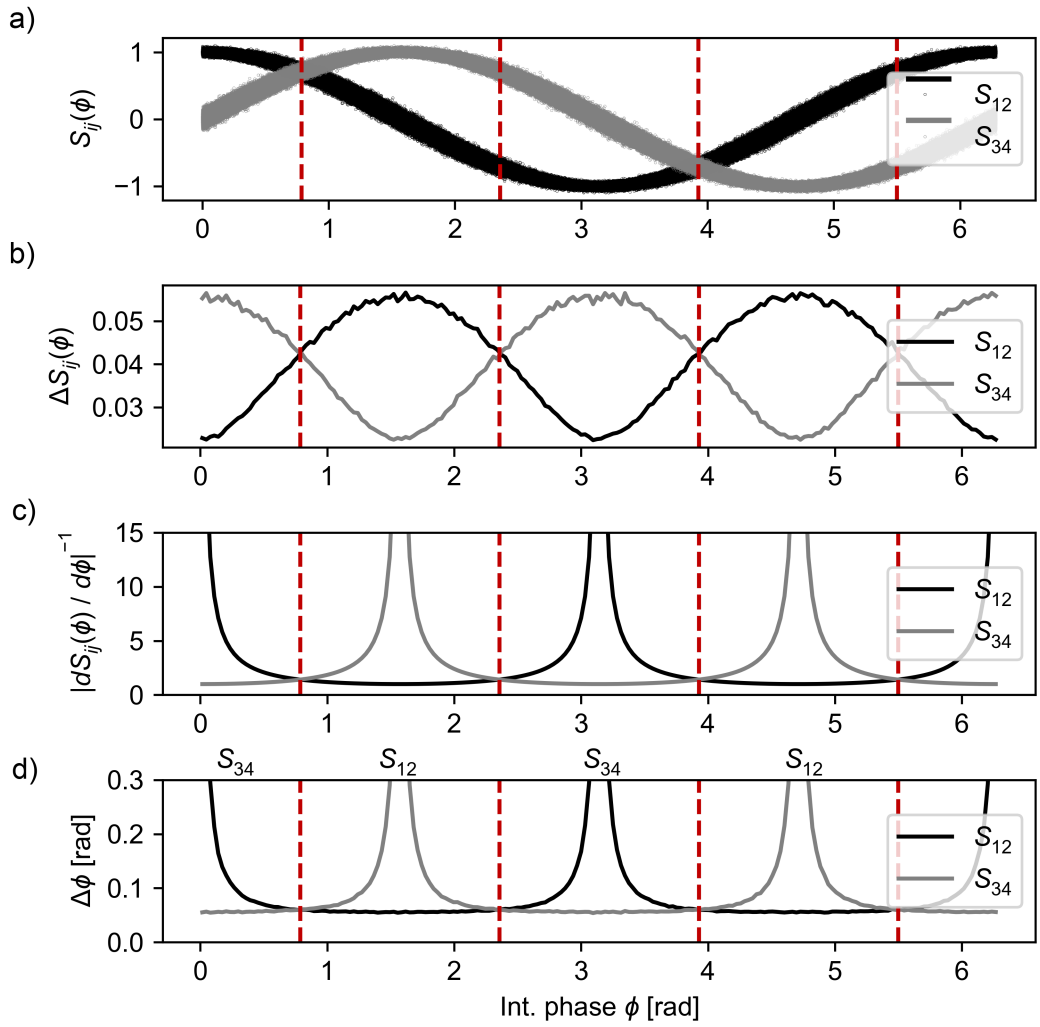


**Figure 4.25: Uncertainty on the interferometer phase $\varphi$ estimation. a)** Numerically generated $S_{12}$ and $S_{34}$, from shot-noise affected single detector signals $D_i$. The signals mimic the photon-detection rates measured in the laboratory, with amplitude $A_i$ and offset $B_i$. **b)** Standard deviation of $S_{ij}$ readouts as a function of $\varphi$, due to propagation of shot-noise from the individual signals $D_i$. **c)** Inverse derivative of $S_{ij}(\varphi)$ as a function of $\varphi$. **d)** Total uncertainty in the phase $\varphi$ readouts as a function of $\varphi$ for $S_{12}$ and $S_{34}$. To minimize the error, the signal providing the lowest $\Delta\varphi$ is taken as the primary one; the other signal is merely employed to lift the ambiguity between the two possible phase values. The labels at the top of the graph identify which signal is used as primary and the respective phase domains are separated by the red dashes, positioned at $\varphi = \varphi_M + \Delta_M/2 + n\pi/2$.

1. If $\Delta\varphi(S_{12}) \geq \Delta\varphi(S_{34})$ then signal $S_{34}$ is primary and used for the retrieval of the two possible phase values $\varphi_1$ and $\varphi_2$, whereas $S_{12}$ is secondary and employed to decide for one of them.

2. If $\Delta\varphi(S_{34}) \geq \Delta\varphi(S_{12})$ then signal $S_{12}$ is primary and used for the retrieval of the two possible phase values $\varphi_1$ and $\varphi_2$, whereas $S_{34}$ is secondary and employed to decide for one of them.

The boundaries between domains where each signal is used as primary are signalled with vertical dashed lines in Fig. 4.25, with a $\varphi$-coordinate given by $\varphi = \varphi_M + \Delta_M/2 + n \cdot \pi/2$, according to the angles defined in the previous Section. Taking a typical experimental run as an exmaple, for a maximum intensity of 382 $\text{Kcs}^{-1}$ per detector, using an integration time $\tau = 1$ ms, the resulting phase uncertainty is $\Delta\varphi = 0.06$ rad. This value is relevant for the tomography on the photonic qubits, as it sets the accuracy with which we can determine in what basis the photons are projected - see Section 6.1.3.

# 5

# Iterative Initialisation of the NV centre spin

## Overview

The ability to initialise a quantum system is a vital requirement of any quantum information protocol, whether to realise a relay in a long-distance quantum communication [83] or a single photon emitter for photonic entanglement generation [41]. In particular, the realisation of quantum memories [89], for which the NV centre is a prime candidate and where the nuclear spin is typically used to store information and the electronic spin as a mediator [146], requires the multi-qubit register to be accurately prepared in some initial state.

Polarisation of the electronic and nuclear spins of the NV centre has been experimentally demonstrated through various approaches. Recursive transfer of the spin polarisation from the electrons onto the nuclei has been attained by means of a sequence of microwave, radio-frequency and optical pulses reaching a nuclear polarisation[1] in the range of

[1] For the remainder of this manuscript, nuclear fidelity, $F_N$, refers to the nuclear polarisation within the electronic spin manifold $m_s = -1$. It can be succinctly expressed as the following population ratio:

$$F_N = \text{pop.}(m_s = -1, m_I = 0)/\text{pop.}(m_s = -1) \tag{5.1}$$

Similarly, the spin qubit fidelity is given by:

$$F_e = \text{pop.}(m_s = -1)/(\text{pop.}(m_s = -1) + \text{pop.}(m_s = 0)) \tag{5.2}$$

$F_N \in [0.76, 0.98]$ [146–148]. Alternatively, single-shot readout of the electronic spin combined with state transfer of the nuclear spin onto the electronic spin have been used to induce projective measurements onto the desired subspaces, in a trial-until-success manner, attaining a nuclear polarisation of $F_N \sim 0.92$ [80, 91]. Single-shot readout places stringent conditions on the NV centre, whose strain regime must minimize spin-mixing in the excited state and ensure spin-preserving optical transitions. Other approaches employ level anti-crossings (LAC) where the electron-nucleus hyperfine coupling is enhanced with respect to other interactions, leading to efficient spin flip-flops, which are harnessed to polarise the nucleus, with $F_N = 0.87$ under cryogenic conditions [149–151]. This requires careful tuning of the energy spectrum to bring the NV centre close to the LAC, typically achieved with high magnetic fields (e.g. 500 G). Adding to the wide assortment of initialisation methods, an all-optical approach has been realised by optical coherent population trapping with $F_N = 0.76$ [152]; and a high microwave power Hartmann-Hahn double resonance was employed to reach $F_N \sim 0.90$ nuclear polarisation [153].

This chapter presents a recursive method for polarising the electronic and nuclear spins of the NV centre, under cryogenic conditions, by shuffling the spin populations around, but the population of the desired target state.

The basic concept is to use an optical pulse to redistribute the spins found within the $m_s = 0$ manifold, where the undesired populations are driven to, by microwave pulses. Contrarily, the target state (e.g. $m_s = -1, m_i = 0$) is never driven or depleted and iteratively accumulates the randomised populations, converging towards an asymptotic limit. The described approach has a low resource overhead, does not require a radio-frequency interface, single-shot readout or careful B-field tuning of the optical spectrum. Furthermore, experimental imperfections in the microwave and optical pulses are well tolerated, due to the recursive nature of the method. A rate equation model was developed to characterise the initialisation process, providing a quantitative description of the electronic and nuclear spin dynamics under optical pumping.

Even though the initialisation schemes were experimentally realised before the physical scheme was developed, here, for clarity, a bottom-to-top approach is taken and we start with the description of the rate equation model, followed by the calibration measurements to establish the value of the spin-flip coefficients. Afterwards, the electronic and nuclear spin initialisation schemes are presented, along with their experimental realisation.

## 5.1 The Physical Model

The initialisation routines involve two categories of operations, which act on the $NV^-$ ground state populations: (1) deterministic high-fidelity microwave driven gates, which realise unitary

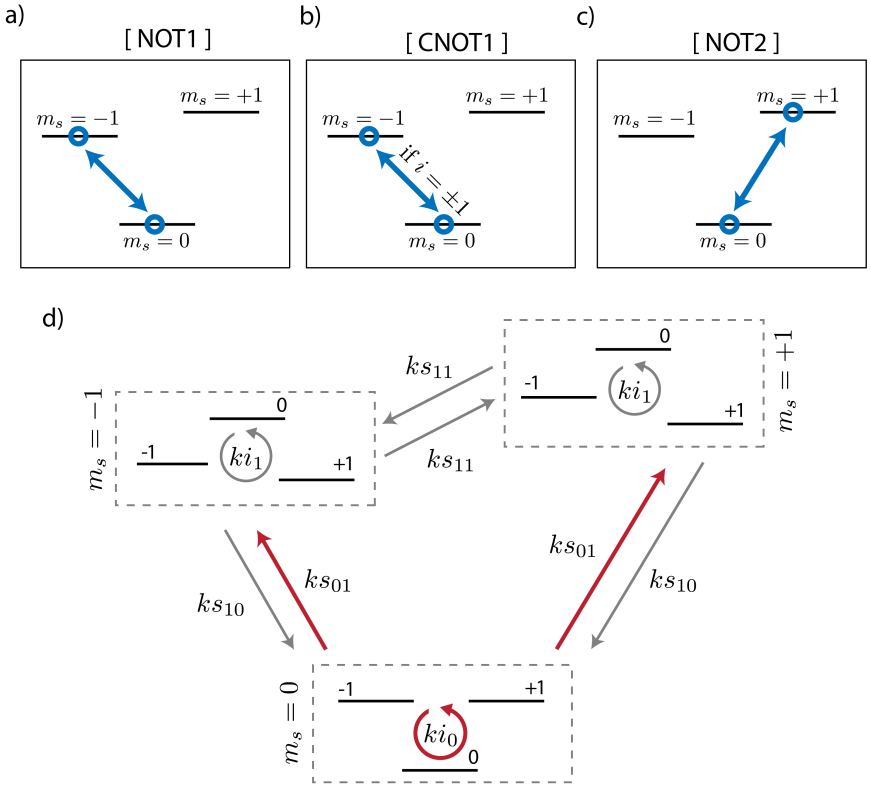


**Figure 5.1: Spin operations on the NV centre ground state, used in the initialisation routines.** a) The [NOT1] gate realizes a $\pi$-rotation between the $m_s = 0$ and $m_s = -1$ manifolds, irrespective of the nuclear spin. b) A [CNOT1] gate implements a population inversion between $m_s = 0$ and $m_s = -1$, only if $m_i = \pm 1$. c) The [NOT2] gate realises a $\pi$-rotation between the $m_s = 0$ and $m_s = +1$ electronic spins, irrespective of the nuclear state. d) The depletion gate [D] is implemented by an optical pulse of arbitrary duration, resonant with the $|0\rangle \rightarrow |0_e\rangle$ transition. The red (gray) arrows illustrate the different spin-flip mechanisms due to resonant (cross-)excitation.

rotations on the electronic and nuclear spin subspace; (2) stochastic electronic and nuclear spin flips, caused by optical pumping of the $|0\rangle \rightarrow |0_e\rangle$ transition, causing the depletion of the $m_s = 0$ population.

The microwave gates are illustrated in Fig. 5.1, comprising the following operations: the [NOT 1] block inverts the $m_s = 0$ and $m_s = -1$ populations, corresponding to a $\pi$-pulse between these two levels; the [CNOT 1] block inverts the $m_s = 0$ and $m_s = -1$ populations, conditional on the nuclear spin being in $m_i = \pm 1$; and the [NOT 2] gate inverts the $m_s = 0$ and $m_s = +1$ populations. These gates exhibit fidelities in excess of $99\%$, as described in Section 4.3.2.

The optical gate $[D]$ promotes the NV centre to its excited, which then spontaneously decays back to the ground state, while shuffling the spin populations. The effective spin flip rates are illustrated in Fig. 5.1 d and have been modelled with the following rate equation:

$$\frac{d\vec{P}}{dt} = \hat{M}\vec{P} \tag{5.3}$$

where $\vec{P}$ describes the populations on the ground state in the following ordered basis:

$$\{(m_s, m_i)\} = \{(-1,-1), (-1,0), (-1,+1), (0,-1), (0,0), (0,+1), (+1,-1), (+1,0), (+1,+1)\} \tag{5.4}$$

$\hat{M}$ is a $9 \times 9$ transfer matrix, explicitly given in Fig. 5.2, which describes the population redistribution due to optical pumping, through the following variables:

1. $ks_{01}$ – electronic spin transfer rate from $m_s = 0$ to $m_s = \pm 1$;
2. $ks_{10}$ – electronic spin transfer rate from $m_s = \pm 1$ to $m_s = 0$;
3. $ks_{11}$ – electronic spin transfer rate from $m_s = -1$ to $m_s = +1$ and vice-versa;
4. $ki_0$ – nuclear spin transfer rate from $m_i = \pm 1$ to $m_i = \pm 0$, when $m_s = 0$;
5. $ki_1$ – nuclear spin transfer rate from $m_i = \pm 1$ to $m_i = 0$, when $m_s = \pm 1$.

Note that some spin-flip mechanisms are caused by resonant excitation, which is the case of $ks_{01}$ and $ki_0$, marked in red in the figure, whereas others only occur due to the undesired cross-excitation of the neighbouring $|\pm 1\rangle \rightarrow |\pm 1_e\rangle$ transitions, covering the rates $ks_{10}$, $ks_{11}$ as well as the nuclear $ki_1$. Recalling the $1\%$ upper bound on the cross-talk probability - see Section 4.2.4 - it is expectable that the resonant spin flip mechanisms play a more relevant role in the dynamics of the overall system, comparatively to the spin flips caused by cross-excitation.

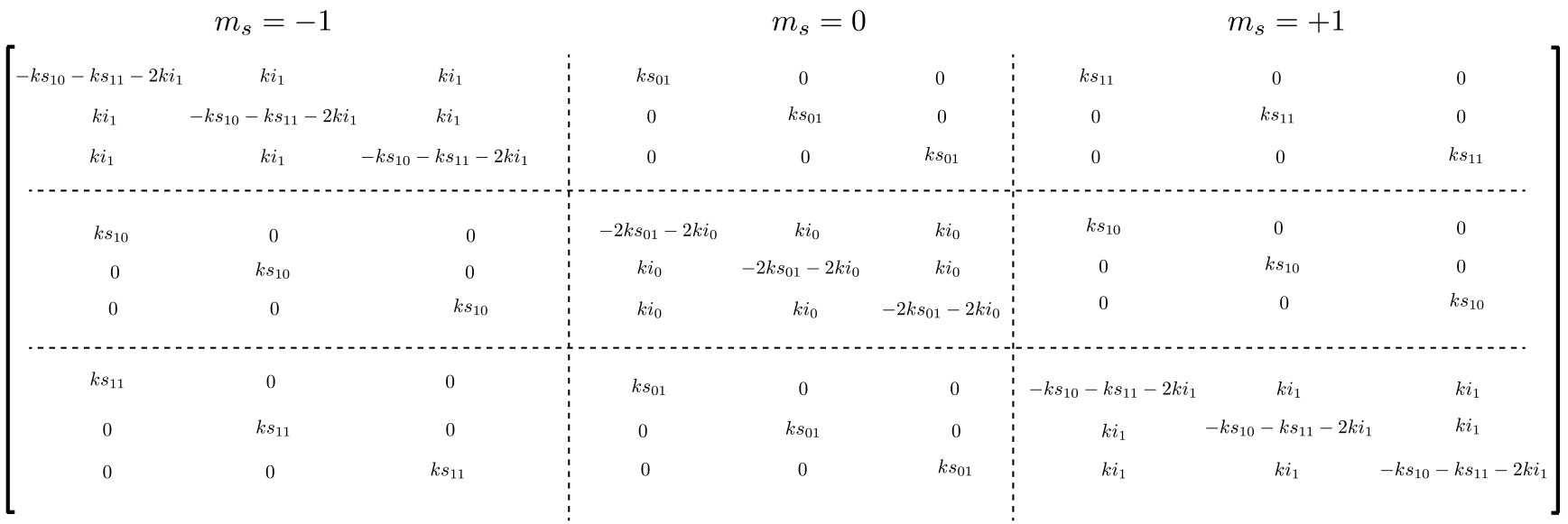


**Figure 5.2: Transfer matrix of the depletion gate in the rate equation model. The matrix is subdivided in blocks corresponding to different electron spin subspaces**. The coefficients within each column sum to zero, as required by the conservation of populations.

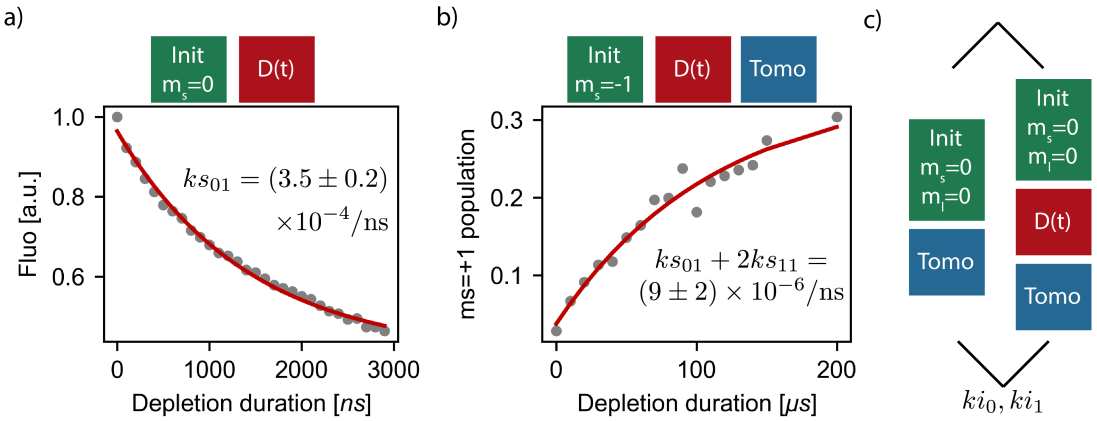


**Figure 5.3: Extraction of spin flip rates. a)** $ks_{01}$ was determined by fitting a mono-exponential to the decay of fluorescence when driving the optical $|0\rangle \rightarrow |0_e\rangle$ transition after initialising the system in the $m_s = 0$ state. The error bars are smaller than the dots. **b)** Retrieval of $ks_{10} + 2ks_{11}$ was performed with a fit to the population evolution, when applying a depletion pulse of variable duration to the same transition, after initialising the system in $m_s = -1$. **c)** The measurement of the nuclear spin flip rates involved initialising the system in the $(m_s = 0, m_i = 0)$ state and monitoring the mixing of the nuclear populations caused by a 10 μs depletion pulse. Fitting the redistributed populations with our numeric model, yielded bounds for the values of $ki_0$ and $ki_1$.

Furthermore, as will become clear in the coming discussion, cross-excitation reduces the initialisation fidelity of the proposed schemes.

### Retrieval of the Spin Flip Rates

To make the rate equation model useful, the spin transfer coefficients had to be determined, through a set of calibration measurements which are described next.

The dynamics of the $m_s = 0$ state depletion by an optical pulse are dominated by the $ks_{01}$ process, due to low cross-talk. This is particularly true for short depletion pulses right after initialisation into $m_s = 0$, where besides the negligible cross-excitation, also the $m_s = \pm 1$ populations are still small, resulting in a minor repopulation of $m_s = 0$ during pumping. Following this argument, the electronic spin flip rate $ks_{01}$ was established by a mono-exponential fit to the phonon-sideband (PSB) fluorescence time-trace, produced by a 3 μs depletion pulse after initialising the system in the $m_s = 0$ manifold [2] - see Fig. 5.3 a. The extracted decay rate was $ks_{01} = (3.5 \pm 0.2) \times 10^{-4}$ ns$^{-1}$.

Determination of the electronic spin flips caused by cross-excitation of the $m_s = \pm 1$

[2] Initialisation of the electronic spin followed the prescription given in Section 5.2.1

| Rate | Value [per ns] | Error [per ns] | Cause |
|---|---|---|---|
| $ks_{01}$ | $3.5 \times 10^{-4}$ | $0.2 \times 10^{-4}$ | resonant excitation |
| $ki_0$ | $[2.15, 2.76] \times 10^{-4}$ | $0.05 \times 10^{-6}$ | resonant excitation |
| $ks_{10} + 2ks_{11}$ | $9 \times 10^{-6}$ | $2 \times 10^{-6}$ | cross excitation |
| $ki_1$ | $[0, 2\% \cdot ki_0^{(0)}]$ | $0.04 \times 10^{-6}$ | cross excitation |

**Table 5.1: Retrieved spin-flip rates, from calibration measurements**. $ki_0$ is specified in terms of range of possible values, compatible with the sweep of $ki_1$ in the range $[0, 2\% \cdot ki_0^{max}]$.

populations, i.e. $ks_{10}$ and $ks_{11}$, required preparing and probing a process for which the influence of the much larger $ks_{01}$ was subdued. To this effect, the electronic spin was initialised in the $m_s = -1$ state and a depletion pulse $[D]$ of variable duration, transferred the population from $m_s = -1$ to the $m_s = +1$ manifold, as represented in Fig. 5.3 b. For an initial population distribution among the three electronic spin manifolds given by $\text{pop}_{init} = [p_{-1}, p_0, p_{+1}]$, in the ordered basis $\{m_s\} = \{-1, 0, +1\}$, the time evolution of the $m_s = +1$ population can be derived by integration of Eq. 5.3, resulting in the following expression:

$$\text{pop}(m_s = +1) \quad = \quad C_1 + C_2 \exp((-2ks_{01} - ks_{10})\, t) + C_3 \exp((-ks_{10} - 2ks_{11})\, t) \tag{5.5}$$

with

$$C_1 = \frac{ks_{01}(p_{-1} + p_0 + p_{+1})}{2ks_{01} + ks_{10}}\,, \quad C_2 = \frac{-p_0 ks_{01} + p_{-1} ks_{10}/2 + p_{+1} ks_{10}/2}{2ks_{01} + ks_{10}}\,, \quad C_3 = \frac{p_{+1} - p_{-1}}{2} \tag{5.6}$$

For our electron spin initialisation conditions, within this experimental run, $[p_{-1}, p_0, p_{+1}] = [92.5, 4.5, 3.0]$ %, and considering $ks_{01} = 3.5 \times 10^{-4}$ ns$^{-1}$ we have established numerically that the $C_2$ pre-factor is significantly smaller than $C_3$, for the whole range of likely $ks_{10}$ values, with $C_2/C_3 \in [3.4, 5.0]\%$. Therefore, one can safely approximate Eq. 5.5 with a simpler mono-exponential:

$$\text{pop}(m_s = +1) = A \cdot \exp((-ks_{10} - 2ks_{11})\, t) + B \tag{5.7}$$

Using this expression to fit the pop.$(m_s = +1)$ curve of Fig. 5.3 b, rendered a combined rate value of $\tilde{k} = ks_{10} + 2ks_{11} = (9 \pm 2) \times 10^{-6}$ ns$^{-1}$.

The determination of the nuclear spin flip rates involved preparing the NV centre in a state with high nuclear polarisation and monitoring the nuclear depolarisation induced by a depletion pulse $[D]$. This comprised two steps: (1) the NV centre was initialized in the

$(m_s = 0, m_i = 0)$ state and the populations $\vec{P}_1$ evaluated through tomography; (2) the NV centre was initialized in the $(m_s = 0, m_i = 0)$ state, a 10 µs depletion pulse was applied and the final populations $\vec{P}_2$ were revaluated.

The population evolution from $\vec{P}_1$ to $\vec{P}_2$ was simulated numerically by integration of the rate equation model to yield a theoretical $\vec{P}_2^{\,t}$, while assuming $ks_{01}$ and $ks_{10} + 2ks_{11}$ as given by the calibration measurements described above. As $ki_1$ is reliant on cross-excitation, its contribution to the overall dynamics are expected to be modest comparatively to the effect of $ki_0$. Therefore, in a first approximation, nuclear spin flips due to cross-excitation were neglected by setting $ki_1 = 0$. Furthermore, $ki_0$ was left as a free parameter in the minimization of the distance $d = \|\vec{P}_2^{\,t} - \vec{P}_2\|$, to render an optimal value $ki_0^{(0)} = 2.76 \times 10^{-4}\ \mathrm{ns}^{-1}$. Later, to ascertain the influence of $ki_1$ on the $ki_0$ fit value, $ki_1$ was swept within the range $[0, 2\% \cdot ki_0^{(0)}]$ and for each iteration an optimal $ki_0^{(j)}$ retrieved, resulting in the following range of values: $ki_0^{(j)} \in [2.15, 2.76] \times 10^{-4}\ \mathrm{ns}^{-1}$. The two coefficients, $ki_1$ on the $ki_0$, were found to be anti-correlated, i.e. an increase of $ki_1$ could be compensated by a decrease of $ki_0$ to render a good fit to the data. The extracted spin flip rates are summarised in Table 5.1, where the upper-bound $ki_0^{max}$ corresponds to the lower bound of $ki_1$ and vice-versa.

Despite being a descriptive model where the exact physical mechanisms underlying each coefficient were not studied, it remains accurate in the prediction of complex experimental sequences. This is explored in the next section, where the model is applied to the spin initialisation routines, showing excellent agreement with the experimental results.

## 5.2 Spin Initialisation Routines

### 5.2.1 Electronic and Nuclear Initialisation

The electronic spin initialisation and characterisation can be succinctly described in block form, by the following expression:

$$[G]\ (\ [\mathrm{NOT}_2][\mathrm{D}]\ )^N\ [\mathrm{Tomo}] \tag{5.8}$$

where $[G]$ is a 1 µs, 380 µW green laser pulse at 520 nm, to initialize the charge state of the NV into $\mathrm{NV}^-$. $[D]$ is a 3 µs resonant depletion pulse. The exponent $N$ indicates the number of repetitions of the unit cell of the sequence and [Tomo] is the tomography block - Section 4.2.4 -, which determines the populations in the three electronic spin ground states. While the [NOT2] gate draws the $m_s = +1$ population to $m_s = 0$, the [D] operation redistributes it onto the $m_s = +1$ and $m_s = -1$ states. Repetition of the [NOT2] [D] block leads to an accumulation of

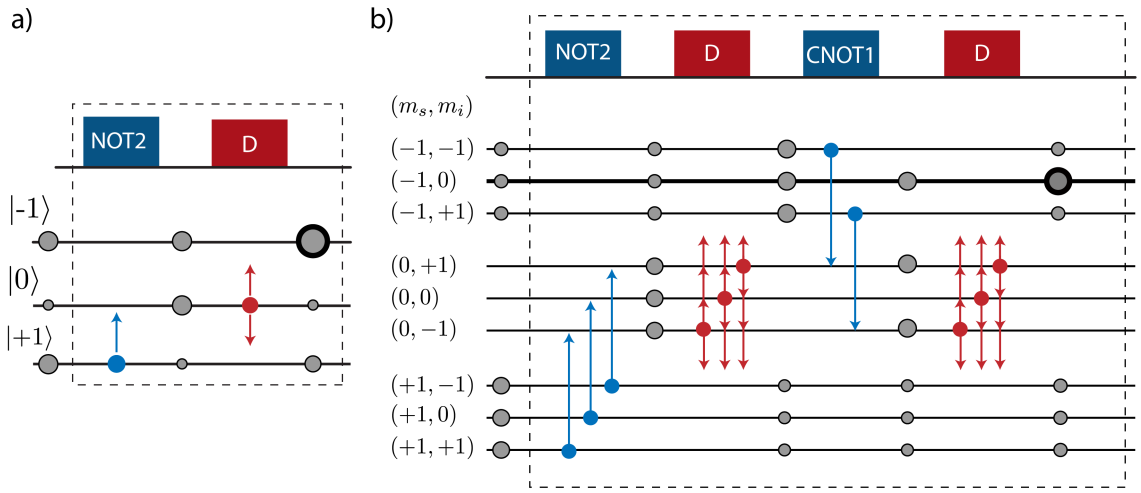


**Figure 5.4: a)** Unit cell of the iterative initialisation of electronic spin into the $m_s = -1$ state. The [NOT2] gate draws the population from the $m_s = +1$ state onto $m_s = 0$, which is then redistributed by the depletion pulse [D]. Repetition of the [NOT2][D] operation leads to an accumulation of population onto the $m_s = -1$ state. **b)** Unit cell of the initialisation of the nuclear and electronic spin into the $(m_s = -1, m_i = 0)$ state. The microwave gates, in blue, bring all populations but the $(m_s = -1, m_i = 0)$ state to the $m_s = 0$ manifold. These are then redistributed by the depletion gate, following the dynamics of the transfer matrix $\hat{M}$ of the main text. Each iteration leads to a fractional increase of the population in the target state.

population onto $m_s = -1$. The electronic initialisation scheme is illustrated in Fig. 5.4 a.

For $N = 8$, where each iteration lasts 4 µs, an initialisation of the electronic spin qubit with a fidelity $F_e = 95.3 \pm 0.5\%$ was achieved [3], where the error is derived from the shot noise contribution. High repetition numbers were not studied for the electronic spin initialisation scheme, as the expected results are redundant with those obtained for the protocol presented next.

The recursive initialisation of the electronic and nuclear spins of the NV centre into the $(m_s = -1, m_i = 0)$ state is realised by the following sequence of operations, illustrated in Fig. 5.4 b:

$$[G]\,(\,[\mathrm{NOT}_2][\mathrm{D}][\mathrm{CNOT}_1][\mathrm{D}]\,)^N\,[\mathrm{Tomo}] \tag{5.9}$$

where the microwave gates $[\mathrm{NOT}_2]$ and $[\mathrm{CNOT}_1]$ bring the $m_s = \pm 1$ populations onto the $m_s = 0$ manifold, to be redistributed by the depletion gate [D], as specified by the transfer matrix $\hat{M}$ in the rate equation model. The target state $(m_s = -1, m_i = 0)$ is never redistributed, as it is left unaffected by the $[\mathrm{CNOT}_1]$ gates, leading to a progressive accumulation of this

[3] The qubit fidelity only takes into account the populations within the $m_s = 0$ and $m_s = -1$ levels. The reported fidelity corresponds to the following population distribution $(m_s = 0, m_s = -1, m_s = +1) = (4.6\,,\,92.5\,,\,2.8\,) \pm 0.5\%$.

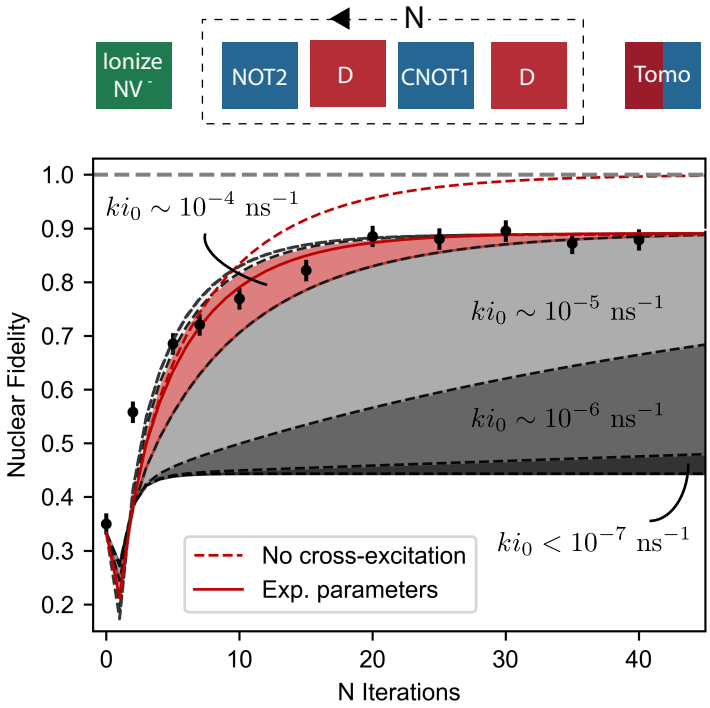


**Figure 5.5: Initialisation of the nuclear spin for different number $N$ of iterations.** The data has a standard error of $\pm 2\%$. For $N = 40$, a nuclear initialisation fidelity of $F_n = (0.88 \pm 2)\%$ was achieved, close to the assymptotic limit. The red line indicates the prediction of the numerical model, using the spin flip rates retrieved in the calibration measurements of Section 5.1. The different shaded areas correspond to the model predictions for nuclear spin flip rates in different ranges.

population. The characterisation block [Tomo] measures the population distribution after $N$ repetitions of the unit cell of the scheme, enabling one to establish the nuclear initialisation fidelity at each repetition number, $F_N(N)$ . Each iteration lasts approximately 8 µs, depending on the waiting times between operations.

The resulting data is plotted in Fig. 5.5, together with the numerical prediction given by our model (red line), where the values of Table 5.1 were taken as an input, reaching a good agreement between the model and experiment. Given the two orders of magnitude of difference between the $ki_0$ and $ki_1$, the nuclear spin flips due to cross-excitation have been neglected in the numeric simulation of the nuclear initialisation scheme. For an iteration number $N = 40$, the nuclear state fidelity reached $F_N = (88 \pm 2)\%$ and the electronic spin fidelity was $F_e = 98 \pm 2\%$, close to the asymptotic limit ($N \to \infty$), as one can deduce from Fig. 5.5.

To estimate the impact nuclear spin flips by optical pumping, $ki_0$, on the $F_N(N)$ curve, its value was swept in the numeric simulation. The resulting curves are grouped in different shaded areas in Fig. 5.1, each corresponding to an order of magnitude of $ki_0$. As expected, lower nuclear spin flip rates lead to a slow convergence to the asymptote. As the nuclear flip rate value overtakes the electronic flip rates at $ki_0 \sim 10^{-4}$ ns$^{-1}$, the effect of changing $ki_0$ becomes less pronounced and the convergence speed is barely affected. For that reason, the regions for $ki_0 \sim 10^{-3}$ ns$^{-1}$ and $ki_0 \sim 10^{-2}$ ns$^{-1}$ cannot be distinguished in the figure.

For a high number of iterations ($N > 20$), the non-unit fidelities are caused by cross-excitation processes ($ks_{10}$, $ks_{11}$ and $ki_1$), which deplete the target population. Within our system this could suppressed by tuning the spectrum through variations of a DC electric field (Stark tuning) or a DC magnetic field (Zeeman tuning), where a maximal $\delta \approx 3.8$ GHz separation between $|0\rangle \to |0_e\rangle$ and $|\pm 0\rangle \to |\pm 1_e\rangle$ optical transitions is achievable, as established by the simulation of the optical spectrum following Section 4.2.4. Within such regime, with a driving field $\Omega = 500$ MHz, a cross-talk of $< 0.2\%$ is expected, leading to nuclear initialisation fidelities in excess of $97\%$. For reference, to date, the best nuclear initialisation fidelity with a NV centre amounts to $F_N \approx 0.98$ [146], with reported values in the range $[0.78, 0.98]$, as mentioned in the overview section of this chapter. For reference, the regime where no-cross talk is present was simulated and it is shown in Fig. 5.5 with a red dashed line, presenting a convergence towards perfect initialisation for $N \to \infty$.

## 5.3 Summary and Outlook

An iterative method for initialisation of the NV centre was proposed and experimentally realised, attaining a nuclear (electronic) initialisation fidelity of $F_N = (88 \pm 2)\%$ ($F_e = 95 \pm 2\%$), in line with typical values found in current literature. The main advantage of

this approach is the low demand on resources, requiring microwave driving, a single laser and no tuning of the energy spectrum. This comes at the cost of long initialisation times ($N = 10 \rightarrow\sim 166\mu s$) required to attain the asymptotic limit of many iterations.

A rate equation model was developed to describe the data and help understanding the restricting elements of this protocol. We have thereby established qualitatively that the limiting factor on the initialisation fidelity is imposed by cross-excitation of the $|1\rangle \rightarrow |1_e\rangle$ optical transition.

In future work, the numeric model could be developed further to optimise the experimental parameters of the initialisation scheme, providing a faster and more reliable state preparation. Furthermore, the model could be used to probe the dynamics of the nuclear spin in more detail, by, for example, investigating the transverse hyperfine coupling constant, $A_{gs}^{\parallel}$, in the excited state [154] under cryogenic conditions, which remain unknown in the literature.

# 6

# Spin-Photon Entanglement Generation and Verification

## Overview

In this chapter the experimental methods of Chapter 4 are brought together to realise the fundamental unit of the TPC entanglement-generation protocol, proposed in Section 2.3. While the optical and microwave interfaces - Sections 4.2 and 4.3 - are used to read/write the electronic spin of the NV centre and generate photonic qubits on a time-bin basis, the time-to-polarisation conversion (TPC) stage - Section 4.4 - maps the time-bin basis into polarisation and performs quantum tomography on the photonic polarisation space.

The experimental sequence used to produce entangled states is described in detail in the upcoming sections. The resulting entanglement is verified by performing partial quantum tomography on the 2-qubit spin-photon state, enabling an estimate of a lower bound on the entanglement fidelity. Finally, a theoretical model of the experiment is developed to account for imperfections of the apparatus and retrieve expectation values for the observed correlations.

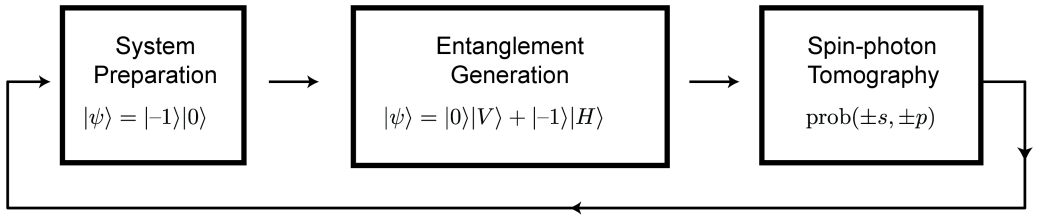


**Figure 6.1: The stages of the experimental cycle for entanglement generation and verification**. Each experimental run starts with the system preparation, consisting of NV ionization into $NV^-$ and initialisation in the state $(m_s = -1, m_I = 0)$, followed by the entanglement-generation block, which ideally produces a Bell state between the NV centre electron spin $\{|0_s\rangle, |-1_s\rangle\}$ and the polarisation $\{|H\rangle, |V\rangle\}$ of a fluorescent photon. In the spin-photon tomography stage, the quantum correlations between the two particles are determined.

## 6.1 Experimental Sequence

The experimental cycle can be conceptually divided into three stages, depicted in Fig. 6.1:

1. **System preparation** - the NV centre is ionized into $NV^-$ and the electronic and nuclear spins are initialized in the $(m_s = -1, m_I = 0)$ level;

2. **Entanglement generation** - creates entanglement between the NV centre electronic spin and the time-bin degree of freedom of a fluorescent ZPL photon, which is later converted to a polarisation qubit;

3. **Tomography** - the 2-qubit state is projected into spin-photon base-pairs to estimate the existing quantum correlations.

A detailed account of the three experimental stages is given in the sections ahead.

### 6.1.1 Preparation

The protocol starts with ionisation of the NV into the $NV^-$ state, by pumping the defect with a 1.3 µs green laser pulse at 380 µW. The initialisation of the electronic and nuclear spin ($^{14}N$ nucleus of the NV defect) is then performed by selectively flipping undesired populations through resonant optical pumping, as described in Chapter 5. This leads to an iterative accumulation of population on the $(m_s = -1, m_I = 0)$ level, attaining a qubit initialisation fidelity of $F_{qubit} = (97.9 \pm 1.6)\%$. By polarising the nuclear spin into $m_I = 0$, where a nuclear

polarisation within the $m_s = -1$ manifold of $83.8 \pm 1.9\%$ was attained[1], dephasing effects are mitigated and the fidelity of rotations on the electronic spin is increased, as discussed in Section 4.3.2. The preparation is the lengthiest step of the whole experimental cycle, taking a total of 170 µs, due to the long optical pulses used to deplete the undesired populations and the high number of required iterations (10) to achieve a suitable initialisation fidelity.

### 6.1.2 Entanglement Generation

This step combines microwave operations on the electronic spin state and resonant optical excitations of the $m_s = 0$ transition that result in the emission of ZPL photons. After initialisation of the electronic spin into $|\psi_s\rangle = |-1_s\rangle$, a microwave pulse performs a $R_y(\pi/2)$ spin rotation, yielding the spin state $|\psi_s\rangle = (|-1_s\rangle - |0_s\rangle)/\sqrt{2}$, where the $s$ subscript was introduced to make a clear distinction between spin ($s$) and photon ($p$) qubits.

The subsequent resonant optical $\pi$ pulse ($P_1$) excites the NV centre, conditional on the NV being in the $m_s = 0$ state, and leads to the emission of a photon $|E\rangle$, where E stands for early emission as it results from the first of a pair of optical excitations. A further $R_y(\pi)$ rotation flips the electronic spin populations and is followed by the second optical $\pi$ pulse ($P_2$), causing another conditional emission $|L\rangle$, for it stems from a late excitation. The resulting state can be represented as:

$$|\psi\rangle = \frac{|m_s = 0\rangle |L\rangle + |m_s = -1\rangle |E\rangle}{\sqrt{2}} \otimes |D\rangle \tag{6.1}$$

where $|D\rangle$ is a reminder of the photon's diagonal polarisation, with respect to the TPC basis. Note that both emission wavepackets have linear polarisation with a direction defined by the emission dipole of the $|0\rangle \rightarrow |0\rangle_e$ optical transition; the time-to-polarisation conversion (TPC) stage sets the reference for the polarisation and it is oriented such that all emitted photons are diagonally ($|D\rangle$) polarised.

In the second step of the entanglement-generation block, illustrated in Fig. 6.3, the TPC interferometer erases the time separation (262 ns) between the two wavepackets and maps the $|E\rangle$ emission into $|H\rangle$ polarisation and $|L\rangle$ into $|V\rangle$, as described in greater detail in Section 4.4. With the photon in a polarization basis, the expected spin-photon entangled state is:

$$|\psi\rangle = \frac{|m_s = 0\rangle |V\rangle + e^{i\varphi} |m_s = -1\rangle |H\rangle}{\sqrt{2}} \tag{6.2}$$

[1]Note that in the experimental run of the spin-photon entanglement verification, the nuclear initialisation fidelity $F_N = 83.8 \pm 1.9\%$ is slightly below what was reported for the dataset of Chapter 5. The cause for this discrepancy was not investigated, but it is hypothetically associated with differences in the optical setup (e.g. fibre coupling, temperature stability, laser stability)

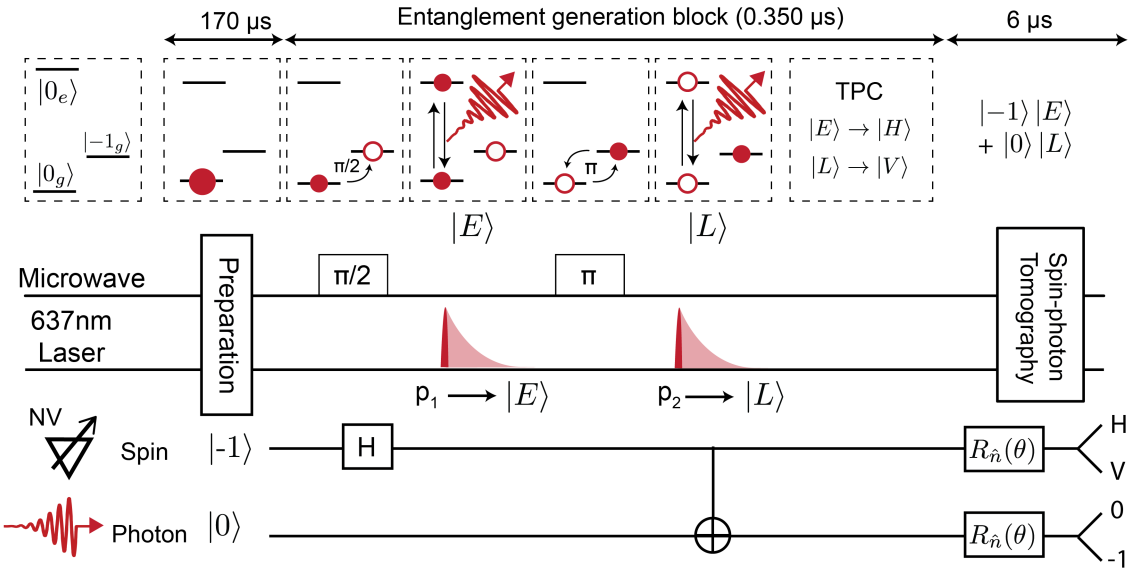


**Figure 6.2: Entanglement generation block and its circuit diagram.** After preparation of the the NV centre, a $R_y(\pi/2)$ rotation, creates a spin superposition. Two optical excitations ($P_1$,$P_2$) of the $|o\rangle \rightarrow |o_e\rangle$ transition, separated by a $R_y(\pi)$ rotation, yield a photon composed by two wavepackets (early and late) and mimic the action of a CNOT gate that targets the photon Hilbert space, conditioned by the spin state. At last, the TPC stage erases the "which-emission information" by removing the time difference between the two wavepackets and maps the early (late) wavepacket into H(V)-polarised light. The result is a spin-photon entangled. Quantum tomography on the individual qubits combines single qubit microwave rotations with projective measurements on the $\hat{\sigma_z}$ basis, by optical resonant readout.

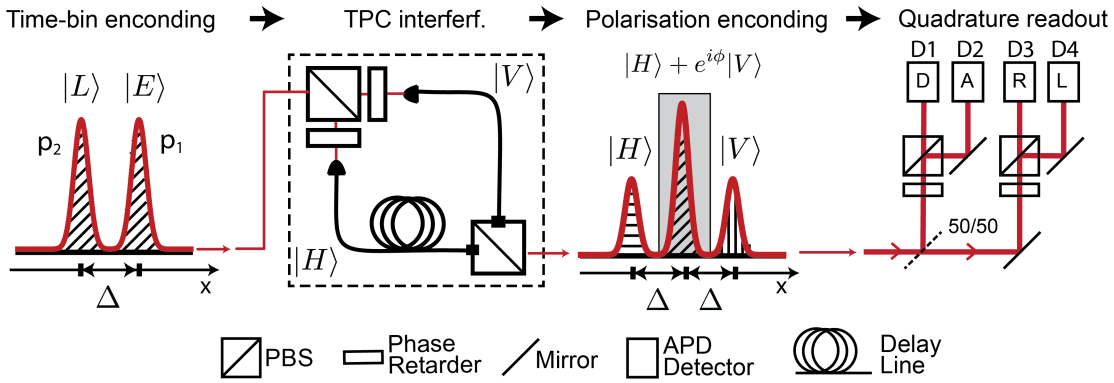


**Figure 6.3: Time-to-polarisation conversion (TPC) by unbalanced interferometer**. An incoming photonic qubit in a time-bin basis propagates through the interferometer and is converted into a polarisation qubit. The TPC is a passive process that succeeds half of the time, producing a photon click in the intermediate of three possible arrival windows (gray box in figure): this central wavepacket constitues the polarisation qubit. The two side lobes are discarded or used to perform a non-destructive z-measurement on the qubit. At last, a quadrature readout step performs a projective measurement on the photon and retrieves the phase accumulated in the interferometer.

$\varphi$ is the phase associated with the TPC interferometer. As a drift in $\varphi$ entails a change in the generated state, the observation of quantum correlations either requires the phase to be fixed by locking the interferometer or to be continuously monitored such that the expected state is known for each cycle. In this work the latter option was implemented and plays a vital role in the tomography of the system.

### 6.1.3 Tomography

The objective of quantum tomography is the reconstruction of the density matrix of a certain physical system. In this work, partial tomography was carried out: the overall set of measured correlations verifies entanglement, but does not suffice for the reconstruction of the entire density matrix. The analysis of the bipartite system comprises simultaneous projective measurement of the NV centre spin along an arbitrary spin basis $\{|\pm s\rangle\}$ and measurement of the photon in an arbitrary polarisation basis $\{|\pm p\rangle\}$, with:

$$\begin{aligned} |\pm s\rangle &= \cos(\theta_1)\,|0_s\rangle \pm e^{i\varphi_1}\sin(\theta_1)\,|-1_s\rangle \\ |\pm p\rangle &= \cos(\theta_2)\,|H\rangle \pm e^{i\varphi_2}\sin(\theta_2)\,|V\rangle \end{aligned} \tag{6.3}$$

for $\theta_1, \theta_2 \in [0, \pi]$ and $\varphi_1, \varphi_2 \in [0, 2\pi]$. For each spin-photon base pair $\{|\pm s\rangle\,, |\pm p\rangle\}$, a correlation $C_{s,p}$ is extracted from the joint probability outcomes, according to the following definition:

$$C_{s,p} = \text{prob}(+s,+p) + \text{prob}(-s,-p) - \text{prob}(+s,-p) - \text{prob}(-s,+p) \tag{6.4}$$

where ,

$$\begin{aligned} \text{prob}(+s,+p) &\rightarrow \text{spin projected in } |+s\rangle \text{ and photon in } |+p\rangle \\ \text{prob}(-s,-p) &\rightarrow \text{spin projected in } |-s\rangle \text{ and photon in } |-p\rangle \\ \text{prob}(-s,+p) &\rightarrow \text{spin projected in } |-s\rangle \text{ and photon in } |+p\rangle \\ \text{prob}(+s,-p) &\rightarrow \text{spin projected in } |+s\rangle \text{ and photon in } |-p\rangle \end{aligned} \tag{6.5}$$

The value of the correlations $C_{s,p}$ then verifies whether the system is separable or entangled - Section 6.2. For now we focus on the experimental implementation of projective measurements both in the photon and electronic spin space.

#### Spin tomography

Tomography on the electron spin is based on the optical resonant readout of the transition $|0\rangle \leftrightarrow |0_e\rangle$, which upon excitation and subsequent detection of a PSB photon performs a projective measurement onto the ground state $|0_s\rangle$ of the NV centre. Applying a $R_y(\theta)$

microwave spin rotation before the readout pulse [2] is then equivalent to a projective measurement along the meridian of the Bloch sphere containing the states $|\psi\rangle = (\cos(\theta/2)\,|0_s\rangle - \sin(\theta/2)\,|-1_s\rangle)$.

The duration (5 µs) and power (80 nW) of the readout pulse were optimized to maximize the readout contrast ($C$), resulting in $C = (98.8 \pm 0.2)\%$, which follows from a probability $F_0 = 16.7 \pm 0.1\%$ ($F_1 = 0.2 \pm 0.1\%$) of yielding a PSB photon per readout if the spin state is $|0\rangle$ ($|\pm 1\rangle$). Due to the high fidelity of the electronic spin rotations, the contrast of the optical readout is the limiting element in the accuracy of the spin tomography. A detailed account of the technical details pertaining to the spin readout can be found in section 4.2.4.

### Photon tomography

The characterization of the photonic wavefunction relies on the time-to-polarisation conversion (TPC) stage. An extensive description of the TPC hardware and function can be found in Section 4.4. The photon tomography results are susceptible to two intepretations: (1) the TPC stage performs tomography on a time-bin qubit and the combined action of the interferometer + quadrature readout stage implements an arbitrary projective measurement on a time-bin basis; or (2) the TPC stage converts the time-bin qubit into a polarisation basis and the interferometer phase is " absorbed" by the detection stage to define a phase-dependent projective basis on the polarisation space. For the remainder of this discussion, the latter interpretation is adopted. By "absorbing" the interferometer phase $\varphi$ into the measurement stage, we fix the generated spin-photon state $|\psi^+\rangle = (|0_s\rangle\,|V\rangle + |-1_s\rangle\,|H\rangle)/\sqrt{2}$, but obtain a dynamic measurement basis, which changes over time with the free-running phase of the interferometer.

After the TPC interferometer, the photon wavepacket emerges as three time-separated wavepackets, illustrated in Fig. 6.3, where a photon click in the time window of the central packet signals the successful conversion from time to a polarisation qubit. The first and third wavepackets have average intensities proportional to $\| \langle H|\psi\rangle \|^2$ and $\| \langle V|\psi\rangle \|^2$, respectively, thereby providing a means to perform a $\hat{\sigma}_z$-measurement.

For projective measurements on the equator of the Bloch sphere, the polarisation of the central sub-packet is analysed in the 4-detector quadrature-readout stage, as illustrated in Fig. 6.3. The-free running phase of the interferometer $\varphi(t)$ implies that the projective measurement realised by a detector $D_i$ is time-dependent. The relation between $\varphi$ and the dynamic

[2] In this experimental work, the $R_y(\theta)$ rotation was not necessarily applied before the final resonant readout pulse. Because the entanglement-generation operations, which includes $R_y(\theta)$ rotations and optical-$\pi$ pulse, approximately commute with the tomographic $R_y(\theta)$ rotation, its position in the overall sequence is irrelevant. For that reason this rotation appears frequently right after the initialisation stage.

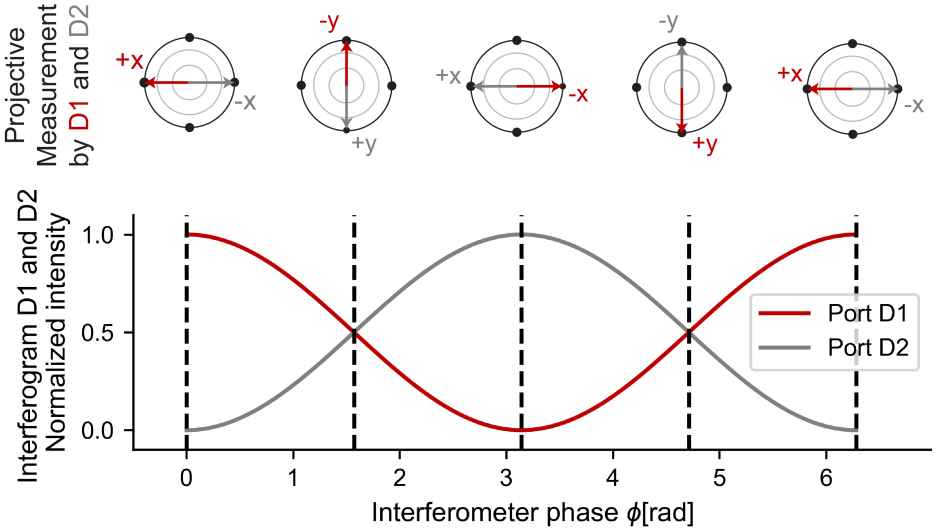


**Figure 6.4: Dynamic measurement basis in the polarisation space, implemented by the detectors $D_1$ and $D_2$, as a function of the interferometer phase.** The graph shows the expected output intensity of the probing field, for a diagonal polarisation input state $|D\rangle$, in port $D_1$ and $D_2$ as a function of the interferometer phase. For $\varphi = 0, \frac{\pi}{2}, \pi, \frac{3\pi}{2}$ and $2\pi$, the projective measurements implemented by the combined measurement device are represented in the x-y plane of the Bloch sphere.

measurement basis implemented by each detector can be succinctly described by:

$$\begin{aligned}
D_1: \quad |+x\rangle &\rightarrow |\varphi\rangle = \cos\left(\tfrac{\varphi}{2}\right)|+x\rangle - \sin\left(\tfrac{\varphi}{2}\right)|-x\rangle \\
D_2: \quad |-x\rangle &\rightarrow |\varphi-\pi\rangle = \sin\left(\tfrac{\varphi}{2}\right)|+x\rangle + \cos\left(\tfrac{\varphi}{2}\right)|-x\rangle \\
D_3: \quad |+y\rangle &\rightarrow \left|\varphi-\tfrac{\pi}{2}\right\rangle = \cos\left(\tfrac{\varphi}{2}-\tfrac{\pi}{4}\right)|+x\rangle - \sin\left(\tfrac{\theta}{2}-\tfrac{\pi}{4}\right)|-x\rangle \\
D_4: \quad |-y\rangle &\rightarrow \left|\varphi-\tfrac{3\pi}{2}\right\rangle = \sin\left(\tfrac{\varphi}{2}-\tfrac{\pi}{4}\right)|+x\rangle + \cos\left(\tfrac{\varphi}{2}-\tfrac{\pi}{4}\right)|-x\rangle
\end{aligned} \tag{6.6}$$

where $|\varphi\rangle$ and $|\varphi-\pi\rangle$ are mutually orthogonal projectors. As the value of $\varphi(t)$ is continuously tracked, the equatorial projective measurement is well defined for each experimental run and the detection events are sorted accordingly.

## 6.2 Partial Tomography and Entanglement Verification

In this work the verification of entanglement on the spin-photon state relies on measuring two correlations $C_{zz} = \langle \hat{\sigma}_{z,s} \otimes \hat{\sigma}_{z,p} \rangle$ and $C_{xx} = \langle \hat{\sigma}_{x,s} \otimes \hat{\sigma}_{x,p} \rangle$. These are also referred to as zz- and xx-basis measurements. While $C_{zz}$ comprises the joint probabilities $p(\pm z_s, \pm z_p)$, expressed in the diagonal elements of the density matrix of the spin-photon state ($\rho_{11}$, $\rho_{22}$, $\rho_{33}$ and $\rho_{44}$), $C_{xx}$ depends on the off-diagonal elements, the coherences. The two quantities can be written

explicitly as:

$$\begin{aligned} C_{zz} &= \text{prob}(+z_s, +z_p) + \text{prob}(-z_s, -z_p) - \text{prob}(+z_s, -z_p) - \text{prob}(-z_s, +z_p) \\ C_{xx} &= \text{prob}(+x_s, +x_p) + \text{prob}(-x_s, -x_p) - \text{prob}(+x_s, -x_p) - \text{prob}(-x_s, +x_p) \end{aligned} \tag{6.7}$$

where as before the $\text{prob}(s, p)$ terms refer to the joint probability outcomes of the projective measurements on the spin and photon.

For an easier reading of the results, it is convenient to write the expected spin-photon state in the basis $(\hat{\sigma}_z \otimes \hat{\sigma}_z)$, $(\hat{\sigma}_x \otimes \hat{\sigma}_x)$ and $(\hat{\sigma}_x \otimes \hat{\sigma}_\varphi)$, where the latter basis refers to the spin being projected in $|\pm x_s\rangle$ and the photon in $\left|\varphi_p\right\rangle$, belonging to the continuum of states in the equator of the Bloch sphere, as determined by the interferometer phase $\varphi$:

$$\begin{aligned} \hat{\sigma}_z \otimes \hat{\sigma}_z : \quad |\psi^+\rangle &= \tfrac{1}{\sqrt{2}}(|0_s\rangle\,|V\rangle + |-1_s\rangle\,|H\rangle) \\ \hat{\sigma}_x \otimes \hat{\sigma}_x : \quad |\psi^+\rangle &= \tfrac{1}{\sqrt{2}}(|+x_s\rangle\,|+x\rangle - |-x_s\rangle\,|-x\rangle) \\ \hat{\sigma}_x \otimes \hat{\sigma}_\varphi : \quad |\psi^+\rangle &= \tfrac{1}{\sqrt{2}}(\cos(\varphi/2)\,|+x_s\rangle\,|\varphi\rangle + \sin(\varphi/2)\,|+x_s\rangle\,\left|\varphi_\perp\right\rangle \\ &\quad - \sin(\varphi/2)\,|-x_s\rangle\,|\varphi\rangle + \cos(\varphi/2)\,|-x_s\rangle\,\left|\varphi_\perp\right\rangle) \end{aligned} \tag{6.8}$$

where $\left\langle\varphi\middle|\varphi_\perp\right\rangle = 0$.

The expected outcomes for the measurements on the spin-photon system are illustrated in Fig. 6.5, where the conditional probability $p(\pm x_s\,|\varphi_p)$, which is the probability of measuring the spin on the $|\pm x_s\rangle$ state, given the photon was projected on the state $\left|\varphi_p\right\rangle$, is plotted against the interferometer phase $\varphi$, for the four detection ports ($D_1$, $D_2$, $D_3$ and $D_4$). Since the only difference between the expected sinusoidal curves in the different ports is a fixed phase shift, e.g. $D(\varphi = 0) = R(\varphi = \pi/4)$, all curves are overlapped for the calculation of the bipartite correlations and for the presentation of the experimental data.

The entanglement of the spin-photon system is quantified by estimating a lower bound on the fidelity of the generated state $\hat{\rho}$, with respect to the maximally entangled Bell-state $\psi^+$, following the same procedure as Refs. [93, 155]:

$$\begin{aligned} F &= \text{Tr}(|\psi^+\rangle\langle\psi^+|\,\hat{\rho}) = \langle\psi^+|\,\hat{\rho}\,|\psi^+\rangle \\ &= \rho_{22} + \rho_{33} + 2\,\text{Re}(\rho_{23}) \end{aligned} \tag{6.9}$$

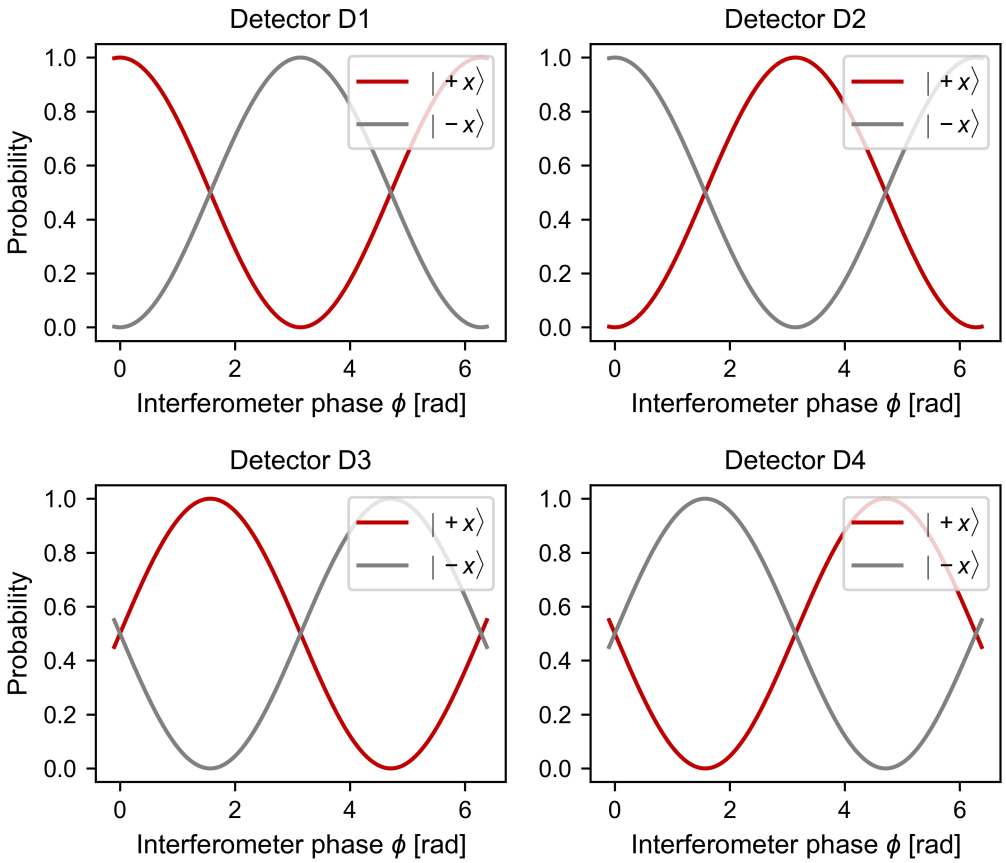


**Figure 6.5: Expected measurement outcomes for the spin-photon $\psi^+$ Bell state, in the four detection ports $D_1$, $D_2$, $D_3$ and $D_4$ of the quadrature readout stage**. Ideal conditions were assumed. The red(gray) curve refers to a spin projection into the $|+x\rangle$ ($|-x\rangle$) vector.

with

$$\left|\psi^{+}\right\rangle\left\langle\psi^{+}\right| = \frac{1}{2}\begin{bmatrix} 0 & 0 & 0 & 0 \\ 0 & 1 & 1 & 0 \\ 0 & 1 & 1 & 0 \\ 0 & 0 & 0 & 0 \end{bmatrix} \quad \text{and} \quad \hat{\rho} = \begin{bmatrix} \rho_{11} & \rho_{12} & \rho_{13} & \rho_{14} \\ \rho_{21} & \rho_{22} & \rho_{23} & \rho_{24} \\ \rho_{31} & \rho_{32} & \rho_{33} & \rho_{34} \\ \rho_{41} & \rho_{42} & \rho_{43} & \rho_{44} \end{bmatrix} \tag{6.10}$$

While the terms $\rho_{22}$ and $\rho_{33}$ are directly extracted from a zz-basis measurement, corresponding to the $|0_s\rangle\,|V\rangle$ and $|1_s\rangle\,|H\rangle$ populations, estimating $2\,\mathrm{Re}(\rho_{23})$ requires measuring on the equatorial xx-basis. To determine the relation between $2\,\mathrm{Re}(\rho_{23})$ and the outcomes of the xx-projection, the rotation of both qubits into the equator of the Bloch sphere is applied and a "rotated" density matrix $\tilde{\rho}$ retrieved:

$$\tilde{\rho} = \left[\mathrm{R}_y(\frac{\pi}{2}) \otimes \mathrm{R}_y(\frac{\pi}{2})\right]\ \hat{\rho}\ \left[\mathrm{R}_y^{\dagger}(\frac{\pi}{2}) \otimes \mathrm{R}_y^{\dagger}(\frac{\pi}{2})\right] \tag{6.11}$$

whose diagonal elements contain the xx-correlations, according to:

$$\begin{aligned} C_{xx} &= \tilde{\rho}_{11} + \tilde{\rho}_{44} - \tilde{\rho}_{22} - \tilde{\rho}_{33} \\ &= 2\,\mathrm{Re}\{\rho_{2,3}\} + 2\,\mathrm{Re}\{\rho_{1,4}\} \end{aligned} \tag{6.12}$$

Following the definition of the density matrix, the term $\mathrm{Re}\{\rho_{1,4}\}$ is bounded by the relation $|\,\mathrm{Re}\{\rho_{14}\}| \leq \sqrt{\rho_{11}\rho_{44}}$, which together with Eq. 6.12 renders the following inequality:

$$\mathrm{Re}\{\rho_{23}\} \geq \frac{1}{2}(C_{xx} - 2\sqrt{\rho_{11}\rho_{44}}) \tag{6.13}$$

By plugging this relation in Eq. 6.9, a lower bound on the entanglement fidelity is found:

$$F \geq \frac{1}{2}\left(\rho_{22} + \rho_{33} + C_{xx} - 2\sqrt{\rho_{11}\rho_{44}}\right) \tag{6.14}$$

This relation verifies a non-classic entangled system for $F > 0.5$. Furthermore, it is particularly useful, because all terms involved can be extracted from xx- and zz-basis measurements.

The results of the partial tomography on the generated state are presented in Fig. 6.6, where background light present in the ZPL detection was subtracted, such that the quality of the source was probed directly. The method used in the deduction of the background counts is explained in Section 6.2. The zz-measurement outcomes fix the value of the diagonal entries of the density matrix $\rho_{ii}$, reaching an estimated zz-correlation of $C_{zz} = \langle\hat{\sigma}_z \otimes \hat{\sigma}_z\rangle = (-83.8 \pm 1.6)\%$. The xx-measurements validate the non-classical behaviour of the system and correspond to an assessed xx-correlation of $C_{xx} = \langle\hat{\sigma}_x \otimes \hat{\sigma}_x\rangle = (40.7 \pm 2.9)\%$.

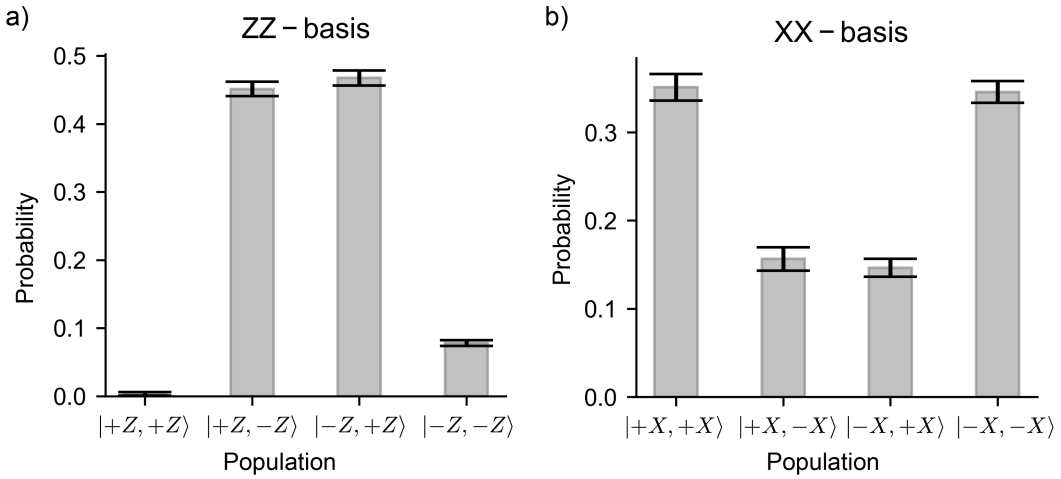


**Figure 6.6: Measured correlations for the spin-photon state $|\psi^+\rangle$, corrected for background noise**. The error bars are estimated from the statistical noise $\sqrt{n}$ of the 2-photon coincidence events associated with the joint spin-photon projective measurement into each population (e.g. $\varepsilon(|+x,+x\rangle) = \sqrt{n_{(+x,+x)}}$). **a)** Measurement outcomes in the zz-basis (e.g. $|+z,+z\rangle = |o_s\rangle\,|H\rangle$), amounting to a correlation $C_{zz} = \langle\hat{\sigma}_z \otimes \hat{\sigma}_z\rangle = (-83.8 \pm 1.6)\%$. **b)** Measurement outcomes in the xx-basis, conforming with $C_{xx} = \langle\hat{\sigma}_x \otimes \hat{\sigma}_x\rangle = (40.7 \pm 2.9)\%$.

Fig. 6.7 generalises the measurement outcomes of Fig. 6.6, by showing the behaviour of the system for an arbitrary photon projection along the equator of the Bloch sphere.

This result is particularly elucidative as in a separable or classical system the spin projection probability into $|\pm x_s\rangle$ would be independent of the measured state of the photon and the presented sinusoidal curves would be flat. More quantitatively, the estimated values for the $\rho_{ii}$ entries and $C_{xx}$ are plugged into the inequality 6.14 to retrieve an entanglement lower bound of $F \geq (64.7 \pm 1.3)\%$, unambiguously establishing entanglement in the system by 11 standard deviations.

The counterpart of the tomographic results, without background subtraction, is also presented, in Fig. 6.8. Background noise leads to an overall degradation of the correlations, but entanglement was verified in this case too. Following the same procedure as before, the estimated correlations are $C_{zz} = \langle\sigma_z \otimes \sigma_z\rangle = (-77.4 \pm 1.4\%)$ and $C_{xx} = \langle\sigma_x \otimes \sigma_x\rangle = (32.7 \pm 1.3)\%$, leading to a bound on the entanglement fidelity of $F \geq (56.0 \pm 0.9)\%$, thereby beating the classical boundary by 6 standard deviations.

The presented $C_{xx}$ correlations result from accumulating photons over $2.5 \times 10^9$ repetitions of the entangling sequence, for each spin projection, which totals 250 hours of experimental run time. Similarly the zz-correlations result from $5 \times 10^9$ repetitions of the experimental cycle. Due to the low ZPL efficiency (detection events per excitation pulse) of $\eta_{ZPL} \sim 2 \times 10^{-5}$ and a PSB

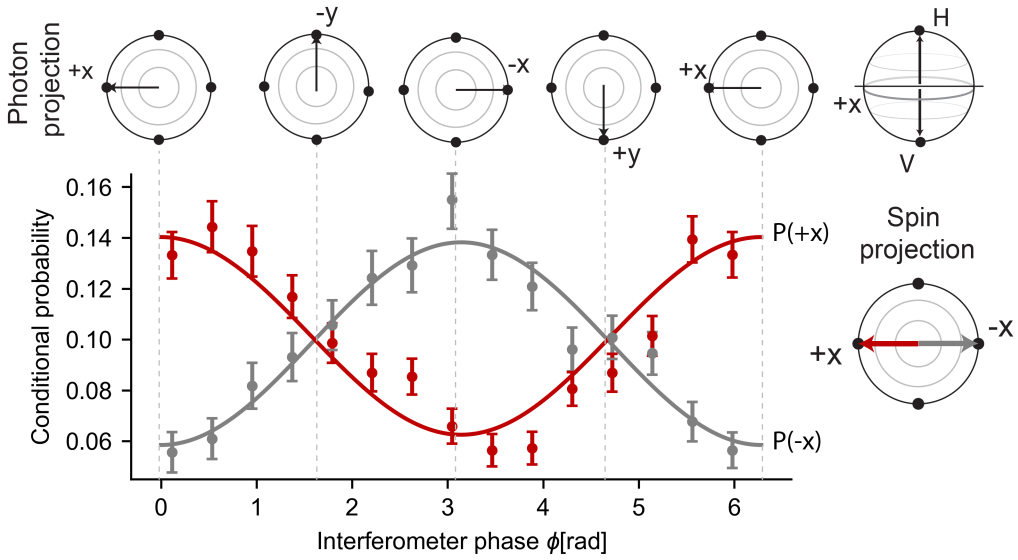


**Figure 6.7: Conditional probability of measuring the spin in $|+x_s\rangle$ or $|-x_s\rangle$, given a photon projection into $|\varphi\rangle$.** The departure from a flat line witnesses a non-classical behaviour. The phase uncertainty for each data point is determined by the resolution of the phase readout: $\pm 0.06$ radians - Section 4.4.2. The Bloch spheres depict the equatorial photon projectors $|\varphi\rangle\langle\varphi|$, as set by the interferometer phase.

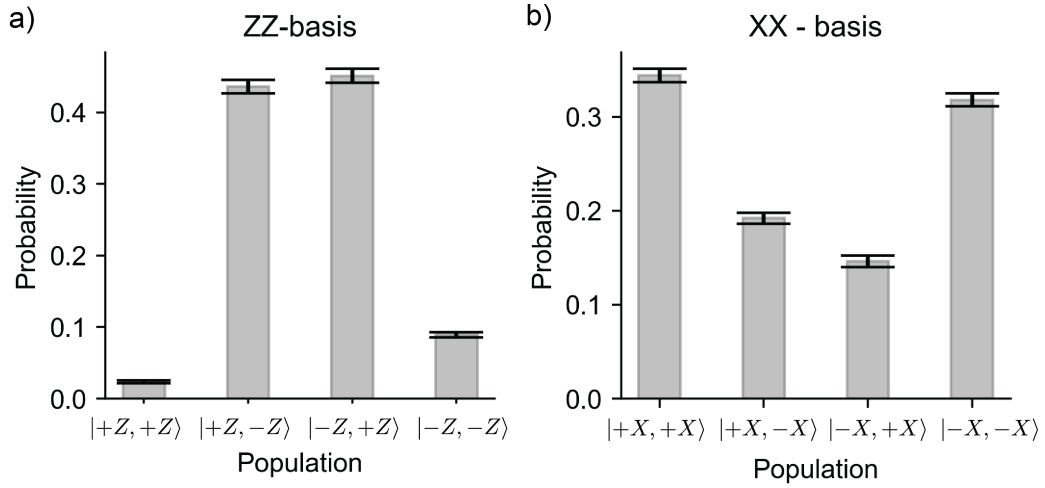


**Figure 6.8: Spin-photon correlations without background subtraction.** **a)** Measurement outcomes in the zz spin-photon basis, with a correlation $C_{zz} = \langle \sigma_z \otimes \sigma_z \rangle = (-77.4 \pm 1.4)\%$. **b)** Measurement outcomes in the xx-basis, with $C_{xx} = \langle \sigma_x \otimes \sigma_x \rangle = (32.7 \pm 1.3)\%$.

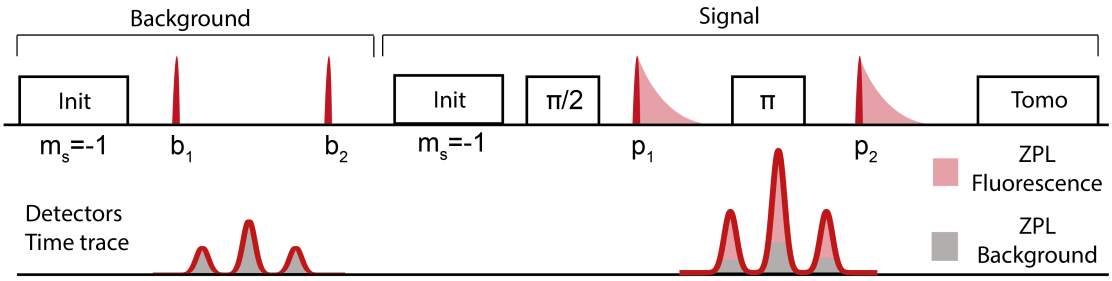


**Figure 6.9: Background subtraction from the ZPL signal**. The first part of the experimental sequence is intended to provide a measure of background counts in the ZPL signal, by applying two optical-$\pi$ pulses on a system initialised on the off-resonant $m_s = -1$ state.

efficiency of $\eta_{PSB} = 16.7 \pm 0.1\%$, we observed an average of 25 PSB-ZPL coincidence events per hour, which sets the entangling rate of the setup.

The non-unit correlation values and fidelities hint at the limitations of the experimental apparatus and the physical system used to implement the entanglement-generation protocol. This topic is developed in Section 6.3.

### Background Subtraction

The evaluation of the presented correlations relies on counting coincidence events between the optical readout of the spin (photon-click in the PSB detector) and projective measurements of the ZPL photons' polarisation (photon-click in the ZPL detectors $D_1/D_2$ or $D_3/D_4$). Whereas the signal-to-background ratio on the PSB detectors is high (SBR $= 130 \pm 1$), as reported in Section 4.2.3, the signal in the ZPL detectors has a significant contribution from background noise (SBR $= 1.6$, per port), due to residual excitation light, detector dark counts, leaking of probe field light, residual ambient light, among others. As these ZPL background clicks lead to uncorrelated coincidence events with the PSB spin readout, isolating the quantum correlations between the NV center and the emitted photons requires discerning the ZPL-clicks emitted by NV center from the spurious technical clicks. The correlations presented in Figs. 6.6 and 6.7 were subject to a background correction. Mathematically the background-corrected conditional probabilitiy of getting a PSB-click, given there was a ZPL-click associated with an interferometer phase $\varphi$, can be represented as:

$$\text{Prob}(PSB \mid ZPL)(\varphi) = \frac{N_{(PSB \wedge ZPL)}(\varphi) - N_{(PSB \wedge Bkg)}(\varphi)}{N_{ZPL}(\varphi) - N_{Bkg}(\varphi)} \tag{6.15}$$

$N_{(PSB \wedge ZPL)}$ is the number of coincidence events between the PSB and ZPL detectors and $N_{ZPL}$ is the total number of times a ZPL detector registered a photon; $N_{(PSB \wedge Bkg)}$ accounts for the

coincidence events between PSB and ZPL background clicks and $N_{Bkg}$ is the total number of ZPL background events. To determine $N_{(PSB \wedge Bkg)}$ and $N_{Bkg}$, a pair of reference optical $\pi$-pulses was placed at the end of the initialisation stage of the experimental sequence - see Fig.6.9. As the optical cross talk on the $m_s = -1$ transition is negligible and the initialisation fidelity into $m_s = 0$ high, the counts registered in the reference detection window do not have a fluorescence component and work as an indicator of the background content of the signal detection.

## 6.3 Imperfections of the System and Outlook

This section addresses the experimental limitations of the apparatus, which degrade the entanglement fidelity and generation rate, followed by a discussion on the multi-photon outlook for an NV-based platform running the TPC entanglement-generation scheme.

The ideal execution of the entangling sequence,

$$[\text{Init}][\pi_s/2][\pi_{\text{opt}}][\pi_s][\pi_{\text{opt}}] \tag{6.16}$$

where [Init] is the initialisation of the electronic spin into $m_s = -1$, $[\theta_s]$ are the y-rotations of the electronic spin and $[\pi_{\text{opt}}]$ are the optical $\pi$ pulses, leads to the production of a maximally entangled Bell-state $\psi^+$. Imperfect spin rotations, spin-mixing in the excited state, erroneous photon-clicks due to scattering of laser light, among others, lead to a departure from the ideal case and to the reduction of the entanglement fidelity. In this section a quantitative analysis of these imperfections is carried out.

To account for the different sources of error, the density matrix of the spin-photon state $\rho_{\text{Total}}$ is decomposed in the following components:

$$\rho_{\text{Total}} = \alpha_{\text{NV}} \left(\alpha_{\text{ent}}\, \rho_{\text{ent}} + \alpha_{\text{NInit}}\, \rho_{\text{NInit}} + \alpha_{\text{oP}}\, \rho_{\text{mix}}\right) + \alpha_{\text{uc}}\, \rho_{\text{mix}} + \alpha_{\text{scat}}\, \rho_{\text{scat}} + \alpha_{\text{prb}}\, \rho_{\text{prb}} \tag{6.17}$$

where, in general, $\rho_{\text{event}}$ is the 4x4 density matrix of an arbitrary state resulting from an "event" and $\alpha_{\text{event}}$ refers to the fraction of spin-photon coincidences resulting from that particular event. All elements, except for $\rho_{Mix}$, are dependent on the interferometer's phase $\varphi$ and are described in the following lines:

- $\alpha_{\text{NV}}$ describes the fraction of coincidence events derived from NV fluorescence;
- $\alpha_{\text{ent}}$ is the fraction of events resulting from a successful initialisation [Init] and an ideal execution of the protocol $[\pi_s/2][\pi_{\text{opt}}][\pi_s][\pi_{\text{opt}}]$, leading to the generation of a state $\rho_{\text{ent}} = |\psi^+\rangle \langle\psi^+|$

- $\alpha_{\text{NInit}}$ is the probability of initialising the electron spin in the $m_s = -1$ state, instead of $m_s = 0$. Followed by a successful execution of the protocol, it renders the output state $\rho_{\text{Ninit}} = |\psi^-\rangle\langle\psi^-|$, which produces opposite correlations to $\rho_{\text{ent}}$.

- $\alpha_{\text{op}}$ is the probability that the initialisation is successful, but the sequence $[\pi_s/2][\pi_{\text{opt}}][\pi_s][\pi_{\text{opt}}]$ leads to an undesired spin-photon trajectory between spin rotation pulses, caused by spin mixing in the optical excited state or spin flips through the meta-stable decay. A classical decision tree was used to model this invalid spin trajectories and it was established that these events are well described by $\rho_{\text{mix}} = \hat{Id}/4$, a classic fully mixed state.

- $\alpha_{\text{uc}}$ is the fraction of coincidence events involving a ZPL detector dark count click, resulting in an uncorrelated spin-photon state $\rho_{\text{mix}}$.

- $\alpha_{\text{scat}}$ is the fraction of coincidences caused by resonant red laser light from the $[\pi_{\text{opt}}]$ pulses leaking through the interferometer into the detection window. This leads to a spin-photon state $\rho_{\text{scat}}$ which is uncorrelated, but whose coincidences have a sinusoidal dependence on the interferometer phase $\varphi$.

- $\alpha_{\text{prb}}$ refers to coincidence events in which a photon derives from the probe field and leaks into the ZPL detection window. The resulting $\rho_{\text{prb}}$ is also spin-photon uncorrelated and has a dependence on the interferometer phase $\varphi$, but shows a phase displacement with respect to $\rho_{\text{scat}}$ due to the 350 MHz frequency change induced by the acousto-optic modulation.

The limited coherence length of the laser also leads to a reduction of the fidelity of the generated state and is therefore taken into account in this model. As the phase of the two photonic wavepackets generated by the $[\pi_{opt}]$ pulses is inherited from the laser, a phase jump between the two excitation pulses will be reflected in the phase of the spin-photon state. To account for this, the density matrices associated with events where one photon propagates through the interferometer (e.g. $\rho_{\text{ent}}$, $\rho_{\text{Ninit}}$, $\rho_{\text{scatter}}$ and $\rho_{\text{probe}}$) and a laser phase jumps $\Delta\varphi$ occurs are modified: $\rho_{\text{event}} \rightarrow \rho^{\text{phase}}_{\text{event}}$. To provide an example of the method, $\rho_{\text{ent}}$ and $\rho_{\text{scatter}}$ become:

$$\rho^{\text{phase}}_{\text{ent}} = \tfrac{1}{2}\begin{bmatrix} 0 & 0 & 0 & 0 \\ 0 & 1 & e^{-i\Delta\varphi} & 0 \\ 0 & e^{i\Delta\varphi} & 1 & 0 \\ 0 & 0 & 0 & 0 \end{bmatrix}; \quad \rho^{\text{phase}}_{\text{scat}} = \tfrac{1}{4}\begin{bmatrix} 1 & e^{-i\Delta\varphi} & 0 & 0 \\ e^{i\Delta\varphi} & 1 & 0 & 0 \\ 0 & 0 & 1 & e^{-i\Delta\varphi} \\ 0 & 0 & e^{i\Delta\varphi} & 1 \end{bmatrix} \tag{6.18}$$

As the phase jumps, $\Delta\varphi$, can take any value in the interval $[0, 2\pi]$, the effective density

| Coefficient | Value (%) | Contribution |
|---|---|---|
| $a_{NV}$ | 59.7 | Both photons originate from NV |
| $a_{ent}$ | 87.5 | Generated the correct $\|\psi^+\rangle\langle\psi^+\|$ state |
| $a_{Ninit}$ | 2.1 | Init. into $m_s = -1$ leads to $\|\psi^-\rangle\langle\psi^-\|$ state |
| $a_{op}$ | 10.5 | Undesired spin trajectory during optical decay |
| $a_{uc}$ | 13.2 | Detection event was caused by dark counts |
| $a_{scat}$ | 4.3 | Detection event caused by laser scatter light |
| $a_{prb}$ | 23.0 | Detection event due to leaking probe field photon |

**Table 6.1: $a_p$ coefficients for the density matrix $\rho_{\text{Total}}$ expansion.**

matrices, denoted with a tilde as $\tilde{\rho}_{\text{event}}$, are calculated as an average over all cases:

$$\tilde{\rho}_{\text{event}} = \underbrace{(1 - P_{pj}) \times \rho_{\text{event}}}_{\text{No Laser phase jump}} + \underbrace{P_{pj} \times \frac{1}{2\pi} \int_0^{2\pi} \rho_{\text{event}}^{\text{phase}}(\varphi)\, d\varphi}_{\text{Laser phase jump occurs}} \tag{6.19}$$

where $P_{pj}$ is the probability of a laser phase jump between the two $[\pi_{\text{opt}}]$ pulses. For the example cases in Eq. 6.18, averaging over the laser phase jump damps the off-diagonal entries to zero. $P_{pj}$ has been established experimentally by letting only laser scatter light into the interferometer and measuring the visibility $V$ of the interference fringes at the output. From the relation $P_{pj} = 1 - V$, we have extracted the laser jump probability: $P_{pj} = 0.10 \pm 0.02$.

The coefficients $a_{NV}$, $a_{uc}$, $a_{scat}$ and $a_{prb}$ from the expansion of $\rho_{\text{Total}}$ in Eq. 6.17 were determined through calibration measurements. Differently, the coefficients $a_{ent}$, $a_{Ninit}$ and $a_{op}$ were retrieved through a classical decision tree which considered the possible evolution paths of the spin-photon system during the protocol execution, taking into account the limited initialisation fidelity of the electron spin and the probability of an electronic spin flip due to $[\pi_{\text{opt}}]$, which is equal to 13.5% - see Section 4.2.4. The decision tree assumes perfect spin gates and perfect population inversion by the optical $\pi$-pulses. It neglects optical cross-talk with the $|\pm 1\rangle \rightarrow |\pm 1_e\rangle$ transition, as it was measured to lay below 1% - Section 4.2.4. A summary of the estimated $a_p$ values is found in Table 6.1, with which the expected spin-system density matrix $\rho_{\text{Total}}$ was calculated. The expected conditional probability of measuring the spin in $|+x_s\rangle$ or $|-x_s\rangle$, given a photon projection in the polarisation state $\left|\varphi_p\right\rangle$ could then be estimated through the relation:

$$\text{prob.}_{\rho}(\pm x_s|\varphi_p) = \left\langle \pm x_s, \varphi_p \right| \rho_{Total} \left| \pm x_s, \varphi_p \right\rangle \tag{6.20}$$

and the corresponding correlations extracted. For simplicity the theoretical and experimental results were compared through their $C_{xx}$ correlations, represented in Table 6.2. Recall that for a maximally entangled state one should observe $C_{xx} = 1$ and a deviation from a unit value mirrors

some experimental imperfection. To understand the impact of the individual experimental limitations, the coefficients $a_p$ were progressively adjusted to their real value and the corresponding decrease in $C_{xx}$ is described in the column $\Delta C_{xx}/C_{xx}$. Reading Table 6.2 from top to bottom, corresponds to gradually correcting experimental imperfections, identified in the last column, until the ideal setup is obtained. The normalized spin readout contrast is quantified by $V_{RO}$.

When all the imperfections are considered (top row, Table 6.2), the expected correlation is $C_{xx} = 45.7\%$, which is greater than the corresponding measured value of $C_{xx} = 32.7 \pm 1.3$, without background subtraction. This suggests that the model is missing sources of error which could not be adequately quantified. Nonetheless, Table 6.2 hints at leading detrimental contributions from the probing field and detector dark counts within the ZPL detection window, associated with a relative decrease in the correlation value of $\Delta C_{xx}/C_{xx} = 24.2\%$ and $22.1\%$, respectively. The excited state spin-mixing and the finite laser coherence have a more modest impact, at $\Delta C_{xx}/C_{xx} = 12.1\%$ and $11.1\%$.

Missing sources of error in our model include the imperfect population inversion upon optical excitation, imperfect spin gates and the neglected optical cross-talk in excitation. The coherence lifetime of the spin qubit $T_2^*$ as well as spectral diffusion of the optical transition have been ignored too. Despite these simplifications, the model provides a clear indication of the weaknesses of the apparatus and what could be improved. Specifically, detectors with lower dark counts would significantly enhance $C_{xx}$ and the leaking probing field could be corrected by employing better modulation through, for example, two AOMs in series. Resorting to low strain NVs would supress spin-mixing in the excited state by one order of magnitude and improve the contrast of the optical spin readout $V_{RO}$[80].

| $\alpha_{\text{ent}}$ | $\alpha_{\text{op}}$ | $\alpha_{\text{NInit}}$ | $\alpha_{\text{NV}}$ | $\alpha_{\text{uc}}$ | $\alpha_{\text{scat}}$ | $\alpha_{\text{prb}}$ | $p_{LD}$ | $V_{RO}$ | $C_{xx}$ | $\Delta C_{xx}/C_{xx}$ | Comment |
|---|---|---|---|---|---|---|---|---|---|---|---|
| 0.875 | 0.105 | 0.0198 | 0.597 | 0.132 | 0.0436 | 0.230 | 0.1 | 0.978 | **0.457** | - | Experimental conditions |
| 0.875 | 0.105 | 0.0198 | 0.775 | 0.171 | 0.0545 | 0 | 0.1 | 0.978 | **0.568** | 0.242 | No leaking of probe field |
| 0.875 | 0.105 | 0.0198 | 0.820 | 0.181 | 0 | 0 | 0.1 | 0.978 | **0.598** | 0.050 | Perfect scatter rejection |
| 0.875 | 0.105 | 0.0198 | 1 | 0 | 0 | 0 | 0.1 | 0.978 | **0.730** | 0.221 | No detector dark counts |
| 0.893 | 0.107 | 0 | 1 | 0 | 0 | 0 | 0.1 | 0.978 | **0.762** | 0.044 | Perfect NV initialisation |
| 1 | 0 | 0 | 1 | 0 | 0 | 0 | 0.1 | 0.978 | **0.854** | 0.121 | No spin mixing in the ES |
| 1 | 0 | 0 | 1 | 0 | 0 | 0 | 0.1 | 1 | **0.9** | 0.054 | With perfect spin-readout |
| 1 | 0 | 0 | 1 | 0 | 0 | 0 | 0 | 1 | **1** | 0.111 | With infinite laser coherence |

**Table 6.2: Expected $C_{xx}$ correlations for the generated $|\psi^+\rangle$ spin-photon state.** Reading from bottom to top, experimental imperfections are gradually added until the experimental conditions are reached. $V_{RO}$ expresses the contrast of the optical spin readout. $P_{LD}$ is the probability of laser dephasing during the entangling sequence.

| Instance | Loss factor | $T_{ZPL}$ | $T_{PSB}$ |
|---|---|---|---|
| Sample surface with anti-reflection coating (PSB) | 0.1 | | 0.9 |
| Sample surface with anti-reflection coating (ZPL) | 0.05 | 0.95 | |
| Cryostat window | 0.57 | 0.41 | 0.39 |
| Objective (numerical aperture and transmission loss) | 0.87 | 0.053 | 0.05 |
| Detector efficiency | 0.35 | 0.034 | 0.032 |
| Other optical elements in PSB path | 0.49 | | 0.017 |
| Fibre coupling to interferometer | 0.5 | 0.017 | |
| Interferometer TPC success rate | 0.5 | 0.009 | |
| Interferometer output PBS | 0.26 | 0.006 | |
| Other optical elements in ZPL path | 0.81 | 0.0012 | |

**Table 6.3: Effective optical transmission through the system.** Read from top to bottom to follow the beam path until detection. The loss factor represents the fractional loss of photons at each stage of the setup. $T_{ZPL}(T_{PSB})$ shows the remaining fractional power in the ZPL(PSB) beam. The entries "Other optical-path elements" encompass the combined loss induced by mirrors, filters and beam splitters. The first two entries express the wavelength dependence of the anti-reflection coating, resulting in a different transmittance for the ZPL and PSB.

So far the discussion was focused on the experimental elements that degrade the entanglement-generation fidelity. Another relevant figure of merit of the apparatus is the collection efficiency (probability of a photon detection per optical excitation) and the closely related entangling rate. The collection efficiency of the system was characterized through calibration measurements and summarized in Table 6.3. The loss factor represents the relative loss of power ($P_{lost}/P_{in}$) at a particular element of the apparatus. The presented values are not to be taken as definite but as a rough indicator, as coupling losses varied among different experimental runs by a few percentage points.

Losses at the anti-reflection coating are wavelength dependent and justify the difference between the loss on the ZPL and PSB beams. The cryostat window is responsible for a wavefront distortion which accounts for a 57% loss. The detector (Excelitas SPCM-APD) efficiencies are given by their factory specifications. The losses in the interferometer output follow the specification of the manufacturer. The time-to-polarisation conversion succeeds in 50% of the trials, as explained in Section 4.4. Taking all contributions into consideration, 0.12% of the overall ZPL fluorescence is detected, against $\eta_{psb} = 1.7\%$ for the PSB system efficiency (photon clicks per excitation). As only $\sim 2.5\%$ of the fluorescence falls within the spectral window of the ZPL, the total ZPL system efficiency is $\eta_{ZPL} \sim 2 \times 10^{-5}$, in accordance with the value observed experimentally and constituting the bottleneck in the observed entangling rate of 25 Bell pairs per hour.

## 6.4 Outlook

Summarising the experimental results, we have realised the fundamental unit of a scalable entanglement-generation protocol based on a single optical transition of a single-photon emitter, facilitated by TPC conversion by an unbalanced polarised interferometer. A nitrogen-vacancy centre was used as emitter, leading to the generation of spin-photon Bell-pairs $|\psi^+\rangle$ with a fidelity $F \geq (64.7 \pm 1.3)\%$, at a rate of 25 pairs per hour. By employing a single optical transition, the TPC scheme lowers the requirements placed on the emitter and broadens the range of physical platforms which could be used for photonic entanglement generation. The scalability of the experiment is dependent on the system efficiency $\eta$ (ratio of collected photons to optical excitations). In our case, a ZPL system efficiency of $\eta_{zpl} \sim 2 \cdot 10^{-5}$ did not permit the generation and detection of multi-photon ($N \geq 2$) entanglement. The experimental requirements for scaling the system and reaching the multi-photon regime are discussed quantitatively in the coming paragraphs.

Repetition of the fundamental unit of the TPC entangling scheme leads to the generation of N-photon cluster states - see Section 2.3. Even though the scheme is, in-principle, deterministic, photon loss leads to non-unit success probability. A low ZPL system efficiency, $\eta_{zpl}$, requires many repetitions until success. Consider an experimental sequence which generates a N-photon cluster state, requiring 2N excitation-emission cycles. The chance of success, i.e. the probability that each of the N-iterations produces a photon which is then detected, is given by $p = \eta_{zpl}^N$. The average number of experimental trials till success is then $\#_{succ} = p^{-1}$, corresponding to an average waiting time of $\tau = \#_{succ} \times T_{cycle}$, where $T_{cycle}$ is the duration of an experimental trial. Therefore the N-photon entangling rate is given by:

$$R(N) = \frac{\eta^N}{(t_{prep} + N \times t_e)} \tag{6.21}$$

where $t_{prep}$ is the preparation time of a cycle (e.g. charge and spin initialisation routine) and $t_e$ is the added time to the cycle per photon. Using Eq. 6.21, the generation time of N-photon states was calculated and represented in Fig. 6.10 a, for different system efficiencies $\eta_{zpl}$, assuming $t_{prep} = 170$ µs and $t_e = 0.350$ µs. The red trace is representative of our current experimental conditions, according to which it takes 10 s to produce a spin-photon state [3]. A 2-photon-cluster state would have required a waiting time of $4 \times 10^5$ s, or 4.6 days, per state.

Even for a very optimistic improvement of the collection efficiency to 25% (for example, by

[3] For comparison with the reported entangling time of 144 s (entangling rate of 25 events per hour), recall that this value is in fact the **entanglement detection** time, where a coincidence detection between ZPL and PSB is required. Because the spin preparation is deterministic, the **entanglement generation** does not require a spin readout and its duration is then reduced to the average time per ZPL detection of $\sim$ 10s

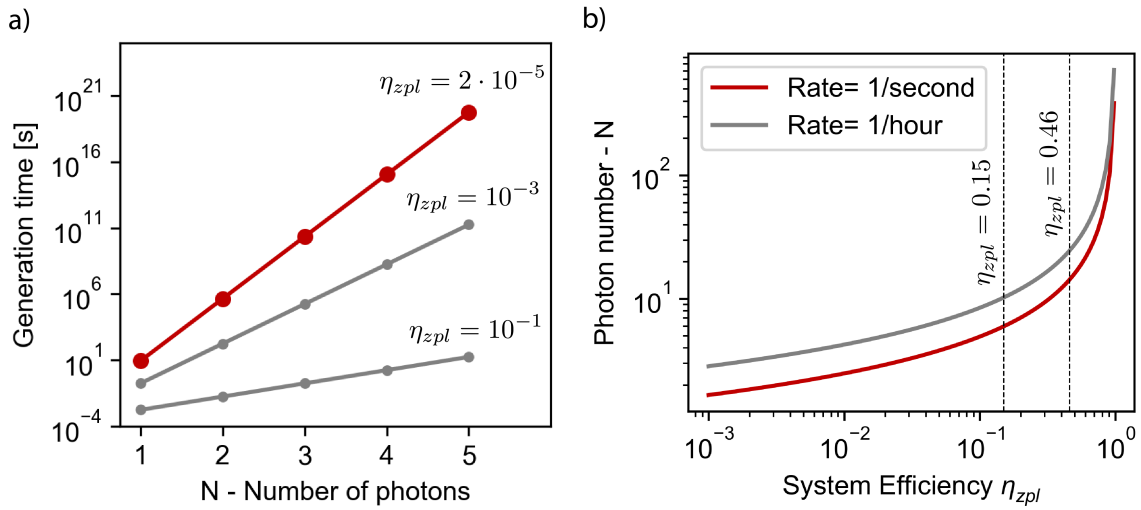


**Figure 6.10: Generation of N-photon cluster states**. a) Presents the average generation time for a N-photon cluster state, for different ZPL system efficiencies $\eta_{ZPL}$. The red trace corresponds to our current experimental conditions. b) Attainable N-photon state for a given system efficiency $\eta_{ZPL}$ at a generation rate of 1 per second (gray curve) and 1 per hour (red trace). The dashed line points the required system efficiency for the system to be competitive with state-of-the-art SPDC generation.

employing superconducting nanowire single photon-detectors, by using a high NA microscope objective installed inside the cryostat and an adaptive optical system to correct for wavefront aberrations), due to the ZPL branching ratio of $\sim 2.5\%$ the system efficiency would still amount to $\eta_{ZPL} \approx 6.25 \times 10^{-3}$, with which one would generate four 2-photon-cluster events per second, or a 4-photon-cluster event every two-hours.

By setting an expected generation rate of 1 state per second or per hour, eq. 6.21 was used to determine which photon number could be achieved for a given system efficiency $\eta_{ZPL}$ - see Fig. 6.10 b. To be competitive with the state-of-the-art SPDC entanglement generation, where a 10-photon entangled state is produced per hour [16], a minimum system efficiency of $\eta_{zpl} = 0.15$ is required.

Which system efficiencies can be realistically achieved? Regarding collection, experimental near unit efficiencies have been reported for systems where the single-photon emitter is embedded in a layered dielectric media, with an architecture compatible with NV centres [156, 157]. Therefore the last standing practical limitation comes from the weak ZPL, which can be adressed through cavity assisted Purcell enhancement of the optical transition.

One of the most recent experimental realizations of Purcell enhanced NV centres reports overall Purcell factors [4] of $F_p = 2$ [158], which corresponds to an enhancement of the Purcell

[4] The Purcell factor is the ratio between the rate of emission of the emitter in the cavity $r_{cav}$ and in free space $r_{free}$: $F_p = r_{cav}/r_{free}$.

factor of the ZPL line by $F_{p,zpl} \sim 30$ and a resulting ZPL branching ratio of 46%. Assuming unit-collection efficiency for the enhanced emission and setting the system efficiency at $\eta_{zpl} = 0.46$, from Eq. 6.21 and Fig. 6.10 b, one would expect to reach N=24 entangled photon states at a rate of one per hour, or N=14 at one per second, beating the current best SPDC sources. Note that at this level of enhancement, the linewidth of the optical transition will have nearly doubled from a Fourier-limited [5] HWHM = 7 MHz to HWHM = 14 MHz and one would expect negligible cross-talk to the neighbouring transitions, detuned by $\delta \geq 0.88$ GHz in our system.

In the outlook of their own experiment, Riedel et. al [158] argue that a ZPL enhancement by a factor $F_{zpl} = 356$, corresponding to a system efficiency $\eta_{zpl} \approx 0.9$ is within imminent reach through refinement of the fabrication conditions and cavity design. In such regime, a Fourier-limited linewidth of 70 MHz is expected and the decreased lifetime of the excited state would require shorter excitation pulses for time-filtering of the fluorescence. At an excitation pulse linewdith of HWHM = 1.28 GHz we have numerically established that 60 % of the fluorescence can still be collected. This can be further boosted by refining the cross-polarisation rejection of the laser scatter. If cross-excitation of other optical transitions becomes problematic, B-field tuning could be used in the NV centre to split the resonance lines up to a maximum of 3.8 GHz. In the optimistic scenario where perfect cross-polarisation rejection of laser scatter light is available and all cavity-enhanced photons are collected, by setting $\eta_{zpl} = 0.9$, our scheme could potentially yield N=140 (80) photon states at a rate of 1 per hour (second). Achieving such values is of course reliant on the development of high performance optical microcavities [159, 160].

A high frequency, high fidelity spin-photon entanglement source finds application in a wide assortment of quantum information protocols. The flying qubit can be used to teleport information, by means of a photon-photon Bell state measurement, onto the long-lived nuclear spin, which can be used as a quantum memory. In a similar way, it assists the creation of spin-spin entanglement through entanglement swapping of photons [83, 94] and thereby supports the distribution of entanglement in a quantum network. By optionally generating photonic qubits in a time-bin basis our protocol lends itself to the robust propagation of quantum information in optical fibres and therefore suits the task of long-distance entanglement distribution, which is a requirement to scaling quantum networks[14]. This has been corroborated, during the preparation of this manuscript, by the publication of a scheme which relies on the TPC entanglement approach and combines it with photon down-conversion into the telecom band for reduced attenuation upon propagation [161]. The future realization of such networks will set a new stage for distributed quantum computing [162], long-distance

[5] HWHM is the half width at half maximum.

secure communication [3] and sensing.

In the context of (measurement-based) quantum computation, the multiphoton outlook of the TPC entanglement discussed above corresponds to the generation of large linear (1D) cluster chains. The next natural step is to generalize the protocol to yield 2D cluster states, a resource for universal quantum computing. The TPC protocol is compatible with the proposal by Russo et. al [72] where an array of emitters with nearest-neighbour interactions can be used for this purpose. Due to the current generous resource overhead required for each emitter, such architecture is still a distant reality. This points at the emergent necessity for on-chip integration of high finess tunable microcavities [163], supporting a RF/microwave interface for spin control and E-field for tuning of optical transitions. A modular platform with cells of precisely harnessed single-photon emitters [164] will produce 3D cluster states on demand and bring us closer to the realization of a fault-tolerant quantum computer.

# 7 Appendix

## 7.1 The Hamiltonian of the NV Optical Ground State

This section provides a rough derivation of the terms found in the ground state Hamiltonian presented in section 3.4.

### The fine spin-spin interaction and the zero-field-splitting (ZFS)

In electron spin resonance it is common to apply a varying DC magnetic field to lift the degeneracy between magnetic sublevels through a Zeeman interaction. In some cases, even when no external field is applied the magnetic sublevels are degenerate: the energy difference is called the zero-field-splitting. It results from each magnetic dipole creating its own magnetic field which steers the magnetic moments in the vicinity. In other words, the ZFS is a spin-spin interaction between unpaired electrons through magnetic dipole coupling averaged over the electronic orbitals. For a triplet system with two electron spins, the interaction is given by [140, 165]:

$$\hat{H}_{ZFS} = \left\langle \frac{\mu_e^2}{|\vec{r}|^3} \left(3(\hat{S}_1 \cdot \hat{r})(\hat{S}_2 \cdot \hat{r}) - \hat{S}_1 \cdot \hat{S}_2\right) \right\rangle \tag{7.1}$$

where $\mu_e$ is the electronic magnetic moment, $\vec{r}$ is the vector separating the two particles and the angled brackets indicate the average over the electronic orbitals. This interaction can be

represented in a more compact form, as a function of the summed 1/2-spins $\hat{S} = \hat{S}_1 + \hat{S}_2$:

$$\begin{aligned} \hat{H}_{ZFS} &= \vec{S} \cdot \hat{D} \cdot \vec{S} \quad , \quad \text{with} \\ D_{ij} &= \mu_e^2 \left\langle \tfrac{1}{r^3}\delta_{ij} + \tfrac{3\hat{r}_i\hat{r}_j}{r^3} \right\rangle \end{aligned} \tag{7.2}$$

where $\vec{S} = (\hat{S}_x, \hat{S}_y, \hat{S}_z)$ is a 3 element vector containing the spin-1 matrices and $\hat{D}$ is the spin-spin coupling tensor. Note that $\hat{D}$ is symmetric $D_{ij} = D_{ji}$, diagonalizable and traceless $Tr(\hat{D}) = 0$. Diagonalization of $D_{ij}$ reduces it to 3 parameters, $D_{xx}$ , $D_{yy}$ and $D_{zz}$ , such that $D_{xx} + D_{yy} + D_{zz} = 0$. Therefore the spin-spin tensor is fully determined by two parameters, as it is conventionally presented in the literature[140]:

$$\hat{H}_{ZFS} = D_{gs}(\hat{S}_z^2 - S(S+1)/3) + E_{gs}(\hat{S}_x^2 - \hat{S}_y^2) \tag{7.3}$$

where $D$ and $E$ quantify the axial and non-axial zero-field-splitting, respectively. Due to the NV centre symmetry, $E = 0$ and $H_{ZFS}$ takes the form used in eq. 3.4, with $D_{gs} = 2.87$ GHz, leading to the splitting between the $s_z = 0$ and $s_z \pm 1$ sublevels. For a more detailed derivation of $H_{ZFS}$ , consult Ref. [140].

### Hyperfine interaction: dipolar and contact terms

The magnetic hyperfine interaction derives from the dipolar coupling between the electronic magnetic moment $\mu_e$ and the nuclear magnetic moment of the nearby nitrogen $\mu_N$ , which can be found in its two isotopic forms: $^{14}$N with total spin $S = 1$ and $^{15}$N with $S = 1/2$. This interaction is formally similar to the spin-spin dipolar coupling between the two unpaired electrons, as presented in eq. 7.2, with the difference that an extra term accounts for the Fermi contact interaction: the energy of the system when the electron is found inside the nucleus. Note that $\psi_e(\vec{r} = 0) \neq 0$ for s-type orbitals only. The contact term is commonly referred in the literature as the isotropic hyperfine interaction. More quantitatively, the (magnetic) hyperfine interaction is governed by the following Hamiltonian:

$$\begin{aligned} \hat{H}_{HF} &= \vec{S} \cdot \hat{A} \cdot \vec{I} \quad , \quad \text{with} \\ A_{ij} &= \mu_e \mu_N \left[ \left( \underbrace{-\frac{8\pi}{3}|\psi_e(0)^2|}_{\text{Fermi contact}} + \left\langle \tfrac{1}{r^3} \right\rangle \right) \delta_{ij} + \left\langle \tfrac{3\hat{r}_i\hat{r}_j}{r^3} \right\rangle \right] \end{aligned} \tag{7.4}$$

where $\hat{A}$ is the hyperfine coupling tensor, $\vec{S} = (S_x, S_y, S_z)$ are the spin components of the electronic spin-1 system and $\vec{I} = (I_x, I_y, I_z)$ are the components of the spin-1 nitrogen nucleus, assuming the most common isotope $^{14}$N. The angled brackets $\langle\ \rangle$ once again refer to an averaged interaction over the electronic orbital and $|\psi_e(\vec{o})|^2$ is the probability of finding an electron in the nitrogen nucleus. $\vec{r}$ connects the position of the electron to the nucleus and $\hat{r} = (\hat{r}_x, \hat{r}_y, \hat{r}_z)$ is a unit vector along $\vec{r}$. Because $\hat{A}$ is a symmetric tensor, it is diagonalizable and eq. 7.4 can be reduced to:

$$\hat{H}_{HF} = A_{gs}^{\parallel}\hat{S}_z\hat{I}_z + A_{gs}^{\perp}\left[\hat{S}_x\hat{I}_x + \hat{S}_y\hat{I}_y\right] \tag{7.5}$$

where $A_{gs}^{\parallel}$ and $A_{gs}^{\perp}$ are the longitudinal and transversal coupling constants, which implicitly contain the Fermi contact and dipolar contributions. According to theoretical estimates, $A_{gs}^{\parallel} = -2.16 \pm 0.01$ MHz and $A_{gs}^{\perp} = -2.7 \pm 0.07$ MHz [118].

For the case of the NV center, due to the large energy mismatch between the zero-field-splitting $D_{gs} \approx 2870$ MHz and the transversal hyperfine coupling $A_{gs}^{\perp} = -2.7$ MHz, it is common to drop the non-axial terms of the hyperfine interaction $A_{gs}^{\perp}\left[\hat{S}_x\hat{I}_x + \hat{S}_y\hat{I}_y\right]$ in what is called the secular approximation. The Hamiltonian term $\hat{H}_{HF}$ is thereby simplified to:

$$\hat{H}_{HF} \approx A_{gs}^{\parallel}\hat{S}_z\hat{I}_z \tag{7.6}$$

leading to a splitting of the three $^{14}$N nuclear sublevels by $A_{gs}$, as represented in Fig. 3.3.

### Hyperfine interaction: nuclear quadrupole term

When the charge distribution inside a nucleus does not have perfect spherical symmetry, an electric quadrupole moment arises, leading to an interaction between the nucleus with the $\vec{E}$-field gradient created by the surrounding electronic cloud. The quadrupole moment can only exist in nuclei with a magnetic moment $I \geq 1$, which includes the $^{14}$N atom of the NV centre and is therefore relevant for this work. NV centres associated with a $^{15}$N nucleus do not display quadrupolar splitting.

Even though such interaction is more naturally formulated in terms of charge distribution, its most useful representation is a function of the nuclear spin variables. A complete derivation can be found in Slichter [165], but for the sake of brevity will be omitted here and the respective Hamiltonian simply provided [140]:

$$\begin{aligned} \hat{H}_{quad} &= \tfrac{eQ}{6I(2I-1)}\textstyle\sum_{\alpha,\beta=x,y,z}\left[V_{\alpha,\beta}\tfrac{3}{2}(\hat{I}_\alpha\hat{I}_\beta + \hat{I}_\beta\hat{I}_\alpha) - \delta_{\alpha,\beta}\hat{I}^2\right], \quad \text{with} \\ eQ &= \textstyle\int \rho_N(3z^2 - r^2)dV \end{aligned} \tag{7.7}$$

where $eQ$ is the nuclear quadrupole moment, $V_{a,\beta} = d^2V/dx_a dx_\beta$ are the second derivatives of the electric potential at the nucleus and $\hat{I}_a$ the nuclear spin-1 operators along the Cartesian coordinate $a \in (x, y, z)$. Through the same steps used for the zero-field-splitting Hamiltonian, $\hat{H}_{quad}$ can be diagonalized into a $3 \times 3$ traceless operator, which is fully characterized by an axial term $P_{gs}^{\parallel}$ along the quantization axis $\hat{z}$ and a non-axial coefficient $P_{gs}^{\perp}$. For the case of the NV centre, due to symmetry, $P_{gs}^{\perp} = 0$ and the nuclear quadrupole energy simplifies to the form:

$$\hat{H}_{quad} = P_{gs}^{\parallel} \left[\hat{I}_z^2 - I(I+1)/3\right] \tag{7.8}$$

which causes an energy splitting between the $I_z = 0$ and $I_z = \pm 1$ terms by $P_{gs}^{\parallel}$, as illustrated in fig. 3.3. Theoretical estimates of its value point at $P_{gs}^{\parallel} = -4.95 \pm 0.01$ MHz [118].

### The Zeeman interaction

The energy of an electronic spin magnetic moment interacting with a static magnetic field $\vec{B}$ is given by the Zeeman Hamiltonian. In its most general form:

$$\hat{H}_{Zm} = \mu_B \, \vec{B} \cdot \hat{g} \cdot \vec{S} \tag{7.9}$$

where $\mu_B$ is the Bohr magneton, $\vec{S} = (\hat{S}_x, \hat{S}_y, \hat{S}_z)$ is the electronic spin vector, $\vec{B} = (B_x, B_y, B_z)$ the magnetic field vector and $\hat{g}$ is the g-tensor, a symmetric, traceless, second-rank tensor that associates a spin with the corresponding magnetic moment: $\vec{\mu} = \mu_B \hat{g} \cdot \vec{S}$. Without loss of generality, this interaction can be represented along its principal axes, leading to the diagonalization of $\hat{g}$ and $\hat{H}_{Zm}$:

$$\hat{H}_{Zm} = \mu_B \left(g_z B_z S_z + g_x B_x S_x + g_y B_y S_y\right) \tag{7.10}$$

Due to the $C_{3V}$ symmetry of the NV centre, $g_x = g_y = g_\perp$ and the Hamiltonian acquires the simplified form:

$$\hat{H}_{Zm} = \mu_B \left( g^{\parallel} B_z S_z + g^{\perp} (B_x S_x + B_y S_y) \right) \tag{7.11}$$

with $g^{\parallel}$ and $g^{\perp}$ denoted as the longitudinal and transversal g-factors. It must be noted that in the experimental runs described in this thesis, the static magnetic field was aligned with the $\hat{z}$ principal axis of the NV centre, such that the Zeeman energy is reduced to its longitudinal term $\hat{H}_{Zm} = \mu_B \left( g^{\parallel} B_z S_z \right)$.

Besides the electronic Zeeman splitting, also the nuclear magnetic moment interacts with a static external magnetic field $\vec{B}$. This interaction is however more simple, because isotropic, allowing to reduce the nuclear $\hat{g}$ tensor to a single scalar, the nuclear g-factor $g_N$. The nuclear

Zeeman Hamiltonian is then given by:

$$\hat{H}_{Zm,N} = \mu_N g_N \vec{I} \cdot \vec{B} \tag{7.12}$$

where $\mu_N$ is the nuclear magneton. For practical purposes, this term is neglected, due to its comparatively small magnitude with respect to the electronic Zeeman term:
$\mu_B g^{\|} \approx 10^3 \times \mu_N g_N$.

## 7.2 Demonstrating Elements of Measurement-Based Quantum Error Correction

This section presents the results of the tomographic measurements on the different generated cluster states, corresponding to different Z-rotations applied to qubits 2 and/or 3.

### 7.2.1 Fidelities of Resource Cluster States

The tomographic reconstructions of the density matrices used for the presented results are shown here, for the following cases:

1. Full phase flip on qubit 3, $e^{-(\pi/2)Z_3}$, shown in Fig. 7.1
2. Half phase flip on qubit 3, $e^{-(\pi/4)Z_3}$, shown in Fig. 7.2
3. Full phase flip on qubit 2, $e^{-(\pi/2)Z_2}$, shown in Fig. 7.3
4. Half phase flip on qubit 2, $e^{-(\pi/4)Z_2}$, shown in Fig. 7.4

The density matrices are presented in a $Z \otimes X \otimes X \otimes Z$ basis and the wireframe indicates the ideally expected state.

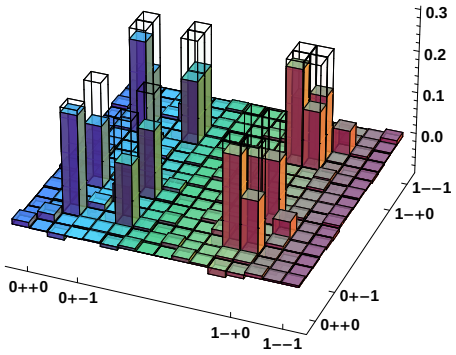


**Figure 7.1:** Real part of density matrix entries of the box cluster state after a full-phase flip occurred on qubit 3, corresponding to $F = 0.656 \pm 0.006$, via local unitary operations. The imaginary components were all below 0.032 and therefore are not presented here.

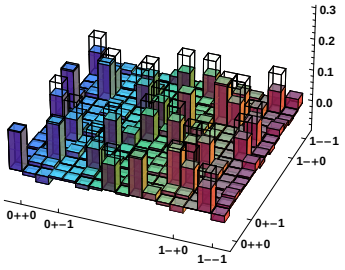


**Figure 7.2:** Real components of the density matrix, after a rotation $e^{-i(\pi/4)Z_3}$ occurred on qubit 3, corresponding to a fidelity $F = 0.667 \pm 0.009$.

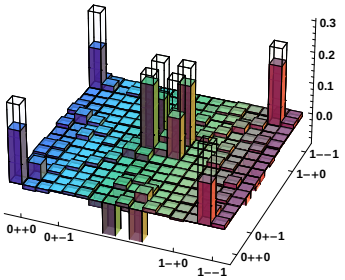


**Figure 7.3:** Real components of the density matrix, after a full phase flip ($e^{-i(\pi/2)Z_3}$) occurred on qubit 2, corresponding to a fidelity $F = 0.646 \pm 0.008$.

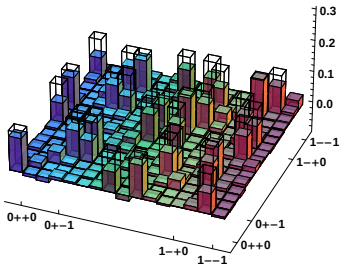


**Figure 7.4:** Real part of density matrix of the box cluster state, after a rotation ($e^{-i(\pi/4)Z_3}$) was applied to qubit 2, amounting to a fidelity $F = 0.641 \pm 0.009$.

### 7.2.2 Encoded States and Decoding Fidelities

The set of encoded states with respective analytic description can be found in Table 7.1.

| Measured State Lab | | Measured State Box | | Encoded State Box | | | | |
|---|---|---|---|---|---|---|---|---|
| Qubit | Basis | Qubit | Basis | Qubit | | Basis | $\theta$ | $\varphi$ |
| $\|+\rangle$ | $\sigma_x$ | $\|0\rangle$ | $\sigma_z$ | $\|0\rangle$ | | $\sigma_z$ | 0° | 0° |
| $\|0\rangle$ | $\sigma_z$ | $\|+\rangle$ | $\sigma_x$ | $\|+\rangle$ | $\frac{1}{\sqrt{2}}(\|0\rangle + \|1\rangle)$ | $\sigma_x$ | 90° | 0° |
| $\|-_i\rangle$ | $-\sigma_y$ | $\|+_i\rangle$ | $\sigma_y$ | $\|-_i\rangle$ | $\frac{1}{\sqrt{2}}(\|0\rangle - i\|1\rangle)$ | $-\sigma_y$ | 90° | −90° |
| $\|P\rangle$ | $\sigma_x + \sigma_y$ | $\|U\rangle$ | $\sigma_z - \sigma_y$ | $\|T\rangle$ | $\frac{1}{\sqrt{2}}(\|+\rangle + e^{-i\pi/4}\|-\rangle)$ | $\sigma_z + \sigma_y$ | 45° | 90° |
| $\|M\rangle$ | $\sigma_x - \sigma_y$ | $\|T\rangle$ | $\sigma_z + \sigma_y$ | $\|U\rangle$ | $\frac{1}{\sqrt{2}}(\|+\rangle + e^{i\pi/4}\|-\rangle)$ | $\sigma_z - \sigma_y$ | 45° | −90° |
| $\|Q\rangle$ | $\sigma_x + \sigma_z$ | $\|Q\rangle$ | $\sigma_z + \sigma_x$ | $\|Q\rangle$ | $\frac{1}{\sqrt{2}}(\|+_i\rangle + e^{i\pi/4}\|-_i\rangle)$ | $\sigma_z + \sigma_x$ | 45° | 0° |
| $\|S\rangle$ | $\sigma_x - \sigma_z$ | $\|N\rangle$ | $\sigma_z - \sigma_x$ | $\|N\rangle$ | $\frac{1}{\sqrt{2}}(\|+_i\rangle + e^{-i\pi/4}\|-_i\rangle)$ | $\sigma_z - \sigma_x$ | 45° | 180° |
| $\|T\rangle$ | $\sigma_z + \sigma_y$ | $\|M\rangle$ | $\sigma_x - \sigma_y$ | $\|P\rangle$ | $\frac{1}{\sqrt{2}}(\|0\rangle + e^{+i\pi/4}\|1\rangle)$ | $\sigma_x + \sigma_y$ | 90° | 45° |
| $\|U\rangle$ | $\sigma_z - \sigma_y$ | $\|P\rangle$ | $\sigma_x + \sigma_y$ | $\|M\rangle$ | $\frac{1}{\sqrt{2}}(\|0\rangle + e^{-i\pi/4}\|1\rangle)$ | $\sigma_x - \sigma_y$ | 90° | −45° |

**Table 7.1:** Initial states of qubit 1 reported in different notations: the "measured state lab" shows the projection state $a^*|0\rangle + \beta^*|1\rangle$ of qubit 1 of $|\psi_{lab}\rangle$ (see main text) and corresponding basis; the "measured state box" entry shows the projection state $a^*|0\rangle + \beta^*|1\rangle$ of qubit 1 of $|\psi_{box}\rangle$ and corresponding basis; and the encoded state box notation shows the encoded qubit 1 in the box cluster notation. In this case, the table specifies the explicit qubit definition per input state, the corresponding basis and the respective spherical coordinates.

In the following tables, it is reported the fidelities related to decoded qubits per type of implemented error: $e^{-i\frac{\pi}{2}Z}$ error on qubit 2, $e^{-i\frac{\pi}{2}Z}$ error on qubit 3, $e^{-i\frac{\pi}{4}Z}$ error on qubit 2 and $e^{-i\frac{\pi}{4}Z}$ error on qubit 3. The different syndrome outcomes are considered, each associated with a corrective operation $X_4$ or no operation at all. Specifically two tables are shown for the full phase flip $Z$ error type, the first related to the outcomes with no need of recovery operation and the second related to the results after the recovery operation $X$. The same is shown for the half-flip $e^{-i\frac{\pi}{4}Z}$ error type.

The last column of each table shows fidelities for decoded qubits in the presence of two errors, on both qubit 2 and 3. When this case happens the results have to be discarded since the relative syndrome outcomes can be confused with the ones where just one error occurs.

| **Encoded State** | **NO Error** | **Error $Z_3$** | **Error $Z_2$** | **Error $Z_2Z_3$** |
|---|---|---|---|---|
| $\|0\rangle$ | F=0.967 $\pm$ 0.011 | F=0.874 $\pm$ 0.022 | F=0.904 $\pm$ 0.021 | F=0.886 $\pm$ 0.022 |
| $\|+\rangle$ | F=0.944 $\pm$ 0.017 | F=0.945 $\pm$ 0.016 | F=0.943 $\pm$ 0.015 | F=0.969$\pm$ 0.009 |
| $\|-_i\rangle$ | F=0.956 $\pm$ 0.012 | F=0.925 $\pm$ 0.019 | F=0.912 $\pm$ 0.019 | F=0.905 $\pm$ 0.019 |
| $\|T\rangle$ | F=0.820 $\pm$ 0.030 | F=0.965 $\pm$ 0.021 | F=0.971 $\pm$ 0.014 | F=0.907 $\pm$ 0.028 |
| $\|U\rangle$ | F=0.863 $\pm$ 0.025 | F=0.957 $\pm$ 0.013 | F=0.927 $\pm$ 0.025 | F=0.885 $\pm$ 0.028 |
| $\|Q\rangle$ | F=0.938 $\pm$ 0.026 | F=0. 898$\pm$ 0.033 | F=0.915 $\pm$ 0.026 | F=0.976 $\pm$ 0.009 |
| $\|N\rangle$ | F=0.967 $\pm$ 0.020 | F=0.940 $\pm$ 0.024 | F=0.915 $\pm$ 0.026 | F=0.922 $\pm$ 0.024 |
| $\|P\rangle$ | F=0.895 $\pm$ 0.033 | F=0.902 $\pm$ 0.026 | F=0.810 $\pm$ 0.036 | F=0.910 $\pm$ 0.028 |
| $\|M\rangle$ | F=0.918 $\pm$ 0.026 | F=0.965 $\pm$ 0.016 | F=0.947 $\pm$ 0.023 | F=0.970 $\pm$ 0.018 |

**Table 7.2:** Fidelities of different encoded and decoded states after a full phase flip, $e^{-(\pi/2)Z}$, ocurred on qubit 2 and/or 3, but no recovery operation was necessary.

| **Encoded State** | **NO Error** | **Error $Z_3$** | **Error $Z_2$** | **Error $Z_2Z_3$** |
|---|---|---|---|---|
| $\|0\rangle$ | F=0.767 $\pm$ 0.032 | F=0.716 $\pm$ 0.035 | F=0.793 $\pm$ 0.030 | F=0.784 $\pm$ 0.028 |
| $\|+\rangle$ | F=0.948 $\pm$ 0.016 | F=0.945 $\pm$ 0.018 | F=0.944 $\pm$ 0.014 | F=0.943 $\pm$ 0.015 |
| $\|-_i\rangle$ | F=0.684 $\pm$ 0.036 | F=0.674 $\pm$ 0.038 | F=0.710 $\pm$ 0.036 | F=0.658 $\pm$ 0.034 |
| $\|T\rangle$ | F=0.686 $\pm$ 0.033 | F=0.809 $\pm$ 0.031 | F=0.792 $\pm$ 0.032 | F=0.700 $\pm$ 0.028 |
| $\|U\rangle$ | F=0.681 $\pm$ 0.037 | F=0.771 $\pm$ 0.032 | F=0.662 $\pm$ 0.034 | F=0.740 $\pm$ 0.038 |
| $\|Q\rangle$ | F=0.741 $\pm$ 0.044 | F=0.776 $\pm$ 0.034 | F=0.833 $\pm$ 0.031 | F=0.813 $\pm$ 0.029 |
| $\|N\rangle$ | F=0.793 $\pm$ 0.047 | F=0.875 $\pm$ 0.029 | F=0.843 $\pm$ 0.029 | F=0.962 $\pm$ 0.027 |
| $\|P\rangle$ | F=0.750 $\pm$ 0.029 | F=0.811 $\pm$ 0.031 | F=0.790 $\pm$ 0.028 | F=0.862 $\pm$ 0.024 |
| $\|M\rangle$ | F=0.800 $\pm$ 0.035 | F=0.801 $\pm$ 0.038 | F=0.823 $\pm$ 0.029 | F=0.895 $\pm$ 0.030 |

**Table 7.3:** Fidelities of different encoded and decoded states after a full phase flip, $e^{-(\pi/2)Z}$, ocurred on qubit 2 and/or 3 and a recovery operation was performed.

| Encoded State | $e^{-i(\pi/4)\ Z_3}$ Error | | $e^{-i(\pi/4)\ Z_2}$ Error | |
|---|---|---|---|---|
| | **NO Error** * | **Error** $Z_3$ | **NO Error** | **Error** * $Z_2$ |
| $\|0\rangle$ | F=0.896 $\pm$ 0.027 | F=0.865 $\pm$ 0.035 | F=0.909 $\pm$ 0.021 | F=0.927 $\pm$ 0.015 |
| $\|+\rangle$ | F=0.861 $\pm$ 0.034 | F=0.913 $\pm$ 0.022 | F=0.936 $\pm$ 0.021 | F=0.986 $\pm$ 0.007 |
| $\|-_i\rangle$ | F=0.908 $\pm$ 0.024 | F=0.865 $\pm$ 0.025 | F=0.945 $\pm$ 0.017 | F=0.914 $\pm$ 0.022 |
| $\|T\rangle$ | F=0.850 $\pm$ 0.042 | F=0.880 $\pm$ 0.040 | F=0.823 $\pm$ 0.036 | F=0.842 $\pm$ 0.030 |
| $\|U\rangle$ | F=0.951 $\pm$ 0.034 | F=0.951 $\pm$ 0.013 | F=0.930 $\pm$ 0.028 | F=0.903 $\pm$ 0.028 |
| $\|Q\rangle$ | F=0.849 $\pm$ 0.037 | F=0.854 $\pm$ 0.035 | F=0.905 $\pm$ 0.031 | F=0.937 $\pm$ 0.028 |
| $\|N\rangle$ | F=0.963 $\pm$ 0.023 | F=0.942 $\pm$ 0.024 | F=0.894 $\pm$ 0.027 | F=0.923 $\pm$ 0.025 |
| $\|P\rangle$ | F=0.871 $\pm$ 0.030 | F=0.964 $\pm$ 0.021 | F=0.972 $\pm$ 0.011 | F=0.972 $\pm$ 0.015 |
| $\|M\rangle$ | F=0.956 $\pm$ 0.022 | F=0.984 $\pm$ 0.016 | F=0.990 $\pm$ 0.009 | F=0.929 $\pm$ 0.025 |

**Table 7.4:** Fidelities of different encoded and decoded states after a half phase flip, $e^{-(\pi/4)Z}$, ocurred on qubit 2 and/or 3, but no recovery operation was necessary.

| Encoded State | $e^{-i(\pi/4)\ Z_3}$ Error | | $e^{-i(\pi/4)\ Z_2}$ Error | |
|---|---|---|---|---|
| | **NO Error** * | **Error** $Z_3$ | **NO Error** | **Error** * $Z_2$ |
| $\|0\rangle$ | F=0.702 $\pm$ 0.038 | F=0.843 $\pm$ 0.280 | F=0.690 $\pm$ 0.036 | F=0.721 $\pm$ 0.029 |
| $\|+\rangle$ | F=0.948 $\pm$ 0.015 | F=0.981 $\pm$ 0.008 | F=0.896 $\pm$ 0.024 | F=0.837$\pm$ 0.023 |
| $\|-_i\rangle$ | F=0.629. $\pm$ 0.039 | F=0.814 $\pm$ 0.035 | F=0.697 $\pm$ 0.040 | F=0.644 $\pm$ 0.030 |
| $\|T\rangle$ | F=0.658 $\pm$ 0.033 | F=0.691 $\pm$ 0.038 | F=0.699 $\pm$ 0.037 | F=0.656 $\pm$ 0.033 |
| $\|U\rangle$ | F=0.677 $\pm$ 0.032 | F=0.814 $\pm$ 0.037 | F=0.813 $\pm$ 0.039 | F=0.776 $\pm$ 0.034 |
| $\|Q\rangle$ | F=0.832 $\pm$ 0.032 | F=0.818 $\pm$ 0.031 | F=0.842 $\pm$ 0.0345 | F=0.734 $\pm$ 0.033 |
| $\|N\rangle$ | F=0.932 $\pm$ 0.028 | F=0.857 $\pm$ 0.038 | F=0.794 $\pm$ 0.041 | F=0.894 $\pm$ 0.031 |
| $\|P\rangle$ | F=0.749 $\pm$ 0.029 | F=0.919 $\pm$ 0.028 | F=0.799 $\pm$ 0.031 | F=0.706 $\pm$ 0.031 |
| $\|M\rangle$ | F=0.775 $\pm$ 0.034 | F=0.941 $\pm$ 0.025 | F=0.906$\pm$ 0.028 | F=0.823 $\pm$ 0.032 |

**Table 7.5:** Fidelities of different encoded and decoded states after a half phase flip, $e^{-(\pi/4)Z}$, ocurred on qubit 2 and/or 3 and a recovery operation was performed.

# References


[1] Jonathan P. Dowling and Gerard J. Milburn. Quantum technology: The second quantum revolution. *Philosophical Transactions of the Royal Society of London. Series A: Mathematical, Physical and Engineering Sciences*, 361(1809):1655–1674, August 2003.

[2] C. L. Degen, F. Reinhard, and P. Cappellaro. Quantum sensing. *Reviews of Modern Physics*, 89(3):035002, July 2017.

[3] Nicolas Gisin and Rob Thew. Quantum communication. *Nature Photonics*, 1(3): 165–171, March 2007.

[4] Michael A. Nielsen and Isaac L. Chuang. *Quantum Computation and Quantum Information*. Cambridge University Press, Cambridge ; New York, 10th anniversary ed edition, 2010.

[5] Herbert Walther, Benjamin T. H. Varcoe, Berthold-Georg Englert, and Thomas Becker. Cavity quantum electrodynamics. *Reports on Progress in Physics*, 69:1325–1382, May 2006.

[6] Alexandre Blais, Ren-Shou Huang, Andreas Wallraff, S. M. Girvin, and R. J. Schoelkopf. Cavity quantum electrodynamics for superconducting electrical circuits: An architecture for quantum computation. *Physical Review A*, 69(6):062320, June 2004.

[7] Nicolai Friis, Oliver Marty, Christine Maier, Cornelius Hempel, Milan Holzäpfel, Petar Jurcevic, Martin B. Plenio, Marcus Huber, Christian Roos, Rainer Blatt, and Ben Lanyon. Observation of Entangled States of a Fully Controlled 20-Qubit System. *Physical Review X*, 8(2):021012, April 2018.

[8] P Walther, K J Resch, T Rudolph, E Schenck, H Weinfurter, V Vedral, M Aspelmeyer, and a Zeilinger. Experimental one-way quantum computing. *Nature*, 434(7030): 169–76, March 2005.

[9] Pieter Kok, Kae Nemoto, T. C. Ralph, Jonathan P. Dowling, and G. J. Milburn. Linear optical quantum computing with photonic qubits. *Reviews of Modern Physics*, 79(1): 135–174, January 2007.

[10] David G. Cory, Amr F. Fahmy, and Timothy F. Havel. Ensemble quantum computing by NMR spectroscopy. *Proceedings of the National Academy of Sciences*, 94(5):1634–1639, March 1997.

[11] Daniel Loss and David P. DiVincenzo. Quantum computation with quantum dots. *Physical Review A*, 57(1):120–126, January 1998.

[12] Jörg Wrachtrup and Fedor Jelezko. Processing quantum information in diamond. *Journal of Physics: Condensed Matter*, 18(21):S807–S824, May 2006.

[13] H. J. Briegel, D. E. Browne, W. Dür, R. Raussendorf, and M. Van den Nest. Measurement-based quantum computation. *Nature Physics*, 5(1):19–26, January 2009.

[14] Stephanie Wehner, David Elkouss, and Ronald Hanson. Quantum internet: A vision for the road ahead. *Science*, 362(6412):eaam9288, October 2018.

[15] Xing-Can Yao, Tian-Xiong Wang, Ping Xu, He Lu, Ge-Sheng Pan, Xiao-Hui Bao, Cheng-Zhi Peng, Chao-Yang Lu, Yu-Ao Chen, and Jian-Wei Pan. Observation of eight-photon entanglement. *Nature Photonics*, 6(4):225–228, April 2012.

[16] Xi-Lin Wang, Luo-Kan Chen, W. Li, H.-L. Huang, C. Liu, C. Chen, Y.-H. Luo, Z.-E. Su, D. Wu, Z.-D. Li, H. Lu, Y. Hu, X. Jiang, C.-Z. Peng, L. Li, N.-L. Liu, Yu-Ao Chen, Chao-Yang Lu, and Jian-Wei Pan. Experimental Ten-Photon Entanglement. *Physical Review Letters*, 117(21), November 2016.

[17] Terry Rudolph. Why I am optimistic about the silicon-photonic route to quantum computing. *APL Photonics*, 2(3):030901, March 2017.

[18] Netanel Lindner and Terry Rudolph. Proposal for Pulsed On-Demand Sources of Photonic Cluster State Strings. *Physical Review Letters*, 103(11):113602, September 2009.

[19] C. Schön, E. Solano, F. Verstraete, J. Cirac, and M. Wolf. Sequential Generation of Entangled Multiqubit States. *Physical Review Letters*, 95(11):110503, September 2005.

[20] Igor Aharonovich, Dirk Englund, and Milos Toth. Solid-state single-photon emitters. *Nature Photonics*, 10(10):631–641, 2016.

[21] E. Knill. Quantum computing with realistically noisy devices. *Nature*, 434(7029): 39–44, March 2005.

[22] J. Brendel, N. Gisin, W. Tittel, and H. Zbinden. Pulsed Energy-Time Entangled Twin-Photon Source for Quantum Communication. *Physical Review Letters*, 82(12): 2594–2597, 1999.

[23] Kristiaan De Greve, Leo Yu, Peter L. McMahon, Jason S. Pelc, Chandra M. Natarajan, Na Young Kim, Eisuke Abe, Sebastian Maier, Christian Schneider, Martin Kamp, Sven Höfling, Robert H. Hadfield, Alfred Forchel, M. M. Fejer, and Yoshihisa Yamamoto. Quantum-dot spin–photon entanglement via frequency downconversion to telecom wavelength. *Nature*, 491(7424):421–425, November 2012.

[24] G. D. Fuchs, G. Burkard, P. V. Klimov, and D. D. Awschalom. A quantum memory intrinsic to single nitrogen–vacancy centres in diamond. *Nature Physics*, 7(10):789–793, October 2011.

[25] Richard P. Feynman, Frank L. Vernon, and Robert W. Hellwarth. Geometrical Representation of the Schrödinger Equation for Solving Maser Problems. *Journal of Applied Physics*, 28(1):49–52, January 1957.

[26] Serge Haroche and Jean-Michel Raimond. *Exploring the Quantum*, volume 1. Oxford Graduate Texts, 2012.

[27] L. Allen and J. H. Eberly. *Optical Resonance and Two-Level Atoms*. Dover, New York, 1987.

[28] Malcolm H. Levitt. *Spin Dynamics: Basics of Nuclear Magnetic Resonance*. John Wiley & Sons, Chichester, England ; Hoboken, NJ, 2nd ed edition, 2008.

[29] N Bar-Gill, L M Pham, A Jarmola, D Budker, and R L Walsworth. Solid-state electronic spin coherence time approaching one second. *Nature communications*, 4:1743, 2013.

[30] Dik Bouwmeester, Jian-Wei Pan, Klaus Mattle, Manfred Eibl, Harald Weinfurter, and Anton Zeilinger. Experimental quantum teleportation. *Nature*, 390(6660):575–579, December 1997.

[31] Mattle, Weinfurter, Kwiat, and Zeilinger. Dense coding in experimental quantum communication. *Physical review letters*, 76(25):4656–4659, 1996.

[32] Michael a. Nielsen. Optical Quantum Computation Using Cluster States. *Physical Review Letters*, 93(4):040503, July 2004.

[33] H J Kimble. The quantum internet. *Nature*, 453(7198):1023–30, June 2008.

[34] S. J. van Enk, N. Lütkenhaus, and H. J. Kimble. Experimental procedures for entanglement verification. *Physical Review A*, 75(5):052318, May 2007.

[35] Martin B. Plenio and Shashank S. Virmani. An Introduction to Entanglement Theory. In Erika Andersson and Patrik Öhberg, editors, *Quantum Information and Coherence*, Scottish Graduate Series, pages 173–209. Springer International Publishing, Cham, 2014.

[36] Daniel Gottesman and Isaac L. Chuang. Demonstrating the viability of universal quantum computation using teleportation and single-qubit operations. *Nature*, 402 (6760):390, November 1999.

[37] E Knill, R Laflamme, and G J Milburn. A scheme for efficient quantum computation with linear optics. *Nature*, 409(6816):46–52, January 2001.

[38] Robert Raussendorf and Hans J. Briegel. A One-Way Quantum Computer. *Physical Review Letters*, 86(22):5188–5191, May 2001.

[39] Robert Prevedel, Philip Walther, Felix Tiefenbacher, Pascal Böhi, Rainer Kaltenbaek, Thomas Jennewein, and Anton Zeilinger. High-speed linear optics quantum computing using active feed-forward. *Nature*, 445(7123):65–9, January 2007.

[40] Yuuki Tokunaga, Shin Kuwashiro, Takashi Yamamoto, Masato Koashi, and Nobuyuki Imoto. Generation of High-Fidelity Four-Photon Cluster State and Quantum-Domain Demonstration of One-Way Quantum Computing. *Physical Review Letters*, 100(21): 210501, May 2008.

[41] I Schwartz, D Cogan, E R Schmidgall, Y Don, L Gantz, and O Kenneth. Deterministic Generation of a Cluster State of Entangled Photons. *Science*, 1, 2016.

[42] Ming Gong, Ming-Cheng Chen, Yarui Zheng, Shiyu Wang, Chen Zha, Hui Deng, Zhiguang Yan, Hao Rong, Yulin Wu, Shaowei Li, Fusheng Chen, Youwei Zhao, Futian Liang, Jin Lin, Yu Xu, Cheng Guo, Lihua Sun, Anthony D. Castellano, Haohua Wang, Chengzhi Peng, Chao-Yang Lu, Xiaobo Zhu, and Jian-Wei Pan. Genuine 12-Qubit Entanglement on a Superconducting Quantum Processor. *Physical Review Letters*, 122 (11):110501, March 2019.

[43] B. P. Lanyon, P. Jurcevic, M. Zwerger, C. Hempel, E. A. Martinez, W. Dür, H. J. Briegel, R. Blatt, and C. F. Roos. Measurement-Based Quantum Computation with Trapped Ions. *Physical Review Letters*, 111(21):210501, November 2013.

[44] Shota Yokoyama, Ryuji Ukai, Seiji C. Armstrong, Chanond Sornphiphatphong, Toshiyuki Kaji, Shigenari Suzuki, Jun-ichi Yoshikawa, Hidehiro Yonezawa, Nicolas C. Menicucci, and Akira Furusawa. Ultra-large-scale continuous-variable cluster states multiplexed in the time domain. *Nature Photonics*, 7(12):982–986, December 2013.

[45] Moran Chen, Nicolas C. Menicucci, and Olivier Pfister. Experimental Realization of Multipartite Entanglement of 60 Modes of a Quantum Optical Frequency Comb. *Physical Review Letters*, 112(12):120505, March 2014.

[46] E. Knill, R. Laflamme, A. Ashikhmin, H. Barnum, L. Viola, and W. H. Zurek. Introduction to Quantum Error Correction. *arXiv:quant-ph/0207170*, July 2002.

[47] Daniel Gottesman. An Introduction to Quantum Error Correction and Fault-Tolerant Quantum Computation. *arXiv:0904.2557*, April 2009.

[48] R. Barends, J. Kelly, A. Megrant, A. Veitia, D. Sank, E. Jeffrey, T. C. White, J. Mutus, A. G. Fowler, B. Campbell, Y. Chen, Z. Chen, B. Chiaro, A. Dunsworth, C. Neill, P. O'Malley, P. Roushan, A. Vainsencher, J. Wenner, A. N. Korotkov, A. N. Cleland, and John M. Martinis. Superconducting quantum circuits at the surface code threshold for fault tolerance. *Nature*, 508(7497):500–503, April 2014.

[49] Simon J Devitt, William J Munro, and Kae Nemoto. Quantum error correction for beginners. *Reports on Progress in Physics*, 76(7):076001, July 2013.

[50] Peter W. Shor. Scheme for reducing decoherence in quantum computer memory. *Physical Review A*, 52(4):R2493–R2496, October 1995.

[51] Andrew Steane. Multiple-particle interference and quantum error correction. *Proceedings of the Royal Society of London. Series A: Mathematical, Physical and Engineering Sciences*, 452(1954):2551–2577, November 1996.

[52] A. R. Calderbank and Peter W. Shor. Good quantum error-correcting codes exist. *Physical Review A*, 54(2):1098–1105, August 1996.

[53] Daniel Gottesman. Stabilizer Codes and Quantum Error Correction. *arXiv:quant-ph/9705052*, May 1997.

[54] D. G. Cory. Experimental Quantum Error Correction. *Physical Review Letters*, 81(10): 2152–2155, 1998.

[55] T. B. Pittman, B. C. Jacobs, and J. D. Franson. Demonstration of quantum error correction using linear optics. *Physical Review A*, 71(5):052332, May 2005.

[56] J. Chiaverini, D. Leibfried, T. Schaetz, M. D. Barrett, R. B. Blakestad, J. Britton, W. M. Itano, J. D. Jost, E. Knill, C. Langer, R. Ozeri, and D. J. Wineland. Realization of quantum error correction. *Nature*, 432(7017):602–605, December 2004.

[57] J. I. Cirac and P. Zoller. Quantum Computations with Cold Trapped Ions. *Physical Review Letters*, 74(20):4091–4094, May 1995.

[58] M. Zwerger, W. Dür, and H. J. Briegel. Measurement-based quantum repeaters. *Physical Review A*, 85(6):062326, June 2012.

[59] M. Zwerger, H. J. Briegel, and W. Dür. Universal and Optimal Error Thresholds for Measurement-Based Entanglement Purification. *Physical Review Letters*, 110(26): 260503, June 2013.

[60] M. Zwerger, H. J. Briegel, and W. Dür. Hybrid architecture for encoded measurement-based quantum computation. *Scientific Reports*, 4:5364, June 2014.

[61] Daniel E. Browne and Terry Rudolph. Resource-Efficient Linear Optical Quantum Computation. *Physical Review Letters*, 95(1):010501, June 2005.

[62] Chao-Yang Lu, Xiao-Qi Zhou, Otfried Gühne, Wei-Bo Gao, Jin Zhang, Zhen-Sheng Yuan, Alexander Goebel, Tao Yang, and Jian-Wei Pan. Experimental entanglement of six photons in graph states. *Nature Physics*, 3(2):91–95, February 2007.

[63] Wei-Bo Gao, Chao-Yang Lu, Xing-Can Yao, Ping Xu, Otfried Gühne, Alexander Goebel, Yu-Ao Chen, Cheng-Zhi Peng, Zeng-Bing Chen, and Jian-Wei Pan. Experimental demonstration of a hyper-entangled ten-qubit Schrödinger cat state. *Nature Physics*, 6 (5):331–335, May 2010.

[64] Christopher Gerry and Peter Knight. *Introductory Quantum Optics*. Cambridge University Press, Cambridge, UK ; New York, 1 edition edition, November 2004.

[65] Paul G. Kwiat, Klaus Mattle, Harald Weinfurter, Anton Zeilinger, Alexander V. Sergienko, and Yanhua Shih. New High-Intensity Source of Polarization-Entangled Photon Pairs. *Physical Review Letters*, 75(24):4337–4341, December 1995.

[66] Mag Robert Prevedel. *Experimental All-Optical One-Way Quantum Computing*. PhD thesis, University of Vienna, 2008. Publication Title: PhD Thesis.

[67] Harald Weinfurter and Marek Żukowski. Four-photon entanglement from down-conversion. *Physical Review A*, 64(1):010102, June 2001.

[68] Warren Paul Grice and Ian Alexander Walmsley. Spectral Information and Distinguishability in Type-II Down-Conversion with a Broadband Pump. 10.1103/PhysRevA.56.1627, 1997.

[69] G. Di Giuseppe, L. Haiberger, F. De Martini, and A. V. Sergienko. Quantum interference and indistinguishability with femtosecond pulses. *Physical Review A*, 56(1):R21–R24, July 1997.

[70] Peter J. Mosley, Jeff S. Lundeen, Brian J. Smith, Piotr Wasylczyk, Alfred B. U'Ren, Christine Silberhorn, and Ian A. Walmsley. Heralded Generation of Ultrafast Single Photons in Pure Quantum States. *Physical Review Letters*, 100(13):133601, April 2008.

[71] Christoph Simon and Jian-Wei Pan. Polarization Entanglement Purification using Spatial Entanglement. *Physical Review Letters*, 89(25):257901, December 2002.

[72] Antonio Russo, Edwin Barnes, and Sophia E. Economou. Generation of arbitrary all-photonic graph states from quantum emitters. *New Journal of Physics*, 21(5):055002, May 2019.

[73] Sophia E. Economou, Netanel Lindner, and Terry Rudolph. Optically Generated 2-Dimensional Photonic Cluster State from Coupled Quantum Dots. *Physical Review Letters*, 105(9), August 2010.

[74] Antonio Russo, Edwin Barnes, and Sophia E. Economou. Photonic graph state generation from quantum dots and color centers for quantum communications. *Physical Review B*, 98(8):085303, August 2018.

[75] A. Gruber, A. Dräbenstedt, C. Tietz, L. Fleury, J. Wrachtrup, and C. von Borczyskowski. Scanning Confocal Optical Microscopy and Magnetic Resonance on Single Defect Centers. *Science*, 276(5321):2012–2014, June 1997.

[76] Christian Kurtsiefer, Sonja Mayer, Patrick Zarda, and Harald Weinfurter. Stable Solid-State Source of Single Photons. *Physical Review Letters*, 85(2):4, 2000.

[77] V. M. Acosta, E. Bauch, M. P. Ledbetter, C. Santori, K.-M. C. Fu, P. E. Barclay, R. G. Beausoleil, H. Linget, J. F. Roch, F. Treussart, S. Chemerisov, W. Gawlik, and D. Budker. Diamonds with a high density of nitrogen-vacancy centers for magnetometry applications. *Physical Review B*, 80(11):115202, September 2009.

[78] F.C. Waldermann, P. Olivero, J. Nunn, K. Surmacz, Z.Y. Wang, D. Jaksch, R.A. Taylor, I.A. Walmsley, M. Draganski, P. Reichart, A.D. Greentree, D.N. Jamieson, and S. Prawer. Creating diamond color centers for quantum optical applications. *Diamond and Related Materials*, 16(11):1887–1895, November 2007.

[79] Boris Naydenov, V. Richter, Johannes Beck, Matthias Steiner, Philipp Neumann, Gopalakrishnan Balasubramanian, Jocelyn Achard, Fedor Jelezko, Jörg Wrachtrup, and Rafi Kalish. Enhanced generation of single optically active spins in diamond by ion implantation. *Applied Physics Letters*, 96(16):163108, April 2010.

[80] L Robledo, L Childress, H Bernien, B Hensen, P F Alkemade, and R Hanson. High-fidelity projective read-out of a solid-state spin quantum register. *Nature*, 477 (7366):574–578, 2011.

[81] E van Oort, N B Manson, and M Glasbeek. Optically detected spin coherence of the diamond N-V centre in its triplet ground state. *Journal of Physics C: Solid State Physics*, 21 (23):4385–4391, August 1988.

[82] David A. Hopper, Henry J. Shulevitz, and Lee C. Bassett. Spin Readout Techniques of the Nitrogen-Vacancy Center in Diamond. *Micromachines*, 9(9):437, September 2018.

[83] Peter C. Humphreys, Norbert Kalb, Jaco P. J. Morits, Raymond N. Schouten, Raymond F. L. Vermeulen, Daniel J. Twitchen, Matthew Markham, and Ronald Hanson. Deterministic delivery of remote entanglement on a quantum network. *Nature*, 558 (7709):268–273, June 2018.

[84] G. D. Fuchs, V. V. Dobrovitski, D. M. Toyli, F. J. Heremans, and D. D. Awschalom. Gigahertz Dynamics of a Strongly Driven Single Quantum Spin. *Science*, 326(5959): 1520–1522, December 2009.

[85] A. Jarmola, V. M. Acosta, K. Jensen, S. Chemerisov, and D. Budker. Temperature- and magnetic-field-dependent longitudinal spin relaxation in nitrogen-vacancy ensembles in diamond. *Physical Review Letters*, 108(19):1–5, 2012.

[86] T. Astner, J. Gugler, A. Angerer, S. Wald, S. Putz, N. J. Mauser, M. Trupke, H. Sumiya, S. Onoda, J. Isoya, J. Schmiedmayer, P. Mohn, and J. Majer. Solid-state electron spin lifetime limited by phononic vacuum modes. *Nature Materials*, 17(4):313, April 2018.

[87] Gopalakrishnan Balasubramanian, Philipp Neumann, Daniel Twitchen, Matthew Markham, Roman Kolesov, Norikazu Mizuochi, Junichi Isoya, Jocelyn Achard, Johannes Beck, Julia Tissler, Vincent Jacques, Philip R. Hemmer, Fedor Jelezko, and Jörg Wrachtrup. Ultralong spin coherence time in isotopically engineered diamond. *Nature Materials*, 8(5):383–387, May 2009.

[88] F. Jelezko, T. Gaebel, I. Popa, M. Domhan, A. Gruber, and J. Wrachtrup. Observation of Coherent Oscillation of a Single Nuclear Spin and Realization of a Two-Qubit Conditional Quantum Gate. *Physical Review Letters*, 93(13):130501, September 2004.

[89] M. V. G. Dutt, L. Childress, L. Jiang, E. Togan, J. Maze, F. Jelezko, A. S. Zibrov, P. R. Hemmer, and M. D. Lukin. Quantum Register Based on Individual Electronic and Nuclear Spin Qubits in Diamond. *Science*, 316(5829):1312–1316, June 2007.

[90] Matthias Pfender, Nabeel Aslam, Patrick Simon, Denis Antonov, Gergő Thiering, Sina Burk, Felipe Fávaro de Oliveira, Andrej Denisenko, Helmut Fedder, Jan Meijer, Jose A. Garrido, Adam Gali, Tokuyuki Teraji, Junichi Isoya, Marcus William Doherty, Audrius Alkauskas, Alejandro Gallo, Andreas Grüneis, Philipp Neumann, and Jörg Wrachtrup. Protecting a Diamond Quantum Memory by Charge State Control. *Nano Letters*, 17 (10):5931–5937, October 2017.

[91] Philipp Neumann, Johannes Beck, Matthias Steiner, Florian Rempp, Helmut Fedder, Philip R. Hemmer, Jörg Wrachtrup, and Fedor Jelezko. Single-Shot Readout of a Single Nuclear Spin. *Science*, 329(5991):542–544, July 2010.

[92] E Togan, Y Chu, a S Trifonov, L Jiang, J Maze, L Childress, M V G Dutt, a S Sørensen, P R Hemmer, a S Zibrov, and M D Lukin. Quantum entanglement between an optical photon and a solid-state spin qubit. *Nature*, 466(7307):730–4, August 2010.

[93] H Bernien, B Hensen, W Pfaff, G Koolstra, M S Blok, L Robledo, T H Taminiau, M Markham, D J Twitchen, L Childress, and R Hanson. Heralded entanglement between solid-state qubits separated by three metres. *Nature*, 497(7447):86–90, May 2013.

[94] W. Pfaff, B. J. Hensen, H. Bernien, S. B. van Dam, M. S. Blok, T. H. Taminiau, M. J. Tiggelman, R. N. Schouten, M. Markham, D. J. Twitchen, and R. Hanson. Unconditional quantum teleportation between distant solid-state quantum bits. *Science*, 345(6196):532–535, August 2014.

[95] G. Waldherr, Y. Wang, S. Zaiser, M. Jamali, T. Schulte-Herbrüggen, H. Abe, T. Ohshima, J. Isoya, J. F. Du, P. Neumann, and J. Wrachtrup. Quantum error correction in a solid-state hybrid spin register. *Nature*, 506(7487):204–207, February 2014.

[96] T H Taminiau, J Cramer, T van der Sar, V V Dobrovitski, and R Hanson. Universal control and error correction in multi-qubit spin registers in diamond. *Nature nanotechnology*, 9(3):171–176, February 2014.

[97] Norbert Kalb, Andreas A. Reiserer, Peter C. Humphreys, Jacob J. W. Bakermans, Sten J. Kamerling, Naomi H. Nickerson, Simon C. Benjamin, Daniel J. Twitchen, Matthew Markham, and Ronald Hanson. Entanglement Distillation between Solid-State Quantum Network Nodes. *Science*, 932(June):928–932, 2017.

[98] Alexios Beveratos, Rosa Brouri, Thierry Gacoin, André Villing, Jean-Philippe Poizat, and Philippe Grangier. Single Photon Quantum Cryptography. *Physical Review Letters*, 89 (18):187901, October 2002.

[99] R. Alléaume, F. Treussart, G. Messin, Y. Dumeige, J.-F. Roch, A. Beveratos, R. Brouri-Tualle, J.-P. Poizat, and P. Grangier. Experimental open-air quantum key distribution with a single-photon source. *New Journal of Physics*, 6:92–92, July 2004.

[100] L Childress, M V Gurudev Dutt, J M Taylor, a S Zibrov, F Jelezko, J Wrachtrup, P R Hemmer, and M D Lukin. Coherent dynamics of coupled electron and nuclear spin qubits in diamond. *Science (New York, N.Y.)*, 314(5797):281–5, October 2006.

[101] V. M. Acosta, E. Bauch, M. P. Ledbetter, A. Waxman, L.-S. Bouchard, and D. Budker. Temperature Dependence of the Nitrogen-Vacancy Magnetic Resonance in Diamond. *Physical Review Letters*, 104(7), February 2010.

[102] J. M. Taylor, P. Cappellaro, L. Childress, L. Jiang, D. Budker, P. R. Hemmer, A. Yacoby, R. Walsworth, and M. D. Lukin. High-sensitivity diamond magnetometer with nanoscale resolution. *Nature Physics*, 4(10):810–816, October 2008.

[103] Gopalakrishnan Balasubramanian, I. Y. Chan, Roman Kolesov, Mohannad Al-Hmoud, Julia Tisler, Chang Shin, Changdong Kim, Aleksander Wojcik, Philip R. Hemmer, Anke Krueger, Tobias Hanke, Alfred Leitenstorfer, Rudolf Bratschitsch, Fedor Jelezko, and Jörg Wrachtrup. Nanoscale imaging magnetometry with diamond spins under ambient conditions. *Nature*, 455(7213):648–651, October 2008.

[104] F. Dolde, H. Fedder, M. W. Doherty, T. Nöbauer, F. Rempp, G. Balasubramanian, T. Wolf, F. Reinhard, L. C. L. Hollenberg, F. Jelezko, and J. Wrachtrup. Electric-field sensing using single diamond spins. *Nature Physics*, 7(6):459–463, June 2011.

[105] M. Howard, J. Twamley, C. Wittmann, T. Gaebel, F. Jelezko, and J. Wrachtrup. Quantum process tomography and Linblad estimation of a solid-state qubit. *New Journal of Physics*, 8(3):33–33, March 2006.

[106] B. Hensen, N. Kalb, M. S. Blok, A. E. Dréau, A. Reiserer, R. F. L. Vermeulen, R. N. Schouten, M. Markham, D. J. Twitchen, K. Goodenough, D. Elkouss, S. Wehner, T. H. Taminiau, and R. Hanson. Loophole-free Bell test using electron spins in diamond: Second experiment and additional analysis. *Scientific Reports*, 6(1), September 2016.

[107] G. Waldherr, P. Neumann, S. F. Huelga, F. Jelezko, and J. Wrachtrup. Violation of a Temporal Bell Inequality for Single Spins in a Diamond Defect Center. *Physical Review Letters*, 107(9):090401, August 2011.

[108] Neil W. Ashcroft and N. David Mermin. *Solid State Physics*. Holt, Rinehart and Winston, New York, 1976.

[109] J Walker. Optical absorption and luminescence in diamond. *Reports on Progress in Physics*, 42(10):1605–1659, October 1979.

[110] Igor Aharonovich and Elke Neu. Diamond Nanophotonics. *Advanced Optical Materials*, 2(10):911–928, October 2014.

[111] Element Six. The Element Six CVD Diamond Handbook. *Www.E6.Com*, 2016.

[112] N. Aslam, G. Waldherr, P. Neumann, F. Jelezko, and J. Wrachtrup. Photo-induced ionization dynamics of the nitrogen vacancy defect in diamond investigated by single-shot charge state detection. *New Journal of Physics*, 15(1):013064, January 2013.

[113] S. Pezzagna, B. Naydenov, F. Jelezko, J. Wrachtrup, and J. Meijer. Creation efficiency of nitrogen-vacancy centres in diamond. *New Journal of Physics*, 12(6):065017, June 2010.

[114] Faruque M. Hossain, Marcus W. Doherty, Hugh F. Wilson, and Lloyd C. L. Hollenberg. Ab Initio Electronic and Optical Properties of the NV- Center in Diamond. *Physical Review Letters*, 101(22):226403, November 2008.

[115] Yiwen Chu and Mikhail D Lukin. Quantum optics with nitrogen-vacancy centers in diamond. 2015.

[116] J. R. Maze, A. Gali, E. Togan, Y. Chu, A. Trifonov, E. Kaxiras, and M. D. Lukin. Properties of nitrogen-vacancy centers in diamond: The group theoretic approach. *New Journal of Physics*, 13(2):025025, February 2011.

[117] M. W. Doherty, F. Dolde, H. Fedder, F. Jelezko, J. Wrachtrup, N. B. Manson, and L. C. L. Hollenberg. Theory of the ground-state spin of the NV - center in diamond. *Physical Review B*, 85(20), May 2012.

[118] Marcus W. Doherty, Neil B. Manson, Paul Delaney, Fedor Jelezko, Jörg Wrachtrup, and Lloyd C.L. Hollenberg. The nitrogen-vacancy colour centre in diamond. *Physics Reports*, 528(1):1–45, July 2013.

[119] A. M. Stoneham. *Theory of Defects in Solids: Electronic Structure of Defects in Insulators and Semiconductors*. Oxford Classic Texts in the Physical Sciences. Clarendon Press ; Oxford University Press, Oxford : New York, 2001.

[120] Lee C. Bassett, F. Joseph Heremans, David J. Christle, Christopher G. Yale, Guido Burkard, Bob B. Buckley, and David D. Awschalom. Ultrafast optical control of orbital and spin dynamics in a solid-state defect. *Science*, 345(6202):1333–1337, September 2014.

[121] Ph Tamarat, N B Manson, J P Harrison, R L McMurtrie, A Nizovtsev, C Santori, R G Beausoleil, P Neumann, T Gaebel, F Jelezko, P Hemmer, and J Wrachtrup. Spin-flip and spin-conserving optical transitions of the nitrogen-vacancy centre in diamond. *New Journal of Physics*, 10(4):045004, April 2008.

[122] a. Batalov, V. Jacques, F. Kaiser, P. Siyushev, P. Neumann, L. Rogers, R. McMurtrie, N. Manson, F. Jelezko, and J. Wrachtrup. Low Temperature Studies of the Excited-State Structure of Negatively Charged Nitrogen-Vacancy Color Centers in Diamond. *Physical Review Letters*, 102(19):195506, May 2009.

[123] G. D. Fuchs, V. V. Dobrovitski, R. Hanson, A. Batra, C. D. Weis, T. Schenkel, and D. D. Awschalom. Excited-State Spectroscopy Using Single Spin Manipulation in Diamond. *Physical Review Letters*, 101(11):117601, September 2008.

[124] Keunhong Jeong, Anna J. Parker, Ralph H. Page, Alexander Pines, Christophoros C. Vassiliou, and Jonathan P. King. Understanding the Magnetic Resonance Spectrum of Nitrogen Vacancy Centers in an Ensemble of Randomly Oriented Nanodiamonds. *The Journal of Physical Chemistry C*, 121(38):21057–21061, September 2017.

[125] Lucio Robledo, Hannes Bernien, Toeno van der Sar, and Ronald Hanson. Spin dynamics in the optical cycle of single nitrogen-vacancy centres in diamond. *New Journal of Physics*, 13(2):025013, February 2011.

[126] M L Goldman, A Sipahigil, N Y Yao, S D Bennett, M Markham, D J Twitchen, A Kubanek, and M D Lukin. Phonon-Induced Population Dynamics and Intersystem Crossing in Nitrogen-Vacancy Centers. *Physical Review Letters*, 2:1–7, 2014.

[127] M. L. Goldman, M. W. Doherty, A. Sipahigil, N. Y. Yao, S. D. Bennett, N. B. Manson, A. Kubanek, and M. D. Lukin. State-selective intersystem crossing in nitrogen-vacancy centers. *Physical Review B*, 91(16):165201, April 2015.

[128] Peter W. Atkins and Ronald S. Friedman. *Molecular Quantum Mechanics*. Oxford University Press, Oxford, New York, fifth edition edition, November 2010.

[129] M W Doherty, N B Manson, P Delaney, and L C L Hollenberg. The negatively charged nitrogen-vacancy centre in diamond: The electronic solution. *New Journal of Physics*, 13 (2):025019, February 2011.

[130] Kai-Mei C. Fu, Charles Santori, Paul E. Barclay, Lachlan J. Rogers, Neil B. Manson, and Raymond G. Beausoleil. Observation of the Dynamic Jahn-Teller Effect in the Excited States of Nitrogen-Vacancy Centers in Diamond. *Physical Review Letters*, 103(25): 256404, December 2009.

[131] F. Kaiser, V. Jacques, A. Batalov, P. Siyushev, F. Jelezko, and J. Wrachtrup. Polarization properties of single photons emitted by nitrogen-vacancy defect in diamond at low temperature. page 4, 2009.

[132] M. Irie. Photochromism: Memories and Switches-Introduction. *Chemical Reviews*, 100 (5):1683–1684, May 2000.

[133] P. Siyushev, H. Pinto, M. Vörös, a. Gali, F. Jelezko, and J. Wrachtrup. Optically controlled switching of the charge state of a single nitrogen-vacancy center in diamond at cryogenic temperatures. *Physical Review Letters*, 110(16):1–5, 2013.

[134] D. Le Sage, L. M. Pham, N. Bar-Gill, C. Belthangady, M. D. Lukin, A. Yacoby, R. L. Walsworth, and R. L. Walsworth. Efficient photon detection from color centers in a diamond optical waveguide. *Physical Review B*, 85(12):121202, March 2012.

[135] Robert H Webb. Confocal optical microscopy. *Rep. Prog. Phys*, 59(October 1995): 427–471, 1996.

[136] Taras Plakhotnik, W.E Moerner, Victor Palm, and Urs P Wild. Single molecule spectroscopy: Maximum emission rate and saturation intensity. *Optics Communications*, 114(1-2):83–88, January 1995.

[137] Mohammad Jamali, Ilja Gerhardt, Mohammad Rezai, Karsten Frenner, Helmut Fedder, and Jörg Wrachtrup. Microscopic diamond solid-immersion-lenses fabricated around single defect centers by focused ion beam milling. *Review of Scientific Instruments*, 85 (12):123703, December 2014.

[138] C. J. Foot. *Atomic Physics*. Number 7. Atomic, Optical, and laser physics in Oxford Master Series in Physics. Oxford University Press, Oxford ; New York, 2005.

[139] G. Davies and M. F. Hamer. Optical studies of the 1.945 eV vibronic band in diamond. *Proceedings of the Royal Society of London. A. Mathematical and Physical Sciences*, February 1976.

[140] N. M. Atherton. *Principles of Electron Spin Resonance*. Ellis Horwood Series in Physical Chemistry. Ellis Horwood, Chichester, 1993.

[141] A. Dréau, M. Lesik, L. Rondin, P. Spinicelli, O. Arcizet, J.-F. Roch, and V. Jacques. Avoiding power broadening in optically detected magnetic resonance of single NV defects for enhanced dc magnetic field sensitivity. *Physical Review B*, 84(19):195204, November 2011.

[142] Springfield C.;, Chia-Chen Hsu, Tzer-Hsiang Huang, Wei-Ching Chuang, Yu-Sheng Tsai, Jen-Yu Shieh, and Chung-Yee Leung. Heterodyne interferometric Measurement of the thermo-optic coefficient of single mode fiber. *Chinese Journal of Physics*, 2000 / 06 / 01, 2000.

[143] T. S. Priest, K. T. Jones, G. B. Scelsi, and G. A. Woolsey. Thermal Coefficients of Refractive Index and Expansion in Optical Fibre Sensing. In *12th International Conference on Optical Fiber Sensors (1997), Paper OWC41*, page OWC41. Optical Society of America, October 1997.

[144] I. H. Malitson. Interspecimen Comparison of the Refractive Index of Fused Silica. *JOSA*, 55(10):1205–1209, October 1965.

[145] Norman Richard Draper and Harry Smith. *Applied Regression Analysis*. Wiley Series in Probability and Statistics. Wiley, New York, 3rd ed edition, 1998.

[146] Sen Yang, Ya Wang, D. D. Bhaktavatsala Rao, Thai Hien Tran, Ali S. Momenzadeh, M. Markham, D. J. Twitchen, Ping Wang, Wen Yang, Rainer Stöhr, Philipp Neumann, Hideo Kosaka, and Jörg Wrachtrup. High-fidelity transfer and storage of photon states in a single nuclear spin. *Nature Photonics*, 10(8):507–511, August 2016.

[147] Daniela Pagliero, Abdelghani Laraoui, Jacob D. Henshaw, and Carlos A. Meriles. Recursive polarization of nuclear spins in diamond at arbitrary magnetic fields. *Applied Physics Letters*, 105(24):242402, December 2014.

[148] Tanmoy Chakraborty, Jingfu Zhang, and Dieter Suter. Polarizing the electronic and nuclear spin of the NV-center in diamond in arbitrary magnetic fields: Analysis of the optical pumping process. *New Journal of Physics*, 19(7), 2017.

[149] V. Jacques, P. Neumann, J. Beck, M. Markham, D. Twitchen, J. Meijer, F. Kaiser, G. Balasubramanian, F. Jelezko, and J. Wrachtrup. Dynamic Polarization of Single Nuclear Spins by Optical Pumping of Nitrogen-Vacancy Color Centers in Diamond at Room Temperature. *Physical Review Letters*, 102(5):057403, February 2009.

[150] Hai-Jing Wang, Chang S. Shin, Claudia E. Avalos, Scott J. Seltzer, Dmitry Budker, Alexander Pines, and Vikram S. Bajaj. Sensitive magnetic control of ensemble nuclear spin hyperpolarization in diamond. *Nature Communications*, 4(1):1–7, June 2013.

[151] M. L. Goldman, T. L. Patti, D. Levonian, S. F. Yelin, and M. D. Lukin. Optical Control of a Single Nuclear Spin in the Solid State. *arXiv:1808.04346*, August 2018.

[152] E. Togan, Y. Chu, A. Imamoglu, and M. D. Lukin. Laser cooling and real-time measurement of the nuclear spin environment of a solid-state qubit. *Nature*, 478(7370): 497–501, October 2011.

[153] P. London, J. Scheuer, J.-M. Cai, I. Schwarz, A. Retzker, M. B. Plenio, M. Katagiri, T. Teraji, S. Koizumi, J. Isoya, R. Fischer, L. P. McGuinness, B. Naydenov, and F. Jelezko. Detecting and Polarizing Nuclear Spins with Double Resonance on a Single Electron Spin. *Physical Review Letters*, 111(6), August 2013.

[154] F. Poggiali, P. Cappellaro, and N. Fabbri. Measurement of the excited-state transverse hyperfine coupling in NV centers via dynamic nuclear polarization. *Physical Review B*, 95 (19):195308, May 2017.

[155] B. B. Blinov, D. L. Moehring, L.-M. Duan, and C. Monroe. Observation of entanglement between a single trapped atom and a single photon. *Nature*, 428(6979):153–157, March 2004.

[156] K. G. Lee, X. W. Chen, H. Eghlidi, P. Kukura, R. Lettow, A. Renn, V. Sandoghdar, and S. Götzinger. A planar dielectric antenna for directional single-photon emission and near-unity collection efficiency. *Nature Photonics*, 5(3):166–169, March 2011.

[157] Xiangzhi Li, Robert A. Scully, Kamran Shayan, Yue Luo, and Stefan Strauf. Near-Unity Light Collection Efficiency from Quantum Emitters in Boron Nitride by Coupling to Metallo-Dielectric Antennas. *ACS Nano*, 13(6):6992–6997, June 2019.

[158] Daniel Riedel, Immo Söllner, Brendan J. Shields, Sebastian Starosielec, Patrick Appel, Elke Neu, Patrick Maletinsky, and Richard J. Warburton. Deterministic Enhancement of Coherent Photon Generation from a Nitrogen-Vacancy Center in Ultrapure Diamond. *Physical Review X*, 7(3):031040, September 2017.

[159] Suzanne B. van Dam, Maximilian Ruf, and Ronald Hanson. Optimal design of diamond-air microcavities for quantum networks using an analytical approach. *New Journal of Physics*, 20(11):115004, November 2018.

[160] Georg Wachter, Stefan Kuhn, Stefan Minniberger, Cameron Salter, Peter Asenbaum, James Millen, Michael Schneider, Johannes Schalko, Ulrich Schmid, André Felgner, Dorothee Hüser, Markus Arndt, and Michael Trupke. Silicon microcavity arrays with open access and a finesse of half a million. *Light: Science & Applications*, 8(1):37, December 2019.

[161] Anna Tchebotareva, Sophie L. N. Hermans, Peter C. Humphreys, Dirk Voigt, Peter J. Harmsma, Lun K. Cheng, Ad L. Verlaan, Niels Dijkhuizen, Wim de Jong, Anaïs Dréau, and Ronald Hanson. Entanglement between a Diamond Spin Qubit and a Photonic Time-Bin Qubit at Telecom Wavelength. *Physical Review Letters*, 123(6):063601, August 2019.

[162] R. Van Meter and S. J. Devitt. The Path to Scalable Distributed Quantum Computing. *Computer*, 49(9):31–42, September 2016.

[163] Christian Derntl, Michael Schneider, Johannes Schalko, Achim Bittner, Jörg Schmiedmayer, Ulrich Schmid, and Michael Trupke. Arrays of open, independently tunable microcavities. *Optics Express*, 22(18):22111–22120, September 2014.

[164] Kae Nemoto, Michael Trupke, Simon J. Devitt, Ashley M. Stephens, Burkhard Scharfenberger, Kathrin Buczak, Tobias Nöbauer, Mark S. Everitt, Jörg Schmiedmayer, and William J. Munro. Photonic Architecture for Scalable Quantum Information Processing in Diamond. *Physical Review X*, 4(3):031022, August 2014.

[165] Charles P. Slichter. *Principles of Magnetic Resonance*. Harper and Row, New York, 1963.